

**Studies of inorganic and organic interactions
with supported and free standing phospholipid
monolayers and bilayers**

Ashi Rashid

*Submitted in accordance with the requirements for the degree of
Doctor of philosophy*

School of Chemistry
The University of Leeds

July, 2015

The candidate confirms that the work submitted is her own, except where work which has formed part of jointly-authored publications has been included. The contribution of the candidate and the other authors to this work has been explicitly indicated below. The candidate confirms that appropriate credit has been given within the thesis where reference has been made to the work of others.

The work in Chapter 3 of the thesis has appeared in the publication as follows:

Role of electrolyte in the occurrence of the voltage induced phase transitions in a dioleoyl phosphatidylcholine monolayer on Hg published in *Electrochimica Acta*, 2015, A. Rashid, A. Vakurov and A. Nelson.

This copy has been supplied on the understanding that it is copyright material and that no quotation from the thesis may be published without proper acknowledgement.

The right of Ashi Rashid to be identified as Author of this work has been asserted by her in accordance with the Copyright, Designs and Patents Act 1988.

© 2015 The University of Leeds and Ashi Rashid

Acknowledgements

My first and the foremost thanks are to Almighty Allah (SWT) for his blessing on me in my entire life and for enabling me to achieve my goals successfully.

I owe my deepest gratitude to my supervisor *Prof. Andrew Nelson* for his kind supervision. I am extremely thankful and indebted to him for sharing his expertise, skills and knowledge and for his sincere and valuable guidance and encouragement extended to me whilst allowing me the room to work in my own way. I can say that “one simply could not wish for a better or friendlier supervisor”. I would also like to thank my lab colleagues especially *Dr Alexander Vakurov* for always being a great help and giving the best suggestions. *Dr Terence Kee* and *Dr David Bryant* are thanked for their collaboration in electrochemical study of small peptides. Furthermore, *Commonwealth scholarship commission* and *University of Engineering and Technology (Lahore)* are thanked for granting scholarship and study leave respectively. I wish to acknowledge *Dr Inam-ul-Haque* (my ex-supervisor) who always encouraged me for higher studies.

I would like to mention the role of tiring efforts by my father late *Ahmad Ali Awan* to educate me. It was always a major stimulus behind my studies. I also wish to make a special mention of my mother *Kishwer Sultana*. Without her help, sincere efforts and prayers, I wouldn't have done it. My brothers *Adnan Awan* and *Rizwan Awan* helped me to their best in times of need. Thanks to *Moon* and *Naveed bhai* for hosting us and providing entertainment on all event holidays!

Thanks to my lovely daughters *Ayesha* and *Fatima* for making my stay in Leeds beautiful!

Lastly, I feel short of words and expression to thank my husband *Muhammad Rashid* for his patience, encouragement and moral support during this period. He always boosted my drooping spirits. Without his help, I would not have been able to move on with this venture.

Abstract

The application of self-assembled monolayers on Hg in biosensor technology dictates the need to develop a thorough understanding of the system by using it to develop the structure-activity relations of biologically active compounds and upgrading the system to stable bilayer configurations on Hg. In this thesis four aspects of the properties of phospholipid layers on Hg in electric fields have been investigated as follows:

(1) Effects of electrolyte ions on the potential-induced phase transitions exhibited by 1,2-dioleoyl phosphatidylcholine (DOPC) monolayer on hanging mercury drop electrode (HMDE) and mercury film electrode (MFE) are examined using alternating current voltammetry (ACV) and chronoamperometry. Results show that the underlying mechanism of phase transitions is affected by the concentration and sizes of electrolyte ions affecting the structure of electrical double layer at the lipid electrolyte and Hg electrolyte interface.

(2) Fluorescence spectroscopic and electrochemical impedance techniques have been applied to study the interaction of substituted biphenyls with DOPC vesicles and Hg supported monolayers. The extent and type of interaction of substituted biphenyls with membrane models depends on the position and electron withdrawing/donating properties of substituents.

(3) Electrochemical impedance used to study the interactions of small di- and tri-peptides of prebiotic relevance with DOPC monolayers on Hg shows that dispersion and electrostatic forces are responsible for interactions between DOPC monolayer and relatively apolar, and polar charged peptides respectively. In addition, an increase in their chain length causes an increase in DOPC/peptide interactions.

(4) DOPC bilayers can be supported on HMDE and their lipid density varied by controlling the electrode area using RCV. The bilayer configurations are found less permeable than monolayers to aqueous Zn^{2+} at potentials positive to -1.2 V using chronoamperometry. Impedance studies have highlighted the ion movements into the DOPC bilayer as dielectric relaxation. Furthermore, silica nanoparticles have also been found to interact with bilayer configurations using RCV.

Contents

Acknowledgement	iii
Abstract	iv
Contents	v
List of Figures	x
List of Tables	xxiii
Abbreviations	xxiv
Commonly used symbols and physical constants	xxv
Chapter-1	
Introduction	1
1.1 Biomembranes	1
1.1.1 Structure of bio membranes	2
1.1.2 Composition	3
1.1.2.1 Phospholipids	3
1.1.2.2 Sterols	5
1.1.2.3 Proteins	5
1.1.3 Biomembrane function	6
1.1.4 Electrical properties of biomembranes	6
1.1.4.1 Dielectric properties	6
1.1.4.2 Membrane capacitance	7
1.1.4.3 Membrane potential	8

1.2	<i>RC</i> series circuit.....	9
1.2.1	Biomembrane as a series <i>RC</i> circuit	10
1.3	Membranes in toxicology	11
1.4	Membrane Models.....	12
1.4.1	Lipid bilayers	13
1.4.1.1	Lipid Vesicles	13
1.4.1.2	Black lipid membranes (BLMs)	14
1.4.1.3	Supported lipid bilayers (SLBs)	14
1.4.1.4	Tethered lipid bilayer membranes (t-LBMs)	14
1.4.2	Lipid self-assembled monolayers (SAMs).....	15
1.5	Interfacial electrochemical studies	18
1.5.1	Electrical double layer	18
1.5.1.1	Helmholtz model	18
1.5.1.2	Gouy-Chapman model	19
1.5.1.3	Stern model.....	20
1.5.2	Electrocapillarity	22
1.5.3	HMDE as an electrode material	23
1.5.3.1	Adsorption effects at Hg.....	25
1.5.4	Self assembled monolayers on Hg	26
1.5.4.1	Phase transitions	27
1.5.4.2	Interaction of biologically active compounds with phospholipid monolayer on Hg	29
1.5.5	Phospholipid bilayer on Hg	30
1.6	Biphenyls and their interaction with membrane systems	31
1.7	Aims and objectives	33
1.8	References	34
Chapter-2	Material and methods.....	40
2.1	Electrochemical set-up	40
2.1.1	Electrochemical cell and electrode assembly	40
2.1.1.1	Reference electrode	40
2.1.1.2	Counter/Auxiliary electrode	41

2.1.1.3	Working/Indicator electrode.....	41
2.1.2	Instrumentation	42
2.1.2.1	Potentiostat sensitivity.....	44
2.1.2.2	Potentiostat calibration and speed test.....	44
2.1.2.3	Lock-in amplifier calibration.....	46
2.2	Electrochemical techniques	48
2.2.1	RCV48	
2.2.2	Impedance measurements	49
2.2.2.1	AC Voltammetry	51
2.2.2.2	Electrochemical impedance.....	52
2.2.3	Potential step experiments	56
2.3	Experimental Protocol.....	58
2.3.1	Preparation of electrolyte solution	58
2.3.2	Electrochemical measurements on Hg electrode	59
2.3.3	Formation of DOPC monolayers	63
2.3.4	Electrochemical measurements of DOPC monolayer on Hg	63
2.4	MFE: Pt vs Au.....	66
2.4.1	Pt based MFE	67
2.4.2	Au based MFE	68
2.5	Experimental procedures	73
2.5.1	Capillary treatment.....	73
2.5.2	Assembling a new capillary	74
2.5.3	Initial filling of HMDE with a new capillary.....	74
2.5.4	Re-filling of HMDE	74
2.5.5	Equipment cleaning.....	74
2.6	Fluorescence spectroscopy.....	75
2.6.1	Materials.....	78
2.6.2	Preparation of liposomes.....	79
2.6.3	Instrumentation	79
2.6.4	Experimental procedure	79
2.7	References	81

Chapter-3	Role of electrolyte ions in the occurrence of voltage induced phase transitions in a DOPC monolayer on Hg	83
3.1	Introduction	83
3.2	Results and discussion	86
3.2.1	Effect of inorganic ions on capacitance peak-1	86
3.2.1.1	Ionic strength	86
3.2.1.2	Ionic composition	92
3.2.2	Effect of inorganic ions on capacitance peak-2	97
3.2.2.1	Ionic strength	97
3.2.2.2	Ionic composition	105
3.2.3	Effect of Organic electrolytes	107
3.2.3.1	Capacitance peak-1	107
3.2.3.2	Capacitance peak -2	108
3.2.4	Interaction of phosphorous containing electrolytes with DOPC monolayers on Hg	110
3.3	Conclusions	116
3.4	References	118
Chapter-4	Interaction of di- and tri- peptides with phospholipid monolayers on Hg	122
4.1	Introduction	122
4.2	Results and discussion	126
4.2.1	Aliphatic, apolar and neutral dipeptides	126
4.2.2	Aliphatic, polar, hydrophilic and charged dipeptide	127
4.2.3	Aliphatic, polar, hydrophilic and neutral dipeptide	129
4.2.4	Aromatic, polar, hydrophilic and charged dipeptide	129
4.2.5	Aromatic, apolar and charged dipeptide	136
4.2.6	Effect of chain length	137
4.3	Conclusion	141
4.4	References	142

Chapter-5	Interaction of biphenyl and derivatives with biomimetic lipid membranes	144
5.1	Introduction	144
5.2	Results and discussion	146
5.2.1	Effect of position of substitution	150
5.2.2	Effect of nature of substitution	160
5.3	Conclusions	168
5.4	References	169
Chapter-6	Characterization and application of DOPC bilayer on Hg in the presence of electric field	172
6.1	Introduction	172
6.2	Experimental	173
6.2.1	Materials and methods	173
6.2.2	Electrochemical set-up	174
6.2.3	Electrochemical techniques	174
6.2.3.2	Potential step experiments	175
6.2.3.3	Electrochemical impedance	177
6.2.3.4	Interaction of DOPC bilayer with SiO ₂ nanoparticles	178
6.3	Results and discussion	179
6.3.1	Bilayer formation	179
6.3.2	Permeability studies	184
6.3.3	Impedance studies	191
6.3.4	Interaction of DOPC bilayer with SiO ₂ nanoparticles	198
6.4	Conclusion	200
6.5	References	201
Chapter-7	Conclusion and Future work	203

List of Figures

Figure 1.1: Structural models of a biological membrane (a) Danielli and Davison's model (b) Robertson's model and (c) Singer's model.....	2
Figure 1.2: Schematic diagram of the structure of a phospholipid.	4
Figure 1.3: Electrostatic potentials associated with a lipid bilayer [27].	8
Figure 1.4: Dipole potential of phospholipids with different head groups [35].....	9
Figure 1.5: Equivalent resistor-capacitor circuit for a membrane.....	10
Figure 1.6: A simplified membrane equivalent model.....	11
Figure 1.7: Different supported and unsupported model membrane systems [60].	17
Figure 1.8: Capacitance-potential plot of HMDE in 0.1 mol dm ⁻³ KCl.	19
Figure 1.9: Differential capacitance trends predicted from Helmholtz model (a) Gouy-Chapman model (b) and Stern model (c) of electrical double layer plotted against applied potential.....	21
Figure 1.10: Different models of electrical double layer.	22
Figure 1.11: A diagram showing the relation between surface tension, charge and capacitance of an electrode with respect to applied potential.	23
Figure 1.12: Current (a) and thickness (b) of DOPC bilayer on Hg vs. applied potential plot measured by AFM [81].	31
Figure 1.13: Chemical structure of biphenyl.....	32
Figure 1.14: <i>o</i> , <i>m</i> and <i>p</i> positions of biphenyls.	32
Figure 2.1: HMDE (left) and MFE (right).	41
Figure 2.2: The first electrochemical set up: a photograph of fully assembled electrochemical cell connected to Autolab potentiostat.....	42

Figure 2.3: The second electrochemical set up: a photograph of fully assembled electrochemical cell connected to potentiostat, function generator, lock-in-amplifier and signal generator.....	43
Figure 2.4: The schematic diagram showing the hierarchy of connections made during RCV and ACV measurements using second electrochemical.	43
Figure 2.5: Current versus time plots of 658 Ω resistor and 0.15 μF capacitor in series connected to ACM potentiostat with e-corder (a), ACM potentiostat with powerLab (b) and AutoLab potentiostat with powerLab (c) at a sampling rate of 256 samples (100 KHz) in 2ms. Theoretical current (.....), Experimental current (__), Voltage applied (__ __).....	47
Figure 2.6: Applied potential versus time in CV.	48
Figure 2.7: A sinusoidal AC voltage signal showing peak to peak amplitude and changing polarity over time [118]......	50
Figure 2.8: <i>In phase</i> AC signals (a) <i>Out of phase</i> AC signals (b) [120]......	50
Figure 2.9: An AC potential application to an electrode surface.....	51
Figure 2.10: An AC potential signal superimposed on a DC potential used in AC voltammetry.....	51
Figure 2.11: Double potential step (a) applied to the electrode and resulting non faradaic current response (b) in chronoamperometry.	56
Figure 2.12: Full potential step versus time plots (a) and resulting current-time transients (b) following double potential steps as indicated applied to DOPC monolayer on Hg in 0.1 mol dm ⁻³ KCl solution.	57
Figure 2.13: A current-time transient following a potential step from -0.980 V to -1.019 V applied to DOPC monolayer on Hg in 0.1 mol dm ⁻³ KCl solution.....	58
Figure 2.14: Capacitance current versus potential plots of uncoated HMDE in 0.1 mol dm ⁻³ KCl in the presence (red) and absence (black) of O ₂ acquired using RCV at 40 Vs ⁻¹	60
Figure 2.15: Capacitance-potential plot of uncoated HMDE in the aerated (red) and deaerated (black) 0.1 mol dm ⁻³ KCl solution acquired using ACV at scan rate 5 mVs ⁻¹ , frequency 75 Hz, amplitude 0.0046 V and 90° <i>out of phase</i>	61
Figure 2.16: Impedance data transformed to complex capacitance plane of uncoated HMDE in the deaerated 0.1 mol dm ⁻³ KCl with 0.001 mol dm ⁻³ phosphate buffer, acquired using EIS at -0.4 V, 0.005 V amplitude and 65000-0.1 Hz frequency.	61

Figure 2.17: Capacitance current and capacitance versus potential plots (a, b respectively) and impedance data transformed to complex capacitance plane (c) of uncoated HMDE in the 0.1 mol dm ⁻³ KCl containing organic impurity obtained using RCV at 40 Vs ⁻¹ , ACV at 5 mVs ⁻¹ and EIS at -0.4 V respectively.	62
Figure 2.18: Transfer of DOPC monolayer on MFE from lipid- gas.....	63
Figure 2.19: Capacitance current versus potential plot of DOPC coated HMDE in 0.1 mol dm ⁻³ KCl at 40 Vs ⁻¹ obtained using RCV at switching potential -1.2 V (black) and -1.6 V (red).....	64
Figure 2.20: Capacitance-potential plot of DOPC coated HMDE in the 0.1 mol dm ⁻³ KCl solution obtained using ACV at scan rate 5 mVs ⁻¹ , frequency 75 Hz, amplitude 0.0046 V and 90° <i>out of phase</i>	65
Figure 2.21: Capacitance current and capacitance-potential plot of DOPC coated HMDE in the 0.1 mol dm ⁻³ KCl solution obtained using (a) RCV at 40 Vs ⁻¹ and (b) ACV at 5 mVs ⁻¹ , frequency 75 Hz, amplitude 0.0046 V and 90° <i>out of phase</i>	65
Figure 2.22: Impedance data transformed to complex capacitance plane of DOPC coated HMDE in the 0.1 mol dm ⁻³ KCl solution in the absence (a) and presence (b) of contamination, acquired using EIS at -0.4 V, 0.005 V amplitude and 65000-0.1 Hz frequency.....	66
Figure 2.23: Capacitance current versus potential plots of MFE and DOPC coated MFE immediately after deposition (red), after 5 hr (green) and after 1 month (blue), using Pt as substrate in 0.1 mol dm ⁻³ KCl, obtained using RCV at 40V s ⁻¹	67
Figure 2.24: Microscopic images of MFE using Pt as substrate.....	68
Figure 2.25: Capacitance current versus potential plots of MFE (a) and DOPC coated MFE (b) using Au as substrate, immediately after deposition (black) and after 1 hr (red) in 0.1 mol dm ⁻³ KCl using RCV at 40 Vs ⁻¹	69
Figure 2.26: Microscope images of MFE formed by manual deposition of Hg on Au based MFE.	70
Figure 2.27: Capacitance current versus potential plots of electrochemically deposited MFE (a) and DOPC coated MFE (b) using Au as substrate immediately after deposition (black), after 5 hr (green) and after 24 hr (red), in 0.1 mol dm ⁻³ KCl, obtained using RCV at 40 Vs ⁻¹	71

Figure 2.28: Microscopic images of Au based MFE formed by electrodeposition of Hg from $\text{Hg}(\text{NO}_3)_2$ solution.	72
Figure 2.29: Jablonski's diagram explaining molecular excitations, A-Absorption, F-Fluorescence and S-singlet states [133].....	75
Figure 2.30: A typical Stern Volmer plot for a single class of accessible fluorophore.....	76
Figure 2.31: A typical modified Stern Volmer plot indicating two different fluorophore populations.	78
Figure 2.32: Kinetic plot of re-emitted light intensity for iodide ($0.047 \text{ mol dm}^{-3}$) quenching of <i>o</i> -Cl-BPs in the presence of $0.254 \text{ mmol dm}^{-3}$ DOPC GUV in 0.1 mol dm^{-3} of KCl containing $0.001 \text{ mol dm}^{-3}$ of phosphate buffer. Inset showing subsequent increase in intensity of emitted light after exposing the same solution to light.	80
Figure 3.1: Capacitance (C_{sp}) versus potential ($-E$) plots of DOPC coated HMDE in (a) KCl and (b) KNO_3 obtained using ACV at 0.005 V s^{-1} , 75 Hz, $0.005 \text{ V } \Delta E$ and 90° out of phase.	87
Figure 3.2: $-E_1$ versus $-\log$ ionic strength plot of DOPC coated (a) HMDE (closed triangle) and MFE (open triangle) in KCl and (b) HMDE (closed circles) in KNO_3 obtained using ACV at 0.005 V s^{-1} , 75 Hz, $0.005 \text{ V } \Delta E$ and 90° out of phase.	88
Figure 3.3: Schematic total potential (Ψ_0) profile across DOPC monolayer on Hg electrode showing diffuse layer potential (Ψ_δ) beginning at distance, δ	89
Figure 3.4: Potential shift of capacitance peak-1 (red filled circles) and change of diffuse layer potential at electrode charge value of 0.02 C m^{-2} (black line) ($\Delta-E_1$) versus the concentration of KCl (c_{KCl}). For red filled circles error bars are within symbol size.....	91
Figure 3.5: A diagrammatic representation of EDL and potential drop at the electrode-electrolyte interface varying with electrolyte concentration. \oplus Cation, $-$ water molecule.	92
Figure 3.6: Capacitance (C_{sp}) versus potential ($-E$) plots of DOPC coated HMDE in the 0.1 mol dm^{-3} solution of metal (a) chlorides (b) fluorides and (c) hydroxides, obtained using ACV at 0.005 V s^{-1} , 75 Hz, $0.005 \text{ V } \Delta E$ and 90° out of phase.	93

- Figure 3.7: $-E_1$ versus \log (cation-PC binding constant) of alkali and alkaline earth metal cations of chloride (open triangle), fluoride (open square) and hydroxides (close triangle), (b) an expanded version of (a) (All the error bars are within the symbol size) in 0.1 mol dm^{-3} electrolyte obtained using ACV at 0.005 V s^{-1} , 75 Hz, $0.005 \text{ V } \Delta E$ and 90° out of phase..... 94
- Figure 3.8: A pictorial representation of ion binding with the phospholipid on Hg (L-lithium, N-sodium, K-potassium, R-rubidium and Cs-cesium). 95
- Figure 3.9: $-E_1$ versus \log (anion-PC binding constant) of halide anions of potassium in 0.1 mol dm^{-3} electrolyte obtained using ACV at 0.005 V s^{-1} , 75 Hz, $0.005 \text{ V } \Delta E$ and 90° out of phase. 96
- Figure 3.10: $-E_2$ versus $-\log$ ionic strength plot of DOPC coated (a) HMDE (closed triangle) and MFE (open triangle) in KCl and (b) HMDE (closed circles) in KNO_3 obtained using ACV at 0.005 V s^{-1} , 75 Hz, $0.005 \text{ V } \Delta E$ and 90° out of phase..... 98
- Figure 3.11: I-t transients obtained on application of (a) negatively increasing successive second potential steps from -1.015 V to -1.025 V (b) following potential step from -0.982 V to -0.987 V , red circles show data and black circles show fit, with parameters of the fit shown (c) with removed RC contribution and (d) Q-t transient on integration of RC subtracted I-t transients, from DOPC coated Hg electrode in 0.1 mol dm^{-3} KCl solution..... 100
- Figure 3.12: Step potential ($-E_s$) versus time (t) plots of DOPC monolayer on Hg in (a) 0.05 and (b) 0.1 mol dm^{-3} KCl (solid lines) and corresponding potential pulses after IR correction (dotted lines). Vertical dashed line bisecting potential plateau ($-E_s$) taken as potential initiating N & G transition. Current (I)-time (t) transient following potential step applied to DOPC monolayer on Hg in (c) 0.05 and (d) 0.1 mol dm^{-3} KCl. 101
- Figure 3.13: Composite rate constant (b_f) versus step potential ($-E_s$) plot of DOPC coated HMDE in solutions of 0.05 (closed triangle), 0.1 (open triangle), 0.5 (closed square) and 1.0 (open square) mol dm^{-3} KCl solution. All the error bars are within the symbol size. 102
- Figure 3.14: $-E_0$ versus $-\log$ ionic strength plot of DOPC coated HMDE in KCl solution. All the data in solid line is corrected for IR drop and plots are also shown in dotted line obtained prior to IR drop correction. All the error bars are within the symbol size. 103

Figure 3.15: $\Delta b_f / -\Delta E_s$ versus ionic strength plot of DOPC coated HMDE in KCl solution. All the data in solid line is corrected for <i>IR</i> drop and plots are also shown in dotted line obtained prior to <i>IR</i> drop correction. All the error bars are within the symbol size.	104
Figure 3.16: A diagram representing the electrical double layer at Hg-electrolyte interface in solutions with varying ionic strength.	104
Figure 3.17: $\Delta b_f / -\Delta E_s$ versus cationic hydrated radius (R_h) plot of the DOPC monolayer on Hg in 0.1 mol dm ⁻³ solutions of chlorides (closed triangle), hydroxides (open triangle) and fluorides (open square). All the data presented is corrected for <i>IR</i> drop and error bars are within the symbol size.	106
Figure 3.18: A diagram representing the screening of Hg by various hydrated alkali metal cations (Li^+ , Na^+ and K^+).....	107
Figure 3.19: $-E_1$ versus $-\log$ organic cation concentration ($-\log c$) plot of DOPC coated Hg electrode in 0.1 mol dm ⁻³ KCl electrolyte containing BMIM ⁺ (open triangle), TEA ⁺ (closed triangle) and Cho ⁺ (open square). All the data presented is corrected for <i>IR</i> drop and error bars are within the symbol size.....	108
Figure 3.20: $\Delta b_f / -\Delta E_s$ versus c plot of BMIM ⁺ (open square) and TEC ⁺ (close square) in 0.1 mol dm ⁻³ KCl electrolyte. All the data presented is corrected for <i>IR</i> drop and error bars are within the symbol size.	109
Figure 3.21: $\Delta b_f / -\Delta E_s$ versus $-\log$ water-octanol partition coefficient ($-\log Kow$) plot of different anions of BMIM ⁺ in 0.1 mol dm ⁻³ KCl electrolyte. All the data presented is corrected for <i>IR</i> drop and error bars are within the symbol size.....	109
Figure 3.22: Capacitance (C_{sp}) versus potential ($-E$) plots of DOPC coated HMDE in 0.1 mol dm ⁻³ of KCl and Na ₂ H ₂ P ₂ O ₅ in (a) 3:1, (b) 1:1, (c) 1:3 and (d) 0:1 ratio obtained using ACV at 0.005 V s ⁻¹ , 75 Hz, 0.005 V ΔE and 90° out of phase. Green is after 30 minutes and all black is in 100 % 0.1 mol dm ⁻³ KCl solution.	111
Figure 3.23: Capacitance (C_{sp}) versus potential ($-E$) plots of HMDE in 0.1 mol dm ⁻³ of KCl (black) and Na ₂ H ₂ P ₂ O ₅ (red) obtained using ACV at 0.005 V s ⁻¹ , 75 Hz, 0.005 V ΔE and 90° out of phase.	112

- Figure 3.24: Capacitance (C_{sp}) versus potential ($-E$) plots of DOPC coated HMDE in 0.1 mol dm^{-3} of KCl (50 %), 50 % $\text{Na}_2\text{H}_2\text{P}_2\text{O}_5$ (green), 50 % Na_2HPO_3 (blue), 50 % Na_2HPO_4 (purple) and 50 % H_3PO_3 (red) obtained using ACV at 0.005 V s^{-1} , 75 Hz, $0.005 \text{ V } \Delta E$ and 90° out of phase. Black is in 100% 0.1 mol dm^{-3} KCl solution. 113
- Figure 3.25: Impedance data transformed to complex capacitance plane of DOPC coated HMDE in 0.1 mol dm^{-3} of KCl (50 %) and (a) 50 % Na_2HPO_3 , (b) 50 % Na_2HPO_4 , (c) 50 % H_3PO_3 and (d) 50 % $\text{Na}_2\text{H}_2\text{P}_2\text{O}_5$, obtained using EIS at -0.4 V . All black data is in 100% 0.1 mol dm^{-3} KCl solution. 114
- Figure 3.26: Capacitance current (a) and capacitance (b) versus potential ($-E$) plots and Impedance data transformed to complex capacitance plane (c) of DOPG coated MFE in 0.1 mol dm^{-3} of KCl (50 %) and 50 % $\text{Na}_2\text{P}_2\text{O}_7$ (red) obtained using RCV at 40 Vs^{-1} , ACV at 0.005 V s^{-1} , 75 Hz, $0.005 \text{ V } \Delta E$ and 90° out of phase and EIS at -0.4 V respectively. All black data is in 100% 0.1 mol dm^{-3} KCl solution. 116
- Figure 4.1: (a) Capacitance versus potential plots and (b) Impedance data transformed to complex capacitance plane of DOPC coated wafer based Pt/Hg electrode in 0.1 mol dm^{-3} KCl with $0.001 \text{ mol dm}^{-3}$ phosphate buffer (black) containing 10 mmol dm^{-3} of the Gly-Gly (blue), Gly-Ala (purple), Ala-Gly (green) and Ala-Ala (red) acquired using ACV at 5 mVs^{-1} , 75 Hertz, $\Delta V = 5 \text{ mV}$ and EIS at -0.4 V respectively. 127
- Figure 4.2: (a) Capacitance versus potential plots and (b) Impedance data transformed to complex capacitance plane of DOPC coated wafer based Pt/Hg electrode in 0.1 mol dm^{-3} KCl with $0.001 \text{ mol dm}^{-3}$ phosphate buffer (black) containing 10 mmol dm^{-3} of the Glu-Glu (red) acquired using ACV at 5 mVs^{-1} , 75 Hertz, $\Delta V = 5 \text{ mV}$ and EIS at -0.4 V respectively. 128
- Figure 4.3: (a) Capacitance versus potential plots and (b) Impedance data transformed to complex capacitance plane of DOPC coated wafer based Pt/Hg electrode in 0.1 mol dm^{-3} KCl with $0.001 \text{ mol dm}^{-3}$ phosphate buffer (black) containing 0.2 mmol dm^{-3} of the Ser-Ser (red) acquired using ACV at 5 mVs^{-1} , 75 Hertz, $\Delta V = 5 \text{ mV}$ and EIS at -0.4 V respectively. 130

Figure 4.4: Capacitance versus potential plots of DOPC coated wafer based Pt/Hg electrode in 0.1 mol dm ⁻³ KCl with 0.001mol dm ⁻³ phosphate buffer containing 10 mmol dm ⁻³ of the following dipeptides: (a) Gly-His, (b) Ala-His, (c) His-Ser (red) and DOPC without dipeptide (black). First peak potential versus concentration plots of (d) Gly-His, (e) Ala-His and (f) His-Ser (filled triangle) and lines representing the fits to the plots.....	131
Figure 4.5: Capacitance of peak-1 versus concentration plots of DOPC coated wafer based Pt/Hg electrode in 0.1 mol dm ⁻³ KCl with 0.001mol dm ⁻³ phosphate buffer containing 10 mmol dm ⁻³ of the following dipeptides: (a) Gly-His, (b) Ala-His, (c) His-Ser (red).....	132
Figure 4.6: Impedance data transformed to complex capacitance plane of DOPC coated wafer based Pt/Hg electrode in 0.1 mol dm ⁻³ KCl with 0.001 mol dm ⁻³ phosphate buffer containing 10 mmol dm ⁻³ of of the following dipeptides: (a) Gly-His, (b) Ala-His, (c) His-Ser (red) and DOPC without dipeptide (black), acquired using EIS at -0.4 V.....	133
Figure 4.7: ZFC versus concentration plot of DOPC coated wafer based Pt/Hg electrode in 0.1 mol dm ⁻³ KCl with 0.001 mol dm ⁻³ phosphate buffer containing 10 mmol dm ⁻³ of the following dipeptides: (a) Gly-His, (b) Ala-His, (c) His-Ser, lines representing the linear fits to the plots, acquired using EIS at -0.4 V.....	135
Figure 4.8: Capacitance versus potential plots of DOPC coated wafer based Pt/Hg electrode in 0.1 mol dm ⁻³ KCl with 0.001mol dm ⁻³ phosphate buffer containing 0.5 mmol dm ⁻³ of the Phe-Phe OMe HCl dipeptide (red) and DOPC without dipeptide (black).	136
Figure 4.9: Impedance data transformed to complex capacitance plane of DOPC coated wafer based Pt/Hg electrode in 0.1 mol dm ⁻³ KCl with 0.001 mol dm ⁻³ phosphate buffer containing 0.5 mmol dm ⁻³ of Phe-Phe OMe HCl (red) and DOPC without it (black) (a), and ZFC versus concentration plot of Phe-Phe OMe HCl (b), acquired using EIS at -0.4 V.	137
Figure 4.10: Impedance data transformed to complex capacitance plane of DOPC coated wafer based Pt/Hg electrode in 0.1 mol dm ⁻³ KCl with 0.001 mol dm ⁻³ phosphate buffer containing 10 mmol dm ⁻³ of Gly-Gly (a), Gly-Gly-Gly (b), Ala-Ala (c) and Ala-Ala-Ala (d) acquired using EIS at -0.4 V.....	138

Figure 4.11: ZFC versus concentration plot of DOPC coated wafer based Pt/Hg electrode in 0.1 mol dm^{-3} KCl with $0.001 \text{ mol dm}^{-3}$ phosphate buffer containing Gly-Gly (closed triangle), Gly-Gly-Gly (open triangle) (b), Ala-Ala (closed square) (c) and Ala-Ala-Ala (d) acquired using EIS at -0.4 V (open square).	139
Figure 4.12: Capacitance versus potential plots of DOPC coated wafer based Pt/Hg electrode in 0.1 mol dm^{-3} KCl with $0.001 \text{ mol dm}^{-3}$ phosphate buffer containing 10 mmol dm^{-3} of Leu-Gly-Gly, acquired using ACV.	140
Figure 4.13: (a) Impedance data transformed to complex capacitance plane of DOPC coated wafer based Pt/Hg electrode in 0.1 mol dm^{-3} KCl with $0.001 \text{ mol dm}^{-3}$ phosphate buffer containing 10 mmol dm^{-3} of Leu-Gly-Gly and (b) ZFC versus concentration plot of Leu-Gly-Gly, acquired using EIS at -0.4 V	141
Figure 5.1: Modified Stern Volmer plots for iodide quenching of biphenyl in the presence of 0.127 (open circle), 0.254 (close square), 0.381 (open triangle), 0.508 close triangle) and $0.636 \text{ mmol dm}^{-3}$ (open square) DOPC GUV in 0.1 mol dm^{-3} of KCl containing $0.001 \text{ mol dm}^{-3}$ of phosphate buffer.	147
Figure 5.2: Capacitance versus potential plot of DOPC coated Hg electrode in 0.1 mol dm^{-3} KCl containing $0.001 \text{ mol dm}^{-3}$ phosphate buffer (black) in the presence of $1.0 \text{ } \mu\text{mol dm}^{-3}$ biphenyl (red) acquired using ACV at 5 mVs^{-1}	148
Figure 5.3: Capacitance of peak-1 versus concentration plot of DOPC coated Hg electrode in 0.1 mol dm^{-3} KCl containing $0.001 \text{ mol dm}^{-3}$ phosphate buffer in the presence of biphenyl.	149
Figure 5.4: (a) Impedance data transformed to complex capacitance plane and (b) ZFC versus concentration plot of DOPC coated Hg electrode in 0.1 mol dm^{-3} KCl containing $0.001 \text{ mol dm}^{-3}$ phosphate buffer (black) in the presence of biphenyl acquired using EIS at -0.4 V respectively.	150
Figure 5.5: Modified Stern Volmer plots for iodide quenching of <i>p</i> - (circle), <i>m</i> - (triangle) and <i>o</i> - (square) OH-BPs in the presence of $0.254 \text{ mmol dm}^{-3}$ DOPC GUV in 0.1 mol dm^{-3} of KCl containing $0.001 \text{ mol dm}^{-3}$ of phosphate buffer.	151

Figure 5.6: (a) Capacitance versus potential plot of DOPC coated Hg electrode in 0.1 mol dm ⁻³ KCl containing 0.001 mol dm ⁻³ phosphate buffer (black) in the presence of 1.0 μmol dm ⁻³ of <i>o</i> - (red), <i>m</i> - (blue) and <i>p</i> -OH-BP (green) (b) capacitance of peak-1 versus concentration plots of <i>o</i> - (close triangle), <i>m</i> - (close inverted triangle) and <i>p</i> - (open square) OH-BP and (c) potential of peak-1 versus concentration plots of <i>o</i> - (open triangle), <i>m</i> - (open square) and <i>p</i> - (closed circles) OH-BP, acquired using ACV at 5 mVs ⁻¹	152
Figure 5.7: Plot capacitance of peak-1 against the accessible fraction for 1.0 μmol dm ⁻³ of OH-BPs on the vesicle surface.	153
Figure 5.8: Impedance data transformed to complex capacitance plane of DOPC coated Hg electrode in 0.1 mol dm ⁻³ KCl containing 0.001 mol dm ⁻³ phosphate buffer (black) in the presence of <i>o</i> - (red), <i>m</i> - (blue) and <i>p</i> -OH-BP (green) and ZFC versus concentration of DOPC coated Hg electrode in 0.1 mol dm ⁻³ KCl containing 0.001 mol dm ⁻³ phosphate buffer in the presence of <i>o</i> - (open triangle), <i>m</i> - (close triangle) and <i>p</i> - (close square) OH-BP, acquired using EIS at -0.4 V respectively.....	154
Figure 5.9: Schematic view of OH-BPs DOPC monolayer interaction.....	155
Figure 5.10: Modified Stern Volmer plots for iodide quenching of <i>p</i> - (square), <i>m</i> - (triangle) and <i>o</i> - (circle) Cl-BPs in the presence of 0.254 mmol dm ⁻³ DOPC GUV in 0.1 mol dm ⁻³ of KCl containing 0.001 mol dm ⁻³ of phosphate buffer.....	155
Figure 5.11: Capacitance versus potential plot of DOPC coated Hg electrode in 0.1 mol dm ⁻³ KCl containing 0.001 mol dm ⁻³ phosphate buffer (black) in the presence of <i>o</i> - (red), <i>m</i> - (blue) and <i>p</i> -Cl-BP (green) acquired using ACV at 5 mVs ⁻¹	156
Figure 5.12: (a) Peak-1 capacitance: versus concentration and (b) Peak-1 potential versus concentration plots of DOPC coated Hg electrode in 0.1 mol dm ⁻³ KCl containing 0.001 mol dm ⁻³ phosphate buffer in the presence of <i>o</i> - (close triangle), <i>m</i> - (open triangle) and <i>p</i> -Cl-BP (close square).....	157
Figure 5.13: Plot capacitance of peak-1 against the accessible fraction for 1.0 μmol dm ⁻³ of Cl-BPs on the vesicle surface.	158

Figure 5.14: (a) Impedance data transformed to complex capacitance plane of DOPC coated Hg electrode in 0.1 mol dm ⁻³ KCl with 0.001 mol dm ⁻³ phosphate buffer (black) containing 1.0 μmol dm ⁻³ of <i>o</i> -Cl-BP (red), <i>m</i> - (blue) and <i>p</i> -Cl-BP (green) (b) ZFC versus concentration plot of <i>o</i> -Cl-BP (closed triangle), <i>m</i> -Cl-BP (open triangle) and <i>p</i> -Cl-BP (closed square), acquired using EIS at -0.4 V applied potential.....	159
Figure 5.15: Schematic view of Cl-BPs DOPC monolayer interaction.....	160
Figure 5.16: Modified Stern Volmer plots for iodide quenching of <i>p</i> -substituted biphenyls (a) -OH (square), -OCH ₃ (triangle) and -CH ₃ (circle) and (b) -Cl (square), -CN (triangle) and -SO ₃ ⁻ (circle) in the presence of 0.254 mmol dm ⁻³ DOPC GUV in 0.1 mol dm ⁻³ of KCl containing 0.001 mol dm ⁻³ of phosphate buffer.	161
Figure 5.17: Plot of Hammett's constants of biphenyl substituents (σ _i) against the accessible fraction for <i>p</i> -substituted biphenyls on the vesicle surface.....	162
Figure 5.18: Plot of Hammett's constants of biphenyl substituents (σ _M) against the accessible fraction for <i>p</i> -substituted biphenyls on the vesicle surface.....	163
Figure 5.19: A schematic representation of effect of <i>p</i> -substituted biphenyls and their electron density (σ _m) on their interactions with lipid membranes.	164
Figure 5.20: Plot of shift in capacitance peak-1 against substituent Hammett's constants of biphenyl substituents (σ _M) for <i>p</i> -substituted biphenyls.	165
Figure 5.21: Impedance data transformed to complex capacitance plane of DOPC coated Hg electrode in 0.1 mol dm ⁻³ KCl with 0.001 mol dm ⁻³ phosphate buffer containing (a) <i>p</i> -OCH ₃ (red), <i>p</i> -CH ₃ (blue) <i>p</i> -OH (green) and (b) <i>p</i> -CN (red), <i>p</i> -O ₃ SH (blue) <i>p</i> -Cl (green) substituted biphenyls, acquired using EIS at -0.4 V applied potential.	165
Figure 5.22: ZFC versus concentration plots of DOPC coated Hg electrode in 0.1 mol dm ⁻³ KCl with 0.001 mol dm ⁻³ phosphate buffer containing (a) <i>p</i> -OCH ₃ (close triangle), <i>p</i> -CH ₃ (open square) <i>p</i> -OH (close square) and (b) <i>p</i> -CN (close triangle), <i>p</i> -O ₃ SH (open triangle) <i>p</i> -Cl (close square) substituted biphenyls acquired using EIS at -0.4 V applied potential.....	166
Figure 5.23: Plot of ZFC against the accessible fraction for <i>p</i> -substituted biphenyls on the vesicle surface and error bars are within the symbol size.	167

Figure 6.1: Capacitance current versus potential plots of DOPC coated HMDE in 0.1 mol dm ⁻³ KCl with added phosphate buffer (0.001 mol dm ⁻³) measured by RCV at 40 Vs ⁻¹ in potential range -0.2 to -1.65 V (black) and -0.9 to -1.65 V (red).	179
Figure 6.2: Capacitance current versus potential plots of DOPC coated HMDE in 0.1 mol dm ⁻³ KCl with added phosphate buffer (0.001 mol dm ⁻³) measured by RCV at 40 Vs ⁻¹ in potential range -0.9 to -1.65 V with electrode area ratio of 1 (black):0.88 (red).	180
Figure 6.3: Capacitance current versus potential plots of DOPC bilayers deposited on HMDE in 0.1 mol dm ⁻³ KCl with added phosphate buffer (0.001 mol dm ⁻³) measured by RCV at 40 Vs ⁻¹ (a) monolayer (b) low density (c) intermediate density (c) high density.	182
Figure 6.4: Capacitance current versus potential plots of DOPC coated HMDE in 0.1 mol dm ⁻³ KCl with added phosphate buffer (0.001 mol dm ⁻³) measured by RCV at 40 Vs ⁻¹ in potential range -0.9 to -1.65 V with electrode area ratio of 0.67 (black): 0.59 (red): 0.39 (blue).	183
Figure 6.5: Capacitance current versus potential plots of DOPC coated HMDE in 0.1 mol dm ⁻³ KCl with added phosphate buffer (0.001 mol dm ⁻³) measured by RCV at 40 Vs ⁻¹ before decreasing the electrode area to form bilayer and after increasing the electrode area to restore monolayer shown as black and red respectively.	184
Figure 6.6: Current (I) - time (t) transients of uncoated HMDE, DOPC monolayer and an intermediate density DOPC bilayer in the 0.1 mol dm ⁻³ KCl containing 0.2 mmol dm ⁻³ Zn ²⁺ at -1.1 V, acquired using chronoamperometry.	185
Figure 6.7: Sampled current voltammograms of uncoated HMDE (black), DOPC monolayer (red) and DOPC (a) low (b) intermediate and (c) high density bilayer (blue) in the 0.1 mol dm ⁻³ KCl containing 0.2 mmol dm ⁻³ Zn ²⁺ , acquired using chronoamperometry and all the currents sampled at 10 ms.	186
Figure 6.8: Plots of the I vs 1/t ^{1/2} of uncoated HMDE in the 0.1 mol dm ⁻³ KCl containing 0.2 mmol dm ⁻³ Zn ²⁺ at different potentials, acquired using chronoamperometry. Solid lines represent the linear fit to the data.	187

Figure 6.9: Plots of the I vs $1/t^{1/2}$ of (a) DOPC monolayer and (b) an intermediate density DOPC bilayer in the 0.1 mol dm^{-3} KCl containing 0.2 mmol dm^{-3} Zn^{2+} at different potentials, acquired using chronoamperometry. Solid lines represent the linear fit to the data.....	188
Figure 6.10: I-t transients of intermediate density bilayer (red) at potentials shown in the figure in the 0.1 mol dm^{-3} KCl containing 0.2 mmol dm^{-3} Zn^{2+} , acquired using chronoamperometry with corresponding fits (black) to equation-2.....	190
Figure 6.11: Rate constant vs potential plot of intermediate density bilayer on Hg in the 0.1 mol dm^{-3} KCl containing 0.2 mmol dm^{-3} Zn^{2+}	191
Figure 6.12: Plots (crosses) of (a) $\text{Re } Y\omega^{-1}$ and (b) $\text{Im } Y\omega^{-1}$ versus $\log \omega$ derived from impedance data of the DOPC-coated electrode in 0.1 mol dm^{-3} KCl buffered with $0.001 \text{ mol dm}^{-3}$ phosphate buffer at -1.1 V together with fits (solid red line) using equation-3.	192
Figure 6.13: Impedance data transformed to complex capacitance plane derived from the intermediate density DOPC bilayer supported on Hg in 0.1 mol dm^{-3} KCl containing $0.001 \text{ mol dm}^{-3}$ phosphate buffer at the potentials indicated on the diagram. Data are represented by cross and equation-3 fits are the solid red lines. α and β values with errors (SD) from the fits are indicated on the diagram.....	194
Figure 6.14: Impedance data transformed to complex capacitance plane derived from the intermediate density DOPC bilayer supported on Hg in 0.1 mol dm^{-3} KCl containing $0.001 \text{ mol dm}^{-3}$ phosphate buffer at the potentials indicated on the diagram. Data are represented by cross and equation-3 fits are the solid red lines. α and β values with errors (SD) from the fits are indicated on the diagram.....	195
Figure 6.15: (a) α , (b) β , (c) C , (d) C_s-C and (e) τ values derived from fits to admittance data using equation-2 for the intermediate density DOPC bilayer on Hg as a function of the potential.	197
Figure 6.16: Capacitance current versus potential plots of (a) low density (b) intermediate density (c) high density DOPC bilayers deposited on HMDE in 0.1 mol dm^{-3} KCl with added phosphate buffer ($0.001 \text{ mol dm}^{-3}$) (black) containing 0.0012% of SM-30 silica nanoparticles at 40 Vs^{-1} after 45 s (blue) and 200 s (red) exposure time.	199

List of Tables

Table 1.1: Different types of phospholipids and their subclasses.....	5
Table 3.1: Binding constants of the studied cations and anions to correlate their effect on the capacitance peak-1.....	96
Table 3.2: Radii of the hydrated ions used in the present study and their calculated charge to diameter ratio and diffusion coefficients.	106
Table 3.3: Organic salts and log of their octanol-water partition coefficients.....	110
Table 4.1: Di- and tri-peptides and their chemical structure and physical properties.....	124
Table 5.1: Biphenyl and derivatives and their abbreviation.	146
Table 5.2: Log P [37], Hammett's constant (σ_t [38] and σ_m) and torsional angle values of biphenyls used in this study.....	162
Table 6.1: Potential dependant rate constant for Zn^{2+} reduction at intermediate density bilayer supported on Hg electrode.....	189

Abbreviations

ACV	Alternating current voltammetry
AC	Alternating current
BLM	Black lipid membrane
CV	Cyclic voltammetry
DC	Direct current
DOPC	1,2-Dioleoyl-sn-glycero-3-phosphocholine
DOPG	1,2-Dioleoyl-sn-glycero-3-[phospho-rac-(1-glycerol)] (sodium salt)
EDL	Electrical double layer
FRA	Frequency response analysis
GUV	Giant unilamellar vesicles
HMDE	Hanging mercury drop electrode
MFE	Mercury film electrode
PECVD	Plasma enhanced chemical vapour deposition
PZC	Potential of zero charge
RC	Resistor and capacitor in series
RCV	Rapid cyclic voltammetry
SAM	Self-assembled monolayer
ZFC	Zero frequency capacitance

Commonly used symbols and physical constants

A	Area (cm ²)
b _f	Composite rate constant (s ⁻²)
C	Concentration (mol dm ⁻³)
C _{sp}	Specific capacitance (μF cm ⁻²)
d	Distance (m)
ε ₀	Permittivity of free space (8.854 × 10 ⁻¹² F m ⁻¹)
e	Electron charge (-1.60218 × 10 ⁻¹⁹ C)
E _{crit}	Critical electric field (V cm ⁻¹)
E _s	Step potential (V)
E	Potential (V)
F	Faradays constant (9.648 53 × 10 ⁴ C mol ⁻¹)
I	Electric current (μA cm ⁻²)
<i>i</i>	Complex number (√-1)
k	Boltzmann constant (1.3806488 × 10 ⁻²³ m ² kg s ⁻² K ⁻¹)
K	Quenching constant
K _{ow}	Octanol water partition coefficient
n	Number of electron transferred
N _A	Avogadro's number (6.02214129 × 10 ²³)
ω	Angular frequency (Radians)
q	Electric charge (C)
R	Resistance (Ω)
R _h	Radius of hydrated ions (Å ⁻¹)
σ	Surface charge density (C cm ⁻²)
σ _t	Hammett's constant

σ_i	Inductive Hammett's constant
σ_m	Mesomeric Hammett's constant
ψ_0	Surface potential (V)
ψ_δ	Diffuse layer potential (V)
T	Temperature (K)
t	Time (s)
τ	Time constant (s)
ν	Potential scan rate (V s^{-1})
Y	Admittance (S)
Z	Impedance (Ω)

List of publications

A. Rashid, A. Vakurov and A. Nelson, Role of electrolyte in the occurrence of the voltage induced phase transitions in a dioleoyl phosphatidylcholine monolayer on Hg, *Electrochimica Acta*, **155**, 458–465 (2015).

A. Rashid, A. Nelson and A. Vakurov, Interaction of substituted biphenyls with model lipid membranes, Submitted, *JACS*, (2015).

A. Rashid, A. Nelson and A. Vakurov, DOPC bilayers supported on Hg, *in preparation*.

A. Rashid, D. Bryant, T. Kee and A. Nelson, Interaction of di- and tri-peptides with Hg supported phospholipid monolayers, *in preparation*.

Chapter-1

Introduction

1.1 Biomembranes

According to the cell theory, all living organisms are made of cells as their building blocks and all the vital functions of the organism occurs within the cell or its immediate environment. Cells are generally classified as prokaryotic (bacteria and archaea) and eukaryotic (all others except viruses) cells depending upon the presence or absence of the membrane boundary around the cell itself, genetic material and other cell organelles [1].

The membrane boundary separating the intracellular fluid called cytoplasm from the extracellular fluid is known as cell membrane or plasma membrane. In addition to functioning as the plasma membrane, membranes also form the structural part of the cellular organelles by surrounding them such as nucleus, mitochondria, chloroplast (in plants), lysosomes, Golgi apparatus and lining of the intestine and lungs [2]. Bio membranes have dynamic structures [3] and are semi-permeable [2, 4]. Selective permeation of different substances through these membranes depends on the structure and properties of these substances. Constant activity and constant movements in bilayers both in transverse and lateral direction facilitates the fluid nature of the membranes responsible for their successful physiologic function [4].

1.1.1 Structure of bio membranes

Because of their critical role in many important cell functions, plasma membranes have been the subject of investigation to understand their structure, composition and mechanism of action. The first model that proposed the structure of a cell membrane was the “Sandwich Model” by Danielli and Davson in 1935 [5]. According to this model, the cell membrane consists of a double layer of phospholipid molecules with a single continuous layer of protein on both sides of lipid bilayer. In 1959, Robertson proposed a “Unit Membrane Model” describing a tri-lamellar structure of cell membrane [6]. This model explains the structure of a cell membrane as comprised of two outer parallel and thick osmophilic protein layers surrounding a thin osmophobic lipid layer in between.

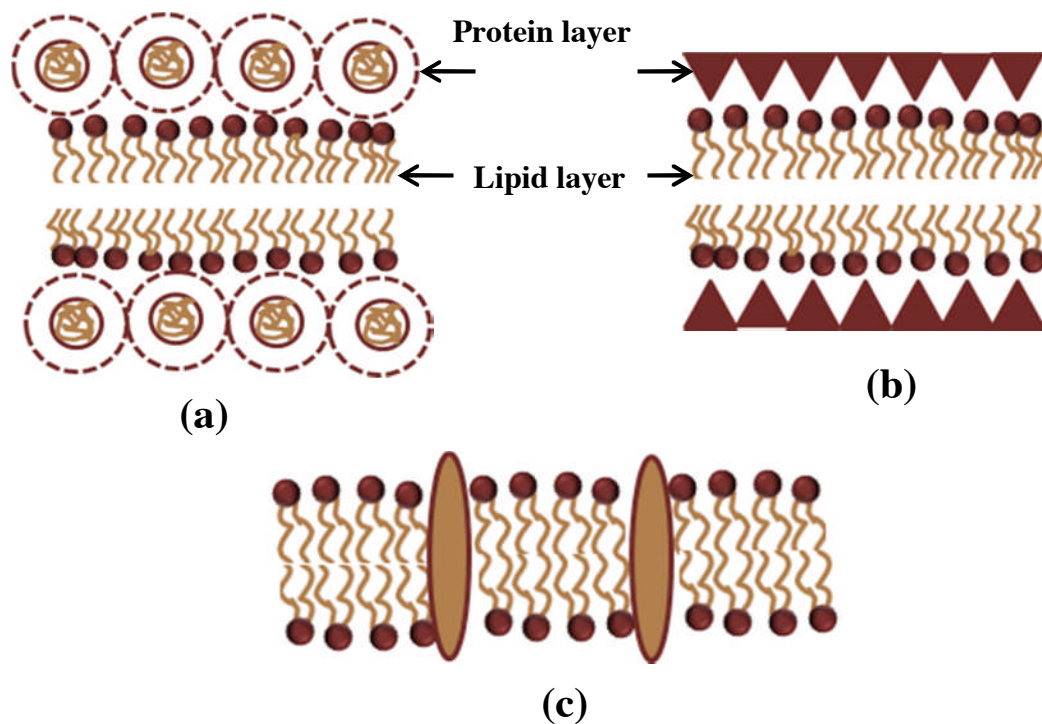


Figure 1.1: Structural models of a biological membrane (a) Danielli and Davison's model (b) Robertson's model and (c) Singer's model.

The most authentic theoretical model of the plasma membrane called the fluid mosaic model was provided by Singer et al in 1971 [7]. According to this model the plasma membranes are made up of a bilayer and each leaflet of a bilayer is composed of homogeneous and alternative distribution of lipids and globular

proteins in fluid state. A picture of a biomembrane based on fluid mosaic model is presented in Figure 1.1 (c). Later on a significant development was made to the fluid mosaic model by Simons [8] and Brown [9]. According to these workers the membrane lipids are organized into lateral micro domains called lipid rafts with specific composition and molecular dynamics that are different in the composition and dynamics to the surrounding liquid crystalline phase.

1.1.2 Composition

In general, all biomembranes consist of lipids, proteins and carbohydrates. The membrane lipids are amphiphilic and are mainly composed of phospholipids, sphingolipids and sterols. The primary site for the biosynthesis of all lipids is the endoplasmic reticulum which produces the bulk of structural phospholipids, cholesterol and triglycerides. The main eukaryotic membranes lipids are phospholipids esterified with glycerol. Lipid composition is asymmetric in biological membranes i.e. different within the two leaflets of the same membrane [10]. This asymmetry is responsible for the membrane curvature and is essential for biological processes such as vesicle budding and membrane fusion [11]. The membrane potential arises from ionic imbalance on either side of the membrane and can also receive a contribution from the dipole moment difference of the two leaflets of the asymmetric membrane [12, 13].

1.1.2.1 Phospholipids

Plasma membranes consists of about 50% of lipids of its total mass, with 50% of proteins. Different cell membranes contain different composition of lipids comprising of mainly four different phospholipids: phosphatidylcholine, phosphatidylserine, phosphatidylethanolamine, and sphingomyelin constituting about 50 - 60% of total membrane lipid. The plasma membranes also contain glycolipids and cholesterol comprising about 40% of the total lipid molecules [4]. Phospholipids are water insoluble amphipathic [14] molecules and due to this characteristic property, lipids self-assemble into bilayers in all membranes having their polar head groups facing the surface with polar acyl chains in between [15, 16] in the presence of aqueous media [4]. The structure of phospholipids consists of a glycerol unit, a phosphate group and two fatty acyl chains (Figure 1.2). The glycerol

backbone consists of three carbon atoms; the two fatty acyl chains attached to two carbon atoms respectively whilst the phosphate group is attached to the remaining carbon atom. The glycerol head group together with the phosphate group are polar and hydrophilic, whereas the fatty acyl chains are non-polar and hydrophobic [4].

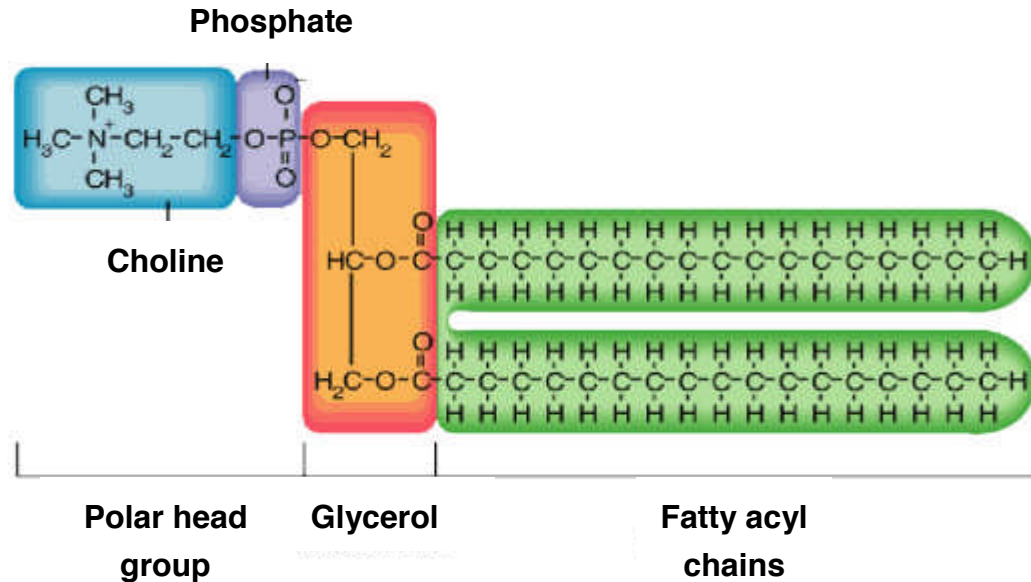


Figure 1.2: Schematic diagram of the structure of a phospholipid.

The fatty acyl chains in biomembranes usually contain an even number of carbon atoms. They may be saturated or unsaturated. The extent of unsaturation controls the mechanical and thermodynamical properties of the membrane [17]. Membrane mobility and fluidity are among the most important properties of biomembranes and are controlled by the length of the fatty acid chain, number of bends and the extent of unsaturation of the fatty acid chain. The longer the fatty acid chain, the greater is the interaction due to more area. Likewise, the greater the unsaturation, the greater is the fluidity (e.g. the physical state of butter compared to vegetable oil) [2]. Temperature also plays an important role in determining the phase of phospholipids. Most of the lipids change from liquid/mobile phase to solid/gel on decreasing the temperature. Since these transitions are temperature dependent (transition temperature) they are termed thermotropic phase transitions and are dependent on many factors.

The first natural phospholipid identified was egg lecithin also known as phosphatidylcholine (PC) but currently there are several synthetic phospholipids derivatives and are classified into two major classes as shown in Table-1 [18]. The

polar head group area contributes more to the shape of the membrane lipid as compared to its non-polar hydrophobic moiety.

Table 1.1: Different types of phospholipids and their subclasses.

Phospholipids	Subclass	Symbol
Glycophospholipid	Phosphatidylcholine	PC
	Phosphatidylserine	PS
	Phosphatidylethanolamine	PE
	Phosphatidic acid	PA
	Phosphatidylglycerol	PG
	Phosphatidylinositol	PI
Sphingophospholipids	Sphingomyelins	SPHM

1.1.2.2 Sterols

Among sterols, the major non-polar lipid is cholesterol in mammalian membranes and ergosterol is the membrane sterol in fungi [18]. Cholesterol inserts into bilayer membranes with its hydroxyl group oriented toward the aqueous phase and its hydrophobic ring system adjacent to the fatty acid tails of phospholipids. The hydroxyl group of cholesterol forms hydrogen bonds with polar phospholipid head groups. Interaction with the relatively rigid cholesterol decreases the mobility of the hydrocarbon tails of phospholipids. The presence of cholesterol in a phospholipid membrane interferes with the close packing of fatty acid tails in the crystal state, and thus inhibits transition to the crystalline state. Phospholipid membranes with a high concentration of cholesterol exhibit liquid ordered phase [2].

1.1.2.3 Proteins

In lipid bilayers, the integral proteins are embedded as trans-membrane segment interacting with nearby lipids and proteins. The peripheral proteins are generally associated at the membrane surface and the anchored proteins are held by covalent bonds [1, 7].

1.1.3 Biomembrane function

Biomembranes transduce energy from chemical and charge gradients, manage enzyme activities, aid the transduction of information and provide a substrate for biosynthesis and for signalling molecules to the cell. Some biomembranes have special functions as well such as the brush-like appearance of the intestine lining enhances the absorption of nutrients and myelin acts as insulator covering the nerves. An important function of all the biomembranes is their selective permeability towards specific nutrients and biological wastes [2]. This property is dependent on the lipids and proteins. The transport of all non-polar substances is regulated by diffusion through the lipids and the transport of all polar substances is facilitated by protein channels and/or transporters.

1.1.4 Electrical properties of biomembranes

Biological membranes are usually electrically insulators due to their phospholipid bilayer structure and are impermeable to ions. Passive leakage of electric charges across the bio membranes through special proteins; channels, pumps and carriers is mainly responsible for all their electrical properties such as membrane conductance, capacitance, and potential. Different ions with their own gradient across the membrane contribute to charge separation and the measured membrane potential. At rest, cells have a potential around -40 to -80 mV (inside relative to outside) and are dominated by K^+ or Cl^- permeability [2].

1.1.4.1 Dielectric properties

Permanent dipoles in the membrane align themselves by translational or rotational motion within the membrane itself on application of electric field and the property is termed electric polarizability. Dielectric constant or permittivity relative to that of vacuum is used as a measure of polarisability because polarisability and dipole moment of a substance cannot be measured directly by experimental methods. Relative dielectric constant is dependent on many variables such as time, applied potential and number of aligned dipoles [19].

At low frequencies, the applied potential results in a maximum polarization within the dielectric because of adequate time available for the dipoles to reorient themselves in response to electric fields. Conversely, at high frequencies, dipoles are not able to reorient and align themselves fully in the given small times. This results in a decreased polarization and permittivity of the dielectric [20]. After the reorientation process stimulated by application of potential, dipoles tend to attain equilibrium and the process is called relaxation. Relaxation is time dependent and the time required for the process is known as relaxation time or time constant (τ).

1.1.4.2 Membrane capacitance

One of the most important properties of the membranes is their ability to function as electrical capacitor having an electrical double layer, in which intracellular cytoplasm and extracellular haemolymph are conducting electrolytes and the cell membrane is an insulating dielectric. Capacitance (C) is defined as the amount of charges stored by a capacitor per unit volt (V) of applied potential and measured in farads (Equation-1.1).

$$C = q/E \qquad \text{Equation 1.1}$$

One farad is the capacitance of a capacitor when it stores one coulomb of charge with voltage difference of one volt across the capacitor plates [21, 22]. The typical value of capacitance of a biological membrane is 1-2 $\mu\text{F cm}^{-2}$ [23, 24]. Therefore, biomembranes are heterogeneous and have surface electrical charge due to the presence of different chemical moieties [25, 26].

Biomembranes also have the ability to sense any changes in pH in their surrounding environment caused by either cell function or the accumulation of various chemical species such as organic and inorganic substances. The solution pH influences the physical and chemical properties of the lipids including the capacitive properties and the membrane layer orientation.

1.1.4.3 Membrane potential

All the living cells maintain a potential difference across their cell membranes due to the imbalance of electric charges on two sides of membrane. This potential difference gives rise to various electrical properties of a biological membrane. The membrane potential is composed of three components namely transmembrane potential, dipole potential and surface potential.

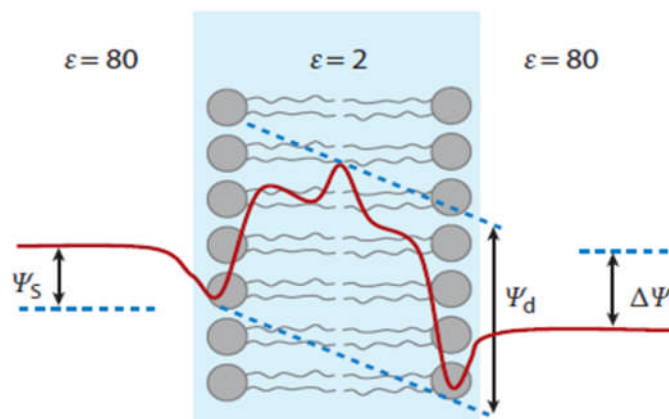


Figure 1.3: Electrostatic potentials associated with a lipid bilayer [27].

1) Transmembrane potential ($\Delta\psi$)

Transmembrane potential is the potential difference between the interior and exterior side of cell and arise due to the difference in ionic concentrations between the two bulk solutions regulating the activity of ion channels [28]. The value of transmembrane potential varies from cell to cell and from species to species for example -10 to -100 mV (-15 mV in erythrocytes [29], -90 mV in nerve and muscle cells [30] and -24 mV in macrophage cells [31]) and is always quoted versus the cell interior.

2) Surface potential (ψ_s)

Surface or double layer potential is the potential difference between the charged lipid head groups and adsorbed ions at the interface and arises due to charged residues at the membrane solution interface [27]. Biological membranes have about 10-20 % negatively charged lipids and the resulting surface potential decays exponentially from the membrane surface and regulate the ionic distribution at the

membrane solution interface. The surface potential varies from -8 to -30 mV [32] and is smaller than the transmembrane and dipole potential.

3) Dipole potential (ψ_d)

The dipole potential arises in the transition region between the aqueous phase and hydrocarbon interior of the membrane due to the specific alignment of lipid dipoles and water molecules in the vicinity [27, 33] with a suggestive value of 145 mV for DOPC monolayers deposited on Hg drop electrode [34]. The dipole potential is much larger than transmembrane and surface potentials (~ 300 mV order of magnitude) [28] and depends on the nature [35] and orientation of water molecules next to lipid dipoles [36] and the structure of the lipid molecules [37].

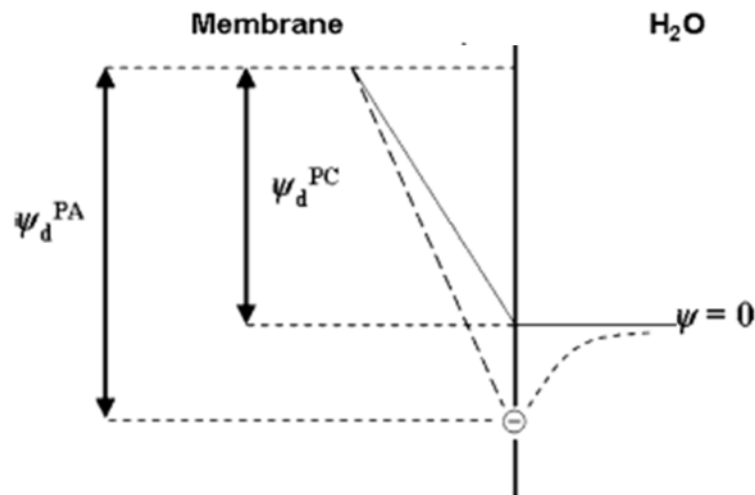


Figure 1.4: Dipole potential of phospholipids with different head groups [35].

1.2 RC series circuit

A series *RC* circuit consists of a resistor and a capacitor connected in series. For a purely resistive circuit, the phase angle between the applied voltage and measured current is zero and the current is a current with waveform in phase with the applied *AC* voltage independent of frequency. For a purely capacitive circuit, the phase angle is 90° and the current is a waveform out-of-phase with the waveform of the applied *AC* voltage. However, for a circuit having both resistor and the capacitor, the phase angle between the applied voltage and the measured current response is

between 0-90° depending on the values of resistance and the capacitance and the frequency of the waveform [38]. In a series connection of a resistor and capacitor (RC series circuit), the current through the individual component is the same as the total current (I_{total}) and the potential (E_{total}) through each component sum up together to give the total potential across the circuit i.e.

$$I_{\text{Total}} = I_R = I_C \quad \text{Equation 1.2}$$

and
$$E_{\text{Total}} = E_R + E_C \quad \text{Equation 1.3}$$

Where
$$E_R(t) = Ee^{-t/RC}$$

$$E_C(t) = E(1 - e^{-t/RC})$$

$RC = \tau$ is the time constant of an RC circuit. This time constant can be related to the frequency (Equation-1.4) [39].

$$\tau = RC = 1/2\pi f_c \quad \text{Equation 1.4}$$

1.2.1 Biomembrane as a series RC circuit

In addition to the membrane capacitance (C_m) and resistance (R_m), the bathing solution also has some resistance R_s . Due to various electrical properties discussed above; the membranes can be modelled as made up of by the combination of electrical analog components of capacitors and resistors. The equivalent electrical circuit for a membrane is presented in Figure 1.5.

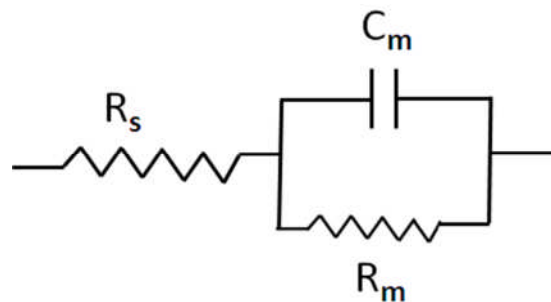


Figure 1.5: Equivalent resistor-capacitor circuit for a membrane.

The membrane resistance is assumed to be very large and the capacitive component is the dominant membrane component. When a membrane is highly impermeable to ions, the simplified circuit can be represented as a membrane capacitor and the solution resistor in series.

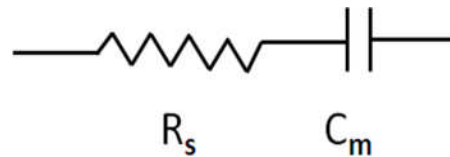


Figure 1.6: A simplified membrane equivalent model.

1.3 Membranes in toxicology

One of the primary functions of the cell membrane is to provide a physical barrier to the penetration of the cell by the various toxins and drugs. These processes depend on the quantity, structure, molecular weight, pH, ionization of the toxin/drug and the maximum extent to which these transport processes can proceed. During the penetration process to the target, the toxin/drug has to pass through various barrier membranes e.g. skin, capillary, cell and cell organelle membranes, differing in their thickness but having similar structure which is made up of lipid matrix. After having penetrated into the body, these substances are transferred to the target either via bulk flow or by diffusion. There are many ways the toxins cross the membrane but the most important are the passive diffusion and active transport. Most drugs and toxins are transported across the membrane by passive diffusion. Passive diffusion involves transport due to concentration gradient. The rate of diffusion depends on the solubility of the substance in the lipid and the partition coefficients [40]. According to the Fick's law, the rate of diffusion is [41];

$$d[C]/dt = D \cdot K \cdot A_m \cdot (C_H - C_L)/d \quad \text{Equation 1.8}$$

Where, C is concentration, D is diffusion coefficient, K is the partition coefficient, d is the thickness of membrane. D , K and d are collectively called the permeability coefficient representing the ease of penetration of a chemical and has units of velocity, distance/time (cm s^{-1}), A_m is the area of the membrane and C_H and C_L are the higher and lower concentrations of the species "A" across the membrane.

Toxicodynamics is the study of the biochemical and physiological effects of toxins and their mechanism of action whereas toxicokinetics is the study of time course of the toxin in various processes in body. According to the first order kinetics of the transport, the rate is proportional to the amount and the rate constant is the first order fractional rate constant representing the fraction of drug transported per unit area. The second important category of transport is carrier mediated membrane transport. It takes place either with the concentration gradient called passive facilitated diffusion or against the concentration gradient requiring energy called active transport. Both of these transportation methods require the involvement of membrane associated proteins [42].

The studies on the binding and interaction of some insecticides on the lipoproteins show the process to be a partitioning rather than a stoichiometric binding process. Lipid content and composition of the lipoproteins play an important role in the distribution of these substances particularly for the water soluble toxicants [43]. Polyaromatic hydrocarbons are unreactive in living organisms and require bioactivation catalysed by cytochrome P-450-1A. The metabolism of these toxins may introduce a reactive group or form a complex with a water soluble moiety ultimately leading to excretion. Very often the introduction of a functional group can lead to an increased toxicity of the toxin if the reactive group facilitates a molecular attack on proteins or DNA [44].

1.4 Membrane Models

A membrane model is a lipid membrane produced or assembled through artificial means, having resemblance to the configurations of the naturally occurring cell membrane or the membranes covering various sub-cellular organelles. As the biological membranes are very complex, many model membranes are configured to investigate the membrane properties, membrane structure and membrane activity of different natural or synthetic compounds for example surfactants, peptides, drugs and various toxic organic and inorganic compounds naturally occurring in water etc. The electrochemical processes can be studied in detail to characterize the lipid membranes. For this purpose, lipid layers can be deposited on the surface of water or any aqueous solvent/electrolyte by dissolving in the appropriate solvent and then

spreading on the electrode surface. To develop a better understanding of the functioning of cell membranes, more sophisticated membrane models are constructed. These membrane models vary from a model containing only phospholipid layer membrane backbone to more complex models incorporating functionalities such as proteins, cholesterol, ion carriers and channels configured as monolayers and bilayers. The most common model membranes are: lipid bilayers mimicking the lipid arrangement of natural cell membranes and lipid self-assembled monolayers (SAMs).

1.4.1 Lipid bilayers

Lipid bilayer models consist of two lipid leaflets and are further classified as (1) lipid vesicles, (2) black lipid membranes (BLMs), (3) supported lipid bilayers (SLBs) and (4) tethered bilayered lipid membranes (t-BLM).

1.4.1.1 Lipid Vesicles

Lipid vesicles also known as liposomes and are phospholipid assemblies that are made up of two lipid layers of the same or different species, enclosing an aqueous compartment. Lipid vesicles can be multi lamellar vesicles (MLVs), large unilamellar vesicles (LUVs) and small unilamellar vesicles (SUVs). Lipid vesicles can be prepared by hydrating a dried lipid film above its transition temperature by gentle hydration through water addition. This method was found to be effective by Rodriguez and others [38]. LUVs and SUVs can be obtained from the MLVs by sonication and extrusion through a porous membrane respectively. Lipid vesicles do not show the lipid asymmetry of the natural biological membrane and they have a short life span. Over a long time period, the vesicles will collapse to form aggregates. However, with specific size, composition, temperature and ionic strength, they can be prepared in a stable form [45] to mimic the biological membranes for investigating many important membrane processes for example membrane fusion, membrane trafficking and the membrane transport of drugs and proteins [46].

1.4.1.2 Black lipid membranes (BLMs)

BLMs are prepared by making a small aperture in a hydrophobic septum followed by the application of the lipid dissolved in the organic solvent using a brush or a syringe. A lipid bilayer is formed giving rise to two organic/aqueous interfaces respectively on both side of aperture. These lipid bilayers are called “black lipid membranes” since they are dark in the reflected light. The layers are effective membrane mimics because both the sides of the bilayers are accessible but their trapped residual solvent interrupts the protein functions and their metastability gives rise to a limited lifetime [47].

1.4.1.3 Supported lipid bilayers (SLBs)

Supported lipid bilayers are the planar structures deposited on to a solid support such as mica and SiO₂ wafer. In this model system polar head groups are facing the support and the non-polar tail groups of both layers are oriented towards each other. Supported lipid bilayers can be formed either using Langmuir Blodgett technique by immersing the solid support successively through the interface containing lipid or by the fusion of lipid vesicles on to the solid substrate by heating the SUVs in contact with support, promoting the adsorption of lipid vesicle on to the surface followed by deformation, flattening and rupturing of the vesicle forming continuous supported bilayers [48]. Electrochemical techniques e.g. voltammetry, EIS, quartz crystal microbalance and atomic force spectroscopy are some of the commonly employed techniques to study the lipid bilayers and their interactions with active compounds [49-51]. These supported lipid bilayers are relatively easy to prepare, more stable, show controlled asymmetry and are much easier to characterize. They are however limited by the possibility of unwanted interactions with the substrate which may affect the adsorbed membrane properties [52].

1.4.1.4 Tethered lipid bilayer membranes (t-LBMs)

The limitation of the supported lipid bilayers is tackled by placing a spacer in between the bilayer and the support giving rise to so-called tethered bilayered lipid membranes. These can be formed in a variety of ways for example by addition of a polymer film or modified lipids on the substrate surface. Thiols are among the most

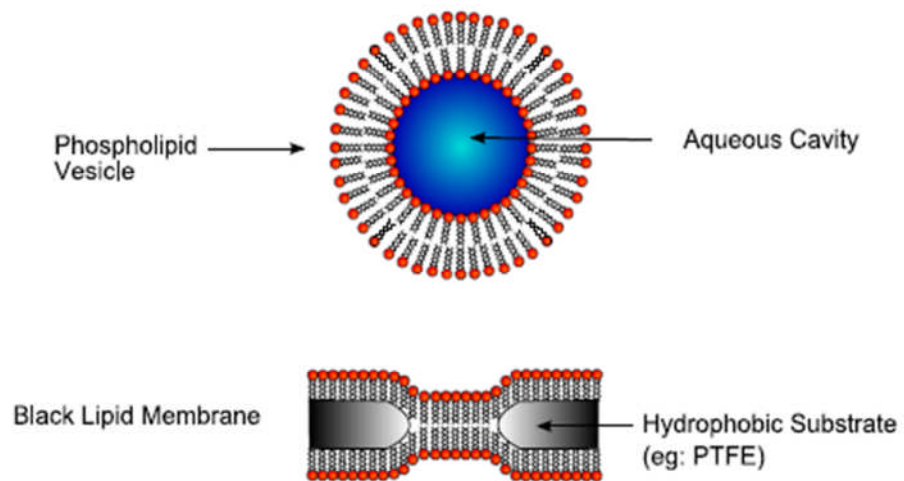
common spacers used for anchoring the lipids on the inert gold surface to form the tethered lipid bilayers [53, 54]. But the system becomes more complicated by the incorporation of additional components such as solid/fluid support and linker/spacers etc. because of involvement of surplus interactions among basic components (lipid molecules) and extra components.

1.4.2 Lipid self-assembled monolayers (SAMs)

Lipid SAMs, also known as Langmuir monolayers are considered as half the bilayers of biological membranes. These have been used to characterize the lipid-lipid interactions and different physical states (solid, liquid ordered, liquid disordered and gaseous) of lipids using varied techniques such as the compression isotherms (plot of surface pressure versus molecular area) obtained from compression of these thin films. Lipid-lipid interactions can be among the molecules of the same lipid or the different lipids but the lipids should be either completely immiscible or completely miscible at the interface and any deviation is supposed to be due to some specific interaction between the two forms. The value of free energy is predictive of the interactions, positive values indicating strong repulsions between the pure lipids and negative values indicating strong associations between the mixed lipids favouring complex formation between the monolayer constituents [55]. Lipid-biologically active compound interactions can also be characterized using these self-assembled lipid monolayers formed at the interface of a Langmuir trough by injecting the active compound and solvent mixture in the sub-phase and observing the increase in surface pressure of the monolayer. Surface pressure gives information about the penetration power of the active compound. The lipid monolayers can also be assembled on a hydrophilic as well as hydrophobic support monitoring the transfer ratio, close to 1 for defect free films. The orientation of the lipid molecules depends on the nature of the support material. Electrochemical studies of supported SAM's are very fundamental in the determination of structure and properties of these layers and help us in understanding the functions of biomembranes. Self-assembled lipid layers on mercury (Hg) have been extensively used to study the lipid interactions at the mercury/water interface involving lipid phase transitions and lipid interactions with biologically active compounds [56-58].

SAMs on Hg show interesting behaviour in response to electric fields and mimic half of the biological bilayered membranes as well as electrically behaving almost as a pure capacitor. The phospholipids monolayers can be supported on the Hg electrode in both head down and tail down orientation ways under the influence of electrode potential as shown by Abruna and others [59]. Phospholipid coated mercury electrode can be used to investigate the nature of the membrane/solution interface and interactions of lipids with membrane active substances such as drugs, pollutants and ions. The biggest disadvantage of SAMs is their structure as a half bilayer composed of single lipid components. On the other hand these monolayers are good models to develop an understanding about the interactions between any two components of a bilayer because the monolayers do not reflect the complexity of biological membranes.

Unsupported Membranes



Supported Membranes

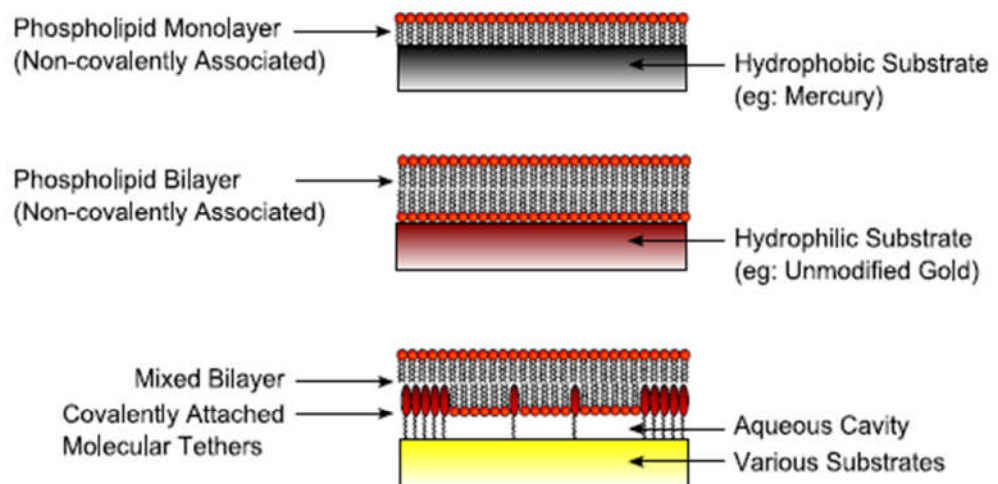


Figure 1.7: Different supported and unsupported model membrane systems [60].

1.5 Interfacial electrochemical studies

1.5.1 Electrical double layer

The electrode electrolyte interface behaves as a capacitor with charged electrode surface and accumulated counter electrode ions acting as two plates of capacitor and the water/solvent acting as a dielectric. In fact, the contact between a charged surface and an electrolyte solution results in ionic rearrangement near the surface and the formation of an electrical double layer. The double layer exists in all heterogeneous systems [19]. The actual electrode-electrolyte interfaces does not behave ideally and different models were proposed in different times to explain the structure of electrical double layer formed at the electrode-electrolyte interface.

1.5.1.1 Helmholtz model

The first model proposed for the double layer was by Helmholtz. It was the simplest model consisting of two planes; one charged electrode surface and the other a layer of compact adsorbed counter ions on the charged surface. The theory defines a linear drop of potential with distance from the surface. This model is equivalent to a parallel plate capacitor having charge density, σ ,

$$\sigma = \epsilon\epsilon_0 \cdot \psi_H/d \quad \text{Equation 1.9}$$

ψ_H is the potential in volts, d is the inter plate spacing, ϵ is the dielectric constant and ϵ_0 is the permittivity of free space. The potential drop across the double layer is,

$$\psi_H = \sigma \cdot d/\epsilon\epsilon_0 \quad \text{Equation 1.10}$$

and

$$C = \epsilon\epsilon_0/d = \sigma/\psi_H \quad \text{Equation 1.11}$$

d and ϵ are constants for a specific capacitor and therefore, parallel plate model predicts a constant capacitance that does not change with potential which is not realised in the case of a solution double layer. The electrical double layer formed at Hg electrode in the 0.1 mol dm^{-3} potassium chloride (KCl) solution as an electrolyte yields a potential capacitance plot (Figure 1.8) where capacitance is not constant over different potentials.

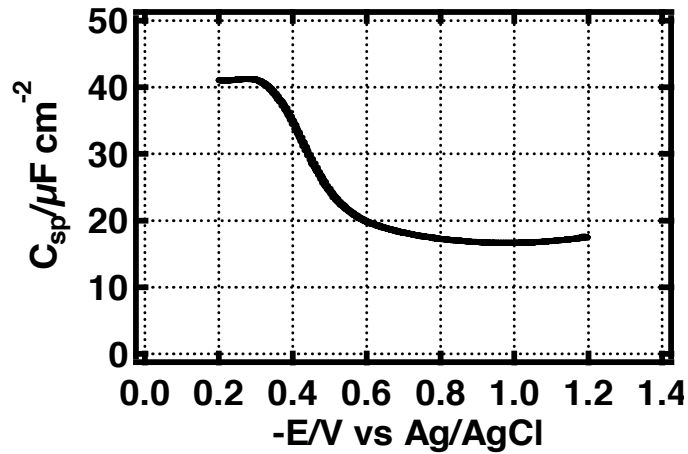


Figure 1.8: Capacitance-potential plot of HMDE in 0.1 mol dm⁻³ KCl.

1.5.1.2 Gouy-Chapman model

Louis George Gouy and David Chapman introduced a diffuse double layer model. According to this model, counter ions are attracted towards the charged surface and the co-ions are repelled by the charged surface described mathematically using Poisson-Boltzmann equation. The movement of counter ions towards the surface is attributed to the electrostatic forces only and the movement of co-ions and counter ions away from surface is due to the both electrostatic forces and diffusive forces. This model defines the exponential decay of the potential away from the surface to the bulk of solution [61].

$$\psi_0 = \psi_\delta e^{(-Kx)} \quad \text{Equation 1.12 a}$$

or

$$\psi_\delta = \psi_0 / e^{(-Kx)} \quad \text{Equation 1.12 b}$$

ψ_0 is the total potential at the metal surface and ψ_δ is the potential drop across the diffuse double layer across the distance x from electrode surface. K is the Debye length and for dilute aqueous ($\epsilon = 78.49$) solutions at 25 °C.

$$K = (2CN_A z^2 e^2 / \epsilon \epsilon_0 kT)^{1/2} \quad \text{Equation 1.13 a}$$

$$K = (3.29 * 10^7) zC^{1/2} \quad \text{Equation 1.13 b}$$

According to Gouy Chapman model capacitance of double layer is given by equation 1.13 [61];

$$C = \sigma/\psi_{\delta} = (z^2 e^2 \epsilon \epsilon_0 C N_A / kT)^{1/2} \cosh(ze\psi_{\delta}/kT) \quad \text{Equation 1.14}$$

The Gouy-Chapman model considers only the electrostatic interactions and considers ions as point charges with no sizes in a diffuse cloud giving rise to an unlimited rise in differential capacitance with increased potential value (Figure 1.9) which is not observed experimentally. In addition, the properties of bulk water are assumed to be the same as those next to the surface giving no attention to the dielectric constant changes.

1.5.1.3 Stern model

Stern suggested the combination of the compact layer (Helmholtz) and the diffuse layer (Gouy and Chapman) models contributed to the experimental double layer model. He introduced an inner Stern layer and an outer diffuse layer resulting in a more realistic calculation of surface potential and surface charge.

$$\psi_0 = \psi_s + \psi_{\delta} \quad \text{Equation 1.15}$$

Whereas, the Stern layer potential (ψ_s) can be calculated using the Helmholtz model of double layer;

$$\psi_s = \psi_H = \sigma \cdot d / \epsilon_0 \epsilon_r \quad \text{Equation 1.16 a}$$

And the diffuse layer potential (ψ_{δ}) is [61];

$$\psi_{\delta} = (2kT/e) * \sinh^{-1}[\sigma / (8cN_A \epsilon_0 \epsilon_r kT)^{1/2}] \quad \text{Equation 1.16 b}$$

This model represents the interface as two capacitors connected in series;

$$\frac{1}{C_d} = \frac{1}{C_H} + \frac{1}{C_{\delta}}$$

The charges were again assumed as point like and the space within the layer as charge free. The dielectric permittivity was also assumed to be constant throughout the double layer by Stern but actually close to the charged surface, water molecules are depleted due to the accumulation of counter ions with significantly reduced relative permittivity and cannot move freely with their dipole moment oriented

towards the surface compared to the bulk of solution where all other orientations are equally probable [62].

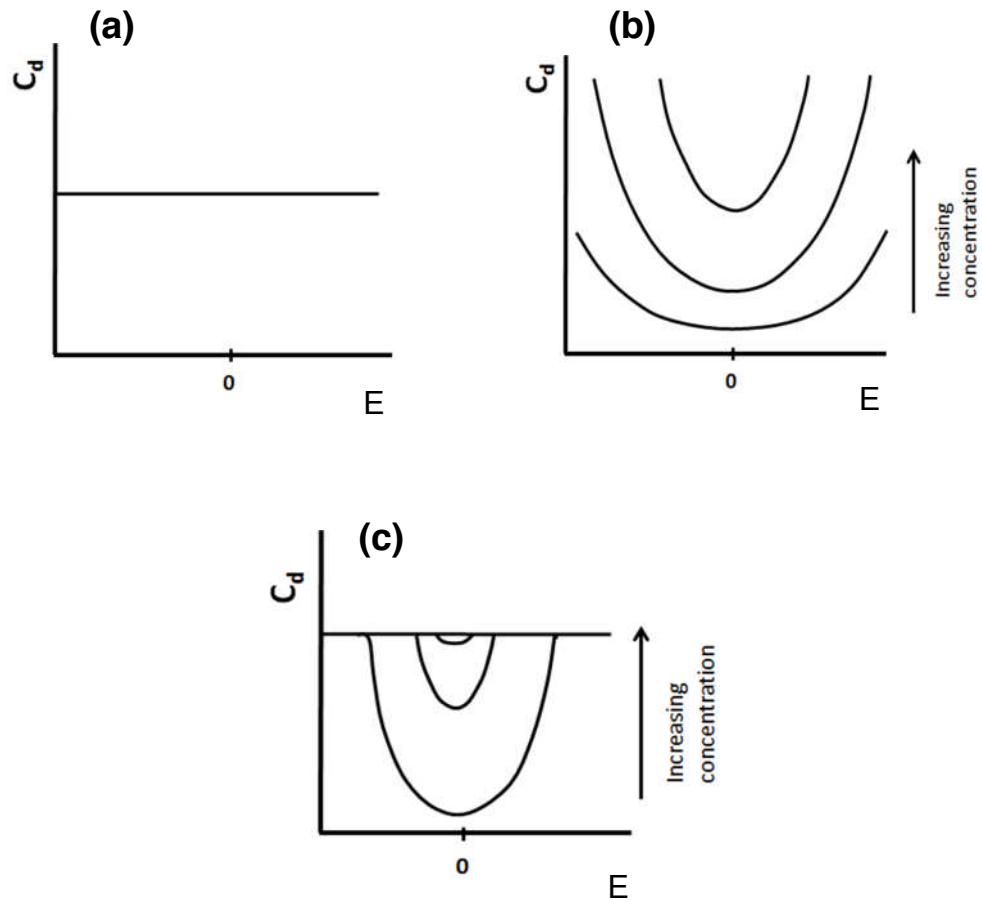


Figure 1.9: Differential capacitance trends predicted from Helmholtz model (a) Gouy-Chapman model (b) and Stern model (c) of electrical double layer plotted against applied potential.

Later on other models were also proposed including Bockris and Grahaime's model. According to a more general picture of the double layer (Figure 1.10), the solution side of the double layer consists of many layers. The inner layer is closest to the electrode surface and contains mostly the solvent molecules and sometimes other ions as well. This layer is also called the compact layer, Helmholtz layer or Stern layer and a plane passing through this layer is called the IHP. Adjacent to the inner layer is a layer of non-specifically adsorbed solvated ions and the plane passing through this layer is termed the OHP. The interaction of the solvated ions with the charged surface is dependent on the nature of the ions as the only interactions possible are the long range electrostatic ones. Adjacent to the OHP is a diffuse layer

consisting of scattered solvate and non-solvated ions due to thermal agitation and this layer extends from the OHP into the bulk of solution. The thickness of the diffuse layer depends on the total ionic concentration of the solution [61].

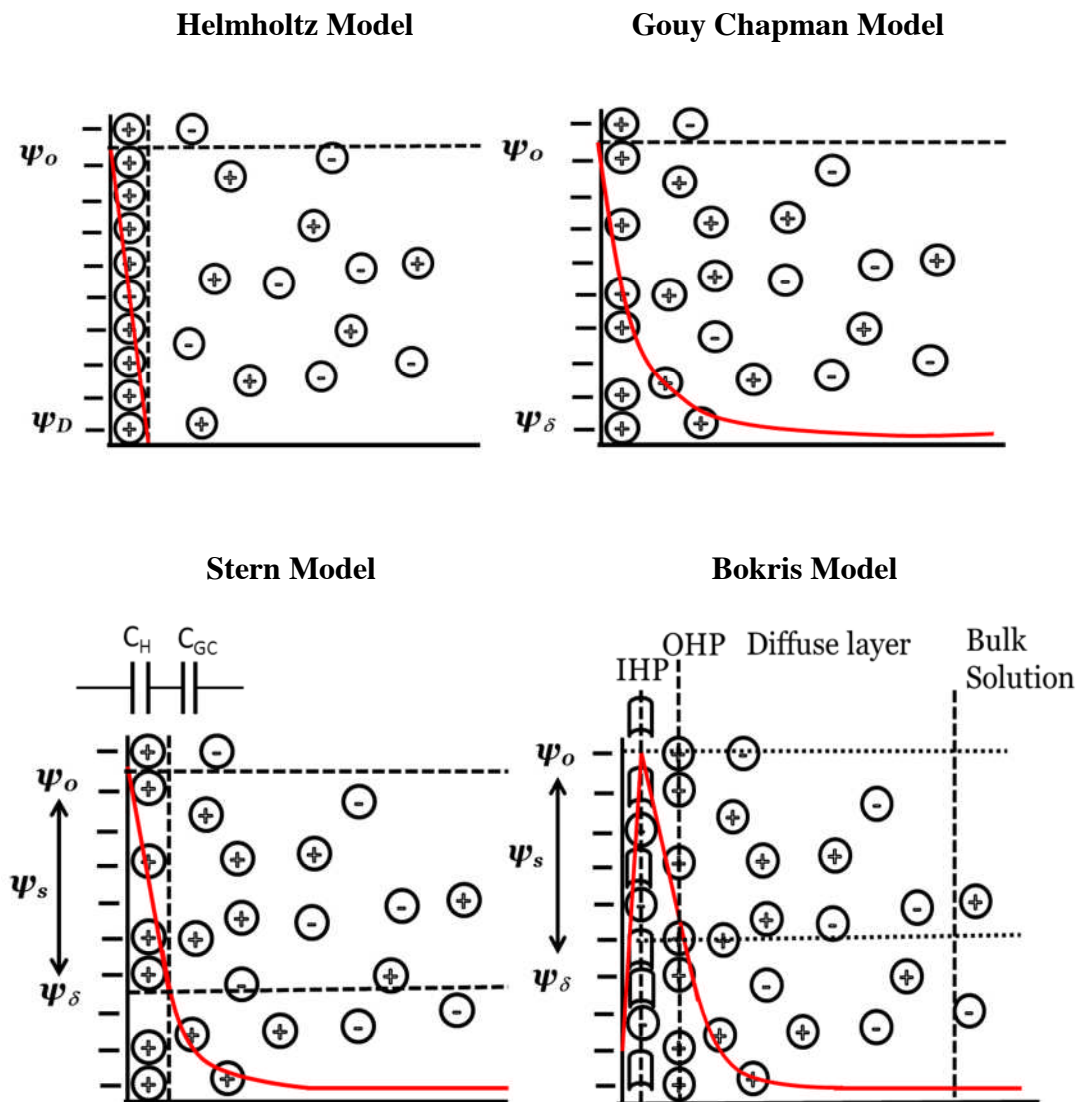


Figure 1.10: Different models of electrical double layer.

1.5.2 Electrocapillarity

Electrocapillary measurements are the measurements of the surface tension of the Hg electrode in contact with electrolyte solution as a function of the electrical potential difference across the interface and are achieved by using a capillary electrometer and electrocapillary curves are plots of interfacial tension versus changes in interfacial potential difference. A typical electrocapillary curve is almost

a parabola. The potential at which the surface tension is at a maximum is called the electrocapillary maximum (ECM). The electrocapillary curves are different for different electrolytes. According to the Lipmann equation;

$$-\sigma_M = \partial\gamma / \partial E \quad \text{Equation 1.17}$$

the slopes of these curves at all potentials give the charge density on the electrode surface. At the ECM, the slope of curve is zero and the corresponding potential difference is characterised as the potential of zero charge (PZC). The capacitance is obtained from the slope of the excess charge on electrode surface versus the potential plot.

$$C = \partial\sigma / \partial E = -\partial^2\gamma / \partial E^2 \quad \text{Equation 1.18}$$

An ideal parabolic γ versus E curve yields a linear q versus E curve with constant differential capacitance [63].

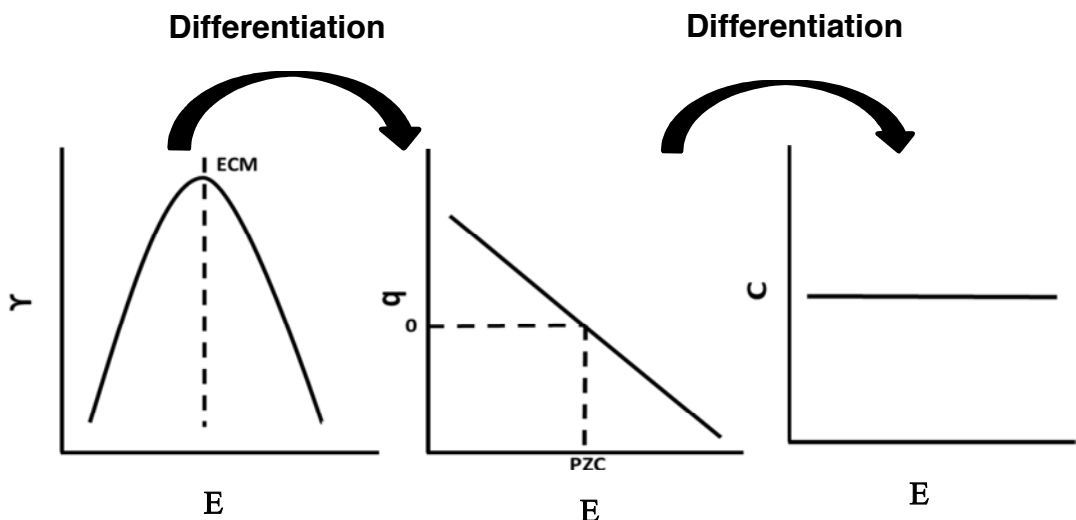


Figure 1.11: A diagram showing the relation between surface tension, charge and capacitance of an electrode with respect to applied potential.

1.5.3 HMDE as an electrode material

Hg offers itself as a potential candidate for use as a working electrode. This is because it is smooth, a good electrical conductor and is also a liquid metal. For Hg because of its fluid nature, surface tension is the property which can be easily

measured and related directly to the potential difference across the interface. In addition, the surface can be renewed. Due to these advantages, Hg has become a benchmark for studying many fundamental electrochemical processes with accuracy and great precision. In contrast, the various solid electrodes suffer the problems of irreproducibility due to a heterogeneous and impure surface. Furthermore, the surfaces are not atomically flat over large areas resulting in the formation of defected adsorbed layers such as the presence of pinholes and grain boundaries in the layers. The hanging mercury drop electrode (HMDE) is an electrode that has been widely used as a working electrode with which a drop of controlled geometry can be produced at the end of the capillary. The studies involving Hg as a dropping electrode (DME) are called polarography and if the Hg drop has a constant size and is maintained in stationary form, as in the HMDE, then the studies are termed voltammetry. Heyrovsky first introduced the concept of polarography in 1922. In the polarographic method, the electrical potential of a Hg drop is varied as a function of time in the electrolyte solution containing the species under investigation and the resulting current response is measured. The total measured current in polarography consists of two components, faradaic current and charging or residual current. Faradaic current is due to the electrochemical reaction of the analyte occurring in electrical double layer. Whereas, charging current is due to charging and discharging effects of the electrical double layer capacitor in response to an applied potential and electrode area change. This current decays faster than the faradaic current.

A polarogram is the plot of current response versus applied potential and it shows that current is very small in the beginning until the applied potential reaches a critical value specific to the potential at which the species is reduced when the voltage is varied. Then, the gradient increases rapidly, reaching a limiting value that remains almost constant with further increase in potential. The current at limiting value is called limiting diffusion current (I_d) and the potential corresponding to half of the limiting diffusion current is called half wave potential ($E_{1/2}$) [64]. HMDE is proved to be useful as compared to the conventional polarography due to its constant surface area causing the increase in speed and reproducibility and decreasing the charging currents [65]. The design of the HMDE has been greatly improved over the time for example, decreasing the weight and dimension of the electrode and increasing the number of drops of Hg. The rotating hanging Hg has also been used

by Barendrecht [66]. The HMDE is reusable as the Hg can be refilled in the Hg reservoir once it gets finished. The HMDE finds its applications in a number of electrochemical processes but in all the studies involving Hg as working electrode the potential should be kept more negative than the oxidation potential of Hg i.e. -0.575 V vs Ag/AgCl saturated KCl. For the studies involving the use of a potential more positive than -0.4 , other electrodes can be applied [67]. The HMDE has been used extensively to study the supported phospholipid monolayer system. The electrode is lowered in the electrolyte containing a layer of lipid at the electrolyte air interface and electrochemical techniques are used to investigate the desired processes. During the lowering process, the lipid layers are deposited on the surface of drop. After each individual study, the drop can be knocked off and a new drop can be created free of lipids. Recently, the Hg film coated platinum (Pt) electrode has been introduced for the same purpose.

1.5.3.1 Adsorption effects at Hg

Adsorption is the accumulation of the molecules of a substance on the surface of the substrate. The substrate is called the adsorbent and the substance whose molecules are adsorbed are known as adsorbate. Adsorption may be physical or chemical depending on the nature of the forces between the adsorbate and the adsorbent. The forces may be weak van der Waal's forces, covalent interactions or columbic attractions. Adsorption is the consequence of surface free energy and is a surface phenomenon always taking place at an interface e.g. air/liquid, liquid/liquid, or solid/liquid. It is usually characterised by isotherms called adsorption isotherms. These isotherm gives the relationship between the amounts of adsorbate adsorbed on the adsorbent surface as a function of the adsorbate concentration or its pressure per unit area at any given constant temperature.

There are many adsorption isotherms based on the number of layers and the nature of the interactions among the molecules of the adsorbate and adsorbent and among themselves. The most commonly encountered are the Freundlich adsorption isotherm, the Langmuir adsorption isotherm, the Brunauer, Emmett and Teller (BET) adsorption isotherm, the Gibbs adsorption isotherm and the Handerson-Kisliuk adsorption isotherm. The Handerson-Kisliuk adsorption isotherm was proposed mainly for the adsorption of self-assembled monolayers on the surface of

the substrate. According to the theory, the self-assembled monolayers adsorb on the surface until the saturation of the surface. During the adsorption process, the orientation of SAM molecules vary from hydrocarbon chain lying flat against the substrate in the lying down configuration to the all SAM molecules in standing up configuration.

Hg electrode adsorbs certain components from the solution due to surface forces of molecular dimensions forming monomolecular layers. The nature of forces is governed by the nature of interactions among the adsorbate and adsorbent e.g. electrical forces persist between the Hg and the surface-active agent because the surfaces are charged in this case. The study of adsorption of surface-active molecules on to the Hg surface is called tensammetry. The adsorption of surface active agents at the Hg electrode leads to changes in charging current or capacity current. Electro-inactive and surface-active agents can affect the polarographic faradaic current by decreasing the limiting current, elimination of a wave, a shift of a reduction wave to more negative potential and the oxidation wave to the more oxidation potential, splitting of a single wave into two waves and lowering the hydrogen evolution overpotential depending on their nature (non-ionic, cationic and anionic). Some of the effects lead to the inhibition of the electrode processes due to repulsive forces between the adsorbed layer and the redox ions [68, 69].

1.5.4 Self assembled monolayers on Hg

Adsorption of lipid molecules on a liquid/solid surface followed by their organization results in the formation of so-called SAMs. SAMs have been the subject of study for the last few decades for their diverse application e.g. as biosensors, lubrication etc. SAMs on Hg meet several advantages of the liquid surface along with the formation of highly stable and well-organized two dimensional arrays of adsorbed molecules. Only the intermolecular interactions determine the organization pattern on Hg. In contrast, with solid surfaces e.g. gold, it is the lattice structure of the solid which govern the organization of adsorbed molecules on the surface. SAMs have been structured on the Hg surface [52, 56, 57, 59, 70-73] both directly and using some anchors/separators e.g. alkanethiols [72] with the latter exhibiting complex electrochemical behaviour. SAM's of

phospholipids on Hg surface shows characteristic phase transitions in response to applied electric fields.

1.5.4.1 Phase transitions

Phase transition or phase transformation refers to the change from one phase of the substance to the other with the phase being the state of matter with uniform physical properties throughout. Phase transitions are driven by many parameters e.g. temperature, pressure, chemical composition, magnetic or electric field etc. Classical phase transitions of amphiphilic molecules at the air-water interface have been extensively studied. For lipids, phase transitions are temperature specific occurring at the temperature called the transition or the critical temperature. Below the transition temperature, lipid molecules are in a condensed liquid or gel phase and above this temperature, a transition to expanded liquid or fluid state takes place [71, 74, 75]. In phase transitions, one phase replaces another at a specific potential or temperature and the competing phases are characterized by the order parameter. Phase transitions are classified as continuous and discontinuous depending on the behaviour of order parameter approaching the transition. In continuous phase transitions, the competing phases becomes indistinguishable at the transition point and order parameter changes continuously. This kind of phase transition is continuous across the transition parameters with stable and continuous thermodynamic quantities but their first derivative is not continuous. In contrast, the particle configuration and order parameter changes abruptly in the discontinuous or first order phase transitions and a small continuous change in the driving parameters results in a large change in the properties dependent on the parameters. It can be seen by sharp current peaks and discontinuities in the charge or capacitance vs potential profiles [76].

Non faradaic phase transitions in adsorbed layers on the electrode surface are those which do not involve electron transfer and show changes in the capacity current only. These phase transitions in adsorbed surfactant films proceed by various mechanisms like adsorption, displacement of surfactant by solvent or other surfactant molecules, reorientation and reorganization of surfactant molecules and other structural changes in the lipid molecules. Electro-adsorbed phospholipids on Hg show various non-faradaic discontinuous phase transitions in the form of

capacitance peaks in the capacity versus potential profile. These phase transitions and the effect of the interaction of biologically active compounds with adsorbed surfactant layers, on the phase transitions have been extensively investigated by Nelson et. al., using electrochemical techniques [56, 58, 70, 77-80]. In voltammetric techniques, these phase transitions appear as characteristic peaks in the current response on applying either *AC* or *DC* potential. These phase transitions are shown to depend on the applied potential, electrolyte composition, nature and composition of phospholipid, surface coverage of the electrode and presence of impurity or organic compounds.

In a rapid cyclic voltammogram (RCV) of a phospholipid layer on Hg, four main capacitance current peaks appear in the cathodic scan. The first peak appearing at about -0.95 V vs Ag/AgCl, originates from the penetration of solvated electrolyte ions into the lipid layer and the displacement of the phospholipid tails from the surface. The second phase transition peak appears at about -1.0 V originating when the energetics of the surface allow for the adsorption of phospholipid head groups and water. In this state, it is more favourable for a second layer to deposit on the first reoriented layer to form a pored bilayers with pores and bilayers in equilibrium leaving some parts of Hg surface exposed to water/electrolyte. The third and fourth phase transition peaks around -1.25 V correspond to formation of semi vesicle which collapse to monolayer of uncertain composition [81].

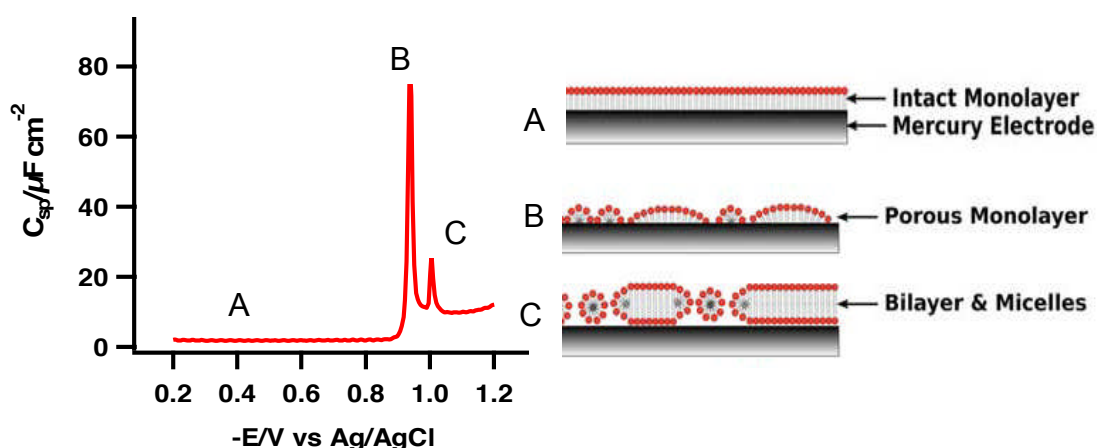


Figure 1.12: Left: Characteristic capacitance-potential plot of DOPC monolayer on HMDE with three different regions at distinct potentials (A -0.40 V, B -0.94 V and

C -1.04V), from an AC voltammetry measurement. Right: Schematic view of the processes at each of these potentials.

Some of the processes of non-faradaic phase transitions in adsorbed surfactant layers are shown to involve nucleation and growth mechanism. Nucleation is the formation of stable and small particles of new phase at the grain boundaries, pores and defects while the growth is expansion of the new phase at the expense of the original phase. During the nucleation process, the changes in the potential, temperature or any driving force must be large enough so that the transformed nuclei of the new phase can combine together to form the smallest clusters of critical sizes called critical nuclei which then result in the transition by the progressive growth process. In the SAMs of phospholipid layers on Hg, the formation of bilayer patches takes place by a nucleation and growth process.

1.5.4.2 Interaction of biologically active compounds with phospholipid monolayer on Hg

The interaction of many biologically active compounds such as nanoparticles and aromatic hydrophobic compounds including pharmaceuticals, peptides, biopolymers, flavonoids, steroids, pesticides and other toxins with model membranes have been studied to predict the significance of membrane processes in their potential biological activity. In addition the mechanism of interaction and the structural characteristics responsible for their activity is also of great interest. Using Hg supported phospholipid monolayers [82-86], these cause changes to the phase transitions underlying capacitance peaks in different ways based on the changes in the structure of monolayer. Hence the system acts as a biosensor and has potential toxicity sensing application as well. Based on their activity, these substances are broadly classified as (bio)membrane-active.

All (bio) membrane-active compounds/particles may result in the suppression of capacitance peaks (due to inhibition of electrolyte penetration), decrease in monolayer capacitance (due to incorporation in pores/gaps in between lipid head groups increasing monolayer thickness) and/or shifting the capacitance peaks to more negative potentials by affecting the transition energetics. Whereas, monolayer

penetration can be accessed from the suppression in capacitance peaks along with an increase in monolayer capacitance (due to surface adsorption followed by penetration into hydrocarbon region) and/or shift of capacitance peaks towards more positive potential (due to decrease in monolayer thickness because of penetration resulting in lipid molecules moving apart from each other facilitating the electrolyte ingress and subsequent phase transitions).

1.5.5 Phospholipid bilayer on Hg

Potential dependent phospholipid bilayer formation directly on the surface of Hg electrode from the lipid electrolyte interface have been reported recently and exist at potentials negative to -1.0 V [81]. Formation of bilayer at these potentials is energetically favourable and consistent with physicochemical and thermodynamical considerations [81]. The DOPC bilayer on Hg was first shown using rapid cyclic voltammetry (RCV) and atomic force spectroscopy (AFM) [81]. In RCV, the DOPC bilayer on Hg has been shown to exhibit a constant low capacitance region between potentials -1.0 V to -1.3 V followed by a sharp, well-defined and reversible capacitance current peak at about -1.3 V. The reverse process is slow and shows hysteresis under rapid voltage scanning conditions [81]. At potentials more negative than those characterising the capacitance current peak, the capacitance increases. The bilayer is stable in the potential range from -1.0 V to -1.4 V. These bilayers are unstable at potentials positive to -0.9 V due to conversion to a monolayer. AFM studies have shown that thickness of this hydrated bilayer (bilayer along with a water layer) is a 6.5-7 nm with ~95 % coverage [81].

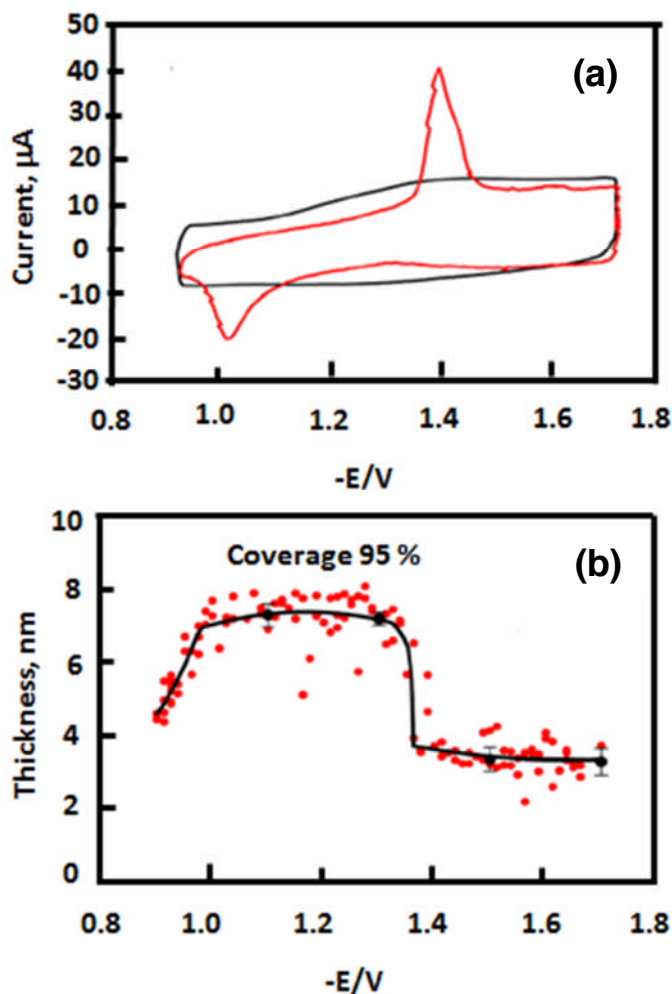


Figure 1.12: (a) Current of uncoated Hg (black) and DOPC bilayer supported on Hg (red) measured by RCV at 40 V s^{-1} and (b) thickness of DOPC bilayer on Hg measured by AFM, vs. applied potential [81].

1.6 Biphenyls and their interaction with membrane systems

Biphenyl had been used in the manufacturing of dye carriers, heat transfer fluids and alkyl derivatives of biphenyl [87] and along with its derivatives had been reported for its carcinogenic and chronic toxicity [88-89] during the past several years. Therefore, it is essential to investigate the mechanism of interaction and structure activity relations of biphenyl derivatives with phospholipid membranes using membrane models. Biphenyl has two aromatic rings connected to each other by a single bond in between the two rings (Figure 1.13). and has a low relative permittivity of ~ 3 [90].

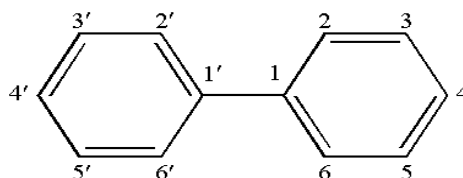


Figure 1.13: Chemical structure of biphenyl.

Biphenyl derivatives have different functional groups attached to them. The number and position of these groups vary in different derivatives. Mono substituted biphenyls have one substituent attached to one of the carbon atom in any of the aromatic rings. Mono derivatives with substitution at position 2, 2', 6' and 6' are called ortho (*-o*) derivatives, at position 3, 3', 5 and 5' are called meta (*-m*) derivatives and 4 and 4' are called para (*-p*) derivatives (Figure 1.14).

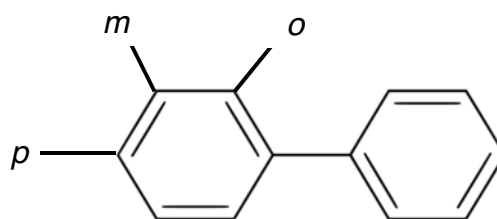


Figure 1.14: *o*, *m* and *p* positions of biphenyls.

Interaction of biphenyl and its various derivatives with plasma membranes have been studied extensively in the past [91-95] using natural biological membranes, membrane models and simulation studies. There have been many studies on the structure-activity relation of these biphenyls with phospholipid bilayers [96, 97]. There are also studies on the potential toxicity of these hazardous substances *in-vivo* [98-100] but not much work has been done on the evaluation of structural characteristics responsible the mechanism of their interaction of at the cellular level. According to some studies, non-planar ortho (*-o*) substituted biphenyls increased the membrane leakiness and decreased the membrane integrity to a greater extent compared to the planar biphenyls [99-101]. While other studies showed that the ortho (*-o*) substituted (non-planar) molecules are less active and less membrane disruptive compared to the para (*-p*) substituted (planar) molecules because of the

steric hindrance offered during the penetration of these species into the phospholipid membrane [102-104].

1.7 Aims and objectives

The main goal of the research work was to develop an understanding about the fundamental properties of the phospholipid monolayer on Hg surface. The study aims to uncover the molecular details of the phase transitions exhibited by the phospholipid monolayers. The work investigates the occurrence of these phase transitions and how these phase transitions are affected by various parameters such as electrolyte concentration and composition. In addition, experiments were carried out to see how these phase transitions differ from the DOPC coated HMDE to the DOPC coated Hg film electrode (MFE) in terms of their underlying structural changes and kinetics and mechanism. This was done to completely characterise differences in the DOPC layer structure from transfer from HMDE to MFE. One section of the thesis (Chapter-3) therefore intends to discuss the techniques used to characterise the phase transitions of phospholipids on DOPC coated MFE and DOPC coated HMDE and extends our knowledge about these techniques and phase transitions in extensive detail.

Another key objective was to investigate the interactions of biologically active substituted biphenyls with the self-assembled phospholipid monolayers on MFE. Substituted biphenyls are well known for their membrane activity and toxicity but there was a need to study the structural characteristics responsible for their membrane activity and hence the toxicity to develop qualitative structure activity relation (QSAR). The work has been done for this purpose using DOPC monolayer on Hg and biphenyls with systematically altered substituted groups on the biphenyl ring. The effect of position and chemical composition of substitution was investigated using electrochemical techniques. Furthermore, the experiments were also performed on DOPC bilayer system using fluorescence technique to validate the findings from the electrochemical measurements discussed in Chapter-5.

A part of the research work also included the study of interaction of simple and short peptides (2-3 amino acids) with DOPC monolayer to understand their effect on the

membrane stabilization with relevance to prebiotic chemistry. The work was done in collaboration with Prof. Terrence Kee in School of chemistry, University of Leeds.

The aim of the last part of the research work presented in the Chapter-6 was to immobilize a stable DOPC bilayer on Hg surface and to characterize the structure and properties of phospholipid bilayers supported on the Hg electrode at more negative applied potentials. For this purpose efforts were made to investigate the lipid density in a bilayer, permeability of bilayer and possibility of ion diffusion occurring in the bilayer. Experiments were also performed to observe the DOPC bilayer/ SiO₂ nanoparticles.

1.8 References

- [1] H. Lodish, A. Berk, S.L. Zipursky, P. Matsudaira, D. Baltimore, J. Darnell, New York, (1995).
- [2] B. Alberts, A. Johnson, J. Lewis, M. Raff, K. Roberts, P. Walter, New York, (2002) 1227-1242.
- [3] M.A. McNiven, A.J. Ridley, Trends in cell biology, 16 (2006) 485-486.
- [4] G.M. Cooper, R.E. Hausman, The cell, ASM press, 2000.
- [5] J.F. Danielli, H. Davson, Journal of cellular and comparative physiology, 5 (1935) 495-508.
- [6] J.D. Robertson, A molecular theory of cell membrane structure, in: Verhandlungen Band II/Biologisch-Medizinischer Teil, Springer, 1960, pp. 159-171.
- [7] S. Singer, G.L. Nicolson, Landmark Papers in Cell Biology, (1972) 296-307.
- [8] K. Simons, E. Ikonen, Nature, 387 (1997) 569-572.
- [9] D.A. Brown, E. London, Biochemical and biophysical research communications, 240 (1997) 1-7.
- [10] J. Op den Kamp, Annual review of biochemistry, 48 (1979) 47-71.
- [11] J. Zimmerberg, L.V. Chernomordik, Advanced drug delivery reviews, 38 (1999) 197-205.
- [12] A.A. Gurtovenko, I. Vattulainen, Journal of the American Chemical Society, 129 (2007) 5358-5359.
- [13] A.A. Gurtovenko, I. Vattulainen, The Journal of Physical Chemistry B, 112 (2008) 4629-4634.

- [14] N.A. Campbell, B. Williamson, R.J. Heyden, *Biology: Exploring Life*. Boston, Massachusetts: Pearson Prentice Hall, in, ISBN 0-13-250882-6. http://www.phschool.com/el_marketing.html, 2006.
- [15] A. Helenius, K. Simons, *Biochimica et biophysica acta*, 415 (1975) 29.
- [16] D. Lichtenberg, R.J. Robson, E.A. Dennis, *Biochimica et Biophysica Acta (BBA)-Reviews on Biomembranes*, 737 (1983) 285-304.
- [17] S. Feng, R.C. MacDonald, *Biophysical journal*, 69 (1995) 460-469.
- [18] G. Van Meer, D.R. Voelker, G.W. Feigenson, *Nature reviews molecular cell biology*, 9 (2008) 112-124.
- [19] P. Atkins, *Physical Chemistry*. 6th, in, Oxford University Press, Oxford, Melbourne, Tokyo, 1998.
- [20] O.G. Martinsen, S. Grimnes, *Bioimpedance and bioelectricity basics*, Academic press, 2011.
- [21] T.L. Floyd, D.M. Buchla, *electronics fundamentals*, Prentice Hall, 1995.
- [22] R.C. Dorf, *The electrical engineering handbook: Circuits, signals, and speech and image processing*, CRC Press, 2006.
- [23] P.W. Gage, R.S. Eisenberg, *The Journal of general physiology*, 53 (1969) 265-278.
- [24] S. Takashima, K. Asami, Y. Takahashi, *Biophysical journal*, 54 (1988) 995-1000.
- [25] B.E. Conway, *Electrochemical supercapacitors: scientific fundamentals and technological applications*, Springer, 1999.
- [26] B.E. Conway, *Electrochemistry Encyclopedia*, (2003).
- [27] L. Wang, *Annual review of biochemistry*, 81 (2012) 615-635.
- [28] J.C. Franklin, D.S. Cafiso, *Biophysical journal*, 65 (1993) 289-299.
- [29] U. Lassen, *Membrane transport in red cells*, (1977).
- [30] B. Hille, *Ion channels of excitable membranes*, Sinauer Sunderland, MA, 2001.
- [31] D. McCaig, R. Berlin, *Experientia*, 39 (1983) 906-907.
- [32] B.H. Honig, W.L. Hubbell, R.F. Flewelling, *Annual review of biophysics and biophysical chemistry*, 15 (1986) 163-193.
- [33] S. Hladky, D. Haydon, *Biochimica et Biophysica Acta (BBA)-Biomembranes*, 318 (1973) 464-468.
- [34] L. Becucci, M.R. Moncelli, R. Herrero, R. Guidelli, *Langmuir*, 16 (2000) 7694-7700.

- [35] T. Starke-Peterkovic, R.J. Clarke, *European Biophysics Journal*, 39 (2009) 103-110.
- [36] K. Gawrisch, D. Ruston, J. Zimmerberg, V. Parsegian, R. Rand, N. Fuller, *Biophysical journal*, 61 (1992) 1213-1223.
- [37] R. Benz, B. Gisin, *The Journal of membrane biology*, 40 (1978) 293-314.
- [38] N. Rodriguez, F. Pincet, S. Cribier, *Colloids and Surfaces B: Biointerfaces*, 42 (2005) 125-130.
- [39] M.E. Starzak, *The physical chemistry of membranes*, Academic Press London, UK:, 1984.
- [40] D. Boal, D.H. Boal, *Mechanics of the Cell*, Cambridge University Press, 2012.
- [41] B.J. Zwolinski, H. Eyring, C.E. Reese, *The Journal of Physical Chemistry*, 53 (1949) 1426-1453.
- [42] E. Hodgson, P.E. Levi, *A textbook of modern toxicology*, Wiley Online Library, 2004.
- [43] B.P. Maliwal, F.E. Guthrie, *Chemico-Biological Interactions*, 35 (1981) 177-188.
- [44] R.C. Smart, E. Hodgson, *Molecular and biochemical toxicology*, Wiley Online Library, 2008.
- [45] G. Sessa, G. Weissmann, *Journal of lipid research*, 9 (1968) 310-318.
- [46] C. Peetla, A. Stine, V. Labhsetwar, *Molecular pharmaceuticals*, 6 (2009) 1264-1276.
- [47] S.H. White, *Biophysical journal*, 12 (1972) 432-445.
- [48] T.H. Anderson, Y. Min, K.L. Weirich, H. Zeng, D. Fygenson, J.N. Israelachvili, *Langmuir*, 25 (2009) 6997-7005.
- [49] E. Wang, X. Han, *Advances in Planar Lipid Bilayers and Liposomes*, 2 (2005) 261-303.
- [50] N.J. Cho, C.W. Frank, B. Kasemo, F. Höök, *nature protocols*, 5 (2010) 1096-1106.
- [51] M.P. Mingeot-Leclercq, M. Deleu, R. Brasseur, Y.F. Dufrêne, *nature protocols*, 3 (2008) 1654-1659.
- [52] M. Kühner, R. Tampe, E. Sackmann, *Biophysical journal*, 67 (1994) 217-226.
- [53] I. Köper, *Mol. Biosyst.*, 3 (2007) 651-657.
- [54] P. Krysinski, A. Zebrowska, A. Michota, J. Bukowska, L. Becucci, M. Moncelli, *Langmuir*, 17 (2001) 3852-3857.

- [55] R. Maget-Dana, *Biochimica et Biophysica Acta (BBA)-Biomembranes*, 1462 (1999) 109-140.
- [56] A. Nelson, A. Benton, *Journal of Electroanalytical Chemistry and Interfacial Electrochemistry*, 202 (1986) 253-270.
- [57] R. Guidelli, G. Aloisi, L. Becucci, A. Dolfi, M. Rosa Moncelli, F. Tadini Buoninsegni, *Journal of Electroanalytical Chemistry*, 504 (2001) 1-28.
- [58] D. Bizzotto, A. Nelson, *Langmuir*, 14 (1998) 6269-6273.
- [59] S. Chen, H.D. Abruna, *Langmuir*, 10 (1994) 3343-3349.
- [60] Z. Coldrick, *Phospholipid monolayers adsorbed on mercury electrodes with applications in sensing*, in, University of Leeds, 2009.
- [61] A.J. Bard, L.R. Faulkner, *Electrochemical methods: fundamentals and applications*, Wiley New York, 1980.
- [62] E. Gongadze, A. Igljč, S. Petersen, U. van Rienen, 2010.
- [63] J.O.M. Bockris, A.K.N. Reddy, *Modern electrochemistry*, Springer, 2000.
- [64] V. Gold, *Advances in physical organic chemistry*, Academic Pr, 1976.
- [65] J.W. Ross, R.D. DeMars, I. Shain, *Analytical Chemistry*, 28 (1956) 1768-1771.
- [66] E. Barendrecht, (1958).
- [67] P. Zuman, *FABADJ. Pharm. Sci.*, 31 (2006) 97-115.
- [68] Y. Frei, I. Miller, *The Journal of Physical Chemistry*, 69 (1965) 3018-3023.
- [69] I. Miller, *Electrochimica acta*, 9 (1964) 1453-1467.
- [70] A. Nelson, N. Auffret, *Journal of Electroanalytical Chemistry and Interfacial Electrochemistry*, 244 (1988) 99-113.
- [71] M.J.Z. C. M. Roland, and A. Georgallas, *Journal of Chemical Physics*, 86 (1987) 7.
- [72] D. Mandler, I. Turyan, *Electroanalysis*, 8 (1996) 207-213.
- [73] N. Muskal, I. Turyan, D. Mandler, *Journal of Electroanalytical Chemistry*, 409 (1996) 131-136.
- [74] J.F. Nagle, *Faraday Discuss. Chem. Soc.*, 81 (1986) 151-162.
- [75] H. Girault, D. Schiffrin, *Journal of Electroanalytical Chemistry and Interfacial Electrochemistry*, 179 (1984) 277-284.
- [76] T. Wandlowski, Chapter 12 in *Encyclopedia of Electrochemistry*.
- [77] A. Nelson, *Biophysical journal*, 80 (2001) 2694-2703.
- [78] E. Protopapa, S. Maude, A. Aggeli, A. Nelson, *Langmuir*, 25 (2009) 3289-3296.

- [79] A. Nelson, *Journal of Electroanalytical Chemistry*, 601 (2007) 83-93.
- [80] A. Nelson, F. Leermakers, *Journal of Electroanalytical Chemistry and Interfacial Electrochemistry*, 278 (1990) 73-83.
- [81] A. Vakurov, M. Galluzzi, A. Podestà, N. Gamper, A.L. Nelson, S.D. Connell, *ACS nano*, 8 (2014) 3242-3250.
- [82] S. Zhang, A. Nelson, P.A. Beales, *Langmuir*, 28 (2012) 12831-12837.
- [83] E. Protopapa, A. Aggeli, N. Boden, P. Knowles, L. Salay, A. Nelson, *Medical engineering & physics*, 28 (2006) 944-955.
- [84] A. Vakurov, R. Brydson, A. Nelson, *Langmuir*, 28 (2011) 1246-1255.
- [85] A. Vakurov, G.M. Lopez, R. Drummond-Brydson, R. Wallace, C. Svendsen, A. Nelson, *Journal of colloid and interface science*, (2013).
- [86] M. Galluzzi, S. Zhang, S. Mohamadi, A. Vakourov, A. Podestà, A. Nelson, *Langmuir*, (2013).
- [87] A. Levstik, C. Filipic, I. Levstik, *Journal of Physics: Condensed Matter*, 2 (1990) 3031.
- [88] W.R. Kirk-Othmer, A. Demaria, *Kirk-Othmer encyclopedia of chemical technology*, 8 (1979) 151-158.
- [89] F. Gersich, E. Bartlett, P. Murphy, D. Milazzo, *Bulletin of environmental contamination and toxicology*, 43 (1989) 355-362.
- [90] Y. Umeda, H. Arito, H. Kano, M. Ohnishi, M. Matsumoto, K. Nagano, S. Yamamoto, T. Matsushima, *Journal of Occupational Health*, 44 (2002) 176-183.
- [91] H.H. Refsgaard, B.F. Jensen, P.B. Brockhoff, S.B. Padkjær, M. Guldbrandt, M.S. Christensen, *Journal of medicinal chemistry*, 48 (2005) 805-811.
- [92] W.J. Dulfer, H.A. Govers, *Environmental science & technology*, 29 (1995) 2548-2554.
- [93] G. Mustata, S.M. Dinh, *Critical Reviews™ in Therapeutic Drug Carrier Systems*, 23 (2006).
- [94] P. Pocar, T.A. Brevini, F. Perazzoli, F. Cillo, S. Modina, F. Gandolfi, *Molecular reproduction and development*, 60 (2001) 535-541.
- [95] H.H. Zepik, P. Walde, E.L. Kostoryz, J. Code, D.M. Yourtee, *CRC Critical Reviews in Toxicology*, 38 (2008) 1-11.
- [96] P.R.S. Kodavanti, T.R. Ward, J.D. McKinney, H.A. Tilson, *Toxicology and applied pharmacology*, 130 (1995) 140-148.

- [97] M. Mor, S. Rivara, A. Lodola, P.V. Plazzi, G. Tarzia, A. Duranti, A. Tontini, G. Piersanti, S. Kathuria, D. Piomelli, *Journal of medicinal chemistry*, 47 (2004) 4998-5008.
- [98] S. Bonora, A. Torreggiani, G. Fini, *Thermochimica acta*, 408 (2003) 55-65.
- [99] Y. Tan, D. Li, R. Song, D. Lawrence, D.O. Carpenter, *Toxicological Sciences*, 76 (2003) 328-337.
- [100] Y. Tan, R. Song, D. Lawrence, D.O. Carpenter, *Toxicological Sciences*, 79 (2004) 147-156.
- [101] Y. Tan, C.-H. Chen, D. Lawrence, D.O. Carpenter, *Toxicological Sciences*, 80 (2004) 54-59.
- [102] J.M. Cullen, K.L. Kaiser, An Examination of the Role of Rotational Barriers in the Toxicology of Pcb's, in: *QSAR in Environmental Toxicology*, Springer, 1984, pp. 39-66.
- [103] A.M. Bobra, W.Y. Shiu, D. Mackay, Structure-activity relationships for toxicity of hydrocarbons, chlorinated hydrocarbons and oils to *Daphnia magna*, in: *QSAR in Environmental Toxicology*, Springer, 1984, pp. 3-16.
- [104] A. Nelson, N. Auffret, J. Borlakoglu, *Biochimica et Biophysica Acta (BBA)-Biomembranes*, 1021 (1990) 205-216.

Chapter-2

Material and methods

2.1 Electrochemical set-up

Electrochemical set-up consisted of a three electrode system controlled with a potentiostat [1].

2.1.1 Electrochemical cell and electrode assembly

The electrochemical cell was made of Pyrex glass and consisted of electrolyte and three electrodes: reference electrode (RE), counter (CE) and working electrode (WE). The cell has three inlets for the electrodes, argon gas aspirator made of glass and sample injection.

2.1.1.1 Reference electrode

The reference electrode is used to provide a stable and reproducible voltage referenced to the working electrode [2]. Very little or no current passes through the reference electrode. Silver (Ag)/silver chloride (AgCl), 3.5 mol dm⁻³ potassium chloride (KCl) solution (Ag/AgCl/Cl⁻) was used as reference electrode. This consisted of a Ag wire coated with AgCl and dipped in a solution of 3.5 mol dm⁻³ or saturated potassium chloride. The potential of this electrode varies with the concentration of KCl solution used. The potential of Ag/AgCl/Cl⁻ electrode is 0.205

V with 3.5 mol dm^{-3} KCl [3] and 0.198 V with saturated KCl [4]. A porous sintered glass frit separated the KCl from the electrolyte solution.

2.1.1.2 Counter/Auxiliary electrode

The counter electrode carries a current equal and opposite to the working electrode. The area of counter electrode or auxiliary electrode is usually kept large to support large currents at the working electrode [2]. A platinum rod was used as counter electrode.

2.1.1.3 Working/Indicator electrode

Hanging mercury (Hg) drop electrode (HMDE) (WK2 Poland) and Hg film electrode (MFE) electrode (Tyndall National Institute, Ireland) were used as working electrodes. No polishing or cleaning process is required to work with HMDE because, unwanted Hg drop can be dislodged and a new clean drop can be produced just by rotating the plunger on the scaled sleeve. A wide range of drop sizes can be produced using HMDE for example, a rotation of 0.5 cm had a calculated drop area of 0.0092 cm^2 . The MFE can be easily cleaned and made free from most organic impurities including DOPC at higher negative potential of about -3.00 V. The advantage of the MFE are that only a small amount of Hg is used at a time, a single electrode can be re-used after cleaning and can function for several months.

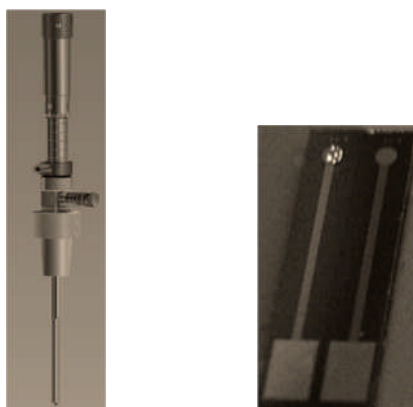


Figure 2.1: HMDE (left) and MFE (right).

2.1.2 Instrumentation

Two different types of instrumental set-ups were used for carrying out experiments and were tested for the calibration and speed analysis. The first instrumental set-up consists of Autolab systems-GPES (general purpose electrochemical studies) for alternating current (AC) voltammetric studies and FRA (frequency response analyser) for impedance studies with PGSTAT 30 Autolab potentiostat (Ecochemie, Utrecht, Netherlands) interfaced to PowerLab 4/25 signal generator (AD Instruments Ltd.) controlled by Scope software [1,5] shown in Figure 2.2.



Figure 2.2: The first electrochemical set up: a photograph of fully assembled electrochemical cell connected to Autolab potentiostat.

The second instrumental set-up (Figure 2.3) which is used for capacitance-potential and current transient measurements consists of ACM potentiostat, EG & G princeton applied research lock-in amplifier and function generator and data acquisition device (e-DAQ e-corder) [6-8]. The electrochemical cell was connected to the ACM potentiostat interfaced to the e-corder signal generator and a computer running Scope software for the rapid cyclic voltammetry (RCV) and chronoamperometric measurements. A lock-in-amplifier was connected to the function generator to support an oscillating sine wave of small amplitude of about 0.005 V on a negatively increasing DC (direct current) potential. The function generator was interfaced to the potentiostat to transfer AC supported DC signal to the potentiostat. Potentiostat had a direct interface with the lock-in-amplifier to separate the resultant current into the real and imaginary current. Lock-in-amplifier was interfaced to the e-corder signal

generator and a computer running chart software for the ACV measurement. A schematic diagram showing all the connections made is presented in Figure 2.4.

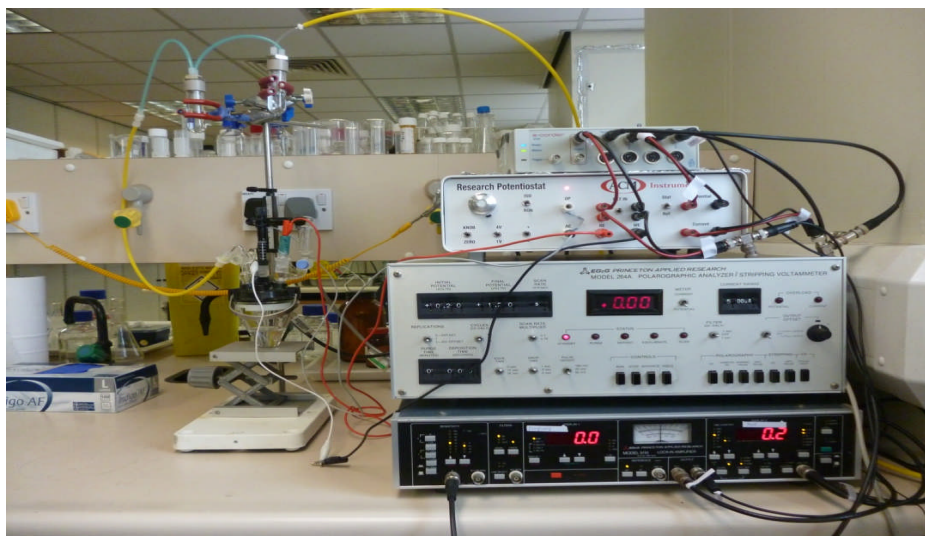


Figure 2.3: The second electrochemical set up: a photograph of fully assembled electrochemical cell connected to potentiostat, function generator, lock-in-amplifier and signal generator.

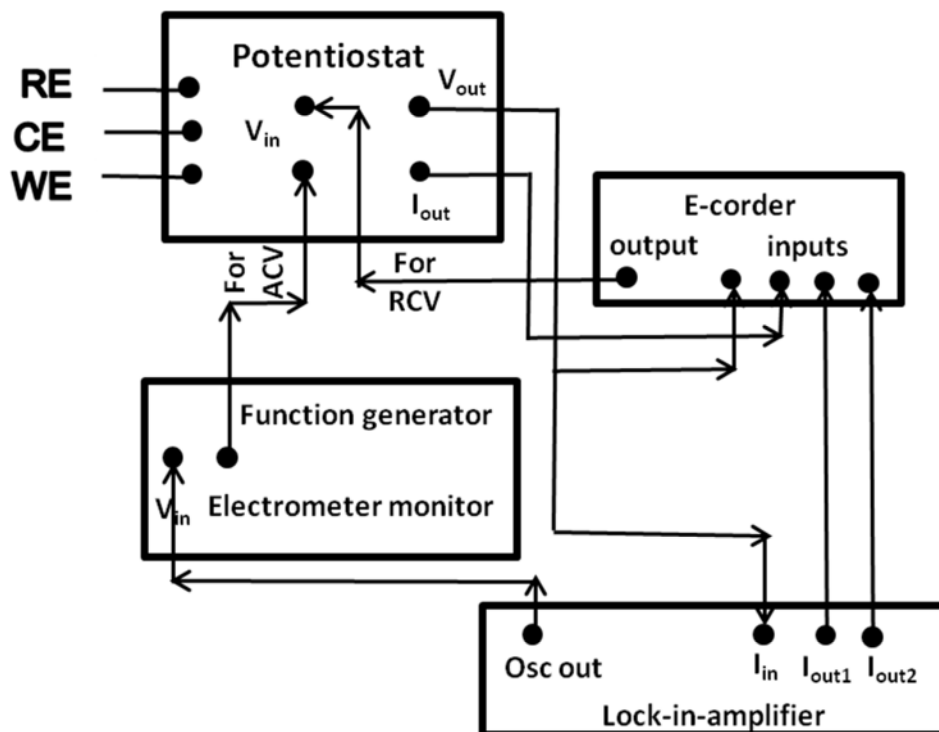


Figure 2.4: The schematic diagram showing the hierarchy of connections made during RCV and ACV measurements using second electrochemical.

2.1.2.1 Potentiostat sensitivity

The potentiostats was calibrated and their sensitivity was checked using a dummy cell. Sensitivity of the ACM potentiostat depends on the counter resistor between the operational amplifier output (OP) inside the potentiostat and the counter electrode (CE). It was calculated between the range 1000-25 $\mu\text{A/V}$ using various counter resistors from 1 $\text{K}\Omega$ to 40 $\text{K}\Omega$. The potentiostat gave best and noise free results for both RCV and impedance studies at a minimum sensitivity 152 $\mu\text{A/V}$ with a counter resistor of 6.53 $\text{K}\Omega$.

Sensitivity of the potentiostat was checked by the following method:

- 1) An appropriate counter resistor e.g. 6.53 $\text{K}\Omega$ was inserted between the OP and the CE.
- 2) A suitable output voltage was configured in the stimulator for example 1V for convenience.
- 3) RE, CE and the WE electrode cables from the potentiostat were connected to the dummy cell consisting of a resistor of 10 $\text{K}\Omega$ only.
- 4) The theoretical current was calculated using ohm's law:

$$E=IR \quad \text{or} \quad I = E/R$$

$$1/10,000 = 0.0001 \text{ A}$$
- 5) The actual output voltage from the input amplifier of the current channel was recorded i.e. 0.6581 V. This voltage corresponds to actual current across the circuit under investigation on dummy cell.
- 6) The sensitivity was calculated:-

$$\begin{aligned} \text{Sensitivity} &= \text{Theoretical current/Observed voltage} \\ &= 0.0001 \text{ A} / 0.6581 \text{ V} = 152 \mu\text{A/V} \end{aligned}$$

The process was repeated using varying different resistor capacitor circuits on dummy cells to reproduce the calculated sensitivity. The sensitivity of the Autolab potentiostat was calculated as 10 $\mu\text{A/V}$.

2.1.2.2 Potentiostat calibration and speed test

The basic principle involved in the speed analysis is sampling the maximum number of samples in the minimum time domain possible during the pulse application of known voltage to the capacitor and/or resistor circuit and measuring the current

response. This experimental current was then compared with the theoretical currents for a capacitor. The difference between the experimental peak current and the theoretical peak current gave information about the time taken by the potentiostat to respond to the system and hence the speed of the potentiostat. The data acquisition device may also contribute to this delay but this contribution can be configured out by comparing the applied voltage pulse with the current response over the time scan. The speed of the potentiostat was checked by the following method:

- 1) Potentiostat was connected to the data acquisition device e.g. e-corder.
- 2) A dummy cell was constructed by connecting a resistor of about 658 Ω and capacitor of 0.15 μF . This dummy cell actually had the capacitance almost equivalent to the "wet" experimental system.
- 3) Reference and counter electrode terminals from the potentiostat were connected to one side of the dummy cell and working electrode terminal to the other side.
- 4) Maximum speed was selected in the acquisition software (Scope) i.e. maximum number of samples in minimum time (100 KHz for e-corder and 200 KHz for Powerlab).
- 5) A voltage pulse of particular amplitude, say 1V for convenience was applied to the home-made dummy cell.
- 6) Current response was measured with respect to time.
- 7) Theoretical current decay of an applied voltage pulse was calculated using the Equation 2.1;

$$I(t) = \frac{E(t)}{R} e^{-\frac{t}{\tau}} \quad \text{Equation 2.1}$$

Where $\tau = RC$ and is the time constant.

R is 658 Ω , C is 0.158 μF , V= 1 V.

- 8) Applied voltage and voltage corresponding to the currents were converted to the current according to the sensitivity of the potentiostat.

Experimentally observed and the theoretical currents and applied voltages were plotted against time. The difference between the experimental peak current and the theoretical current gave potentiostatic delay and the difference between the experimental peak current and voltage peaks gave acquisition device delay. The speed of ACM and Autolab potentiostat and contribution by acquisition device e-corder and powerlab to the speed of the potentiostats is compared and presented in

Figure 2.5. The current response of the ACM potentiostat connected to e-corder is 20 μs delayed compared to the Autolab potentiostat and is approximately 10 μs delayed when connected to powerlab compared to the Autolab potentiostat. Autolab is clearly faster than the ACM potentiostat (Figure 2.5 c). The current response of the AutoLab potentiostat connected to the Powerlab is delayed by about 60 μs from the theoretical current value. Of this, the 50 μs delay is due to the Powerlab with a characteristic potentiostatic delay of 10 μs only.

2.1.2.3 Lock-in amplifier calibration

The lock-in-amplifier was also calibrated before carrying out experiments. The calibration was carried out as follows:

- 1) Reference and counter electrode terminals from the potentiostat were connected to one side of the home-made dummy cell and working electrode terminal to the other side.
- 2) Voltage input to the potentiostat was taken from a function generator connected to the lock-in amplifier.
- 3) Appropriate parameters were adjusted on the lock-in amplifier e.g. frequency 75 Hz, oscillating voltage amplitude 5 mV, phase angle 90° and on the function generator e.g. scan rate 5 mVs^{-1} , number of cycles infinity.
- 4) Imaginary voltage corresponding to the current were recorded from the display-1 as 21.9 on the lock-in amplifier sensitivity set at 10 mV and potentiostat sensitivity $152 \mu\text{A/V}$.
- 5) The capacitance of the dummy cell was calculated experimentally at 10 mV sensitivity as;

$$\text{voltage on display} = 21.9 = 2.19 \text{ mV} = 0.00219 \text{ V}$$

$$\text{current} = 0.00219 \text{ V} \times 152 \mu\text{A/V} = 0.3328 \mu\text{A}$$

$$C = I(t)/2\pi fV \quad \text{Equation 2.2}$$

$$\text{where } f = 75 \text{ Hz, } V = 5 \text{ mV;}$$

$$C = \frac{0.33288}{(2 \times 3.14 \times 75 \times 5)} = 0.154 \mu\text{F}$$

This is in good agreement with the dummy cell capacitance of about 0.158 μF .

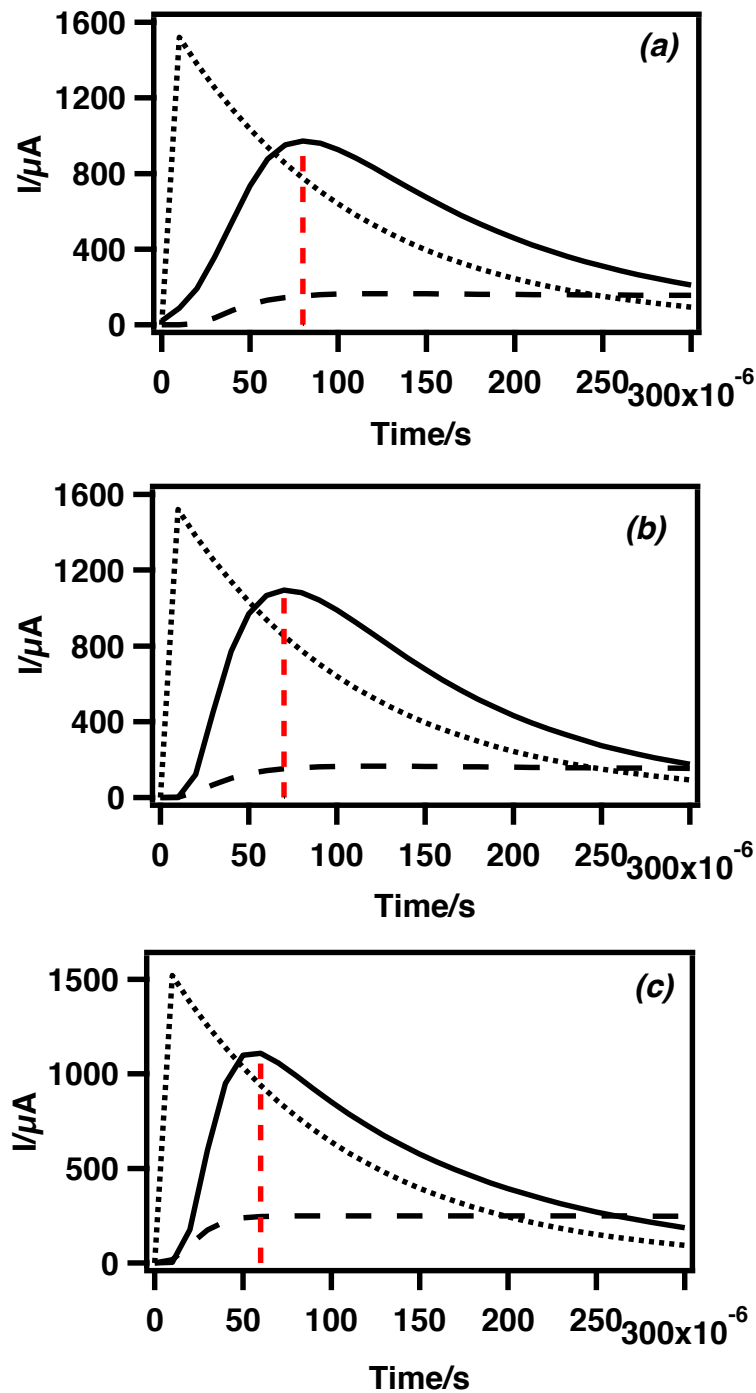


Figure 2.5: Current versus time plots of 658Ω resistor and $0.15 \mu\text{F}$ capacitor in series connected to ACM potentiostat with e-corder (a), ACM potentiostat with powerLab (b) and AutoLab potentiostat with powerLab (c) at a sampling rate of 256 samples (100 KHz) in 2ms. Theoretical current (.....), Experimental current (___), Voltage applied (____).

2.2 Electrochemical techniques

The following techniques were used in the electrochemical studies of the phospholipid monolayers on Hg electrode:

2.2.1 RCV

Cyclic voltammetry (CV) is a voltammetric technique in which the applied potential is ramped linearly as a function of time and is reversed to its initial potential after reaching a set potential (Figure 2.6) and current response is measured. CV is used primarily for diagnostic studies of redox reactions [9-11]. CV is a versatile technique used to obtain the mechanistic information about a redox reaction. Presence or absence of sharp or broad peaks in forward and reverse scan indicates the reversible and irreversible nature of the non-faradaic or faradaic process respectively. Number of peaks in the forward and the backward scan can correspond to the number of electrons transferred by the electroactive species in a redox reaction [6,12]. The plot of current during a voltammetric scan versus the applied potential yields a cyclic voltammogram. The cyclic voltammogram provides chemical information that is unique for each compound.

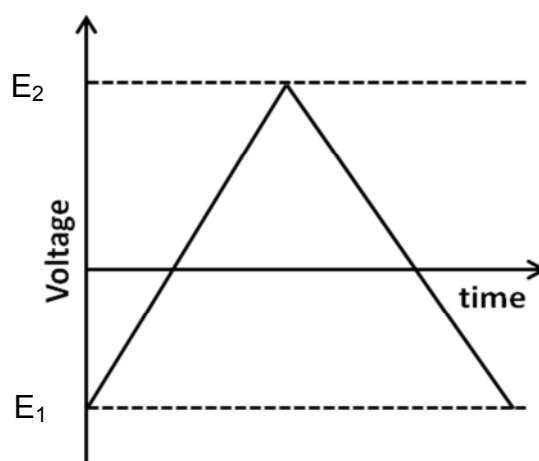


Figure 2.6: Applied potential versus time in CV.

In the absence of faradaic reactions the CV current is proportional to the capacitance of the interface. From CV, the specific capacitance (C_{sp}) of the electrode-electrolyte interface can be obtained by assuming the electrode electrolyte interface is a simple parallel plate capacitor. The charge on the capacitor, q , is proportional to the voltage drop, V , across it:

$$q = CE \quad \text{Equation 2.3}$$

C is the proportionally constant and is called the absolute capacitance of the medium. Charging current is the current produced during the charging of a capacitor and is given by differentiating Equation 2.3 with time, assuming the absolute capacitance of the capacitor to be constant as below:

$$dq/dt = C \times dE/dt \quad \text{Equation 2.4}$$

Where dq/dt is the expression for current and dV/dt is the scan rate (v):

$$I = Cv \quad \text{Equation 2.5}$$

Hence, using charging current and the potential sweep rate from the CV, the absolute capacitance can be calculated. In addition, specific capacitance (C_{sp}) is the absolute capacitance per unit area of the capacitor as follows:

$$C_{sp} = C/A \quad \text{Equation 2.6}$$

The uncompensated resistance and charging current which affect the faradic responses in the various transient and other techniques including CV were shown to be resolved by high speed CV by Howell et. al [13-15]. Rapid or fast scan CV is CV at higher scan rates and has been used to study the kinetics of rapid heterogeneous electrochemical reactions [15].

2.2.2 Impedance measurements

An AC electrical signal is a voltage or current signal alternating its polarity. An AC signal has amplitude and is frequency dependent. A graph of AC sine signal versus time is shown in Figure 2.7 below.

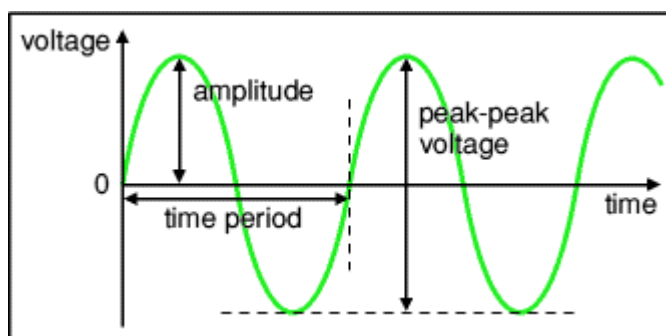


Figure 2.7: A sinusoidal AC voltage signal showing peak to peak amplitude and changing polarity over time [16].

Furthermore, the AC signals can be either *in phase* or *out of phase* when there are more than one signals. In case of *in phase* AC signals (Figure 2.8(a)), the signals arrive at the same point at the same time and in case of *out of phase* AC signals (Figure 2.8(b)), the signals arrive at same point in different times. The extent to which these signals are *out of phase* (phase shift) is determined from the displacement of one signal with respect to the other [17-18].

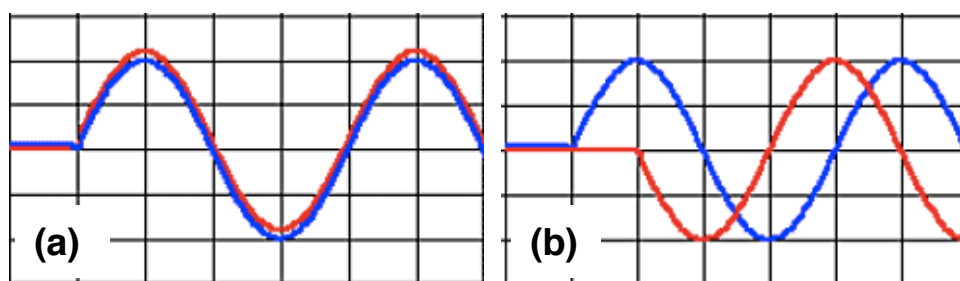


Figure 2.8: *In phase* AC signals (a) *Out of phase* AC signals (b) [19].

An alternating potential applied to an electrode gives rise to an alternating current (AC) (Figure 2.9) resulting from charging and discharging of electrode electrolyte interface and electrochemical charge transfer across the interface. Any resistance to the AC flow is known as impedance (Z) and may change the phase of the signal with respect to the potential as a function of frequency.

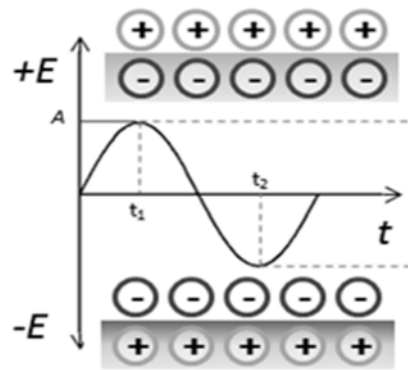


Figure 2.9: An AC potential application to an electrode surface.

2.2.2.1 AC Voltammetry

AC voltammetry is a frequency domain technique and in this method an AC potential of generally low-amplitude of 5-20 mV and single frequency between 50-100 Hz, superimposed on a linear potential ramp (E_{dc}) (Figure 2.10) is applied to the electrode and the resulting AC current separated into in-phase (resistance) and -90° out-of phase (capacitance) components by a lock-in-amplifier and measured as a function of E_{dc} . AC voltammogram is the plot of this AC current versus the potential. AC voltammetry has following advantages over conventional voltammetry [20]:

- 1) High reliability is achieved because of equilibration at successive intervals of potential .
- 2) Measurements can be carried out in the presence of oxygen (O_2) because no AC O_2 wave is obtained due to irreversible reduction of O_2 at Hg.

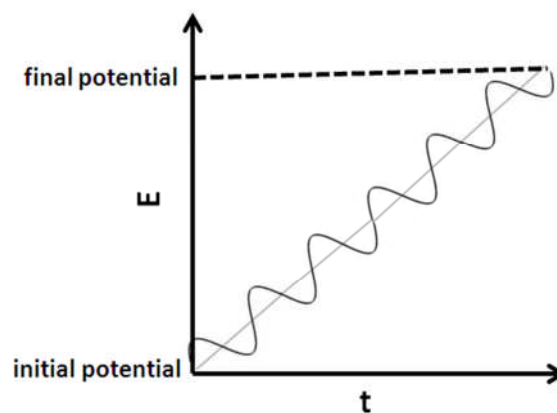


Figure 2.10: An AC potential signal superimposed on a DC potential used in AC voltammetry.

AC voltammetry has also been used to study the kinetics of redox reactions in electroactive monolayer [21], interactions of monolayers on Hg surface by Moncelli, Becucci and Nelson and the adsorption of self-assembled monolayers on Hg by Mandler [22-26]. In AC voltammetry, the specific capacitance of the electrode-electrolyte interface can be obtained by assuming electrical double layer as a simple parallel plate capacitor and which is connected to an alternating source of voltage. The charge on capacitor on application of AC voltage signal with amplitude, V , is given as;

$$q(t) = C \times E \sin \omega t \quad \text{Equation 2.7}$$

Differentiating above equation with respect to time;

$$I(t) = q(t)/d(t) = C \times \omega \times E \quad \text{Equation 2.8}$$

Writing above equation according to Ohm's law:

$$I(t) = C\omega E \quad \text{or} \quad I(t) = C \times 2\pi f E \quad \text{Equation 2.9}$$

Absolute capacitance for the electrical double layer connected to an AC voltage source can be obtained by the following expression:

$$C = I(t)/2\pi f E$$

Where, f is the frequency of the applied voltage and V is the amplitude of the applied voltage. Whereas specific capacitance (C_{sp}) is the absolute capacitance per unit area of the capacitor as follows:

$$C_{sp} = I(t)/2\pi f EA \quad \text{Equation 2. 10}$$

2.2.2.2 Electrochemical impedance

Resistance is the ability of a resistor to resist the flow of current through it. In electrical circuits in the presence of other circuit elements such as capacitors, a more general and complex term impedance is used. Impedance is the ability of the circuit to resist the flow of current through the circuit and is estimated from the measured AC current in response to an application of the AC voltage. In impedance analysis, a cell is assumed to be composed of analog electrical components which make up an equivalent circuit. All the components are assumed to be pure. The AC behaviour of

these pure components is observed as a function of angular frequency. For a resistor, impedance is simply equal to the resistance and is frequency independent,

$$Z_R = R \quad \text{Equation 2.11}$$

On the other hand the impedance of a pure capacitor is a function of angular frequency and increases with decrease in frequency,

$$Z_C = -i/\omega C \quad \text{Equation 2.1}$$

The impedance (Z) of a series RC circuit may be represented by the equation given below:

$$Z = R - i/\omega C = Z' - iZ'' \quad \text{Equation 2.13}$$

Z' is the real part of the impedance and Z'' is the imaginary part of the impedance. The inverse of impedance is admittance " $Y = 1/Z$ ". The admittance for the series RC circuit is:

$$Y = 1/Z = 1/(Z' - iZ'') \quad \text{Equation 2.14}$$

$$Y = \frac{1}{Z' - iZ''} * \frac{Z' + iZ''}{Z' + iZ''}$$

$$Y = \frac{Z' + iZ''}{Z'^2 + Z''^2}$$

$$Y = \frac{Z'}{Z'^2 + Z''^2} + i \frac{Z''}{Z'^2 + Z''^2}$$

$$Y = Y' + iY'' \quad \text{Equation 2.15}$$

$$\frac{Z'}{Z'^2 + Z''^2} = Y' \quad \text{and} \quad \frac{Z''}{Z'^2 + Z''^2} = Y''$$

Y' is the real admittance and Y'' is the imaginary admittance in Equation 2.15. $Y\omega^{-1}$ is the normalized admittance and has units of capacitance. The plot of $Y'\omega^{-1}$ versus $Y''\omega^{-1}$ is called the complex capacitance plane plot [27-29]. The complex plane plots obtained from admittances show a semicircle. In capacitive circuits, the imaginary impedance and capacitance are always negative and the imaginary admittance is positive [28].

Pure Hg and DOPC coated Hg behave like pure capacitor giving a semicircle in the complex capacitance plane in the region of PZC of Hg. Interactions of various biologically active compounds with the DOPC on Hg interface will appear either as

changes in zero frequency capacitance (ZFC) and/or as a secondary element or tail due to low frequency relaxations indicating layer imperfections [30-32]. For developing a profound understanding about the process, the experimental data can also be fitted to the impedance model (Equation 2.16) for the DOPC monolayer on Hg developed by Nelson and others [30]:

$$Y = \frac{1}{R + 1/[(i\omega)^\beta((A_s - A)/1 + (i\omega\tau)^\alpha) + A]} \quad \text{Equation 2.16}$$

Y is admittance, R is solution resistance, τ is the relaxation time constant, α is the coefficient which represents distribution of time constant around the most probable value (either 1 or less than 1) and β characterizes the non-idealities at the interface between the capacitor and resistor.

Where A_s and A are related to capacitance as follows:

$$C_s - C = ((A_s - A) - A) * \tau^{(1-\beta)}$$

$$C = [A * R^{(1-\beta)}]^{1/\beta}$$

C is identified as zero frequency capacitance of the monolayers and $C_s - C$ is the additional low frequency capacitance element.

Relationship between capacitance (C), monolayer thickness (d) and relative permittivity (ϵ):

Capacitance is related to the relative permittivity of the dielectric (ϵ_r) and the spacing between the capacitor plates (d) by the following relation:

$$C = \epsilon_0 \epsilon_r A/d \quad \text{or} \quad C_{sp} = \epsilon_0 \epsilon_r/d \quad \text{Equation 2.17}$$

Where C_{sp} is capacitance per unit area, A is the area of the two plates, ϵ_r is the relative permittivity of the dielectric between the plates, ϵ_0 is the permittivity of free space $\approx 8.854 \times 10^{-12} \text{ F m}^{-1}$ and d is the separation between the plates.

DOPC monolayers on Hg electrode have been reported to behave as almost an ideal capacitor in impedance measurements under low applied field conditions [33] with the DOPC coated Hg surface acting as one plate and the electrolyte counterions as

the other plate at the electrode-electrolyte interface. The DOPC monolayer apolar region acts as a dielectric with ϵ_r of apolar region of ~ 2 [34] and thickness ~ 1.2 nm [34]. In impedance measurements, at -0.4 V (PZC of Hg) [35], the DOPC monolayer on Hg electrode gives rise to an almost perfect RC semicircle in the complex capacitance plane plots with no additional low frequency element. The extrapolation of the semicircle to the real capacitance axis gives the zero frequency capacitance (ZFC) value which is equivalent to the C_{sp} of the monolayer [30] i.e. $\sim 1.78 \mu\text{F cm}^{-2}$ [34]. Interaction of biomembrane active compounds with the DOPC monolayer on Hg has three effects on the impedance data projected into the complex capacitance plane: (i) an additional low frequency capacitive element; (ii) depression of the RC semicircle and (iii) an increase or decrease of the ZFC. A change in the ZFC corresponds to the change in the monolayer thickness and/or the relative permittivity of the dielectric according to Equation-2.17.

Most biomembrane active compounds have a higher relative permittivity than the apolar region of the DOPC monolayer. As a consequence, when these species interact with the DOPC monolayer, a decrease in ZFC can only be associated with an increase in thickness of the monolayer and not a decrease in the relative permittivity of the apolar region. On the other hand, an increase in ZFC following compound/DOPC interaction can be attributed to the following two factors:

- (1) Increase in relative permittivity of dielectric through penetration of compounds with higher relative permittivity into the low dielectric lipid monolayer apolar region resulting in an overall increase in the average relative permittivity of the dielectric.
- (2) Decrease in thickness of the monolayer.

For example a decrease in the ZFC of the DOPC monolayer observed in the case of *p*-Cl-BP/DOPC interaction (Chapter-5) can be only be related to an increase in the thickness of DOPC monolayer because a decrease in relative permittivity of the DOPC apolar region is not possible in the presence of *p*-Cl-BP whose relative permittivity is higher than that of the DOPC apolar region [36-38]. On the other hand, an increase in the ZFC of the DOPC monolayer observed in case of *p*-OH-BP/DOPC interaction can be due to either a decrease in thickness of monolayer or equally to an increase in the relative permittivity of the DOPC monolayer apolar region resulting from penetration of *p*-OH-BP into the monolayer.

2.2.3 Potential step experiments

Chronoamperometry is a transient technique used in electrochemistry to investigate the kinetics and mechanism of an electrochemical reaction. In chronoamperometry, a potential is applied to the working electrode in the form of either a single step or double step (step potential) (Figure 2.11a) for a small period of time. The resulting current response (current transient) from the applied potential steps is measured as a function of time (Figure 2.11b). The current response consists of either charging current alone or both the charging and the faradaic current. The charging current decays exponentially with time and is significant in the initial few milliseconds only.

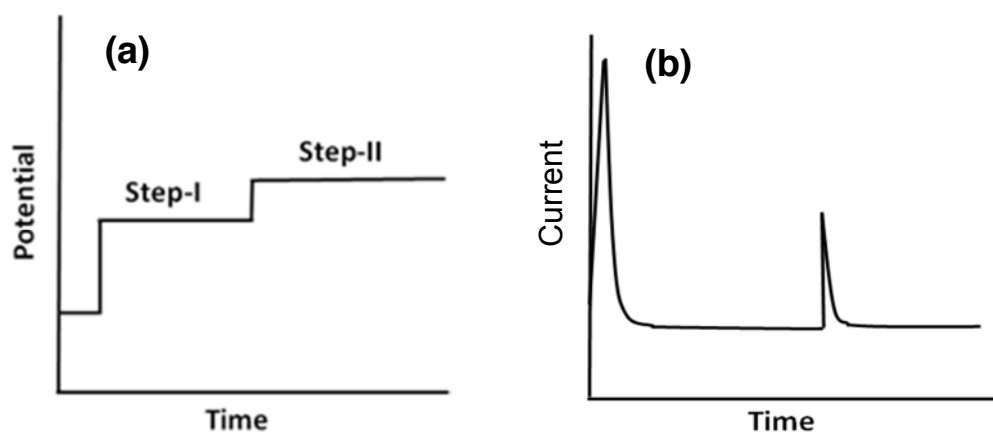


Figure 2.11: Double potential step (a) applied to the electrode and resulting non faradaic current response (b) in chronoamperometry.

Investigation of kinetics of second phase transition by Hg supported DOPC monolayer

The second phase transition of DOPC on Hg has been shown to follow the nucleation and growth mechanism. On applying a double potential step to the DOPC coated Hg electrode, a broader hump evolving into a peak resolved from the double layer relaxation peak in the current transients is attributed to the second phase transition and is characteristic of a classical nucleation and growth (N & G) process (Figure 2.12).

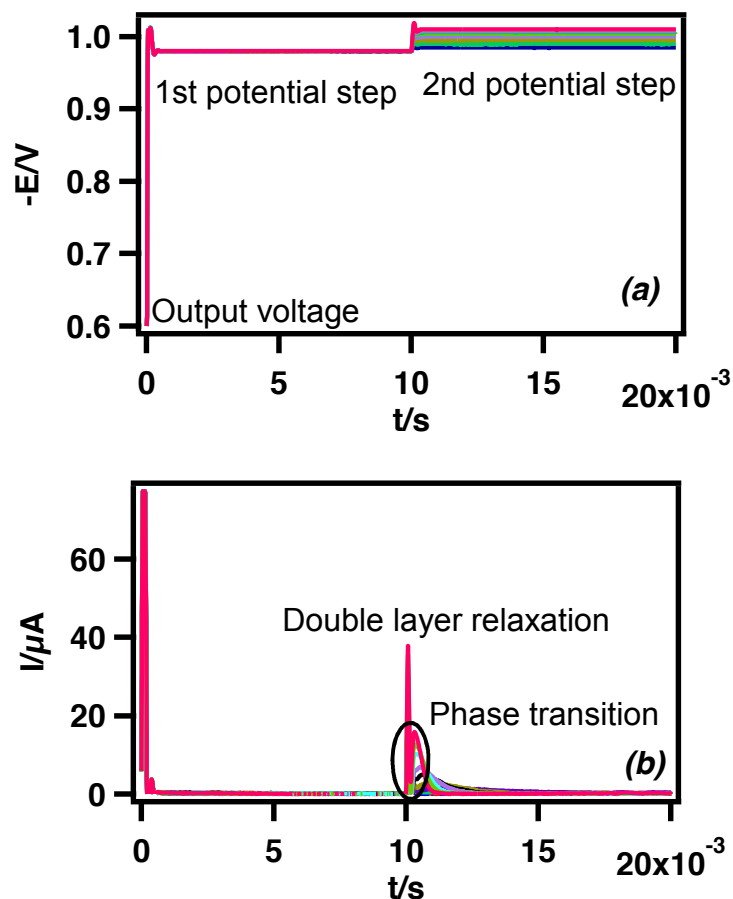


Figure 2.12: Full potential step versus time plots (a) and resulting current-time transients (b) following double potential steps as indicated applied to DOPC monolayer on Hg in 0.1 mol dm^{-3} KCl solution.

The first sharp peak (A in Figure 2.13) represents the double layer relaxation. Double layer relaxation is a fast process and take place in about less than about 0.1 ms. Whereas, the second peak represents a slower process and of about 2-3 ms in length. The rise in current (B in Figure 2.13) corresponds to the growth of the nuclei which are either instantaneously produced or more likely to be formed during the first phase transition. After reaching a certain size, growth process ceases and fully grown nuclei start to coalesce resulting in a decrease in current (C in Figure 2.13). Both the growth and coalescence process are potential dependent and increase in speed on applying higher negative step potential (Figure 2.12).

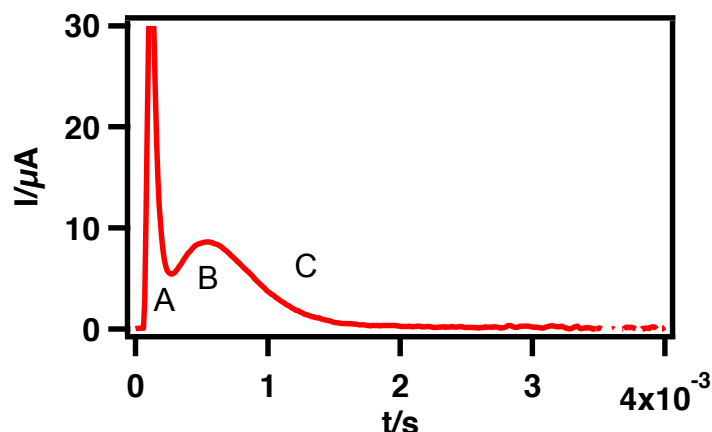


Figure 2.13: A current-time transient following a potential step from -0.980 V to -1.019 V applied to DOPC monolayer on Hg in 0.1 mol dm⁻³ KCl solution.

The combined rate constant for both nucleation and growth process also called the composite rate constant can be extracted from the current-time transients in response to the application of potential steps using the Avrami equation:

$$\alpha = 1 - \exp(-b_f t^2) \quad \text{Equation 2.18}$$

In fact the N and G process represents the adsorption of bilayer patches on the electrode surface [79] and the current peak represents the displacement of charge during this process. As a result α is the fraction of Hg surface covered with the new phase of bilayer patches [33, 35] following the N & G process, b_f is the composite (nucleation and growth) rate constant. When α is 0.5, $t = t_{1/2}$

$$2 * \exp\left(-0.08 - \log t_{\frac{1}{2}}\right) = b_f \quad \text{Equation 2.19}$$

The half life ($t_{1/2}$) of the current transient is the time for the charge-time transient to reach half of the charge density [33]. Hence $t_{1/2}$ can be used to calculate the composite rate constant for the nucleation and growth process.

2.3 Experimental Protocol

2.3.1 Preparation of electrolyte solution

The electrolyte used in all the experiments was 0.1 mol dm⁻³ of KCl with added 0.001 mol dm⁻³ of the buffer (0.002 mol dm⁻³ of Na₂HPO₄ and 0.002 mol dm⁻³ of

NaH₂PO₄) to maintain a pH level of almost 7.6 which is close to the physiological pH of the human body i.e. 7.4. 0.1 mol dm⁻³ salt solutions of KNO₃, NaCl, LiCl, BaCl₂, CaCl₂, NaF, KF, RbF, CsF, LiOH, NaOH, KOH, KBr and KI were also used as electrolytes to characterize the effect of electrolyte on the phase transitions shown by DOPC monolayer on Hg. In permeability experiments conducted on DOPC bilayer on Hg using ZnCl₂, 0.1 mol dm⁻³ of KCl without added buffer was used to avoid any precipitation of Zn. KCl was combusted in muffle furnace at about 650 °C for 6 hours. KCl was provided by Fisher Scientific and Na₂HPO₄ and NaH₂PO₄ were provided by Sigma Aldrich. 25 mL of buffered electrolyte was taken in the electrochemical and placed on a magnetic stirrer for stirring when necessary. Reference, counter and working electrodes were fixed in the electrochemical cell and the electrolyte solution was deaerated by purging argon gas through it to remove O₂ for about 15-20 minutes. After deaeration, a blanket of argon was maintained above the fully deaerated solutions to avoid penetration of any O₂ into the solution during all experiments. Because, O₂ not only oxidizes the lipid but also in the presence of O₂, an O₂ reduction hump appears in RCV and can affect the capacitance measurement.

2.3.2 Electrochemical measurements on Hg electrode

A diagnostic RCV scan was always performed on uncoated Hg electrode between the potential limit -0.2 to -1.6 V to (1) check the presence of impurities or O₂ prior to the addition of DOPC and (2) calculate the electrode area using capacitance potential plots from RCV of uncoated electrode as follows:

$$A = I_{max}/C_{sp}v \quad \text{Equation 2.20}$$

Where, I_{max} and C_{sp} are the maximum current and specific capacitance ($\approx 41 \mu\text{F cm}^{-2}$ for Hg in 0.1 mol dm⁻³ KCl) of Hg respectively, corresponding to PZC of Hg and varies with varying potential and electrolyte and v is the potential scan rate (40 Vs⁻¹). The area of an electrode remains constant irrespective of the nature of electrolyte and potential scan rate. The applied voltage ramp to the Hg at 40 Vs⁻¹ in 0.1 mol dm⁻³ aerated and deaerated KCl solution and the current response is shown in the Figure 2.14.

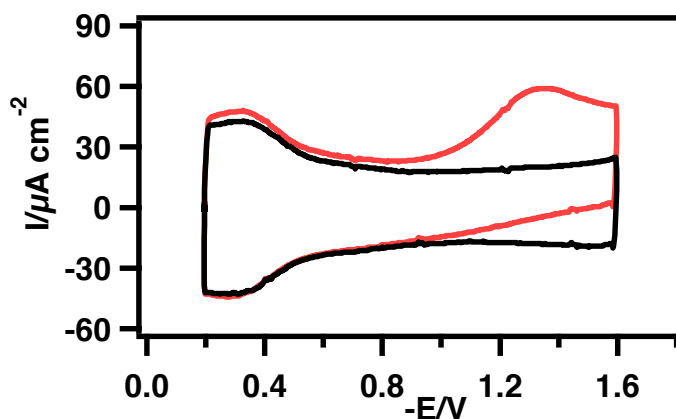


Figure 2.14: Capacitance current versus potential plots of uncoated HMDE in 0.1 mol dm^{-3} KCl in the presence (red) and absence (black) of O_2 acquired using RCV at 40 Vs^{-1} .

It can also be seen that the current measured at uncoated Hg in the presence of O_2 is higher at all potentials than in the absence of O_2 . In addition, in the presence of O_2 , there is a current hump corresponding to the O_2 reduction at more negative potential in addition to the capacitance current water hump [39] at less negative potential around -0.3 to -0.4 V . RCV is a very effective and sensitive technique for preliminary tests in the sense that it is fast and produces a "snapshot" of the electrode interface.

Following RCV, an ACV scan of the Hg electrode was also recorded because ACV is an equilibrium technique compared to RCV and can show the presence of impurities which do not appear in RCV. In ACV, capacity versus potential measurements were carried out by measuring the imaginary current (I) in the potential range between -0.2 V and -1.6 V at a $f = 75 \text{ Hz}$, $\nu = 5 \text{ mV s}^{-1}$ and ΔV of 0.005 V . The potential versus capacitance scan of Hg in 0.1 mol dm^{-3} KCl obtained by ACV (Figure 2.15) is very similar to that obtained by RCV. ACV shows the capacitance maximum corresponding to the water hump of Hg [39] but not the O_2 reduction because the ACV technique is insensitive to the irreversible reduction of O_2 . Only an insignificant increase in the capacitance is observed in the presence of O_2 [20] compared to that in the deaerated solution.

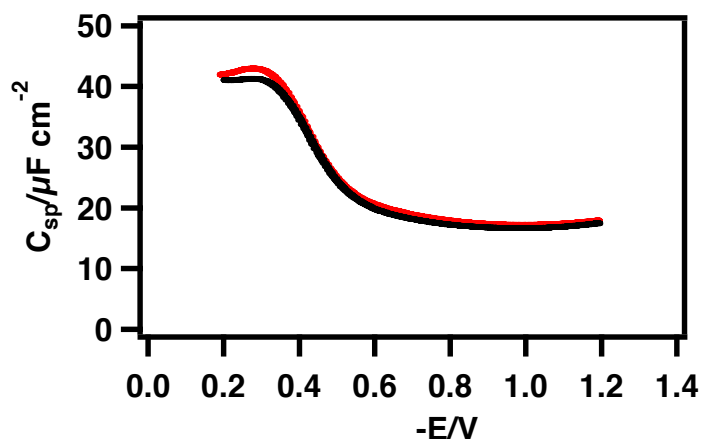


Figure 2.15: Capacitance-potential plot of uncoated HMDE in the aerated (red) and deaerated (black) 0.1 mol dm^{-3} KCl solution acquired using ACV at scan rate 5 mVs^{-1} , frequency 75 Hz , amplitude 0.0046 V and 90° out of phase.

The most sensitive technique for checking the purity of the system is using electrochemical impedance. Even a negligible amount of organic impurity/contamination, not evident in RCV and ACV, shows up in impedance scans.

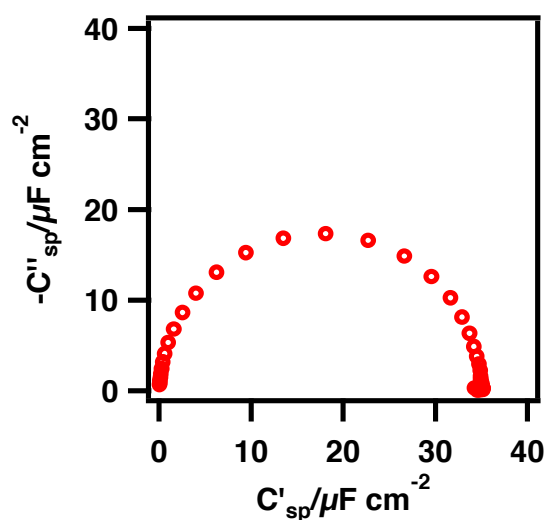


Figure 2.16: Impedance data transformed to complex capacitance plane of uncoated HMDE in the deaerated 0.1 mol dm^{-3} KCl with $0.001 \text{ mol dm}^{-3}$ phosphate buffer, acquired using EIS at -0.4 V , 0.005 V amplitude and $65000\text{-}0.1 \text{ Hz}$ frequency.

A complex capacitance plane plot transformed from the impedance of uncoated Hg in 0.1 mol dm^{-3} of deaerated KCl solution free of impurities is always a perfect

semicircle (Figure 2.16). The main drawback of ACV and impedance measurements are that these are slow techniques.

These techniques are responsive towards small contaminations (less than 1.0 $\mu\text{g/L}$) in the electrolyte solution. If there is any organic contamination present in the electrochemical cell or elsewhere such as in the gas tubing etc., it will appear as

1) small peaks in the RCV and ACV scans of uncoated Hg along with suppression in the capacity current hump corresponding to the potential of zero charge of Hg (PZC) depicted in Figure 2.17a and b.

2) imperfection in the semicircle with suppression of ZFC and appearance of a low frequency extra element in the complex capacitance plane (Figure 2.17c).

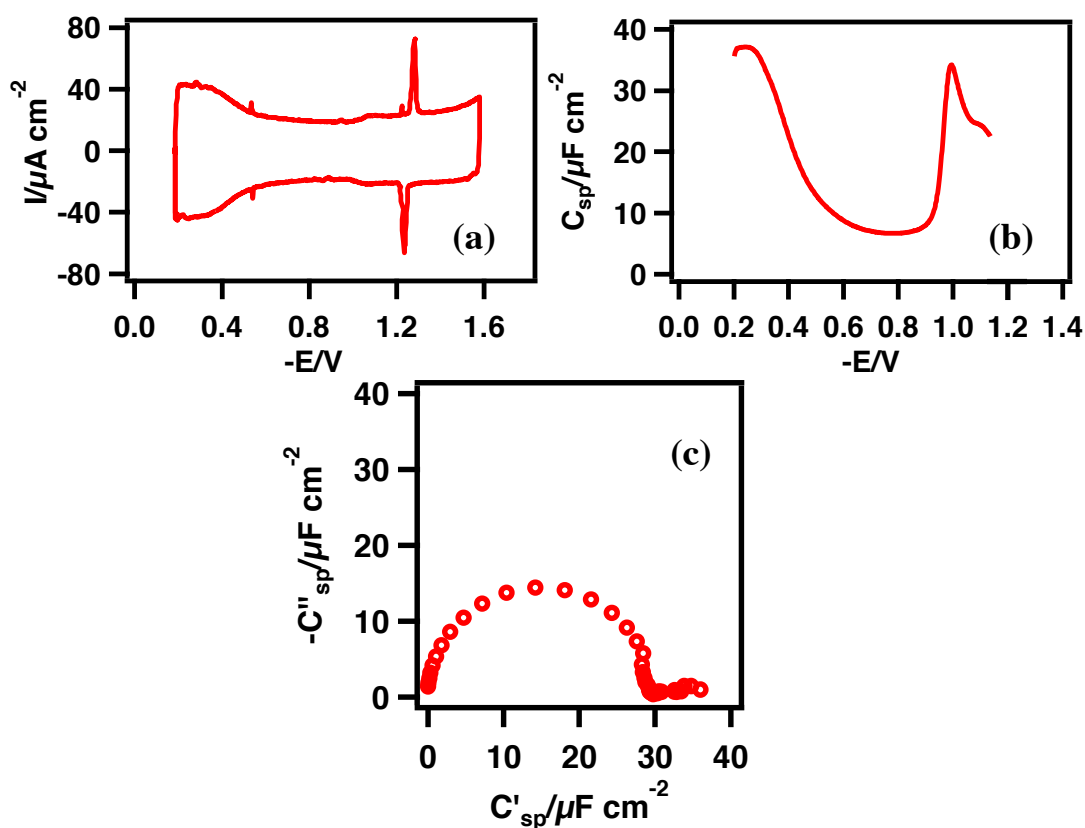


Figure 2.17: Capacitance current and capacitance versus potential plots (a, b respectively) and impedance data transformed to complex capacitance plane (c) of uncoated HMDE in the 0.1 mol dm^{-3} KCl containing organic impurity obtained using RCV at 40 Vs^{-1} , ACV at 5 mVs^{-1} and EIS at -0.4 V respectively.

2.3.3 Formation of DOPC monolayers

DOPC suspension (Ananti Lipid) of 2 mg/mL was prepared in pentane (HPLC grade, Fisher Scientific Chemicals Ltd.) in a clean glass vial and was always stored in freezer. A glass syringe was used to transfer the lipid solution to the electrolyte surface in the electrochemical cell. DOPC monolayers were prepared by spreading about 15-25 μL of DOPC at the argon-electrolyte interface. A period of about 5-10 minutes was required for the pentane to evaporate. The HMDE assembly was then lifted up from the solution, a new drop was raised and electrode was lowered to the surface slowly so that the drop touched the electrolyte surface for a sufficient time to allow monolayer formation. Lipids transfer to the hydrophobic Hg and resulted in the formation of supported lipid monolayer (Figure 2.18). DOPC monolayers on MFE were formed by moving the electrode across the DOPC-argon gas interface and excessive lipid can be removed by cycling a higher negative potential for an appropriate time. Current potential scans and current transients were recorded using electrochemical techniques. For a new measurement, a new drop was produced by lifting the Hg above the interface and gently tapping the electrode to knock the drop off, raising a new drop by turning the scaled sleeve and lowering the electrode down into the solution.

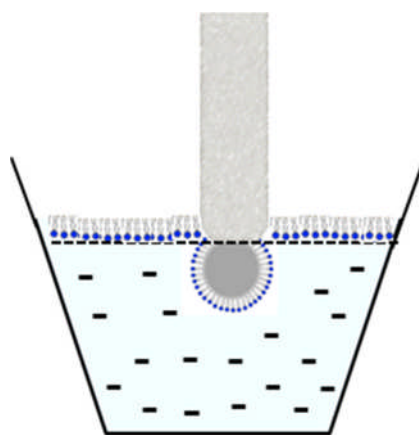


Figure 2.18: Transfer of DOPC monolayer on MFE from lipid- gas.

2.3.4 Electrochemical measurements of DOPC monolayer on Hg

RCV scans were recorded on the DOPC coated Hg to check the (1) surface coverage of the DOPC monolayer (degree of compactness of monolayer) and (2) Integrity of

the DOPC monolayer. Figure 2.19 represents the capacitance current versus potential plot of a DOPC coated Hg drop in 0.1 mol dm^{-3} KCl at switching potential -1.2 V and -1.6 V . The plot shows different potential dependant phase transitions occurring in the DOPC monolayer on the Hg surface. At switching potential of -1.2 V , two completely reversible capacitance current peaks are observed at higher negative potentials due to underlying phase transitions in addition to a constant low capacitance current region (about -0.2 to -0.9 V). Constant and low capacitance current is suggestive of the presence of intact and impermeable DOPC monolayer. The first and second capacitance current peaks are believed to be associated with penetration of electrolyte into the monolayer followed by the reorientation of lipids and bilayers formation. But if the scan terminates at -1.6 V , more phase transitions are observed (Figure 2.19) owing to the liposome formation and partial desorption. Only first two phase transitions are considered to be important and well characterized and were studied in all the investigations. The height and sharpness of peaks gives a clue about the integrity of monolayer formed. For a good monolayer (1) both the capacitance current peaks should be sharp and stable, (2) first capacitance current peak should always have a higher capacitance than the second capacitance current peak and (3) the ratio of first peak capacitance current and capacitance in constant capacitance region should not be less than 2.3.

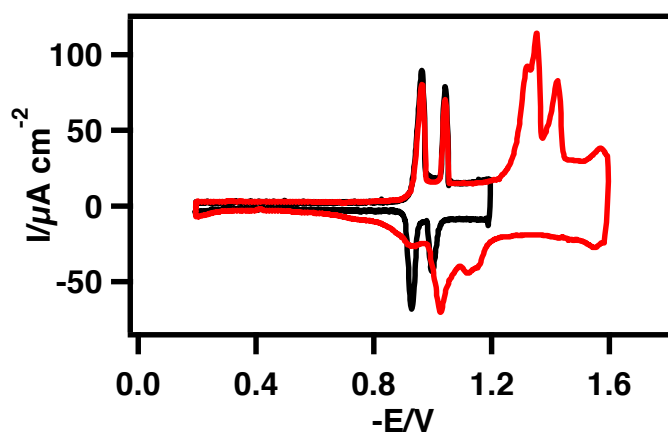


Figure 2.19: Capacitance current versus potential plot of DOPC coated HMDE in 0.1 mol dm^{-3} KCl at 40 Vs^{-1} obtained using RCV at switching potential -1.2 V (black) and -1.6 V (red).

Capacitance-potential plots of the DOPC coated Hg electrode acquired using ACV shows the analogous phase transitions except that the phase transitions at higher negative potentials owing to the desorption process are not very well resolved.

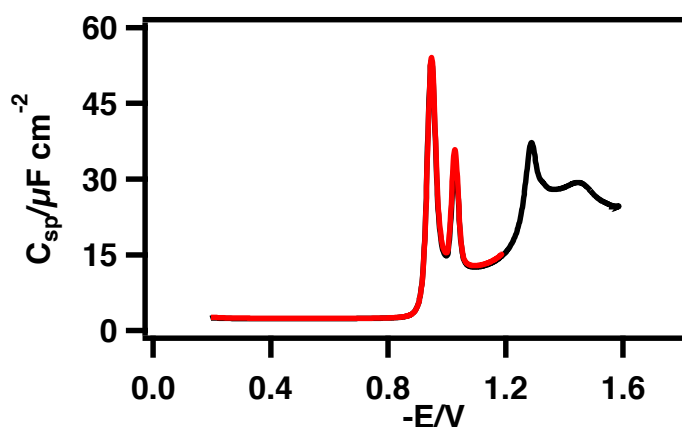


Figure 2.20: Capacitance-potential plot of DOPC coated HMDE in the 0.1 mol dm^{-3} KCl solution obtained using ACV at scan rate 5 mVs^{-1} , frequency 75 Hz , amplitude 0.0046 V and 90° out of phase.

If the amount of lipid on the surface of electrode is less than the required to make a compact layer, the height of the second capacitance current peak increases at the expense of first peak [33]. Presence of impurity/contamination in the system also destroys the monolayer and appears as deformed capacitance current peaks in the capacity current-potential measurements (Figure 2.21) and as a low frequency extra element in the complex capacitance plots (Figure 2.22 (b)).

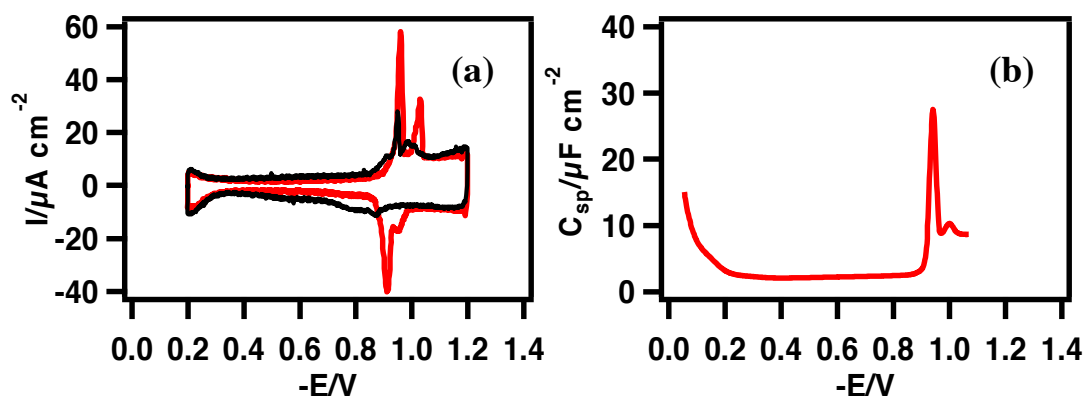


Figure 2.21: Capacitance current and capacitance-potential plot of DOPC coated HMDE in the 0.1 mol dm^{-3} KCl solution obtained using (a) RCV at 40 Vs^{-1} and (b) ACV at 5 mVs^{-1} , frequency 75 Hz , amplitude 0.0046 V and 90° out of phase.

In the impedance measurements of a DOPC coated Hg electrode, the system should behave as an almost ideal capacitor similar to an uncoated Hg electrode and the data is transformed to a perfect semicircle in the complex capacitance plane. But due to a very low dielectric (~ 2) of DOPC compared to the water molecule (~ 80), the time constant (τ) for orientation polarization is increased. Moreover, the zero frequency capacitance (ZFC) of the DOPC coated Hg electrode is significantly reduced to $\sim 1.8 \mu\text{F cm}^{-2}$ compared to the uncoated Hg electrode ($\sim 35 \mu\text{F cm}^{-2}$) because of the low dielectric of DOPC so decreasing the RC time constant.

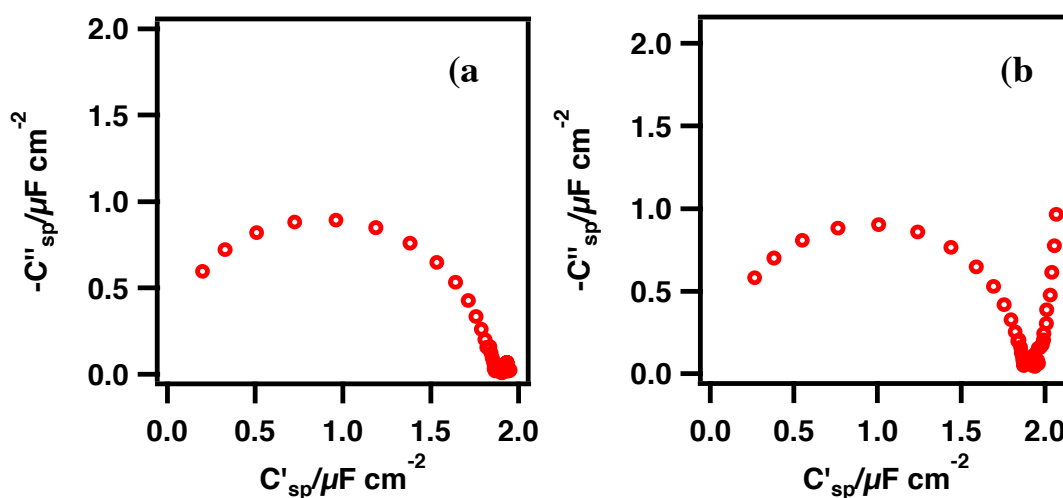


Figure 2.22: Impedance data transformed to complex capacitance plane of DOPC coated HMDE in the 0.1 mol dm^{-3} KCl solution in the absence (a) and presence (b) of contamination, acquired using EIS at -0.4 V , 0.005 V amplitude and $65000\text{-}0.1 \text{ Hz}$ frequency.

2.4 MFE: Pt vs Au

The MFE were prepared on a silicon wafer based microfabricated platinum (Pt) and gold (Au) electrodes separately with a Pt and Au disc diameter of 1 mm . Embedded on the same wafer was a Pt and Au rectangle as a contact pad. The disc was connected to the contact pad by a 0.5 mm thick Pt and Au trace interconnect that was insulated with approximately 1.5 mm of Si_3N_4 deposited by plasma enhanced chemical vapour deposition (PECVD). Pt based MFE compared to the Au based MFE were found to be very stable and durable and were used in all the investigation in the proceeding chapters. A comparison of both the MFEs is presented below.

2.4.1 Pt based MFE

The Pt electrode was cleaned prior to the Hg deposition using a solution of H_2SO_4 (Fisher Scientific) and 30 % H_2O_2 (Fluka) mixture (piranha solution) and rinsed with Milli-Q 18.2 M Ω water (Millipore, U.K.) before drying. The Pt electrode was then subjected to rapid cyclic voltammetry (RCV) from -0.2 to -3.0 V vs Ag/AgCl at 40 Vs^{-1} to remove any remains of organic film. Hg can be deposited on the Pt surface both by manual and electrodeposition methods. Hg deposited by both methods allow the formation of DOPC monolayers similar to those on HMDE. Manual deposition of Hg using an Eppendorf microliter pipette on the dried Pt disk is simpler and quicker. Electrodeposition is the preferred method if the precise quantity of Hg is required to be known.

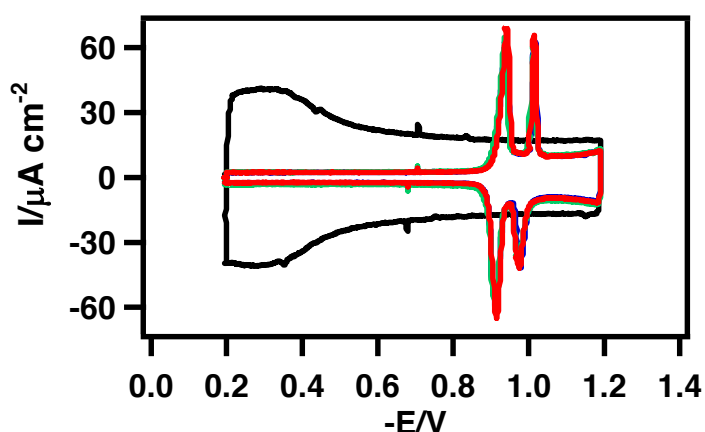


Figure 2.23: Capacitance current versus potential plots of MFE and DOPC coated MFE immediately after deposition (red), after 5 hr (green) and after 1 month (blue), using Pt as substrate in 0.1 mol dm^{-3} KCl, obtained using RCV at 40 V s^{-1} .

MFE is advantageous in terms of its reusability utilizing a small amount of Hg and can be cleaned similarly to the Pt surface by voltammetric cycling with negative potential excursion between -0.2 and -3.0 V vs Ag/AgCl at 40 Vs^{-1} . Strongly adsorbed impurities can be removed from the Hg surface by cycling to a more negative potential of -4.0 V vs Ag/AgCl without causing any damage to the Hg or to the Pt underneath. Hg deposited on the Pt surface is very stable and can remain for long period in spite of limited amalgam formation at the interface between Pt and

Hg. DOPC monolayer on a month old MFE yielded the I-E voltammograms similar to that of a freshly prepared electrode as shown in Figure 2.23.

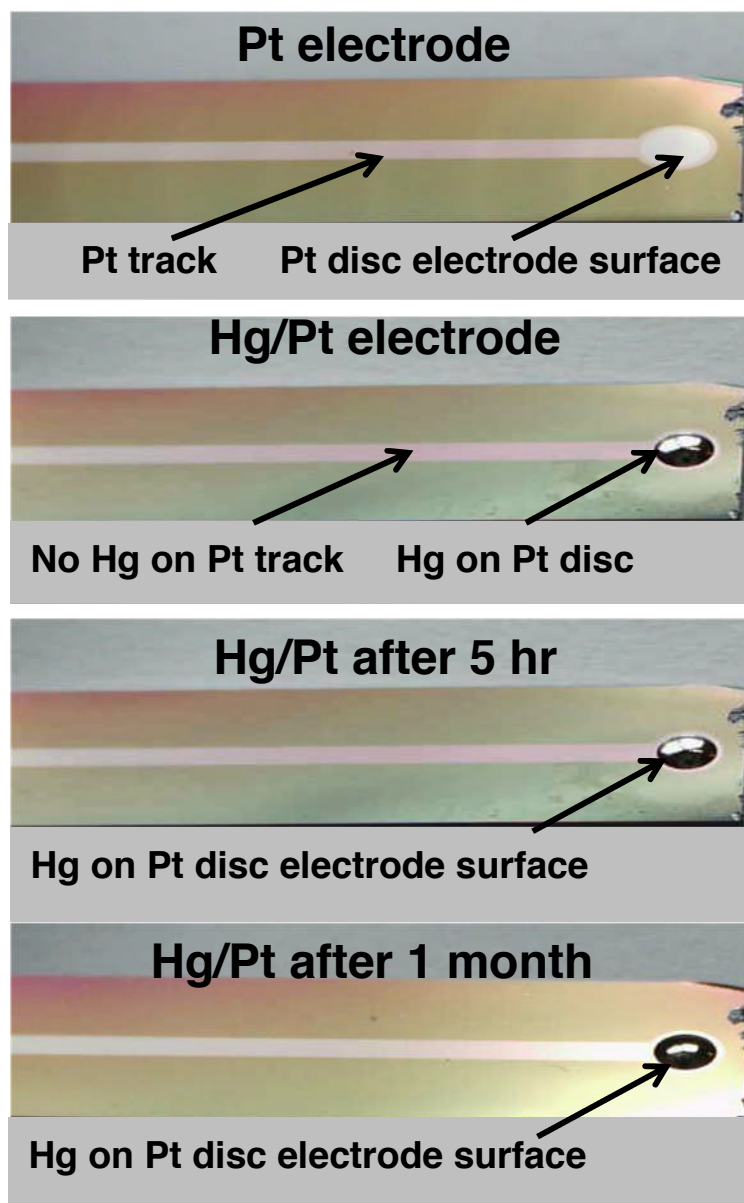


Figure 2.24: Microscopic images of MFE using Pt as substrate.

2.4.2 Au based MFE

Both manual and electrochemical methods were employed to deposit Hg on the Au surface and it is found that Hg on Au electrode is not at all stable. The capacitance current of Hg supported DOPC monolayer on Au (Fig 2.25 b) in constant capacitance current region (-0.2 to -0.9 V) is significantly higher than that on Pt

electrode (Fig 2.23). In addition, it is clear from Figure 2.25 (a) and (b) that the capacitance current of both Hg and DOPC coated Hg on Au surface increases drastically after 5 hours.

Manual deposition

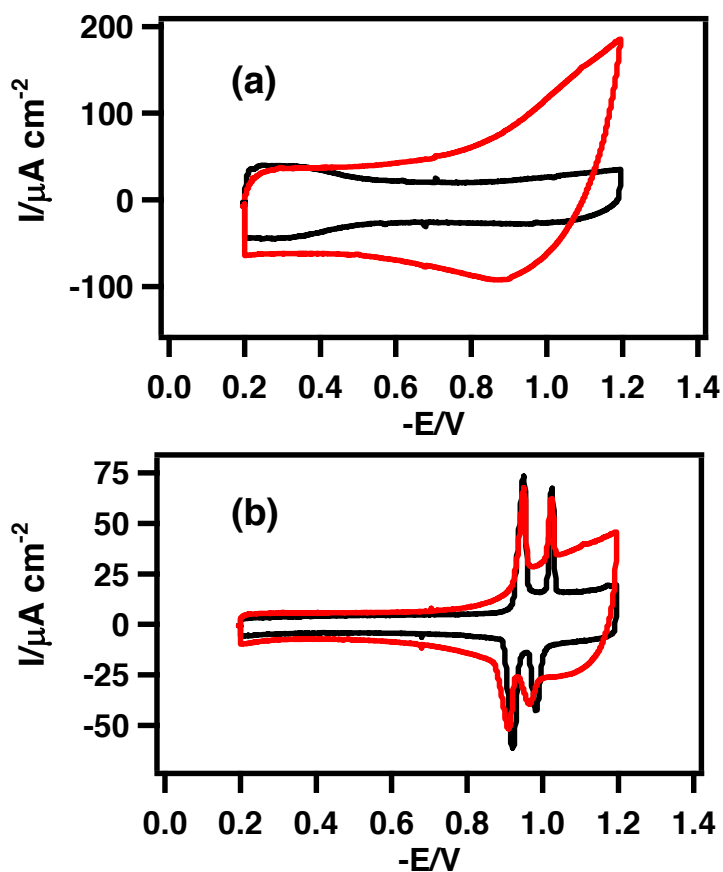


Figure 2.25: Capacitance current versus potential plots of MFE (a) and DOPC coated MFE (b) using Au as substrate, immediately after deposition (black) and after 1 hr (red) in 0.1 mol dm^{-3} KCl using RCV at 40 Vs^{-1} .

Hg is found to readily amalgamate with Au and accounts for the instability of the MFE. Destruction of the electrode surface and the contact pad due to amalgam formation can be seen with a microscope (Fig 2.26).

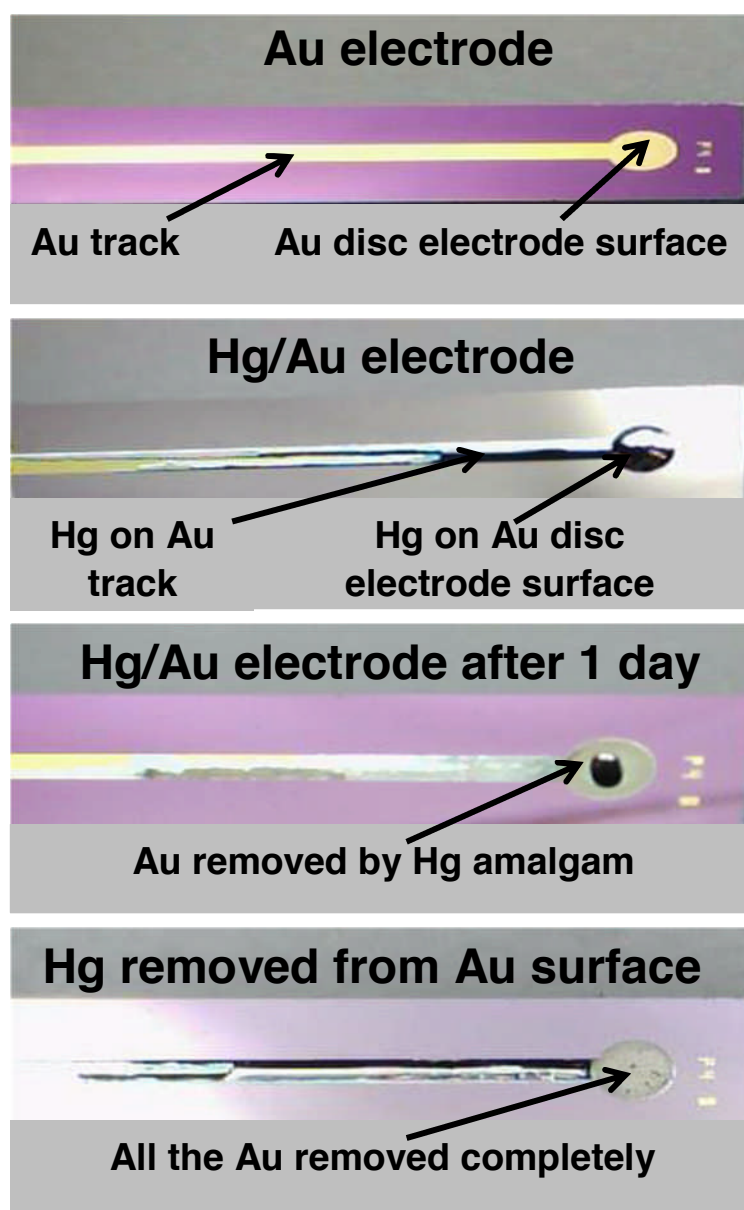


Figure 2.26: Microscope images of MFE formed by manual deposition of Hg on Au based MFE.

Electro-deposition of Hg on Au enhanced the amalgam formation and destroyed the electrode surface more effectively and rapidly. It is clear from the I-E plot of DOPC coated electrochemically deposited Hg on Au, that the capacitance current peaks are less sharp and not observed after 24 hours (Figure 2.27).

Electrodeposition

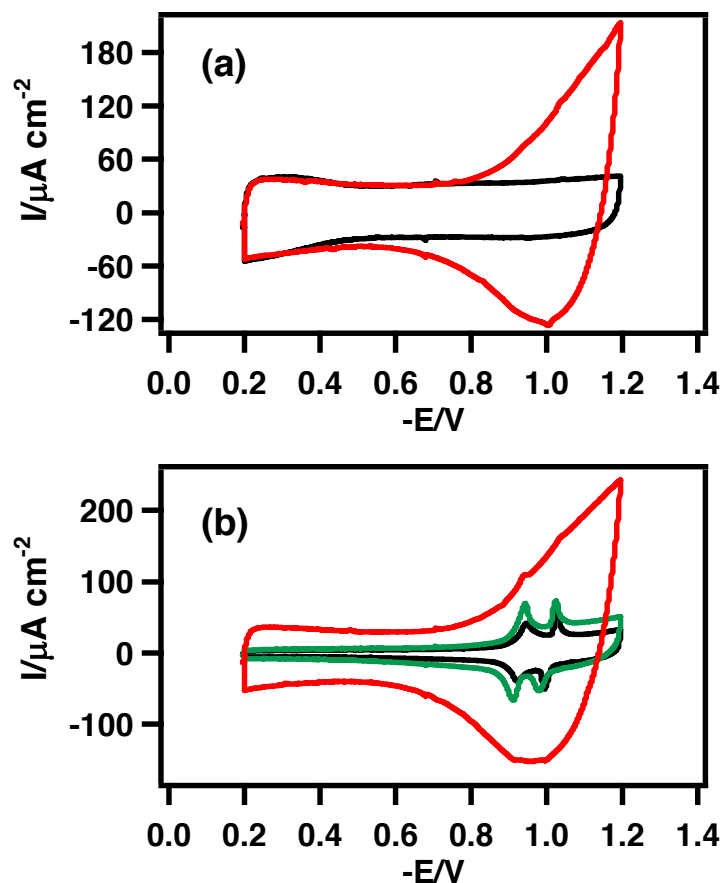


Figure 2.27: Capacitance current versus potential plots of electrochemically deposited MFE (a) and DOPC coated MFE (b) using Au as substrate immediately after deposition (black), after 5 hr (green) and after 24 hr (red), in 0.1 mol dm⁻³ KCl, obtained using RCV at 40 Vs⁻¹.

Electrodeposition

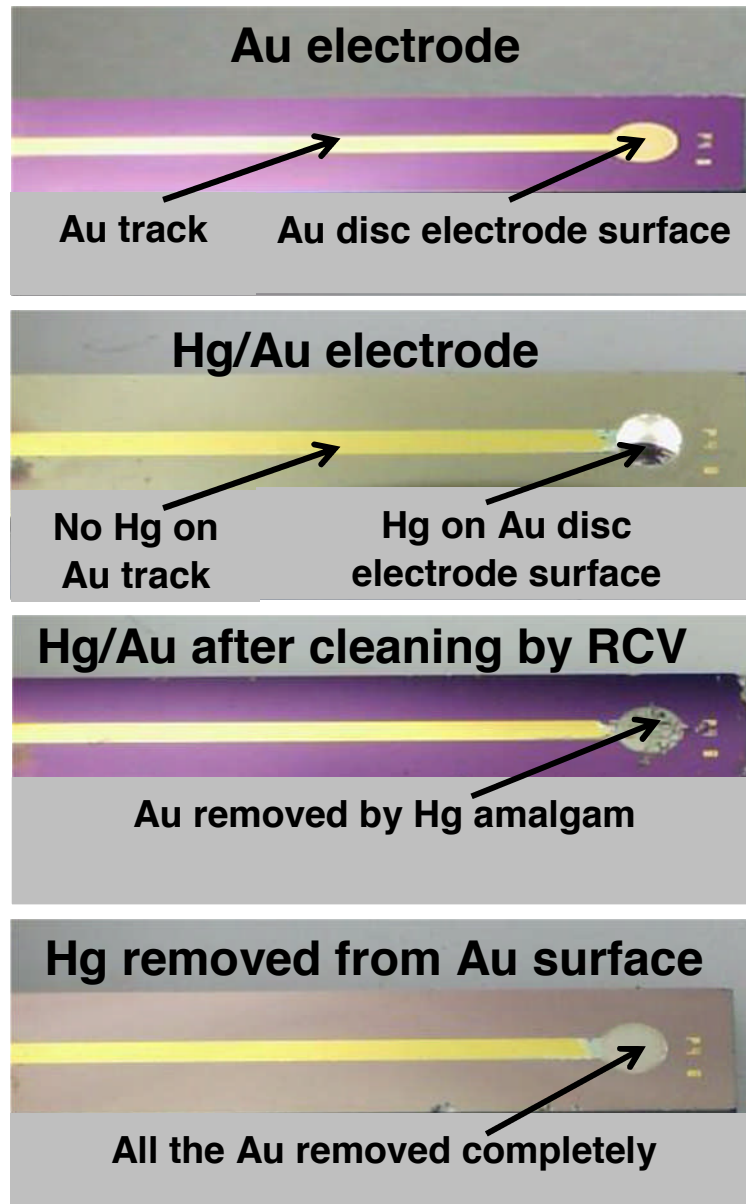


Figure 2.28: Microscopic images of Au based MFE formed by electrodeposition of Hg from $\text{Hg}(\text{NO}_3)_2$ solution.

2.5 Experimental procedures

2.5.1 Capillary treatment

- 1) All Hg was emptied from the working electrode.
- 2) Capillaries were stacked in nitric acid and nitric acid was sucked through so the reservoir at the top was filled. The capillaries were soaked in HNO_3 overnight to remove traces of Hg.
- 3) Nitric acid was removed and capillaries were rinsed and with MilliQ water.
- 4) Water was removed and methanol was sucked through the capillaries.
- 5) About 50 mL of 1 M sodium hydroxide solution in methanol was prepared and stirred overnight to dissolve all NaOH
- 6) Capillaries were left to soak at least overnight in methanol/NaOH overnight.
- 7) NaOH/MeOH was removed and capillaries were rinsed with copious MilliQ water.
- 8) HCl was sucked up through capillary to remove the NaOH.
- 9) Capillaries were then rinsed with MilliQ water followed by methanol.
- 10) Capillaries were dried in oven at about 220 °C for at least 4 hours and allowed to cool.
- 11) Silane solution was prepared by dissolving 5 mL dichloromethyl silane (DCMS) in 100 mL. All glassware was meticulously dried before silanisation as silane is very reactive towards water. The 5 % DCMS was stored in a dark glass bottle with a screw on a plastic cap.
- 12) Some 5 % silane solution was poured in a small 5 mL beaker and was allowed to rise in the capillaries via capillary action. Capillaries were repeatedly immersed in the silane solution for 15 minutes.
- 13) Finally silanized capillaries were put in oven at about 220 degree to dry for at least 4 hours and allowed to cool.

Spare treated capillaries were wrapped in medical wipes, enclosed in plastic bag and stored in oven for later use.

2.5.2 Assembling a new capillary

The plunger was raised to its upper position with the scaled revolving sleeve and both threads of the intermediate joint were left loose after mounting a new capillary. A new lower bi-conical gasket was used on changing a capillary. The plunger was then moved to its lowest position. Subsequently, the upper and then the lower thread of the intermediate joint were tightened firmly.

2.5.3 Initial filling of HMDE with a new capillary

For initial filling, the stopper was removed and a syringe with a tube was attached to the opened end as a suction source. The plunger was raised above the lower gasket through the intermediate joint, by turning the scaled sleeve counter clockwise. The tip of capillary was immersed in a Hg pool and the electrode was held vertically. Hg was then sucked by the suction syringe and plunger was moved below the lower gasket when Hg level reached above the lower gasket. The suction was maintained when the plunger was moved to about 3.5 marks on the scaled sleeve to avoid the air entering the electrode. Subsequently the syringe was removed and the stopper was closed.

2.5.4 Re-filling of HMDE

The electrode was immersed in the Hg pool and held vertically. The plunger was moved anti-clockwise to fill the Hg. There is no need for a suction syringe to re-fill the electrode. It is best not to rotate the plunger more than about 3.5 marks on the scaled sleeve for the capillary to maintain a stable drop and good working of electrode.

2.5.5 Equipment cleaning

The electrochemical cell is washed with piranha, which is a solution of sulphuric acid and hydrogen peroxide in a ratio of 3:1 and is largely used to remove the organic contamination. Piranha solution is kept in cell for at least an hour for efficient cleaning. Also, the counter electrode and reference electrode are dipped in same solution for few seconds to remove any organic contamination and to unblock

the ceramic frit of reference electrode. The cell and the electrodes are then washed with copious amounts of milli-Q water.

2.6 Fluorescence spectroscopy

Emission of light by a substance on absorbing light or electromagnetic radiation is generally termed luminescence. Luminescence can be further classified as photoluminescence, chemiluminescence and electroluminescence depending on the cause of light emission such as emission caused by chemical reaction, electrical energy, light energy etc. Photoluminescence is of two types: fluorescence and phosphorescence. Fluorescence is the emission of light as a result of singlet-singlet electronic relaxation following the absorption of light energy. It has a typical life time of nanoseconds. Phosphorescence is emission of light as a result of triplet-singlet electronic relaxation on absorbing light energy and has a life time of milliseconds to hours.

In Fluorescence spectroscopy, an incident light beam (usually UV) excites the electrons in the fluorophore molecule to the excited electronic states. These excited molecules then lose the vibrational energy to reach the lowest vibrational state of excited electronic state as seen in a Jablonski diagram (Figure 2.29). As a result, an emission spectrum is recorded keeping the excitation wavelength constant and measuring the fluorescent light at different wavelengths.

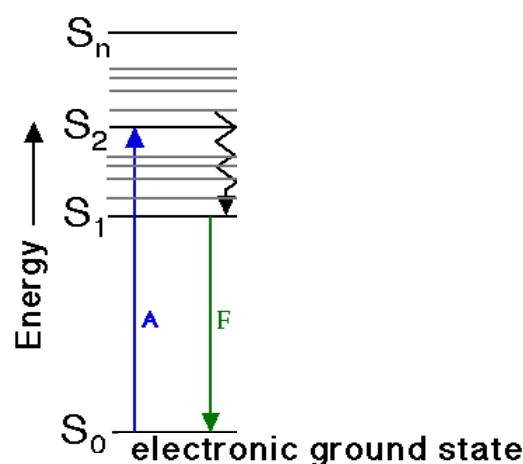


Figure 2.29: Jablonski's diagram explaining molecular excitations, A-Absorption, F-Fluorescence and S-singlet states [40].

The role of the quencher is to quench the fluorescent light from fluorophore and decrease its intensity by various modes of actions such as collisional quenching (dynamic quenching) and quenching due to complex formation (static quenching). Collisional quenching is described by the Stern-Volmer equation:

$$F^{\circ}/F = 1 + K_D [Q] \quad \text{Equation 2.21}$$

F° and F are the fluorescence intensities in the absence and presence of quencher respectively, $[Q]$ is the concentration of quencher, K_D is the Stern-Volmer quenching constant. A plot of F°/F versus $[Q]$ should be linear with an intercept of 1 on y-axis and slope equal to K_D . It is intuitively noteworthy that K_D^{-1} is the quencher concentration at which $F^{\circ}/F = 2$ or 50% of intensity is quenched. A linear Stern-Volmer plot is indicative of a single class of fluorophores, all equally accessible to quencher (Figure 2.30).

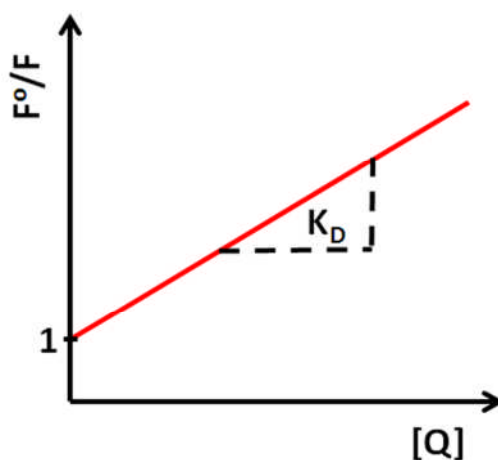


Figure 2.30: A typical Stern Volmer plot for a single class of accessible fluorophore.

In case of two fluorophore populations, where one is not accessible to quencher, Stern-Volmer plots deviate from linearity towards x-axis. At higher quencher concentrations essentially all the accessible fluorophore is quenched. The remaining fluorescence is from the inaccessible fluorophore and is independent of quencher concentration. Quenching of the fluorophores with both accessible and inaccessible populations can be analysed using a modified Stern-Volmer equation.

In the presence of two populations of fluorophore i.e. accessible and inaccessible, the total fluorescence in the absence of quencher is:

$$F^{\circ} = F^{\circ}_a + F^{\circ}_b \quad \text{Equation 2.22}$$

In the presence of quencher, the intensity of accessible fraction is decreased according to Stern-Volmer equation, whereas the inaccessible fraction is not quenched. So,

$$F = F^{\circ}_a/(1 + K[Q]) + F^{\circ}_b \quad \text{Equation 2.23}$$

Where, K is the Stern-Volmer quenching constant of the accessible. Subtraction of Equation 2.22 from Equation 2.23 gives

$$\Delta F = F^{\circ} - F = F^{\circ}_a(K[Q]/(1 + K[Q])) \quad \text{Equation 2.24}$$

ΔF is the difference in the intensities of emitted light in the absence and presence of quencher respectively. Inversion followed by division with Equation 2.22

$$F^{\circ}/\Delta F = \frac{1}{f_a K[Q]} + 1/f_a \quad \text{Equation 2.25}$$

Where f_a is the fraction of initial fluorescence accessible to quencher

$$f_a = F^{\circ}_a/(F^{\circ}_b + F^{\circ}_a) \quad \text{Equation 2.26}$$

This modified form of the Stern-Volmer equation allows accessible fraction (f_a) and K to be determined graphically. A plot of $F^{\circ}/\Delta F$ versus $1/[Q]$ gives f_a as the intercept and $(f_a K)^{-1}$ as slope (Figure 2.31). The **accessible fraction** is defined as the fraction of the fluorophore present in the polar region of the DOPC bilayer and hence available for quenching. The accessible fraction therefore reports on the location of the biphenyl fluorophore in the membrane. The accessible fractions (f_a) for the quenching of biphenyl and substituted biphenyl fluorescence were calculated from the intercept values (intercept = $1/f_a$) with an intercept value of 1.0 indicating complete accessibility of the biphenyl derivatives to quenching by I.

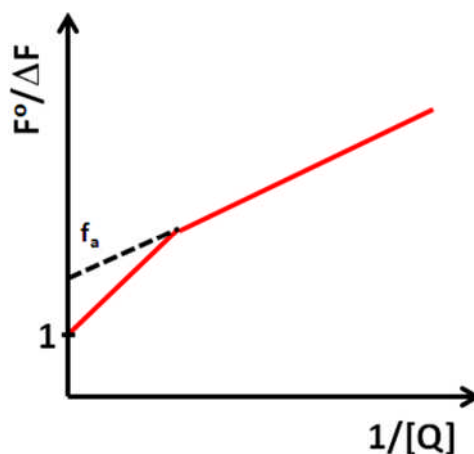


Figure 2.31: A typical modified Stern Volmer plot indicating two different fluorophore populations.

The slope of these plots gives the effective quenching constant (K) for accessible fluorophores which is similar to the binding constant for the quencher-acceptor systems [41] and represents the quenching efficiency of the biphenyl derivatives by Γ . It is not a significant parameter in terms of their interaction with the membrane. At higher concentration of Γ , interactions between DOPC and Γ appeared as a discrete increase in the slope of modified the Stern-Volmer plots. This increase in slope is due to the Γ penetrating the apolar region of the monolayer and quenching penetrated biphenyl. This data is therefore excluded from the plot used to estimate the intercept. Fluorescence spectroscopy is used to (1) investigate the interaction of biphenyl and its derivatives with free standing DOPC bilayers and (2) to compare with those on DOPC monolayer on Hg.

2.6.1 Materials

Biphenyl, 2-chloro-biphenyl, 3-chloro-biphenyl, 4-chloro-biphenyl, 2-hydroxy-biphenyl, 3-hydroxy-biphenyl, 4-hydroxy-biphenyl, 4-methoxy-biphenyl, 4-methyl-biphenyl, 4-cyano-biphenyl and 4-sulphonic acid-biphenyl were purchased from Sigma Aldrich and their stock solutions (1000 μM) were made using acetone for electrochemical studies and using ethanol for fluorescence studies.

2.6.2 Preparation of liposomes

A DOPC stock dispersion of 10 mg/ml was prepared by dissolving DOPC in 0.1 M KCl with added 0.001 M phosphate buffer. Giant unilamellar vesicles (GUV) containing 4.2 % ethanol and 0.2 mg/ml DOPC were prepared by diluting calculated amount of DOPC stock dispersion in a measuring flask containing 4 % ethanol followed by the addition of 0.1 mol dm^{-3} buffered KCl gently along the wall of flask with constant swirling [42]. The resulting vesicles are reported as GUV in high yield varying up to 50 μm in diameter [42].

2.6.3 Instrumentation

FluoroMax-3 Fluorimeter from Horiba Scientific with xenon lamp was used to obtain fluorescence spectra.

2.6.4 Experimental procedure

Fluorescence spectra of DOPC vesicles at the excitation wavelengths specific to different biphenyls were recorded as blanks. Biphenyls solutions were added to the DOPC vesicle solutions with an incubation period of 15 minutes. All the biphenyls were studied at their solution concentration of $1 \mu\text{mol dm}^{-3}$. KI was used as a quencher. Secondary stock solutions of different concentrations of KI ($1.0\text{-}7.0 \text{ mol dm}^{-3}$) were prepared from its primary stock solution of 8.0 mol dm^{-3} in 0.2 mmol dm^{-3} sodium thiosulphate in 18.2 MW MilliQ water. Sodium thiosulphate was used as an oxidant to reduce the oxidation of iodide to iodine. 150 mL portions of the KI secondary stock solutions were added to the 3 mL of vesicle solution containing biphenyls in the cuvette and fluorescence spectra were recorded at appropriate excitation and emission wavelengths. Cuvette was dried using compressed air before taking all the measurements to eliminate the error from small dilutions. Maximum fluorescence intensities were measured from the fluorescence spectra and were plotted versus concentration of the KI according to the Equation 2.25. The amount of the accessible (quenched) and inaccessible (not quenched) biphenyls were calculated from intercept assuming cent percent accessibility with an intercept value of 1.0.

All the biphenyl derivatives were found to be stable on exposure to light (constant intensity of re-emitted light on repetitive exposure to light) except *o*-Cl-BP and were studied using the method described above. Unlike the other substituted biphenyls, *o*-Cl-BP underwent photo degradation on exposure to light (inset of Figure 2.32). Therefore, the spectra were recorded in kinetic acquisition mode with an interval of 0.1 s and 6 s total time, at an excitation wavelength of 260 nm and an emission wavelength of 316 nm to obtain the intensities of emitted light at zero time to eliminate the effects from photo-degradation. The intercept from the linear regression of these intensity versus time spectra yielded the intensity of re-emitted light at zero time (where there is no photo degradation) and is used to plot modified Stern-Volmer plot for *o*-Cl-BP as shown in Figure 2.32.

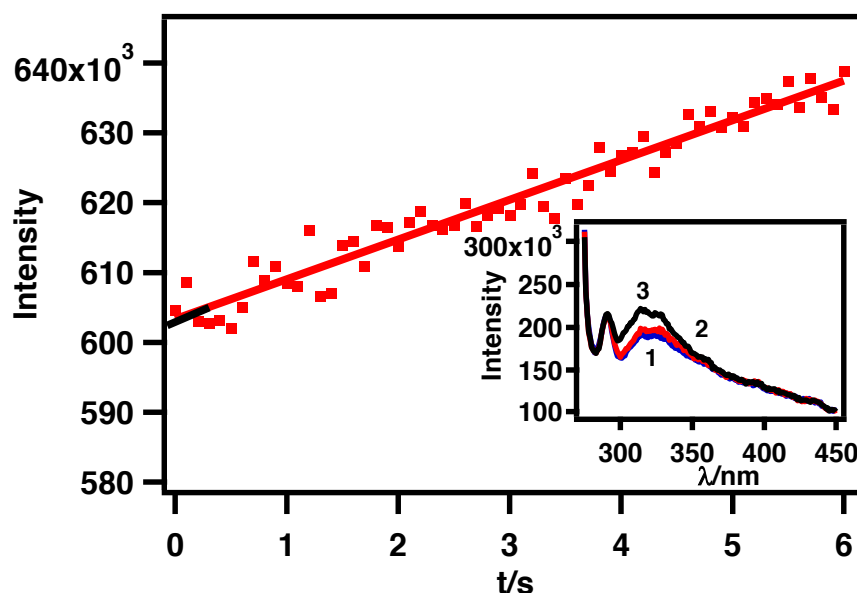


Figure 2.32: Kinetic plot of re-emitted light intensity for iodide ($0.047 \text{ mol dm}^{-3}$) quenching of *o*-Cl-BPs in the presence of $0.254 \text{ mmol dm}^{-3}$ DOPC GUV in 0.1 mol dm^{-3} of KCl containing $0.001 \text{ mol dm}^{-3}$ of phosphate buffer. Inset showing subsequent increase in intensity of emitted light after exposing the same solution to light.

2.7 References

- [1] P.R. Unwin, Encyclopedia of Electrochemistry.
- [2] A.A.M. Bond, F. Scholz, Electroanalytical methods: guide to experiments and applications, Springer, 2010.
- [3] J.H. Nelson, (1996).
- [4] C.H. Hamann, A. Hamnett, W. Vielstich, Completely Revised and Updated Edition, New York, (2007).
- [5] S. Zhang, A. Nelson, Z. Coldrick, R. Chen, Langmuir, 27 (2011) 8530-8539.
- [6] A.J. Bard, L.R. Faulkner, Electrochemical methods: fundamentals and applications, Wiley New York, 1980.
- [7] J. Lecoeur, C. Koehler, J. Bellier, Review of scientific instruments, 69 (1998) 3031-3035.
- [8] E. Protopapa, S. Maude, A. Aggeli, A. Nelson, Langmuir, 25 (2009) 3289-3296.
- [9] <http://www.cheng.cam.ac.uk/research/groups/electrochem/teaching.html>.
- [10] R.S. Nicholson, Analytical Chemistry, 37 (1965) 1351-1355.
- [11] P.T. Kissinger, W.R. Heineman, journal of Chemical Education, 60 (1983) 702.
- [12] R. Holze, (2012) 350.
- [13] J.O. Howell, R.M. Wightman, Analytical Chemistry, 56 (1984) 524-529.
- [14] J.O. Howell, W.G. Kuhr, R.E. Ensman, R. Mark Wightman, Journal of Electroanalytical Chemistry and Interfacial Electrochemistry, 209 (1986) 77-90.
- [15] D.O. Wipf, E.W. Kristensen, M.R. Deakin, R.M. Wightman, Analytical Chemistry, 60 (1988) 306-310.
- [16] <http://www.kpsec.freeuk.com/acdc.htm>.
- [17] R.C. Dorf, The electrical engineering handbook: Circuits, signals, and speech and image processing, CRC Press, 2006.
- [18] B. Benoit, C. Leo, (2005).
- [19] h.w.d.-a.n.r.l.p.a. phase.pdf.
- [20] B. Breyer, H. Bauer, S. Hacobian, Australian journal of chemistry, 8 312-321.
- [21] S.E. Creager, T.T. Wooster, Analytical Chemistry, 70 (1998) 4257-4263.
- [22] D. Mandler, I. Turyan, Electroanalysis, 8 (1996) 207-213.
- [23] P. Kryszynski, A. Zebrowska, A. Michota, J. Bukowska, L. Becucci, M. Moncelli, Langmuir, 17 (2001) 3852-3857.

- [24] F.T. Buoninsegni, L. Becucci, M.R. Moncelli, R. Guidelli, *Journal of Electroanalytical Chemistry*, 500 (2001) 395-407.
- [25] N. Muskal, I. Turyan, D. Mandler, *Journal of Electroanalytical Chemistry*, 409 (1996) 131-136.
- [26] R. Herrero, M.R. Moncelli, L. Becucci, R. Guidelli, *The Journal of Physical Chemistry B*, 101 (1997) 2815-2823.
- [27] P.M.S. Monk, *Fundamentals of electro-analytical chemistry*, Wiley, 2008.
- [28] A. Lasia, *Electrochemical impedance spectroscopy and its applications*, in: *Modern aspects of electrochemistry*, Springer, 2002, pp. 143-248.
- [29] E. Barsoukov, J.R. Macdonald, *Impedance spectroscopy: theory, experiment, and applications*, Wiley. com, 2005.
- [30] C. Whitehouse, R. O'Flanagan, B. Lindholm-Sethson, B. Movaghar, A. Nelson, *Langmuir*, 20 (2004) 136-144.
- [31] L. Yu, J.L. Ding, B. Ho, S.-S. Feng, T. Wohland, *The Open Chemical Physics Journal*, 1 (2008) 62-79.
- [32] E. Protopapa, A. Aggeli, N. Boden, P. Knowles, L. Salay, A. Nelson, *Medical engineering & physics*, 28 (2006) 944-955.
- [33] A. Nelson, *Journal of Electroanalytical Chemistry*, 601 (2007) 83-93.
- [34] A. Nelson, A. Benton, *Journal of Electroanalytical Chemistry and Interfacial Electrochemistry*, 202 (1986) 253-270.
- [35] D. Bizzotto, A. Nelson, *Langmuir*, 14 (1998) 6269-6273.
- [36] B. Sharma, *Industrial chemistry*, Krishna Prakashan Media, 2001.
- [37] J.F. Ross, *Handbook for radio engineering managers*, Elsevier, 2014.
- [38] R.D. Kimbrough, A.A. Jensen, *Halogenated biphenyls, terphenyls, naphthalenes, dibenzodioxins and related products*, Elsevier, 2012.
- [39] J.O.M. Bockris, A.K.N. Reddy, *Modern electrochemistry*, Springer, 2000.
- [40] http://www.shsu.edu/chm_tgc/chemilumdir/JABLONSKI.html.
- [41] M. Sharma, K. Chauhan, R. Shivahare, P. Vishwakarma, M.K. Suthar, A. Sharma, S. Gupta, J.K. Saxena, J. Lal, P. Chandra, *Journal of medicinal chemistry*, 56 (2013) 4374-4392.
- [42] A. Moscho, O. Orwar, D.T. Chiu, B.P. Modi, R.N. Zare, *Proceedings of the National Academy of Sciences*, 93 (1996) 11443-11447.

Chapter-3

Role of electrolyte ions in the occurrence of voltage induced phase transitions in a DOPC monolayer on Hg

3.1 Introduction

Electrolyte ions play a vital role in many biological functions such as nerve functions [1-2], muscle function [3-4], neuropsychiatric manifestations [5], manic depressive disease [6], and cardiac arrhythmias management [7]. Interaction of electrolyte ions with the phospholipids have been studied extensively using various biomimetic models such as supported bilayers [8-10] and monolayers [11-14], phospholipid vesicles [15-16] and tethered bilayers [17-18] with a variety of phospholipids and substrates using different techniques. Interactions between phospholipids and ions is essential for all above processes and particularly for membrane stability [19], signal transduction [20-21] and membrane fusion [22-24]. Ions critical in influencing physiological processes are Li^+ , Na^+ , K^+ , Ca^{+2} , Mg^{+2} , Cl^- .

Most investigations report on the adsorption and binding of cations to the phospholipid head groups. Simulation studies suggest that alkali metal cations in contrast to anions bind to the PO_4^{-2} moiety on the DOPC head group depending on their charge density and the membrane electrostatic potential [25]. Early studies of ion interactions were conducted on the negatively charged lipid phosphatidylserine (PS) [26-27] found in biological membranes. The alkali metal cations compared to

the transition metal ions and quaternary ammonium ions were found to bind strongly to the PS head groups forming a diffuse double layer at the membrane surface. This resulted in the formation of a lipid-ion complex which is anhydrous and hydrophobic in the case of inorganic ion binding and is hydrated and hydrophilic in the case of organic ion binding [26]. A discrepancy is found between the Gouy-Chapman theory of diffuse double layer and its application to experimental data in the study of interactions of alkali metal cations with PS vesicles. The specific adsorption of ions on phospholipids was addressed by Moises and others considering the Stern approach that accounts for both the finite ion size and adsorption of ions on the surfaces [28].

Studies of the adsorption of ions on the neutral PC lipid showed that divalent ions penetrate in between and bind to PC head groups forming a Stern layer next to the hydrated hydrophilic head groups of lipid molecules [29-33]. This cation binding to neutral lipids is effectively enhanced with a secondary cation condensation process in the presence of a negatively charged lipid mixed with the neutral lipid as compared to the neutral lipids alone [34-35]. Studies on interaction of metal cations with DOPC have shown that the strength of alkali metal cation binding to the head group follows the order: $\text{Li}^+ > \text{Na}^+ > \text{K}^+ > \text{Rb}^+ > \text{Cs}^+$ in accordance with the reverse Hofmeister series with no significant adsorption by anions excepting the larger Br^- and I^- [16,25]. This ion specificity can be based on several different physical mechanisms determined by ion pairing, the hard and soft nature of ions, membrane defects and their geometry and membrane properties. Force spectroscopic studies support the findings of Vacha and reveal that a higher force is needed for an AFM tip to penetrate the DOPC membrane in solutions with higher ionic strength and with the cations such as Na^+ and Ca^{2+} demonstrating that penetration/binding of the ion on to phospholipid head group is related:- (a) linearly to an increase in their solution concentration and (b) inversely to the size of the unhydrated cations [36].

It has also been shown that the water structure around the ions and lipid head groups is distorted within the ion-lipid association. In relation to this, some studies report that cation binding to the PC surface involves loss of water of hydration around the ion with no significant effect on water structure around lipid head group [37-38]. A recent study has shown that change in water structure (dehydration) around PC

occurs during the ion binding process and is more noticeable with divalent cations than the monovalent cations [39].

Owing to the well-established association between electrolyte ions and phospholipids as described above, the role of electrolyte ions in the mechanism of the potential-induced lipid phase transitions in the phospholipid-Hg model is of great interest. In this section, the effect of electrolyte ions on the occurrence of potential induced phase transitions exhibited by dioleoyl phosphatidylcholine (DOPC) monolayer on the mercury (Hg) surface in both hanging Hg drop electrode (HMDE) and fabricated Hg film electrode (MFE) configuration is studied and an attempt is made to relate the origin of the phase transitions underlying capacitance peaks-1 and -2 to the involvement of electrolyte ions in their mechanism. These properties are initially characterized by observing the change in the potentials and kinetics characterising two phase transitions represented by the two capacitance peaks respectively. The interactions of both inorganic and organic electrolytes with the DOPC are studied.

Some phosphorus containing electrolytes such as pyrophosphate and pyrophosphite [40-41] are believed to be the precursors [42-43] of energy producing molecules such as adenosine triphosphate (ATP) [44] and phosphoenol pyruvate. Pyrophosphite has also been reported as possible first energy storing molecules in relevance to its importance in prebiotic chemistry [45]. Synthesis of pyrophosphate and pyrophosphite involves other phosphorus containing molecules such as phosphorous acid, sodium phosphite, disodium hydrogen phosphate etc. Some of these phosphorous containing inorganic compounds are also studied to investigate their interactions with the supported phospholipid monolayer on Hg to develop an understanding about these molecules in relation to their role in abiogenesis.

3.2 Results and discussion

3.2.1 Effect of inorganic ions on capacitance peak-1

3.2.1.1 Ionic strength

Figure 3.1(a) and (b) display the capacitance-potential (C_{sp} -E) plots of the DOPC coated Hg electrode in KCl and KNO_3 solutions respectively of differing ionic strength varying from 0.01 up to 2.0 mol dm^{-3} . Any change in the electrolyte concentration and composition leads to a change in the potential characterising the capacitance peaks on the C_{sp} -E plot. It can be seen very clearly that an alteration in ionic strength of the electrolyte solution affects the position of capacitance peak-1. The increased capacitance in the less negative domain of the C_{sp} -E plot of DOPC on Hg in the presence of higher concentration of KCl solution is attributed to the adsorption of chloride ions on the DOPC monolayer [46]. Figure 3.2 (a) and (b) show the potential of capacitance peak-1 ($-E_1$) versus $-\log$ electrolyte concentration plots of DOPC coated Hg electrodes in KCl and KNO_3 solutions respectively. The progressive increase in the ionic strength of the solution up to 1.0 mol dm^{-3} shifts the capacitance peak-1 to a less negative potential (after IR correction) in both electrolytes. A further increase in the solution ionic strength does not affect the potential of capacitance peak-1 ($-E_1$) significantly as shown in both Figure 3.2 (a) and (b). The results in Figure 3.2 (a) are almost identical for experiments carried out on the DOPC coated HMDE as well as on the DOPC coated MFE in KCl solution. All the data obtained using electrolytes of ionic strengths lower than 0.1 mol dm^{-3} are corrected for IR drop. However the shifts due to IR drop are small. For example in the lowest ionic strength solutions of 0.01 mol dm^{-3} KCl, R was measured as 2500 ohms by chronoamperometry and since the current height of the peak is 0.56 μA , the IR drop is 1.0 mV.

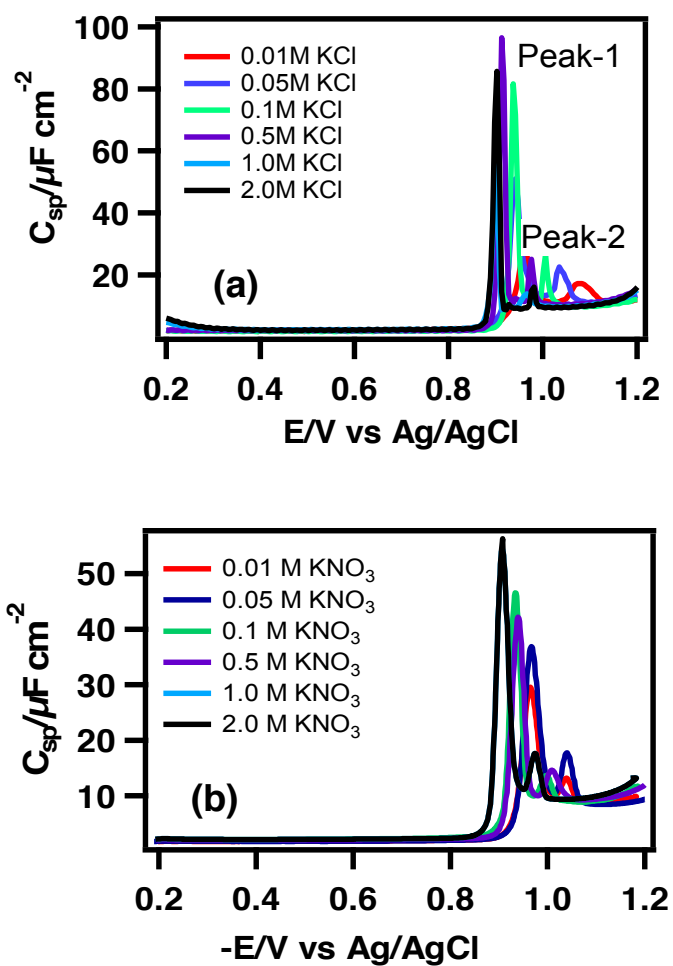


Figure 3.1: Capacitance (C_{sp}) versus potential ($-E$) plots of DOPC coated HMDE in (a) KCl and (b) KNO_3 obtained using ACV at 0.005 V s^{-1} , 75 Hz, $0.005 \text{ V } \Delta E$ and 90° out of phase.

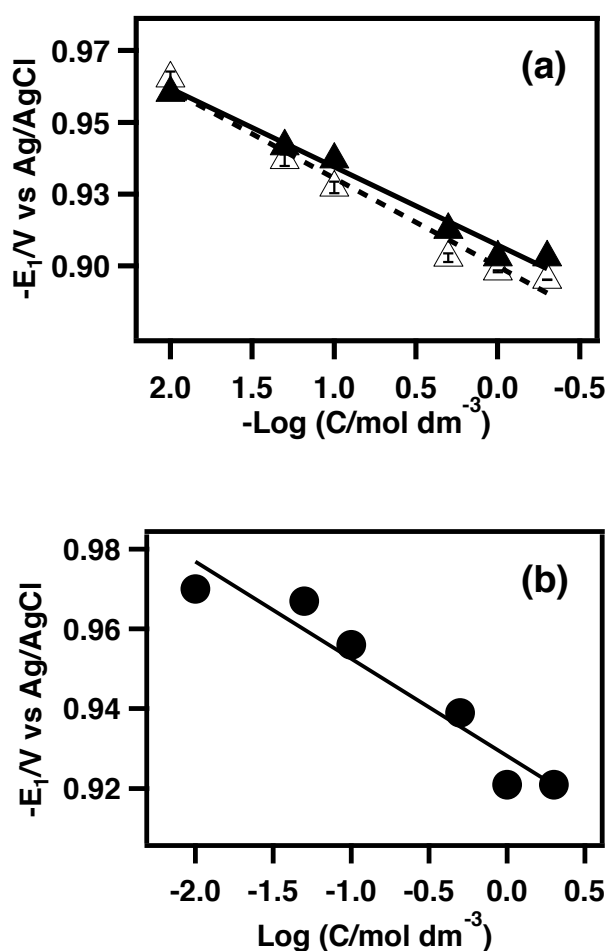


Figure 3.2: $-E_1$ versus $-\log$ ionic strength plot of DOPC coated (a) HMDE (closed triangle) and MFE (open triangle) in KCl and (b) HMDE (closed circles) in KNO_3 obtained using ACV at 0.005 V s^{-1} , 75 Hz, $0.005 \Delta E$ and 90° out of phase.

Based on these results, a model is configured that takes into account the structure of the electrical double layer formed at the lipid-electrolyte interface and can be explained on the basis of the Gouy Chapman theory [47-48] presented in Figure 3.3. As a result, the shift in apparent potential of the capacitance current peak-1 ($-E_1$) arises from the fact that the strength of electric field which initiates the phase transition underlying capacitance peak-1 is a constant value and is independent of solution ionic strength.

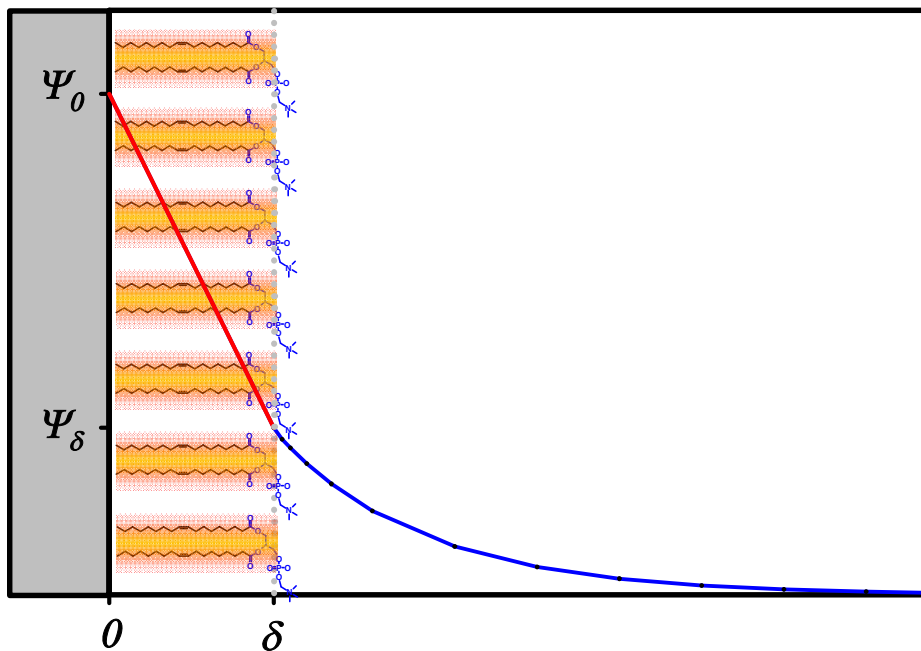


Figure 3.3: Schematic total potential (Ψ_0) profile across DOPC monolayer on Hg electrode showing diffuse layer potential (Ψ_δ) beginning at distance, δ .

According to the Gouy-Chapman theory [47-49], in solutions with higher ionic strength at applied negative potential, the diffuse layer of electrolyte ions is more compact with a higher concentration of counter ion accumulating near the lipid-electrolyte interface leading to a higher potential drop across the lipid. In solutions of low ionic strength, the electrode potential is more diffuse resulting in a relatively smaller potential drop across the lipid with a significant contribution of diffuse potential drop in the bulk solution. Hence, in the latter case a higher negative potential must be applied to the electrode to obtain the electric field required to induce the first phase transition. On the other hand in solutions of higher ionic strength, a more compact layer of counter ions is realised on the lipid surface [36] leading to a steeper drop in potential across the lipid. Because of this, a smaller potential applied to the electrode is required to produce the critical value of field necessary for initiating the phase transition. This gives rise to an apparent positive potential shift in $-E_1$. This model can be expressed quantitatively. The surface potential (ψ_0) of any electrode consists of a Stern layer potential (ψ_{stern}) and diffuse layer potential (ψ_δ) as displayed in Figure 3.3 and can be expressed as:

$$\Psi_0 = \Psi_{\text{stern}} + \Psi_{\delta} \quad \text{Equation 3.1}$$

Stern layer potential can be calculated from surface charge density (σ) and capacitance (C_{stern}) of Stern layer (Equation 3.2).

$$\Psi_{\text{stern}} = \sigma/C_{\text{stern}} \quad \text{Equation 3.2}$$

A DOPC monolayer adsorbed on a Hg electrode can be considered as the Stern layer since it is of constant thickness in the capacitance minimum domain between potentials -0.4 and -0.8 V. The DOPC monolayer in this potential domain consists of a hydrophobic region and a polar interfacial region [50-52]. The interfacial region includes P-N dipoles. According to previous studies [53-55] the P-N dipoles are oriented more or less parallel to the monolayer surface and their influence on the potential drop across the monolayer can be neglected. The capacitance of DOPC monolayer is mainly defined by the hydrophobic region because it possesses the lowest capacitance. The diffuse layer potential in the capacitance minimum potential domain can be calculated:

$$\Psi_{\delta} = (2kT/e) * \sinh^{-1}[\sigma/(8c_{\text{KCl}}N_A\epsilon_0\epsilon_r\text{H}_2\text{O}kT^{1/2})] \quad \text{Equation 3.3}$$

where the assumed value of σ is the charge on the electrode at the potential of capacitance peak-1 given as $\sim -0.02 \text{ C m}^{-2}$ [56], e is the charge of a single electron, k is the Boltzmann constant, T is 298° , c_{KCl} is KCl concentration, N_A is Avogadro's constant, ϵ_0 is the permittivity of a vacuum: $8.854 \times 10^{-12} \text{ F m}^{-1}$ and $\epsilon_r \text{H}_2\text{O}$ is the relative permittivity of water: 80.4 [57]. If it is assumed that a critical electric field across the monolayer defines the potential characterising the phase transition then the relative shift of $-E_1$ is defined by the extent of Ψ_{δ} which depends on the KCl concentration. Figure 3.4 shows both the changes in theoretical diffuse layer potentials and the experimental potential shifts of $-E_1$ as a function of KCl concentration.

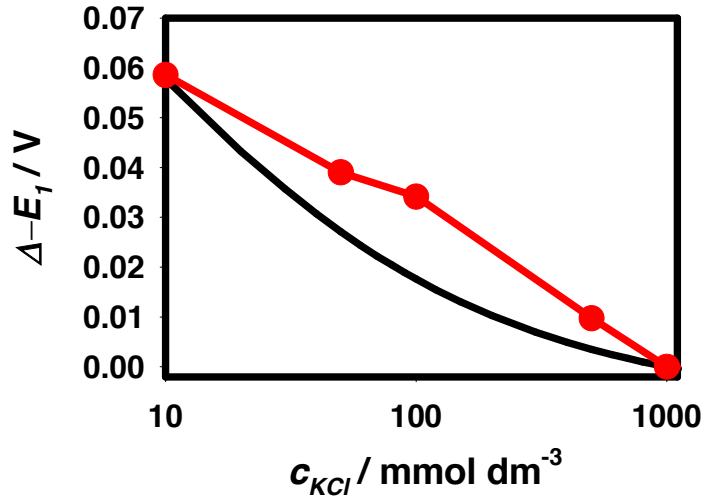


Figure 3.4: Potential shift of capacitance peak-1 (red filled circles) and change of diffuse layer potential at electrode charge value of 0.02 C m^{-2} (black line) ($\Delta-E_1$) versus the concentration of KCl (c_{KCl}). For red filled circles error bars are within symbol size.

Discrepancies between the theoretical and experimental values can be due to a dependence of the P-N dipole-monolayer plane angle with the concentration of electrolyte. The observed correlation between the theoretical and the experimental results supports the critical electric field (E_{crit}) hypothesis. E_{crit} can be estimated from the equation 3.4 below where $\sigma = -0.02 \text{ C m}^{-2}$ at the capacitance peak-1 potential:

$$E_{\text{crit}} = \sigma / \epsilon_0 \epsilon_r \text{DOPC} \quad \text{Equation 3.4}$$

which gives a value of $9.05 \times 10^8 \text{ V m}^{-1}$ when $\epsilon_r \text{DOPC}$ as the relative permittivity of the DOPC hydrocarbon region is taken as that of oleic acid which is 2.5 [58]. Equation 3.4 only gives an approximate value of E_{crit} since the DOPC dielectric constant changes in the potential region ($\sim 0.025 \text{ V}$) where the transition underlying capacitance peak-1 is initiated. Interestingly a value for the critical field which instigates the poration of a phosphatidylcholine L-B monolayer has been calculated from a theory which assumes that poration is a result in switch in P-N dipole orientation in field as $\sim 3 \times 10^9 \text{ V m}^{-1}$ [59]. Figure 3.5 shows a diagrammatic representation of the electrical double layer formed at DOPC coated Hg electrode

and electrolyte interface and accompanying potential drop with different ionic strengths.

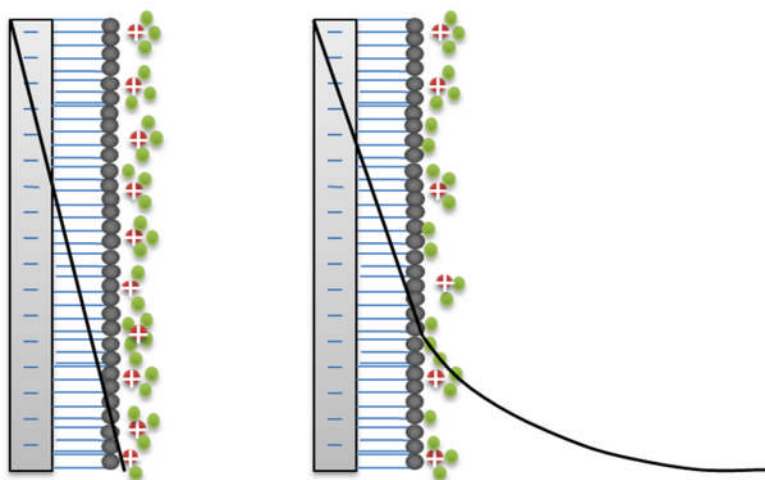


Figure 3.5: A diagrammatic representation of EDL and potential drop at the electrode-electrolyte interface varying with electrolyte concentration. \oplus Cation, \ominus -water molecule.

3.2.1.2 Ionic composition

The C_{sp} -E plots of DOPC coated Hg electrode in the presence of various cations on capacitance peak-1 from three different series of electrolyte: chlorides, fluorides and hydroxides are shown in Figure 3.6. ACV voltammograms show clearly that these ions change the position of capacitance peaks differently depending on their ability to bind with DOPC molecules as explained below. Figure 3.7 (a) is a plot of $-E_1$ versus the log ion-phosphatidyl choline (PC) binding constant [60-62] for univalent and bivalent cations of different electrolytes. It is noted that the alkali and alkaline earth metal cations with a higher binding constant to PC shifts $-E_1$ to a more positive potential as compared to the $-E_1$ shift from cations with lower value of binding constant to PC (Figure 3.7 (a) and (b)). The interaction between the ions and phospholipids is determined by the binding ability of ions with the lipid head groups and their concentration in the electrolyte [25,36]. The cations with higher binding ability to the PC develop a higher concentration at the lipid-water interface. For example Li^+ from group-I and Ca^{2+} from group-II with PC binding constants of 1.37 and $40 \text{ mol}^{-1} \text{ dm}^3$ respectively [28,60-61] are able to form better packed layers on the lipid surface leading to the development of a higher concentration at the interface.

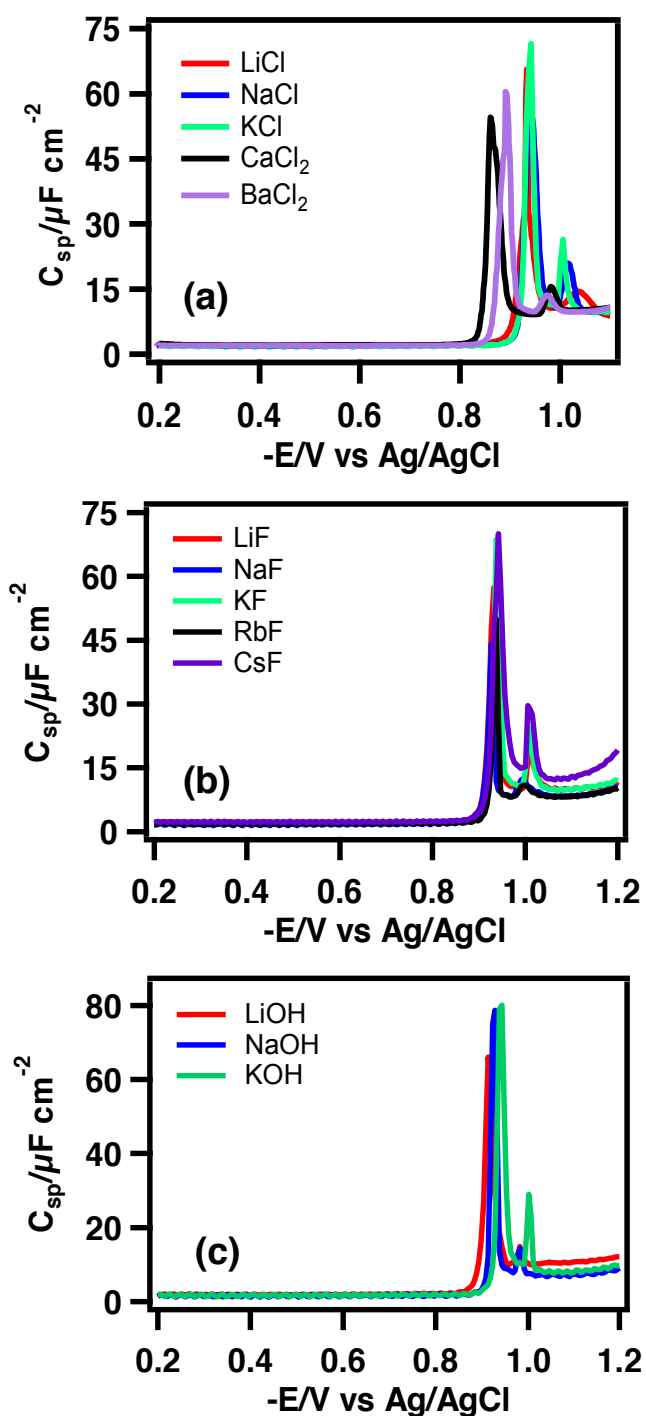


Figure 3.6: Capacitance (C_{sp}) versus potential ($-E$) plots of DOPC coated HMDE in the 0.1 mol dm^{-3} solution of metal (a) chlorides (b) fluorides and (c) hydroxides, obtained using ACV at 0.005 V s^{-1} , 75 Hz , $0.005 \text{ V } \Delta E$ and 90° out of phase.

This layer of bound ions will screen the applied negative potential more effectively leading to a stronger electric field across the lipid layer. As a consequence a lower negative potential need be applied to the electrode to induce the phase transition and an apparent positive potential shift of capacitance peak-1 is observed.

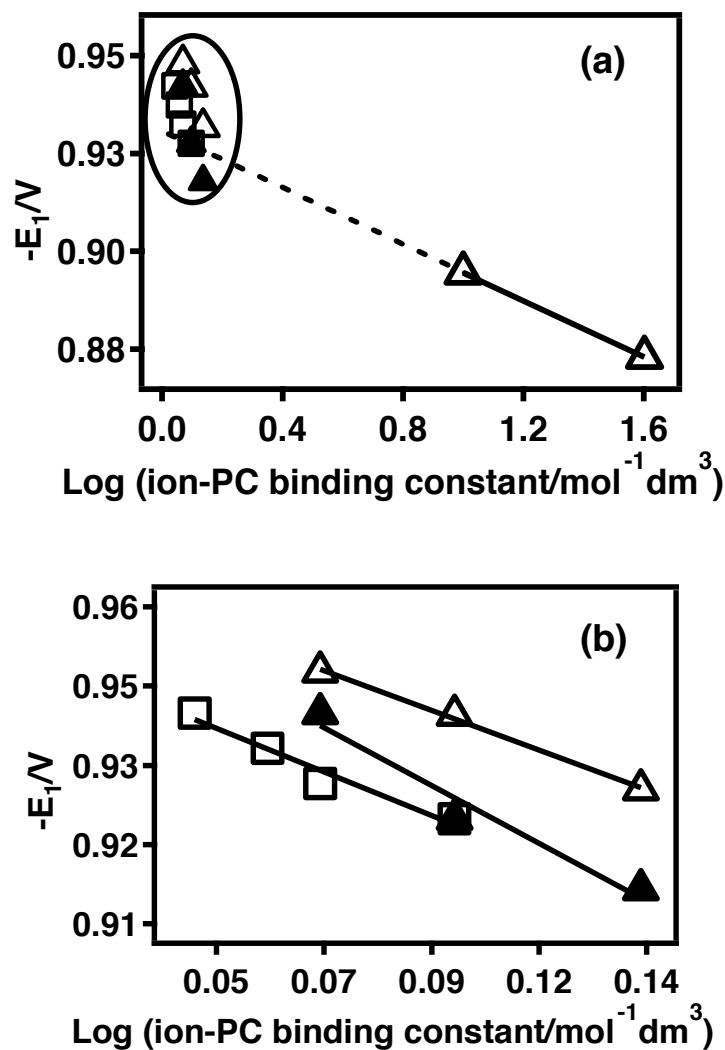


Figure 3.7: $-E_1$ versus \log (cation-PC binding constant) of alkali and alkaline earth metal cations of chloride (open triangle), fluoride (open square) and hydroxides (close triangle), (b) an expanded version of (a) (All the error bars are within the symbol size) in 0.1 mol dm^{-3} electrolyte obtained using ACV at 0.005 V s^{-1} , 75 Hz , $0.005 \text{ V } \Delta E$ and 90° out of phase.

All cations of metal fluorides follow the same order in their shift of $-E_1$ to more positive potential as exhibited by the metal chlorides in the following order:

$\text{Na}^+ > \text{K}^+ > \text{Rb}^+ > \text{Cs}^+$ [24]. Alkali metal hydroxides illustrate the same trend in influencing the potential shift of capacitance peak-1 [25].

A diagrammatic representation of the adsorption of different cations on the phospholipid head groups is shown in Figure 3.8.

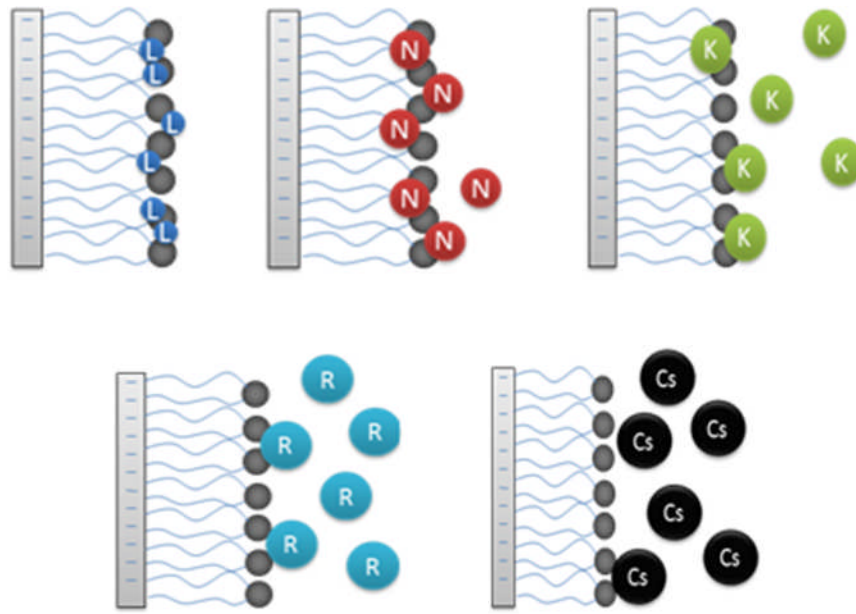


Figure 3.8: A pictorial representation of ion binding with the phospholipid on Hg (L-lithium, N-sodium, K-potassium, R-rubidium and Cs-cesium).

With respect to the effect of electrolyte anions on the capacitance peak-1, only iodide ions (I^-) show a significant effect on its potential (Figure 3.9). I^- adsorbs on DOPC [64]. The bound I^- ions [61,65] extend the potential drop across the DOPC and a less steep field leads to a higher potential, $-E_1$, being applied to initiate the transition. In addition it is significant that the metal chlorides shift $-E_1$ less than the fluorides and hydroxides, the shifts due to the latter two salts falling on almost the same plot. Presumably the polarisable Cl^- is having a similar but not so marked effect as I^- in this case due to its increased affinity for DOPC compared to the less polarisable F^- and OH^- .

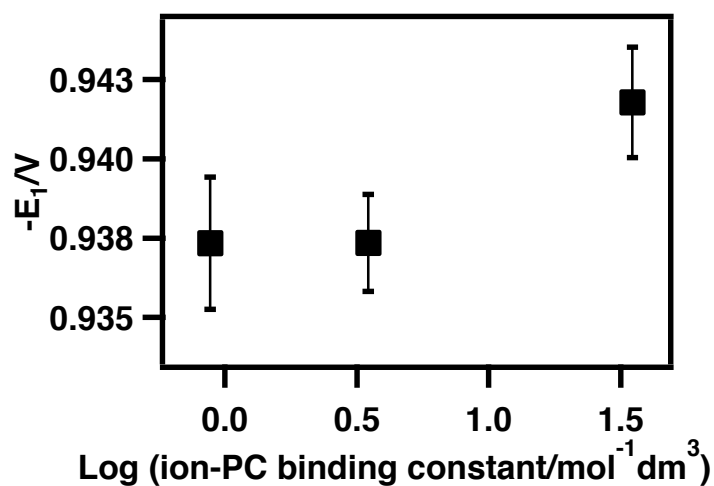


Figure 3.9: $-E_1$ versus \log (anion-PC binding constant) of halide anions of potassium in 0.1 mol dm^{-3} electrolyte obtained using ACV at 0.005 V s^{-1} , 75 Hz, $0.005 \text{ V } \Delta E$ and 90° out of phase.

Alkaline earth metal cations show following order of their decreasing interactions with lipid head group: $\text{Ca}^{+2} > \text{Ba}^{+2}$ in accordance with their intrinsic association constants in Table 3.1.

Table 3.1: Binding constants of the studied cations and anions to correlate their effect on the capacitance peak-1.

Ions	Binding constant $\text{mol}^{-1} \text{ dm}^3$	Ions	Binding constant $\text{mol}^{-1} \text{ dm}^3$
Li^+	0.8	Ba^{+2}	10
Na^+	0.6	F^-	-
K^+	0.15	Cl^-	0.2
Rb^+	0.08	Br^-	2
Cs^+	0.05	I^-	40
Ca^{+2}	40		

3.2.2 Effect of inorganic ions on capacitance peak-2

3.2.2.1 Ionic strength

At potentials negative to that characterising capacitance peak-1 on the ACV plot of the DOPC coated electrode, electrolyte ions penetrate the monolayer and screen the Hg surface by structuring a double layer at the Hg interface [66-67]. This leads into the nucleation and growth (N & G) phase transition characterising capacitance peak-2. The kinetics of this mechanism [57,66] and the molecular mechanism underlying it have been detailed previously and involve an adsorption of bilayer patches [68] on the electrode surface from some structured phospholipid-water emulsion. Figure 3.10 (a) and (b) display the potential of capacitance peak-2 ($-E_2$) versus the log electrolyte concentration plot of DOPC coated Hg electrode in KCl and KNO_3 solutions respectively. It can be seen that capacitance peak-2 is also shifted to less negative potential on increasing the ionic strength of both KCl and KNO_3 in the solution upto 1.0 mol dm^{-3} . A reversal in shift of capacitance peak-2 is observed with a further increase in ionic strength of both KCl and KNO_3 (Figure 3.10 (a) and (b)).

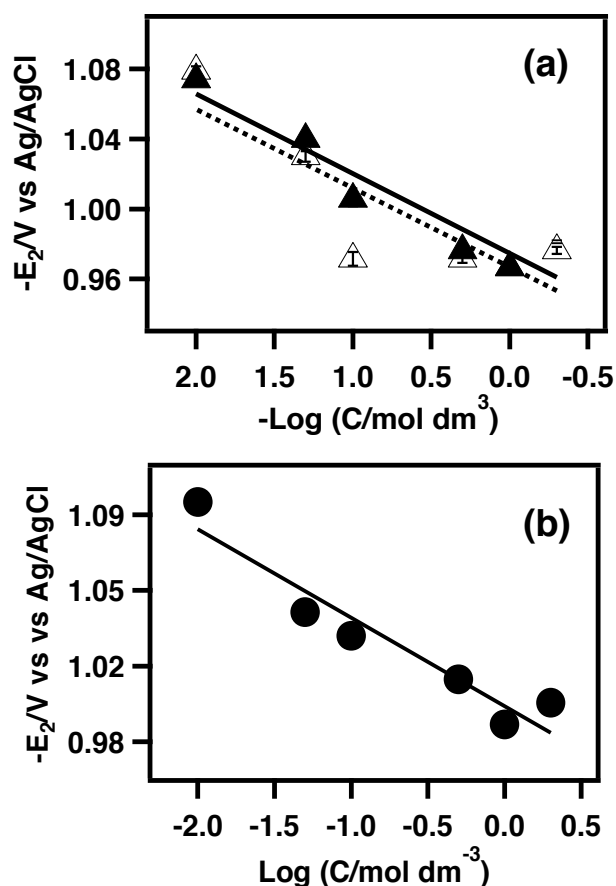


Figure 3.10: $-E_2$ versus $-\log$ ionic strength plot of DOPC coated (a) HMDE (closed triangle) and MFE (open triangle) in KCl and (b) HMDE (closed circles) in KNO_3 obtained using ACV at 0.005 V s^{-1} , 75 Hz, $0.005 \text{ V } \Delta E$ and 90° out of phase.

Interestingly, no significant difference is found for the DOPC coated MFE from DOPC coated HMDE for the position of capacitance peak-2 (Figure 3.10 (a)). Double potential step experiments are used to study the kinetics of the N & G mechanism underlying capacitance peak-2. In these experiments, negatively increasing potential steps are applied starting from a less negative potential (mid potential between the two capacitance peaks taken from ACV) to more negative potential encompassing the capacitance peak-2. The resultant current (I)-time (t) transient showing the second phase transition is displayed in Figure 3.11 (a). Such a potential programme has been well described previously [66].

At small values of step potential increments preceding the phase transition, the I-t transients are characteristic of an ideal RC circuit and are fitted to Equation 3.5 [66] as shown in Figure 3.11 (b):

$$I = \Delta V/R * \exp (-t/R_u C_d) \quad \text{Equation 3.5}$$

Where R_u is the uncompensated solution resistance and C_d is the double layer capacitance. The values of R_u and C_d which gave a good fit to the pure RC circuit for the lowest voltage amplitude step were used to model the RC transient contributing to I-t transients resulting from higher potential steps because the solution resistance remains constant during the application of different step potentials and the values of C_d before and after the phase transition remain the same [66].

The model RC contributions are subtracted from each I-t transient (Figure 3.11 (c)) which is then integrated to obtain charge (Q)-time (t) transients (Figure 3.8 (d)) [66] associated with the phase transition. The half-life ($t_{1/2}$) of these Q-t transients is defined as the time the charge transient takes to reach half of the charge density. $t_{1/2}$ is used to calculate the composite rate constant (b_f) for the N & G processes using the Avrami equation stated and is explained in Chapter 2.

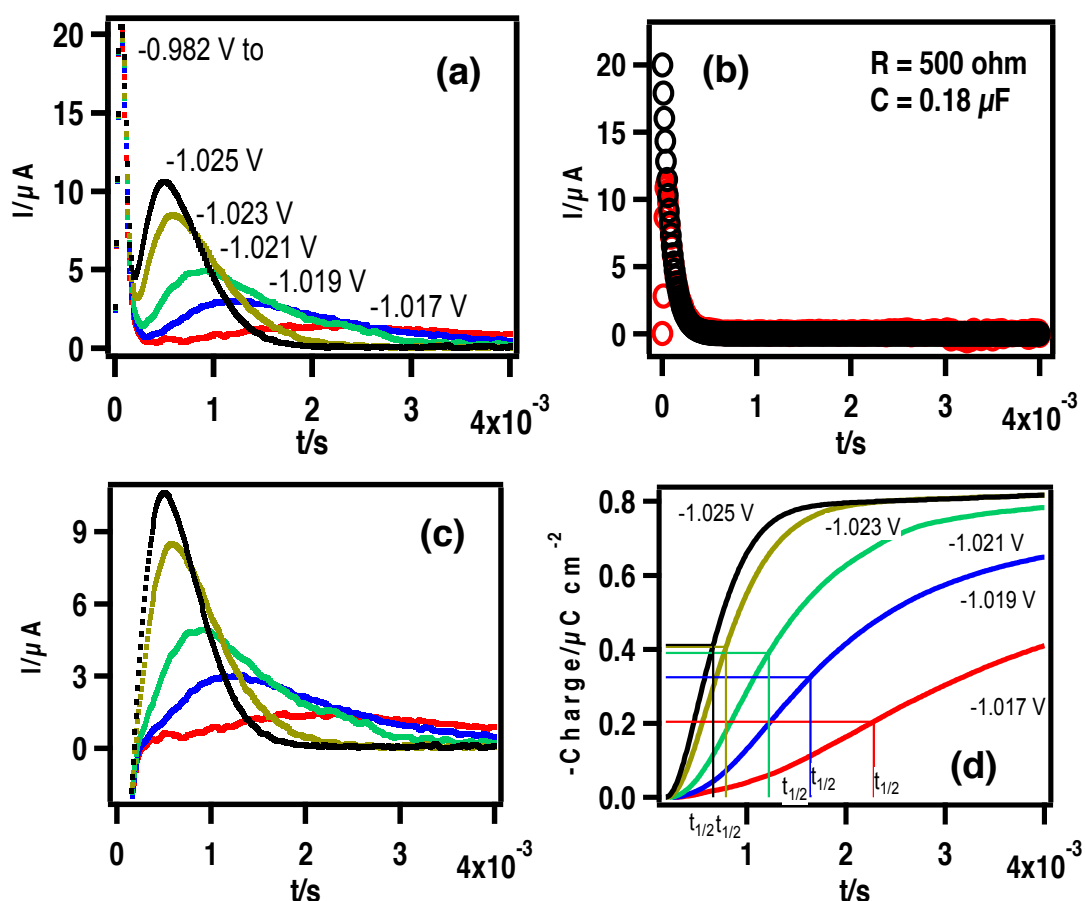


Figure 3.11: I-t transients obtained on application of (a) negatively increasing successive second potential steps from -1.015 V to -1.025 V (b) following potential step from -0.982 V to -0.987 V, red circles show data and black circles show fit, with parameters of the fit shown (c) with removed RC contribution and (d) Q-t transient on integration of RC subtracted I-t transients, from DOPC coated Hg electrode in 0.1 mol dm^{-3} KCl solution.

The potential, where the second phase transition is initiated following the partial decay of the RC capacitance transient, is corrected for IR drop. This potential is assumed to be the potential, which triggers the transition and is quoted as the step potential ($-E_s$) in all the ensuing plots. Figure 3.12 shows the potential profile of the step after IR correction when carried out in 0.1 and 0.05 mol dm^{-3} KCl electrolyte (with $-E_s$ marked) together with the current transients in both electrolytes respectively.

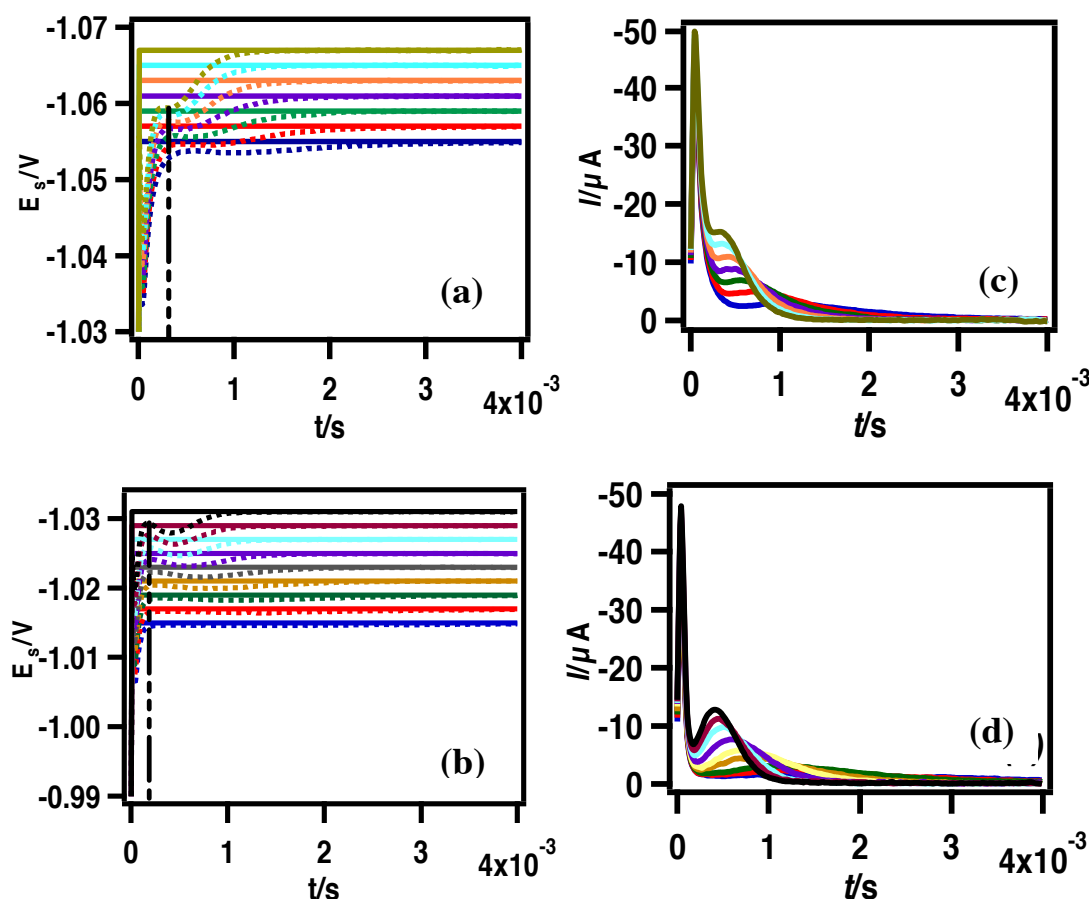


Figure 3.12: Step potential ($-E_s$) versus time (t) plots of DOPC monolayer on Hg in (a) 0.05 and (b) 0.1 mol dm⁻³ KCl (solid lines) and corresponding potential pulses after IR correction (dotted lines). Vertical dashed line bisecting potential plateau ($-E_s$) taken as potential initiating N & G transition. Current (I)–time (t) transient following potential step applied to DOPC monolayer on Hg in (c) 0.05 and (d) 0.1 mol dm⁻³ KCl.

It is assumed that the onset and kinetics of the N & G mechanism is directly related to the strength of the electric field at the Hg interface. Figure 3.13 displays the composite rate constant (b_f) for the N & G process versus the applied negative step potential ($-E_s$) plots obtained with the DOPC coated Hg electrode in electrolyte solutions of varying KCl concentration. It is observed that b_f increases linearly with an increase in the numerical value of $-E_s$. It was also found that b_f is unaffected by altering the potential prior to application of the step to more positive potentials.

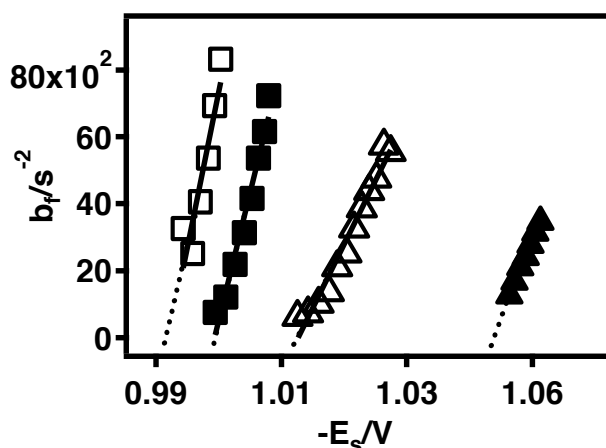


Figure 3.13: Composite rate constant (b_f) versus step potential ($-E_s$) plot of DOPC coated HMDE in solutions of 0.05 (closed triangle), 0.1 (open triangle), 0.5 (closed square) and 1.0 (open square) mol dm⁻³ KCl solution. All the error bars are within the symbol size.

The intercept of the b_f versus $-E_s$ plot with the horizontal axis gives the value $-E_0$. $-E_0$ is the threshold value of the step potential required to trigger the N & G process and has a complex dependence. $-E_0$ is affected by the potential of the first transition represented by capacitance peak 1. Capacitance peak-1 corresponds to the ingress of electrolyte into the monolayer and the monolayer's desorption and rearrangement. This is a process, which physically is a precursor to the transition represented by capacitance peak 2 [67-68]. $-E_0$ also relates to the kinetics of the second transition which is an activated mechanism. Figure 3.14 shows the plot of $-E_0$ versus $-\log$ ionic strength of the DOPC coated electrode using KCl as electrolyte. It is seen in Figure 3.14 that a less negative E_0 is required to instigate the process of the N & G phase transition in the presence of a higher ionic strength of KCl.

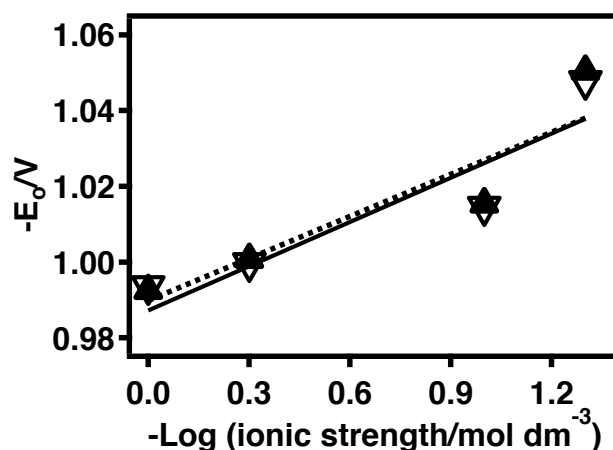


Figure 3.14: $-E_0$ versus $-\log$ ionic strength plot of DOPC coated HMDE in KCl solution. All the data in solid line is corrected for IR drop and plots are also shown in dotted line obtained prior to IR drop correction. All the error bars are within the symbol size.

The slope of the b_f versus $-E_s$ plot ($\Delta b_f / -\Delta E_s$) is also significant because it represents the change in the composite rate constant per unit change in step potential. The $\Delta b_f / -\Delta E_s$ versus ionic strength plot of DOPC coated electrode in KCl solution is presented in Figure 3.15 and it shows that the numerical value of $\Delta b_f / -\Delta E_s$ increases linearly with an increase in the ionic strength of KCl solution. It is seen that IR drop significantly decreases the numerical values of $\Delta b_f / -\Delta E_s$ but notably after IR correction the gradient of $\Delta b_f / -\Delta E_s$ with the ionic strength of the solution (Figure 3.15) remains positive albeit less pronounced.

As a result, the data in Figure 3.13, 3.14 and 3.15 can be interpreted as arising from the following mechanism. In solutions of higher ionic strength, more cations screen the Hg surface generating a steeper field at the Hg-water interface. This leads to a lower apparent value of $-E_0$ required to trigger the second phase transition and an increase in the numerical value of ($\Delta b_f / -\Delta E_s$). Both Figure 3.14 and 3.15 show results before and after correction from IR drop.

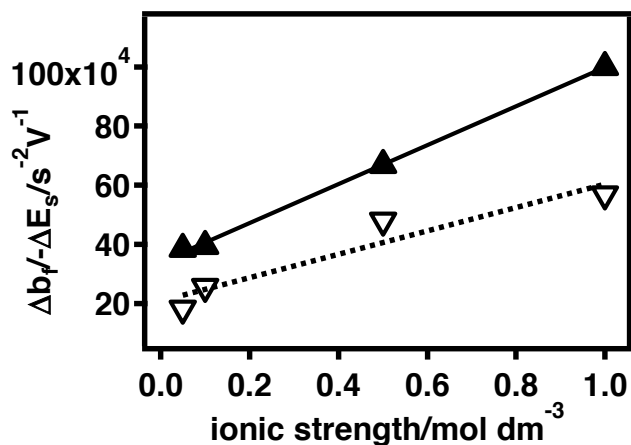


Figure 3.15: $\Delta b_f/\Delta E_s$ versus ionic strength plot of DOPC coated HMDE in KCl solution. All the data in solid line is corrected for *IR* drop and plots are also shown in dotted line obtained prior to *IR* drop correction. All the error bars are within the symbol size.

Figure 3.16 displays a cartoon showing the effect of the ionic strength on the screening of DOPC coated Hg after the ingress of electrolyte into the monolayer

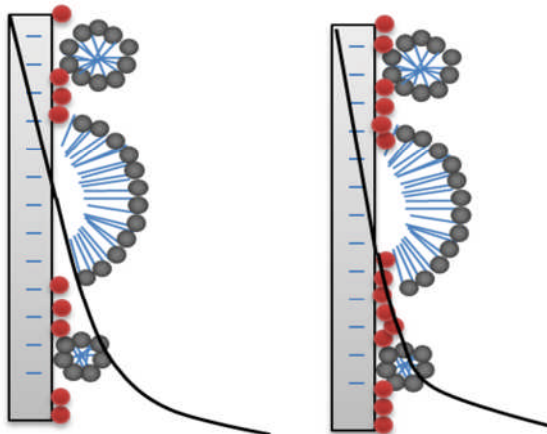


Figure 3.16: A diagram representing the electrical double layer at Hg-electrolyte interface in solutions with varying ionic strength.

3.2.2.2 Ionic composition

The effect of different ions on the potential of capacitance peak-2 is not systematic but the possibility of studying the kinetics of the occurrence of capacitance peak-2 allows the investigation into the mechanism of the associated phase transition process and the factors affecting that process. The trends in the kinetics of second phase transition are very regular and depend on the screening of Hg by the aquated ions. The water structure around the ions also play a vital role in screening the Hg surface and determining the rate of:

- a) Diffusion, movement and penetration of ions into the monolayer.
- b) Screening efficiency of ions and adsorption of ions on Hg surface to form electrical double layer (EDL) on the Hg electrode.

Figure 3.17 shows $\Delta b_f / -\Delta E_s$ versus the hydrated ion radius [69] plots derived from experiments carried out in solutions of alkali metal cations of chloride, fluoride and hydroxide salts. It can be seen that $\Delta b_f / -\Delta E_s$ is smaller in the presence of larger hydrated electrolyte ions. This effect can be interpreted as arising from the varying ability of the hydrated cations to screen the charged Hg/electrolyte interface depending on their size. Not only do the larger hydrated ions penetrate the DOPC-electrolyte phase less effectively compared to the smaller hydrated ions but also their packing at the Hg/electrolyte interface is less dense. An incomplete screening of the Hg surface generates a more diffuse field at the interface leading to numerically smaller $\Delta b_f / -\Delta E_s$ values. A significant numerical increase in $\Delta b_f / -\Delta E_s$ values observed in the presence of hydroxide electrolyte can only be related to a lower tendency for the larger hydrated OH^- to access the Hg interface than the halide ions in counterbalancing the screening effect from the cations. By the same token the Cl^- hydrated anions which are the smallest should have the easiest access to the surface and should decrease the numerical value of $\Delta b_f / -\Delta E_s$ to the greatest extent. This is only observed for the large hydrated cations.

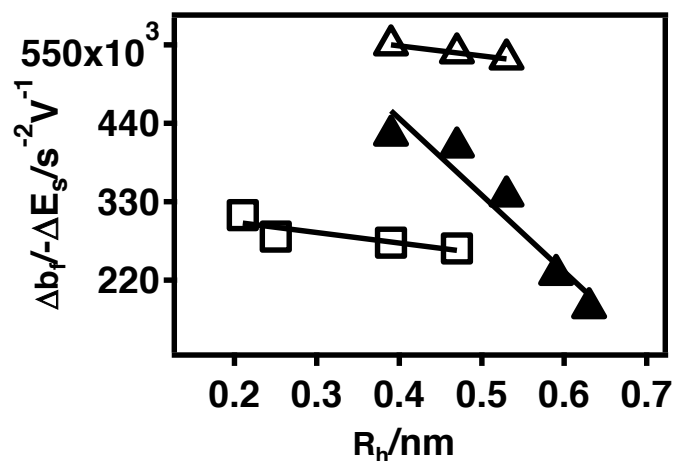


Figure 3.17: $\Delta b_f / -\Delta E_s$ versus cationic hydrated radius (R_h) plot of the DOPC monolayer on Hg in 0.1 mol dm^{-3} solutions of chlorides (closed triangle), hydroxides (open triangle) and fluorides (open square). All the data presented is corrected for IR drop and error bars are within the symbol size.

Table 3.2: Radii of the hydrated ions used in the present study and their calculated charge to diameter ratio and diffusion coefficients.

Ions	$R_h / \text{\AA}^{-1}$	Ions	$R_h / \text{\AA}^{-1}$
Li^+	3	Ba^{2+}	2.5
Na^+	2.25	F^-	1.75
K^+	1.5	Cl^-	1.5
Rb^+	1.25	Br^-	1.5
Cs^+	1.25	I^-	1.5
Ca^{2+}	3		

Figure 3.18 shows a cartoon of the screening of DOPC coated Hg electrode by various hydrated alkali metal cations after the first phase transition.

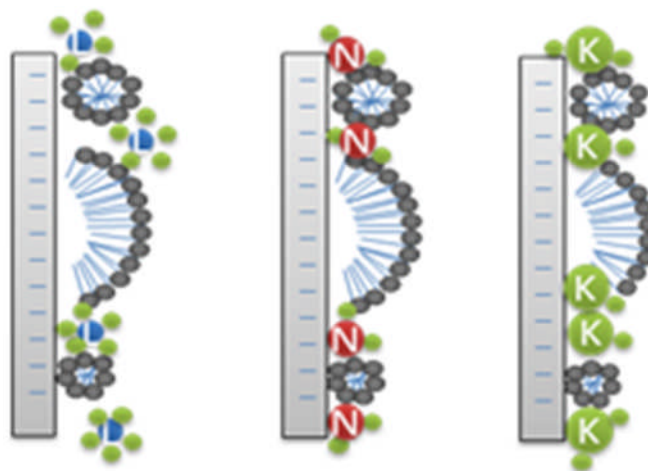


Figure 3.18: A diagram representing the screening of Hg by various hydrated alkali metal cations (Li^+ , Na^+ and K^+).

3.2.3 Effect of Organic electrolytes

3.2.3.1 Capacitance peak-1

Capacitance peak-1 potential versus concentration plots (Figure 3.19) of the different organic cations shows that BMIM^+ shifts $-E_1$ to more positive values than does TEA^+ and Cho^+ . In the presence of 0.1 mol dm^{-3} KCl electrolyte solution, a constant concentration of K^+ maintains a double layer structure at the lipid-electrolyte interface. The octanol-water ($\log K_{\text{OW}}$) partition coefficients of the studied organic cations are as follows in order of increasing polarity:- BMIM^+ : -2.4 [70], TEA^+ : -3.2 [71] and Cho^+ : reported variously as -3.77 [72-73] and -5.16 [74]. The extent of the adsorption of organic cations on the DOPC layer depends on their departure from polarity. The less polar BMIM^+ tends to accumulate on the lipid surface to a greater extent [75] generating a stronger field across the lipid layer. The result of this is to shift $-E_1$ to positive potentials. In the same way, TEA^+ binds to the phospholipid at higher solution concentration than Cho^+ [27] shifting the $-E_1$ to more positive potentials (Figure 3.19).

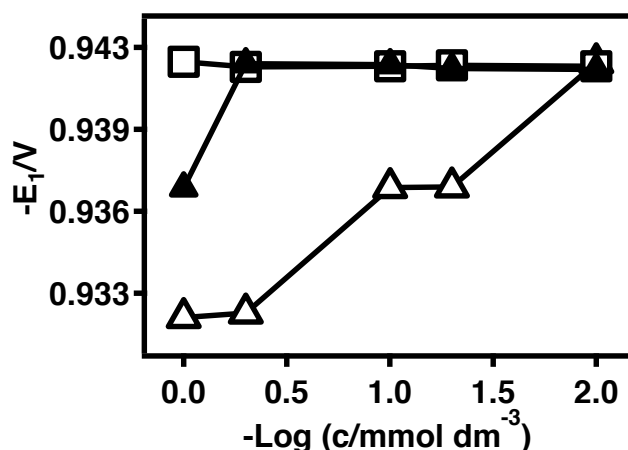


Figure 3.19: $-E_1$ versus $-\log$ organic cation concentration ($-\log c$) plot of DOPC coated Hg electrode in 0.1 mol dm^{-3} KCl electrolyte containing BMIM^+ (open triangle), TEA^+ (closed triangle) and Cho^+ (open square). All the data presented is corrected for IR drop and error bars are within the symbol size.

3.2.3.2 Capacitance peak -2

With respect to the effect of the organic cations on the N & G process underlying capacitance peak-2, Fig. 3.21 displays $\Delta b_f / -\Delta E_s$ versus log concentration plots of BMIMCl and TEAC in 0.1 mol dm^{-3} KCl. Both BMIM^+ and TEA^+ are found to decrease the numerical slope $\Delta b_f / -\Delta E_s$ with their increasing concentration to a more or less similar extent. An explanation for the effect of these ions on $\Delta b_f / -\Delta E_s$, can be that these organic cations with their large and almost equal molecular volume of ~ 0.145 and 0.154 nm^3 respectively [76-77] interfere as cations with the K^+ screening of the Hg interface decreasing the electric field at the interface thus slowing the kinetics of the transition.

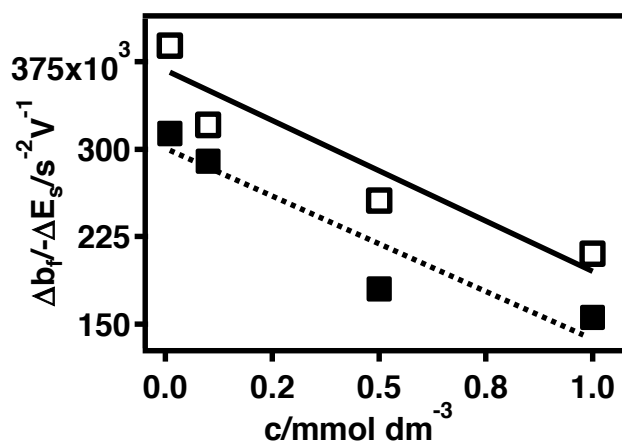


Figure 3.20: $\Delta b_f/\Delta E_s$ versus c plot of BMIM⁺ (open square) and TEC⁺ (close square) in 0.1 mol dm⁻³ KCl electrolyte. All the data presented is corrected for IR drop and error bars are within the symbol size.

A plot of $\Delta b_f/\Delta E_s$ versus $\log K_{ow}$ is shown in Figure 3.21 for the DOPC coated Hg electrode in the KCl solution containing different anions of BMIM⁺. It shows that the most hydrophobic BMIMPF₆ slows down the kinetics of second phase transition. Due to its higher hydrophobicity, it interacts strongly with hydrophobic chains of DOPC and delays the process of bilayer formation by delaying the reorientation of head groups.

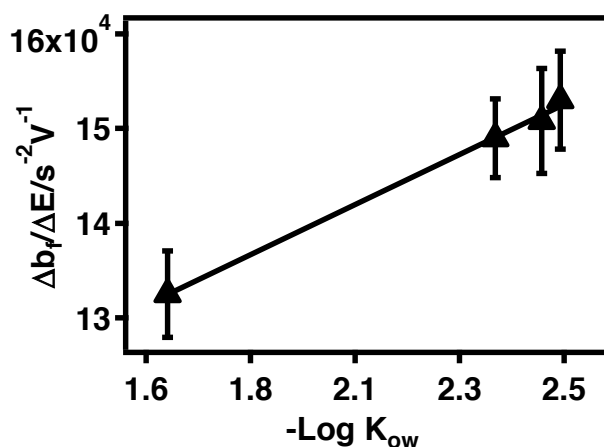


Figure 3.21: $\Delta b_f/\Delta E_s$ versus $-\log$ water-octanol partition coefficient ($-\log K_{ow}$) plot of different anions of BMIM⁺ in 0.1 mol dm⁻³ KCl electrolyte. All the data presented is corrected for IR drop and error bars are within the symbol size.

The log K_{ow} values of different ionic liquids consisting of BMIM⁺ as cation are given in Table 3.3.

Table 3.3: Organic salts and log of their octanol-water partition coefficients

Organic salt	-Log (K_{ow})
BMIMCl	2.397±0.0003
BMIMBr	2.481±0.0005
BMIMBF ₄	2.522±0.0002
BMIMPF ₆	1.657±0.0008

3.2.4 Interaction of phosphorous containing electrolytes with DOPC monolayers on Hg

Sodium pyrophosphate ($\text{Na}_2\text{H}_2\text{P}_2\text{O}_5$) is proposed as a key molecule involved in the synthesis of other energy currency activated phosphorous containing molecules. The effects of $\text{Na}_2\text{H}_2\text{P}_2\text{O}_5$ -DOPC interactions on the C_{sp} -E plots (Figure 3.25) were recorded on the cathodic scans between -0.2 and -1.2 V. These results were obtained from measurements carried out in different composition of KCl and $\text{Na}_2\text{H}_2\text{P}_2\text{O}_5$ solution (3:1, 1:1, 1:3 and 0:1 ratio of KCl and $\text{Na}_2\text{H}_2\text{P}_2\text{O}_5$ respectively) keeping the total ionic strength constant to 0.1 mol dm^{-3} . The data were recorded immediately after DOPC monolayer formation shown as green and after 30 minutes of monolayer formation shown as red. The C_{sp} -E curves of DOPC coated electrode immersed in 0.1 mol dm^{-3} KCl without added $\text{Na}_2\text{H}_2\text{P}_2\text{O}_5$ is shown in black in all the figures. Addition of $\text{Na}_2\text{H}_2\text{P}_2\text{O}_5$ to KCl in different proportions does not alter the DOPC C_{sp} -E profile significantly apart from a little suppression of capacitance peak-1 even after 30 minutes.

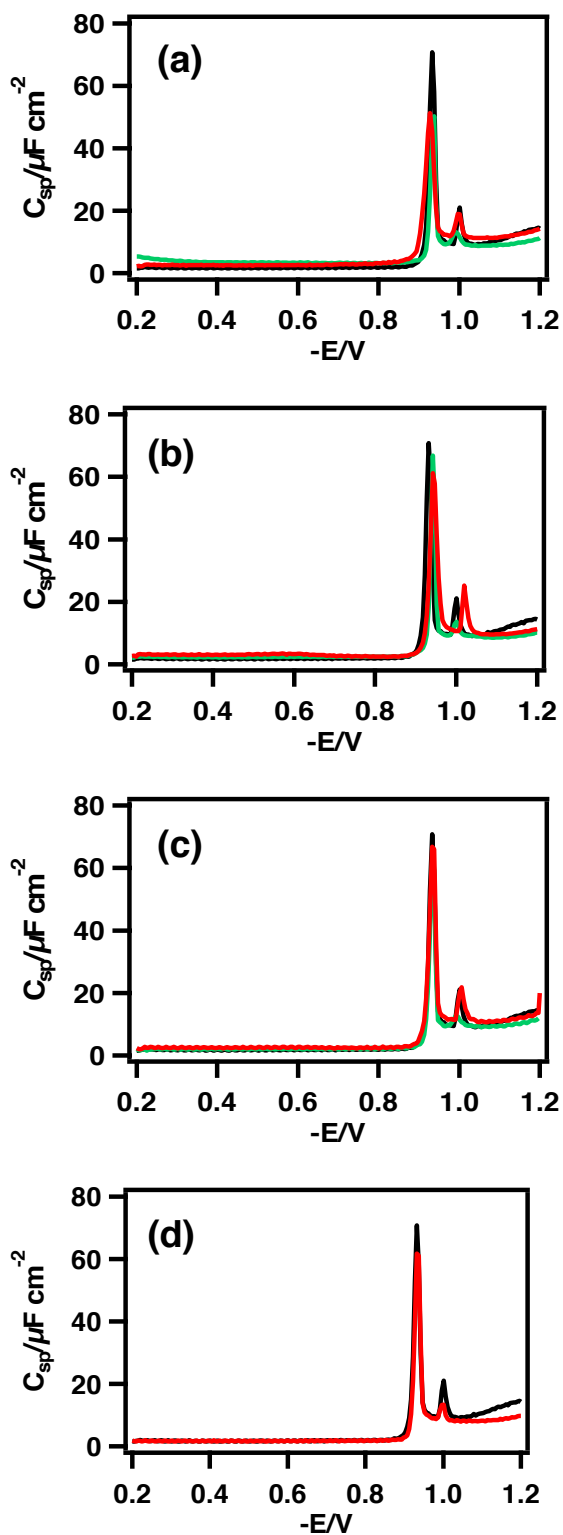


Figure 3.22: Capacitance (C_{sp}) versus potential ($-E$) plots of DOPC coated HMDE in 0.1 mol dm^{-3} of KCl and $\text{Na}_2\text{H}_2\text{P}_2\text{O}_5$ in (a) 3:1, (b) 1:1, (c) 1:3 and (d) 0:1 ratio obtained using ACV at 0.005 V s^{-1} , 75 Hz, $0.005 \text{ V } \Delta E$ and 90° out of phase. Green is after 30 minutes and all black is in 100 % 0.1 mol dm^{-3} KCl solution.

The effect of $\text{Na}_2\text{H}_2\text{P}_2\text{O}_5$ on uncoated Hg electrode without DOPC monolayer was also examined to monitor any adsorption process occurring on its surface. An increase in specific capacitance of Hg is observed at less negative potentials below PZC of Hg (Figure 3.26) most likely to be associated with specific adsorption of $\text{H}_2\text{P}_2\text{O}_5^{-2}$ in this potential window.

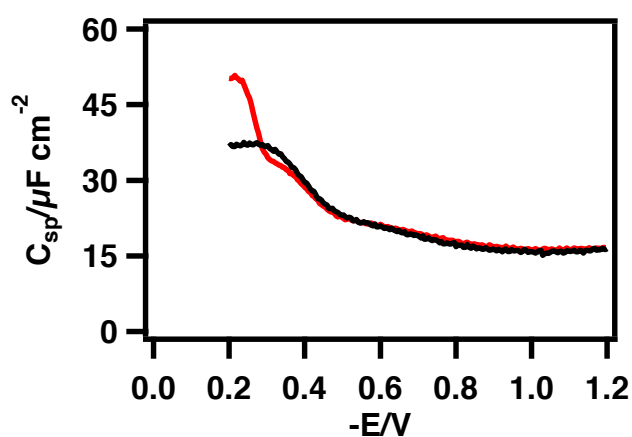


Figure 3.23: Capacitance (C_{sp}) versus potential ($-E$) plots of HMDE in 0.1 mol dm^{-3} of KCl (black) and $\text{Na}_2\text{H}_2\text{P}_2\text{O}_5$ (red) obtained using ACV at 0.005 V s^{-1} , 75 Hz , $0.005 \text{ V } \Delta E$ and 90° out of phase.

Other phosphorous compounds used to synthesize $\text{Na}_2\text{H}_2\text{P}_2\text{O}_5$ such as sodium phosphite (Na_2HPO_3), dibasic sodium hydrogen phosphate (Na_2HPO_4) and phosphorous acid (H_3PO_3) were also inspected for their interactions with DOPC monolayer on Hg. Figure 3.27 displays the C_{sp} - E curves of DOPC coated Hg electrode in KCl obtained after addition of Na_2HPO_3 , Na_2HPO_4 , $\text{Na}_2\text{H}_2\text{P}_2\text{O}_5$ and H_3PO_3 maintaining a ratio of 1:1 and ionic strength of 0.1 mol dm^{-3} . Only a significant interaction was exhibited by H_3PO_3 indicating substantial amount of suppression and shift in capacitance peaks without any disturbance to monolayer structure recognized from impedance studies. All others phosphorous containing compounds showed insignificant change to the capacitance peaks and hence to the structure of DOPC monolayer (Figure 3.27).

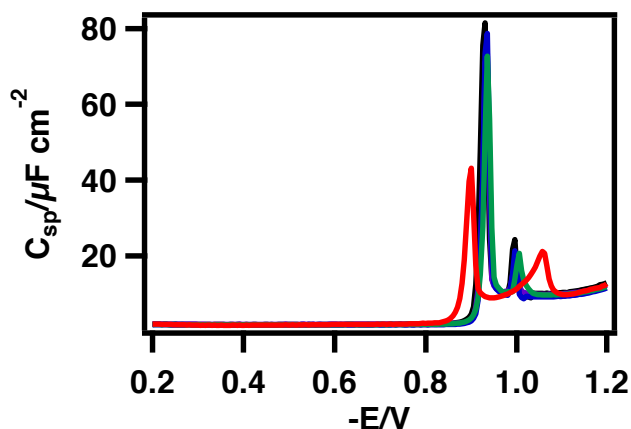


Figure 3.24: Capacitance (C_{sp}) versus potential ($-E$) plots of DOPC coated HMDE in 0.1 mol dm^{-3} of KCl (50 %), 50 % $\text{Na}_2\text{H}_2\text{P}_2\text{O}_5$ (green), 50 % Na_2HPO_3 (blue), 50 % Na_2HPO_4 (purple) and 50 % H_3PO_3 (red) obtained using ACV at 0.005 V s^{-1} , 75 Hz, $0.005 \text{ V } \Delta E$ and 90° out of phase. Black is in 100 % 0.1 mol dm^{-3} KCl solution.

Impedance data at -0.4 V plotted in the complex capacitance plane of DOPC coated Hg electrode and with added $\text{Na}_2\text{H}_2\text{P}_2\text{O}_5$, Na_2HPO_3 , Na_2HPO_4 and H_3PO_3 to KCl electrolyte in a ratio of 1:1 to a total ionic strength of 0.1 mol dm^{-3} were obtained from measurements carried out after injection followed by 5 minute stirring of electrolyte solution (Figure 3.28). Impedance plots of DOPC coated Hg electrode are almost indistinguishable in the presence and absence of $\text{Na}_2\text{H}_2\text{P}_2\text{O}_5$, Na_2HPO_3 , Na_2HPO_4 and H_3PO_3 in KCl solution with no frequency dispersion and without any change in ZFC. H_3PO_3 , showed up as highly interactive in capacitance-potential plots is actually unreactive in impedance plots. Therefore, the effects in capacitance-potential plots can be credited to decrease in pH of electrolyte solution and the triply charged PO_3^{3-} ion interaction with the monolayer. The absence of a "tail" in the complex capacitance plot of DOPC coated Hg in the H_3PO_3 is interesting. The result shows that the effect of H_3PO_3 on the capacitance-potential plot is not due to adsorption of organic contamination on the DOPC layer but comes from the H_3PO_3 .

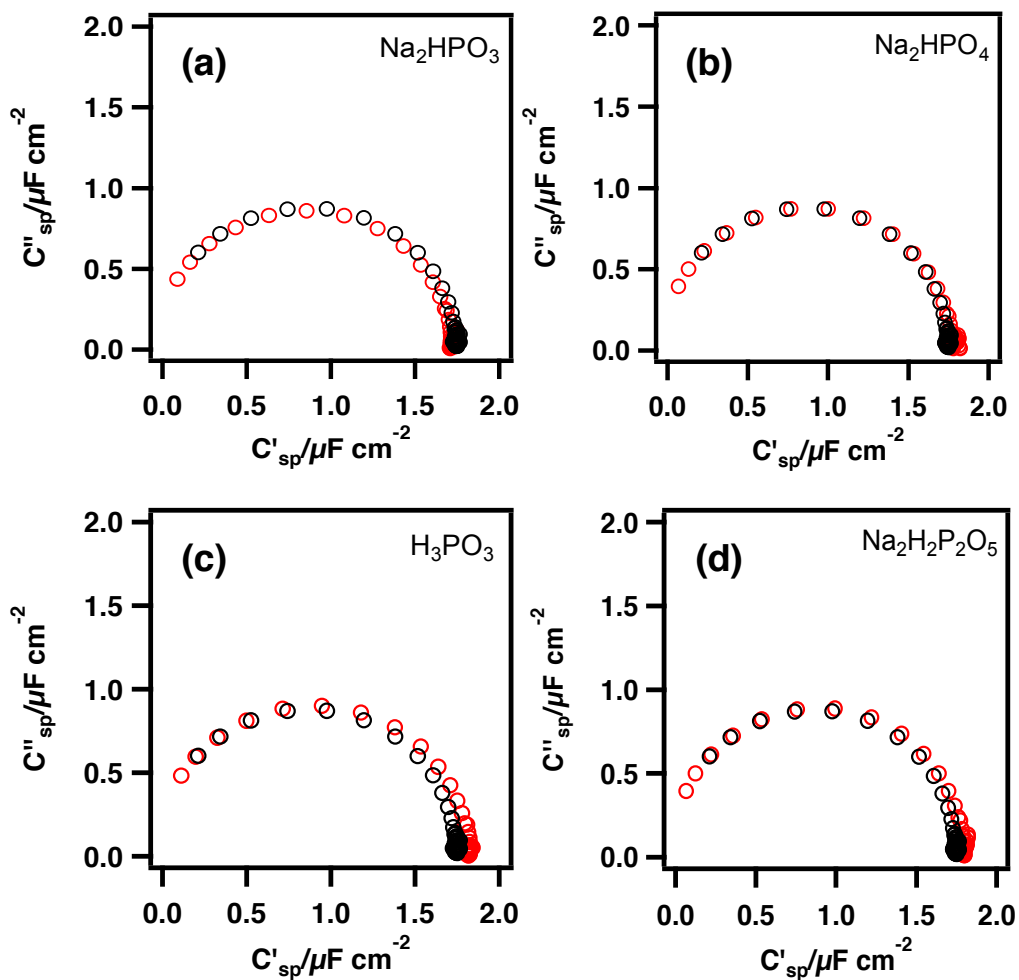


Figure 3.25: Impedance data transformed to complex capacitance plane of DOPC coated HMDE in 0.1 mol dm^{-3} of KCl (50 %) and (a) 50 % Na_2HPO_3 , (b) 50 % Na_2HPO_4 , (c) 50 % H_3PO_3 and (d) 50 % $\text{Na}_2\text{H}_2\text{P}_2\text{O}_5$, obtained using EIS at -0.4 V . All black data is in 100 % 0.1 mol dm^{-3} KCl solution.

It was proposed that that the positively charged nitrogen containing bulky choline group of DOPC molecules might prevents the interaction between the phosphorus from $\text{Na}_2\text{H}_2\text{P}_2\text{O}_5$ and phosphorous from phosphate group of DOPC molecule. This hypothesis has been confirmed by studying the interaction of $\text{Na}_2\text{H}_2\text{P}_2\text{O}_5$ with 1,2-dioleoylphosphatidyl glycerol (DOPG) monolayer supported on the surface of Hg. The two phase transitions at more negative potential in capacitance-potential profiles of DOPG coated Hg in 0.1 mol dm^{-3} KCl solution are not as well resolved as they are in capacitance-potential profiles of DOPC coated Hg in the same solution. In addition the baseline capacitance of DOPG coated Hg is lower. In complex capacitance plane plots, at -0.4 V (\sim PZC of Hg), DOPG monolayer on Hg also showed a semicircle characteristic of series RC circuit similar to that demonstrated by DOPC monolayer. The C_{sp} -E and complex capacitance plane plots of DOPG coated Hg electrode in 0.1 mol dm^{-3} KCl are shown in black in Figure 3.29.

Addition of $\text{Na}_2\text{H}_2\text{P}_2\text{O}_5$ to the KCl solution in a ratio of 1:1 to a total ionic strength of 1.0 mol dm^{-3} resulted in a small shift of both capacitance peaks to more negative potential in capacitance-potential profile obtained from both RCV and ACV. This indicated the adsorption of $(\text{H}_2\text{P}_2\text{O}_5^{-2})$ on the DOPG monolayer countering the effect by adsorption of Na^+ in response to applied negative potential. This resulted in a weak electric field due to decreased potential drop at the DOPG coated Hg electrolyte interface. Therefore, higher negative potentials are required to initiate first phase transition shifting the capacitance peak-1 to a more negative potential. The impedance plots of DOPG coated Hg electrode in the presence of $\text{H}_2\text{P}_2\text{O}_5^{-2}$ showed a significant low frequency element in addition to RC semicircle with no change in ZFC indicating the adsorption of $\text{H}_2\text{P}_2\text{O}_5^{-2}$ on the surface of DOPG monolayer with no penetration or incorporation at all (Figure 3.26).

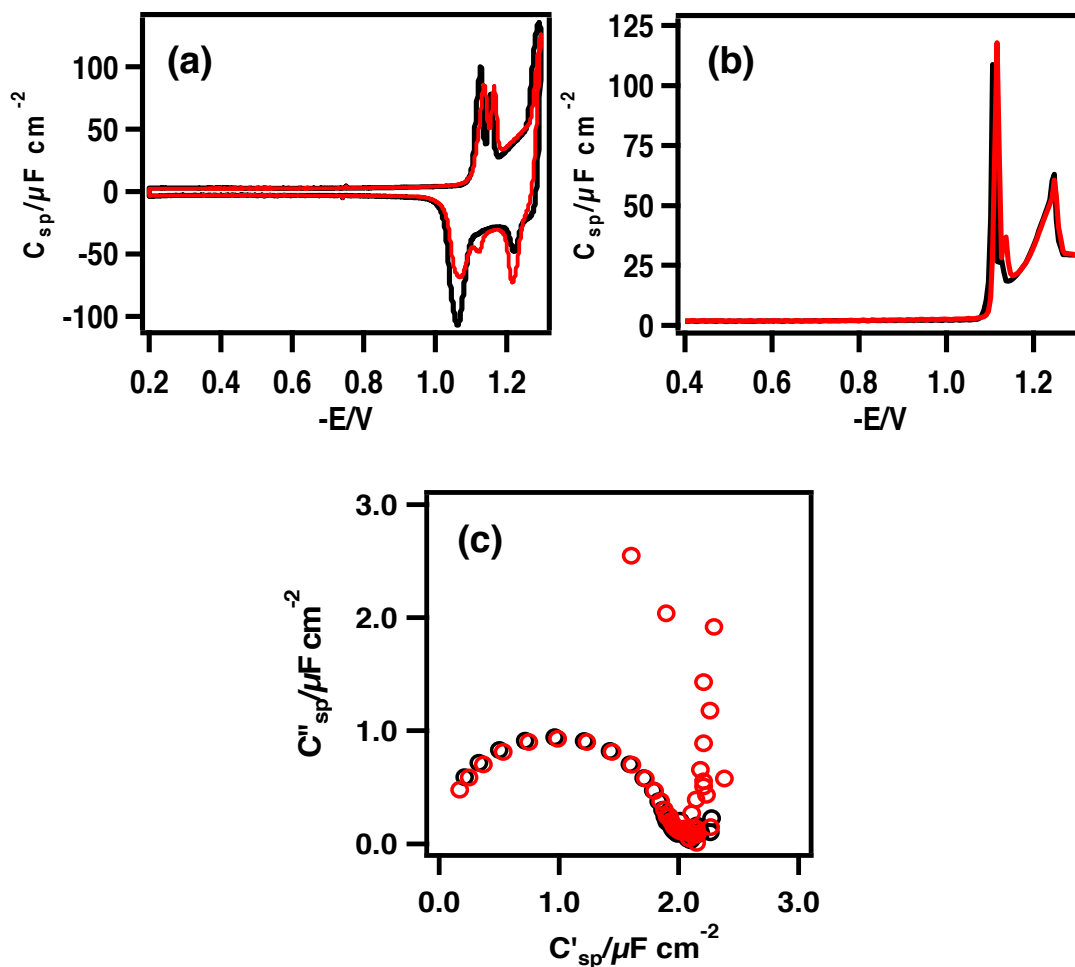


Figure 3.26: Capacitance current (a) and capacitance (b) versus potential ($-E$) plots and Impedance data transformed to complex capacitance plane (c) of DOPG coated MFE in 0.1 mol dm^{-3} of KCl (50 %) and 50 % $Na_2P_2O_7$ (red) obtained using RCV at 40 Vs^{-1} , ACV at 0.005 V s^{-1} , 75 Hz, $0.005 \text{ V } \Delta E$ and 90° out of phase and EIS at -0.4 V respectively. All black data is in 100 % 0.1 mol dm^{-3} KCl solution.

3.3 Conclusions

1. The phase transition underlying capacitance peak-1 are initiated at a critical value of field so an increase or decrease of this field through ion adsorption on DOPC will affect the applied potential required to initiate the transition. Cations in higher ionic strength electrolyte compress the double layer at the DOPC/electrolyte interface increasing the electric field across the lipid and decreasing the applied negative potential necessary to initiate the phase

transition. For the same reason, in identical ionic strength solutions, cations with the strongest binding affinity to the DOPC head groups cause an increase in field strength across the layer also decreasing the applied negative potential necessary to initiate the phase transition. Electrolyte anions e.g. I^- which adsorb on the DOPC polar groups decrease the field strength across the layer at applied negative potentials increasing the applied negative potential necessary to initiate the transition.

2. The influence of inorganic electrolyte ions on the occurrence of capacitance peak-2 underlying the N & G process which leads to re-adsorption of bilayer patches is related to the influence of the ions on the structure of the electrical double layer at the Hg interface following ingress of electrolyte into the DOPC layer. The kinetics of this phase transition is influenced by the strength of the electric field at the Hg interface. Higher concentration of cations compress the double layer increasing the electric field at the Hg interface requiring lower applied negative potentials to initiate the N & G mechanism increasing its rate. Smaller hydrated ions increase the rate of the N & G mechanism due to their more effective screening of the Hg interface so increasing the electric field strength.
3. Organic cations in inorganic electrolyte of constant concentration influence the characteristics of capacitance peak-1 in the same way as effected by the inorganic ions. These effects are directly related to their departure from polarity and their extent of adsorption on the DOPC monolayer. In addition organic cations in inorganic electrolyte of constant concentration slow down the kinetics of the N & G phase transition presumably by decreasing the effectiveness of K^+ to screen the applied potential on the Hg surface.
4. The interactions between the pyrophosphite and other phosphate containing electrolytes and DOPC monolayer on Hg does not appeared to be significant in both the capacitance-potential and complex capacitance plots and becomes noticeable on replacing the DOPC with DOPG (phospholipid lacking choline group).

3.4 References

- [1] M.P. Blaustein, The interrelationship between sodium and calcium fluxes across cell membranes, in: *Reviews of Physiology, Biochemistry and Pharmacology*, Volume 70, Springer, 1974, pp. 33-82.
- [2] H.H. Ussing, *The alkali metal ions in isolated systems and tissues*, Springer, 1960.
- [3] D.F. Bohr, *Pharmacological reviews*, 16 (1964) 85-111.
- [4] B. Elford, C. Walter, *Cryobiology*, 9 (1972) 82-100.
- [5] W.L. Webb Jr, M. Gehi, *Psychosomatics*, 22 (1981) 199-203.
- [6] L. Baer, S.R. Platman, S. Kassir, R.R. Fieve, *Journal of psychiatric research*, 8 (1971) 91-105.
- [7] B. Surawicz, *Progress in cardiovascular diseases*, 8 (1966) 364-386.
- [8] L. Becucci, M.R. Moncelli, R. Naumann, R. Guidelli, *Journal of the American Chemical Society*, 127 (2005) 13316-13323.
- [9] I. Burgess, M. Li, S. Horswell, G. Szymanski, J. Lipkowski, J. Majewski, S. Satija, *Biophysical journal*, 86 (2004) 1763-1776.
- [10] E.T. Castellana, P.S. Cremer, *Surface Science Reports*, 61 (2006) 429-444.
- [11] D. Papahadjopoulos, *Biochimica et Biophysica Acta (BBA)-Biomembranes*, 163 (1968) 240-254.
- [12] D. Mandler, I. Turyan, *Electroanalysis*, 8 (1996) 207-213.
- [13] L. Becucci, M.R. Moncelli, R. Herrero, R. Guidelli, *Langmuir*, 16 (2000) 7694-7700.
- [14] D.O. Shah, J.H. Schulman, *Journal of lipid research*, 8 (1967) 227-233.
- [15] V.A. Hernández, F. Scholz, *Israel Journal of Chemistry*, 48 (2008) 169-184.
- [16] H. Akutsu, J. Seelig, *Biochemistry*, 20 (1981) 7366-7373.
- [17] S. Terrettaz, M. Mayer, H. Vogel, *Langmuir*, 19 (2003) 5567-5569.
- [18] F. Giess, M.G. Friedrich, J. Heberle, R.L. Naumann, W. Knoll, *Biophysical journal*, 87 (2004) 3213-3220.
- [19] R. Lipowsky, E. Sackmann, *Structure and Dynamics of Membranes: I. From Cells to Vesicles/II. Generic and Specific Interactions*, North Holland, 1995.
- [20] B. Alberts, A. Johnson, J. Lewis, M. Raff, K. Roberts, P. Walter, *New York*, (2002) 1227-1242.
- [21] B. Alberts, A. Johnson, J. Lewis, M. Raff, K. Roberts, P. Walter, (2002).

- [22] J.A. Szule, S.E. Jarvis, J.E. Hibbert, J.D. Spafford, J.E. Braun, G.W. Zamponi, G.M. Wessel, J.R. Coorsen, *Journal of Biological Chemistry*, 278 (2003) 24251-24254.
- [23] A. Portis, C. Newton, W. Pangborn, D. Papahadjopoulos, *Biochemistry*, 18 (1979) 780-790.
- [24] J. Wilschut, N. Duzgunes, R. Fraley, D. Papahadjopoulos, *Biochemistry*, 19 (1980) 6011-6021.
- [25] R. Vácha, S.W. Siu, M. Petrov, R.A. Böckmann, J. Barucha-Kraszewska, P. Jurkiewicz, M. Hof, M.L. Berkowitz, P. Jungwirth, *The Journal of Physical Chemistry A*, 113 (2009) 7235-7243.
- [26] H. Hauser, M. Phillips, M. Barratt, *Biochimica et Biophysica Acta (BBA)-Biomembranes*, 413 (1975) 341-353.
- [27] J. Puskin, *The Journal of membrane biology*, 35 (1977) 39-55.
- [28] M. Eisenberg, T. Gresalfi, T. Riccio, S. McLaughlin, *Biochemistry*, 18 (1979) 5213-5223.
- [29] R.A. Böckmann, A. Hac, T. Heimburg, H. Grubmüller, *Biophysical journal*, 85 (2003) 1647-1655.
- [30] R. Lehrmann, J. Seelig, *Biochimica et Biophysica Acta (BBA)-Biomembranes*, 1189 (1994) 89-95.
- [31] S. McLaughlin, G. Szabo, G. Eisenman, *The Journal of general physiology*, 58 (1971) 667-687.
- [32] A. McLaughlin, C. Grathwohl, S. McLaughlin, *Biochimica et Biophysica Acta (BBA)-Biomembranes*, 513 (1978) 338-357.
- [33] S. McLAUGHLIN, N. Mulrine, T. Gresalfi, G. Vaio, A. McLAUGHLIN, *The Journal of general physiology*, 77 (1981) 445-473.
- [34] M. Roux, M. Bloom, *Biophysical journal*, 60 (1991) 38-44.
- [35] C.G. Sinn, M. Antonietti, R. Dimova, *Colloids and Surfaces A: Physicochemical and Engineering Aspects*, 282 (2006) 410-419.
- [36] S. Garcia-Manyes, G. Oncins, F. Sanz, *Biophysical journal*, 89 (2005) 1812-1826.
- [37] S.A. Pandit, D. Bostick, M.L. Berkowitz, *Biophysical journal*, 84 (2003) 3743.
- [38] H. Binder, O. Zschörnig, *Chemistry and physics of lipids*, 115 (2002) 39-61.
- [39] N.N. Casillas-Ituarte, X. Chen, H. Castada, H.C. Allen, *The Journal of Physical Chemistry B*, 114 (2010) 9485-9495.

- [40] T.P. Kee, D.E. Bryant, B. Herschy, K.E. Marriott, N.E. Cosgrove, M.A. Pasek, Z.D. Atlas, C.R. Cousins, *Life*, 3 (2013) 386-402.
- [41] D.E. Bryant, D. Greenfield, R.D. Walshaw, B.R. Johnson, B. Herschy, C. Smith, M.A. Pasek, R. Telford, I. Scowen, T. Munshi, *Geochimica et Cosmochimica Acta*, 109 (2013) 90-112.
- [42] M. Baltscheffsky, A. Schultz, H. Baltscheffsky, *FEBS letters*, 452 (1999) 121-127.
- [43] A. Serrano, J.R. Pérez-Castiñeira, M. Baltscheffsky, H. Baltscheffsky, *IUBMB life*, 59 (2007) 76-83.
- [44] F. Harold, *The Vital Force*, (1986).
- [45] M. Marshall, *New Scientist*, 218 (2013) 13.
- [46] A. Nelson, N. Auffret, *Journal of Electroanalytical Chemistry and Interfacial Electrochemistry*, 244 (1988) 99-113.
- [47] Grahame C. D., *Chemical reviews*, 41 (1947) 61.
- [48] M.R. Moncelli, R. Guidelli, *Journal of Electroanalytical Chemistry*, 326 (1992) 331-338.
- [49] A.J. Bard, L.R. Faulkner, *Electrochemical methods: fundamentals and applications*, Wiley New York, 1980.
- [50] R. Guidelli, G. Aloisi, L. Becucci, A. Dolfi, M. Rosa Moncelli, F. Tadini Buoninsegni, *Journal of Electroanalytical Chemistry*, 504 (2001) 1-28.
- [51] T. Lewis, *Dielectrics and Electrical Insulation*, *IEEE Transactions on*, 10 (2003) 769-777.
- [52] M.R. Moncelli, L. Becucci, F.T. Buoninsegni, R. Guidelli, *Biophysical journal*, 74 (1998) 2388-2397.
- [53] I. Zawisza, A. Lachenwitzer, V. Zamlynyy, S. Horswell, J. Goddard, J. Lipkowski, *Biophysical journal*, 85 (2003) 4055-4075.
- [54] J.N. Sachs, H. Nanda, H.I. Petrache, T.B. Woolf, *Biophysical journal*, 86 (2004) 3772-3782.
- [55] X. Bin, I. Zawisza, J.D. Goddard, J. Lipkowski, *Langmuir*, 21 (2005) 330-347.
- [56] D. Bizzotto, A. Nelson, *Langmuir*, 14 (1998) 6269-6273.
- [57] B. Wathey, J. Tierney, P. Lidström, J. Westman, *Drug Discovery Today*, 7 (2002) 373-380.
- [58] F.F. de Sousa, S.G. Moreira, J. Shirsley, J.D. Nero, P. Alcantara Jr, *Journal of Bionanoscience*, 3 (2009) 139-142.

- [59] P. Bowen, T. Lewis, *Thin Solid Films*, 99 (1983) 157-163.
- [60] B. Klasczyk, V. Knecht, R. Lipowsky, R. Dimova, *Langmuir*, 26 (2010) 18951-18958.
- [61] S.A. TATULIAN, *European Journal of Biochemistry*, 170 (1987) 413-420.
- [62] R. Vácha, P. Jurkiewicz, M. Petrov, M.L. Berkowitz, R.A. Böckmann, J. Barucha-Kraszewska, M. Hof, P. Jungwirth, *The Journal of Physical Chemistry B*, 114 (2010) 9504-9509.
- [63] R. Vácha, P. Jurkiewicz, M. Petrov, M.L. Berkowitz, R.A. Böckmann, J. Barucha-Kraszewska, M. Hof, P. Jungwirth, *The Journal of Physical Chemistry B*, 114 (2010) 9504-9509.
- [64] J. Merrifield, J. Tattersall, M. Bird, A. Nelson, *Electroanalysis*, 19 (2007) 272-279.
- [65] S.A. Tatulian, *Biochimica et Biophysica Acta (BBA)-Biomembranes*, 736 (1983) 189-195.
- [66] A. Nelson, *Journal of Electroanalytical Chemistry*, 601 (2007) 83-93.
- [67] A.V. Brukhno, A. Akinshina, Z. Coldrick, A. Nelson, S. Auer, *Soft Matter*, 7 (2011) 1006-1017.
- [68] A. Vakurov, M. Galluzzi, A. Podestà, N. Gamper, A.L. Nelson, S.D. Connell, *ACS nano*, 8 (2014) 3242-3250.
- [69] J. Kielland, *Journal of the American Chemical Society*, 59 (1937) 1675-1678.
- [70] L. Ropel, L.S. Belvèze, S.N. Aki, M.A. Stadtherr, J.F. Brennecke, *Green Chemistry*, 7 (2005) 83-90.
- [71] R. Kimura, M. Miwa, Y. Kato, M. Sato, S. Yamada, *Archives internationales de pharmacodynamie et de thérapie*, 310 (1990) 13-21.
- [72] N.M. Satchivi, E.W. Stoller, L.M. Wax, D.P. Briskin, *Pesticide biochemistry and physiology*, 84 (2006) 83-97.
- [73] E.A. Baker, A.L. Hayes, R.C. Butler, *Pesticide science*, 34 (1992) 167-182.
- [74] H. Sanderson, M. Thomsen, *Toxicology letters*, 187 (2009) 84-93.
- [75] M. Galluzzi, S. Zhang, S. Mohamadi, A. Vakourov, A. Podestà, A. Nelson, *Langmuir*, (2013).
- [76] A. Bondi, *The Journal of Physical Chemistry*, 68 (1964) 441-451.
- [77] V. Kuz'min, S. Katser, *Bulletin of the Russian Academy of Sciences, Division of chemical science*, 41 (1992) 720-727.

Chapter-4

Interaction of di- and tri- peptides with phospholipid monolayers on Hg

4.1 Introduction

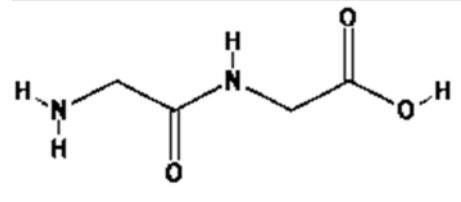
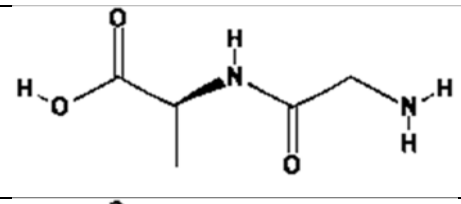
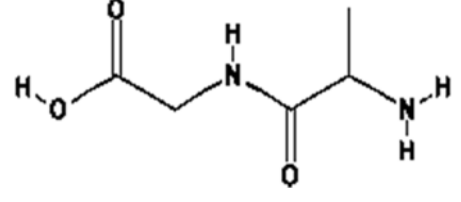
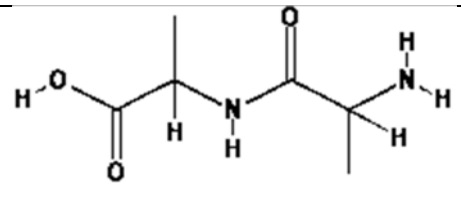
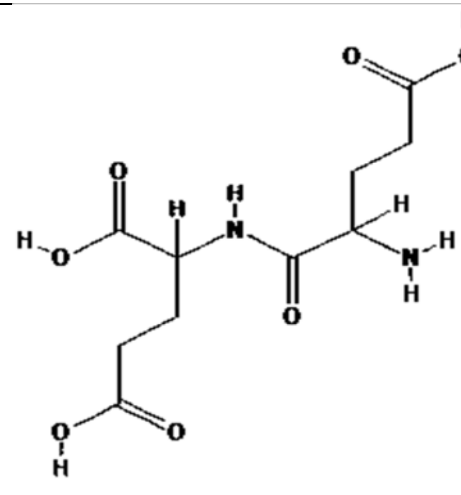
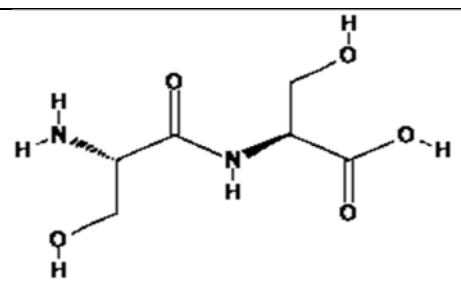
Peptides are the polymer chains composed of two or more of twenty different types of amino acids each connected to each other by a peptide linkage. In a peptide linkage, the nitrogen atom of one amino acid binds to the carboxyl carbon atom of another [1-2]. Simple and small peptides offer themselves as potential candidates involved in prebiotic chemistry because of their presence in many meteorites and their catalytic properties for certain chemical reactions associated with the evolutionary transition from prebiotic peptides to early proteins [3-5].

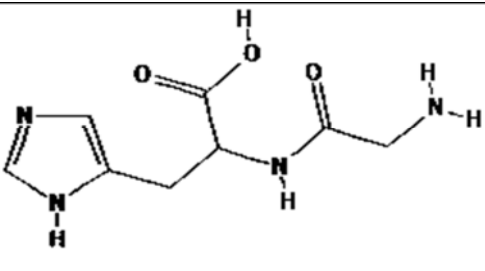
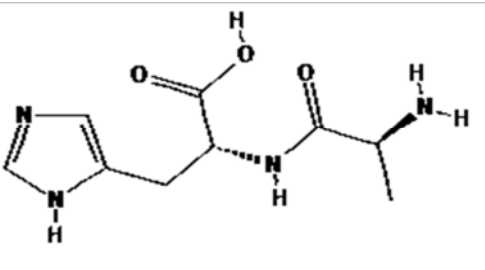
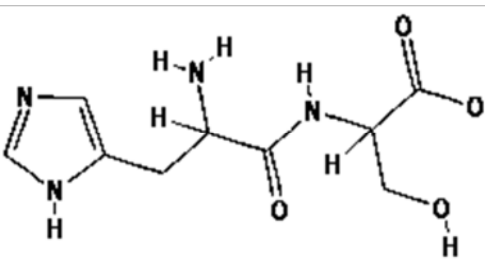
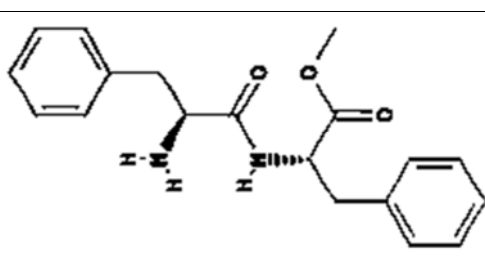
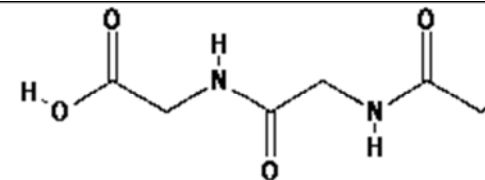
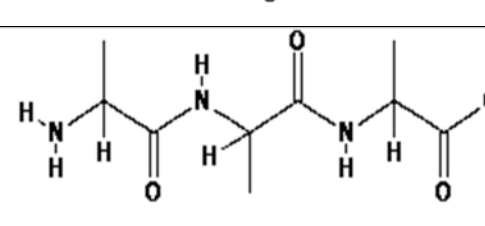
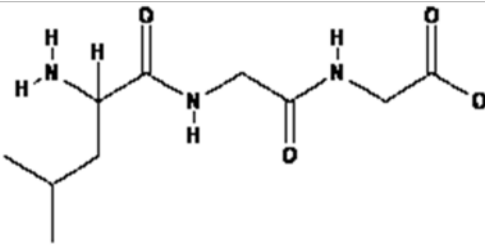
According to the abiogenesis theories, these simple non-living organic precursors were built together to form more complex organic structures necessary to life systems such as proteins commencing the establishment of simple life forms through the production of the necessary structures such as cell membranes. The early peptides are believed to be simple, short (3-8 amino acids) and made of Gly, Ala, Val, Leu, Isoleu, Pro, Ser, Asp and Glu [3] and are those which were either found in meteorites [6-7] or could be synthesized under prebiotic conditions (basic to neutral buffered conditions) [8-13]. These early peptides correspond to the active sites in the host proteins and are expected to perform important catalytic function in early life.

Formation of peptide bonds between amino acids at the air water interface has also been reported in efforts to provide an insight into the emergence of peptides on early earth. According to this aforementioned study, a proper orientation of amino acids and formation of small peptides is influenced by the air-water interface under early earth conditions [14]. In a totally different area, these peptides have a putative application as transporters and targets in drug delivery and development because of simple structure and cost effectiveness [15-16].

Study of interactions between these short peptides and phospholipids is essential to develop an understanding about the accumulation of these species in the lipid matrix to form biomembranes. The experiments were carried out to investigate any interactions between these simple peptides and the phospholipid monolayer on Hg used as membrane model. Electrochemical methods were used to study the interactions between various di- and tri-peptides with dioleoyl phosphatidylcholine (DOPC) monolayer assembled on Hg surface. Capacitance-potential and impedance measurements were recorded for the DOPC monolayer on the mercury film electrode (MFE) in the presence of peptides under the influence of applied electric field. All the changes to the lipid phase transitions appear as a shift and/or suppression in the capacitance peaks and/or increase in the monolayer capacitance in the constant capacitance region on the C_{sp} -E plots. A perfect DOPC monolayer deposited on Hg surface is completely impermeable to ions at the PZC of Hg. This monolayer acts as an ideal capacitor and in impedance measurements gives rise to an almost perfect RC semicircle in the complex capacitance plane plots with no low frequency element. In impedance measurements of electrode supported lipid layers projected onto the complex capacitance plane, any interaction of membrane active compounds with the DOPC monolayer on Hg appears as an additional low frequency capacitive element and/or as a depression of the RC semicircle and/or changes in ZFC. A low frequency capacitive 'tail' is indicative of adsorption of membrane active specie on the monolayer from the electrolyte solution, whereas, changes in the ZFC correspond to the change in the monolayer thickness and/or the relative permittivity of the dielectric. A table of all the peptides studied and their physical properties is given below:

Table 4.1: Di- and tri-peptides and their chemical structure and physical properties.

No.	Peptide	Chemical structure	Physical properties
1	Gly-Gly		Apolar Neutral
2	Gly-Ala		Apolar Neutral
3	Ala-Gly		Apolar Neutral
4	Ala-Ala		Apolar Neutral
5	Glu-Glu		Polar Negatively Charged
6	Ser-Ser		Polar Neutral

7	Gly-His		Polar Positively Charged
8	Ala-His		Polar Positively Charged
9	His-Ser		Polar Positively Charged
10	Phe-Phe- OMe.HCl		Apolar
11	Gly-Gly-Gly		Apolar Neutral
12	Ala-Ala-Ala		Apolar Neutral
13	Leu-Gly-Gly		Apolar Neutral

4.2 Results and discussion

4.2.1 Aliphatic, apolar and neutral dipeptides

The interactions of peptides with the phospholipid monolayer cause changes to the structure of the lipid monolayer modifying the phase transitions underlying the capacitance peaks in the capacitance-potential curve of the phospholipid monolayer. The effects of interactions between DOPC coated Hg and non-polar amphiphilic dipeptides in the C_{sp} -E plot are presented in Figure 4.1 (a). ACV scans of DOPC coated Hg in the presence of aliphatic, apolar and neutral dipeptides showed that capacitance peak-1 on capacitance-potential curve is suppressed which corresponds to the adsorption of dipeptides on the surface of DOPC monolayer from electrolyte solution. This order is as follows from the weakest interaction to the strongest: Gly-Gly < Gly-Ala < Ala-Gly < Ala-Ala.

Figure 4.1 (b) represents the impedance data expressed in the complex capacitance plane of Hg supported DOPC monolayer in the presence of Gly-Gly, Gly-Ala, Ala-Gly and Ala-Ala in the electrolyte solution and shows the appearance of an extra low frequency capacitive element ('tail') in addition to RC semicircle related to an adsorption of these species on the surface of the monolayer.

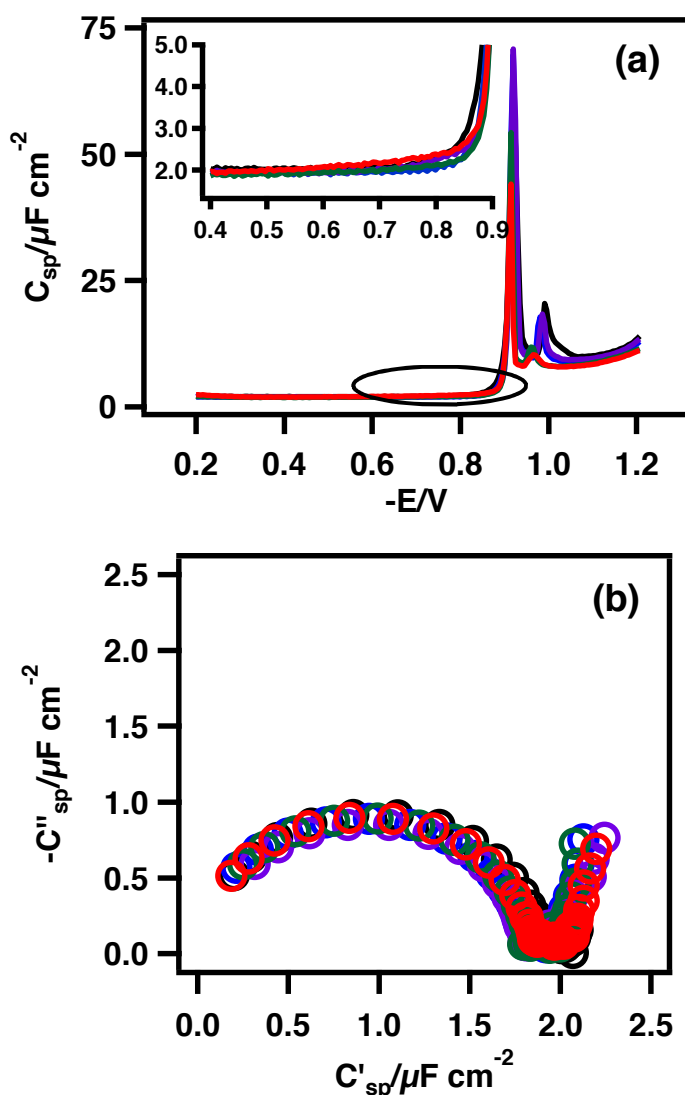


Figure 4.1: (a) Capacitance versus potential plots and (b) Impedance data transformed to complex capacitance plane of DOPC coated wafer based Pt/Hg electrode in 0.1 mol dm^{-3} KCl with $0.001 \text{ mol dm}^{-3}$ phosphate buffer (black) containing 10 mmol dm^{-3} of the Gly-Gly (blue), Gly-Ala (purple), Ala-Gly (green) and Ala-Ala (red) acquired using ACV at 5 mVs^{-1} , 75 Hertz, $\Delta V = 5 \text{ mV}$ and EIS at -0.4 V respectively.

4.2.2 Aliphatic, polar, hydrophilic and charged dipeptide

Figure 4.2 (a) displays the effect of a negatively charged polar dipeptide of glutamic acid (Glu-Glu) on the capacitance-voltage curves of Hg supported DOPC monolayer obtained using ACV. It can be seen from this figure that the capacitance of DOPC monolayer increases in the potential window approaching the base of capacitance peak-1. Increase in monolayer capacitance in this potential region can be explained

by considering the penetration of Glu-Glu into the apolar part of the monolayer. The impedance data expressed in the complex capacitance plane of Hg supported DOPC monolayer in the presence of 10 mmol dm^{-3} Glu-Glu in the electrolyte solution is shown in Figure 4.2 (b). Presence of a capacitive 'tail' at low frequencies indicates the adsorption of Glu-Glu on the surface of monolayer. Glu-Glu also increased the zero frequency capacitance (ZFC) from $1.78 \mu\text{F cm}^{-2}$ to $1.82 \mu\text{F cm}^{-2}$ at -0.4 V (PZC of Hg). An increased value of ZFC represent a decrease in the monolayer thickness and/or increase in the relative permittivity of the dielectric because of penetration of Glu-Glu into monolayer interior.

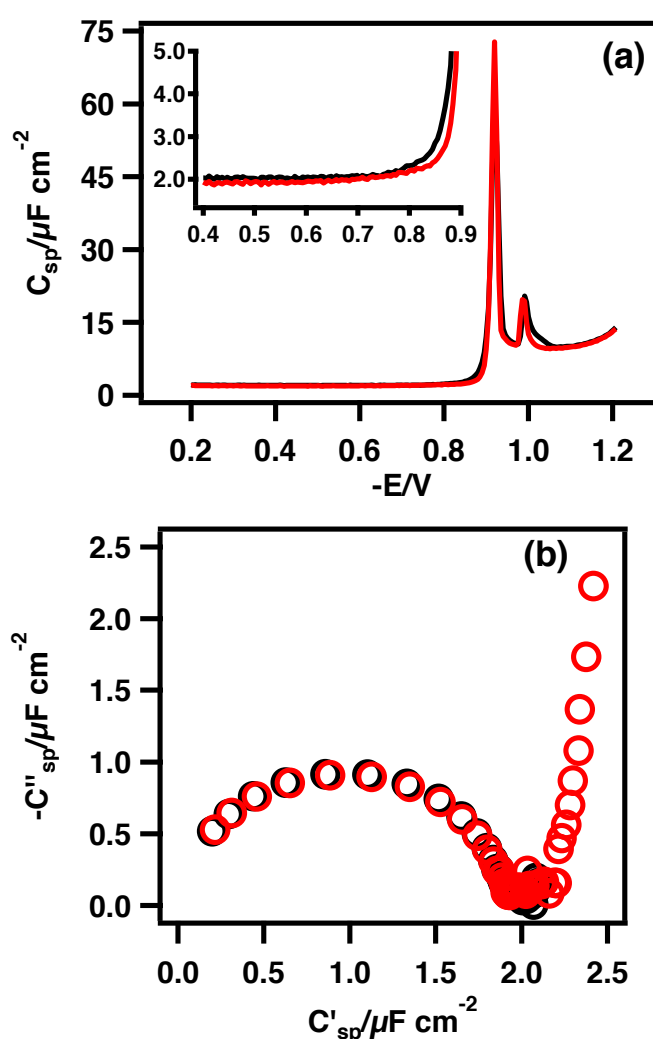


Figure 4.2: (a) Capacitance versus potential plots and (b) Impedance data transformed to complex capacitance plane of DOPC coated wafer based Pt/Hg electrode in 0.1 mol dm^{-3} KCl with $0.001 \text{ mol dm}^{-3}$ phosphate buffer (black) containing 10 mmol dm^{-3} of the Glu-Glu (red) acquired using ACV at 5 mVs^{-1} , 75 Hertz, $\Delta V = 5 \text{ mV}$ and EIS at -0.4 V respectively.

4.2.3 Aliphatic, polar, hydrophilic and neutral dipeptide

Figure 4.3 (a) show the effect of polar, hydrophilic and neutral Ser-Ser on the C_{sp} -E profile of DOPC coated Hg electrode using ACV. It is clear from Figure 4.3 (a) that both phase transitions underlying the capacitance peaks shown by DOPC monolayer are not affected by the presence of Ser-Ser in the electrolyte solution neither is there a clear influence on the monolayer capacitance. The impedance data expressed in the complex capacitance plane of Hg supported DOPC monolayer in the presence of 0.2 mmol dm^{-3} of Ser-Ser in the electrolyte solution is shown in Figure 4.3 (b). This showed a slight decrease in the ZFC of the DOPC monolayer in addition to a small extra capacitive 'tail'. Decrease in the ZFC (Figure 4.3 (b)) indicates a marginal increase in the monolayer thickness (Figure 4.3 (a)).

4.2.4 Aromatic, polar, hydrophilic and charged dipeptide

Figure 4.4 (a), (b) and (c) shows the effect of histidine containing dipeptides (Gly-His, Ala-His and His-Ser) on the capacitance peaks representing the phase transitions exhibited by DOPC monolayer supported on Hg electrode in the electrolyte solution. Figure 4.4 (d), (e) and (f) show a small shift of capacitance peak-1 towards higher potential in the presence of higher concentration of these dipeptides. It has been reported that a stronger electric field developed across the lipid surface is responsible for the shift in applied potential of capacitance peak-1 to more positive potential [17]. Dipeptides containing a positively charged histidine amino acid showed an significant binding to the DOPC monolayer at higher concentration due to electrostatic interactions between positively charged dipeptides and polar lipid head groups. This contributes to steepen the electric field across the lipid-water interface at the lipid coated Hg electrode and a small shift of capacitance peak-1 to less negative potential.

It can be seen from Figure 4.5 (a), (b) and (c) that in the presence of all three histidine containing dipeptides, the capacitance peak-1 is noticeably suppressed. Capacitive peak suppression with no essential change in monolayer capacitance relates directly to the adsorption and interaction of membrane active compounds on the surface of monolayer.

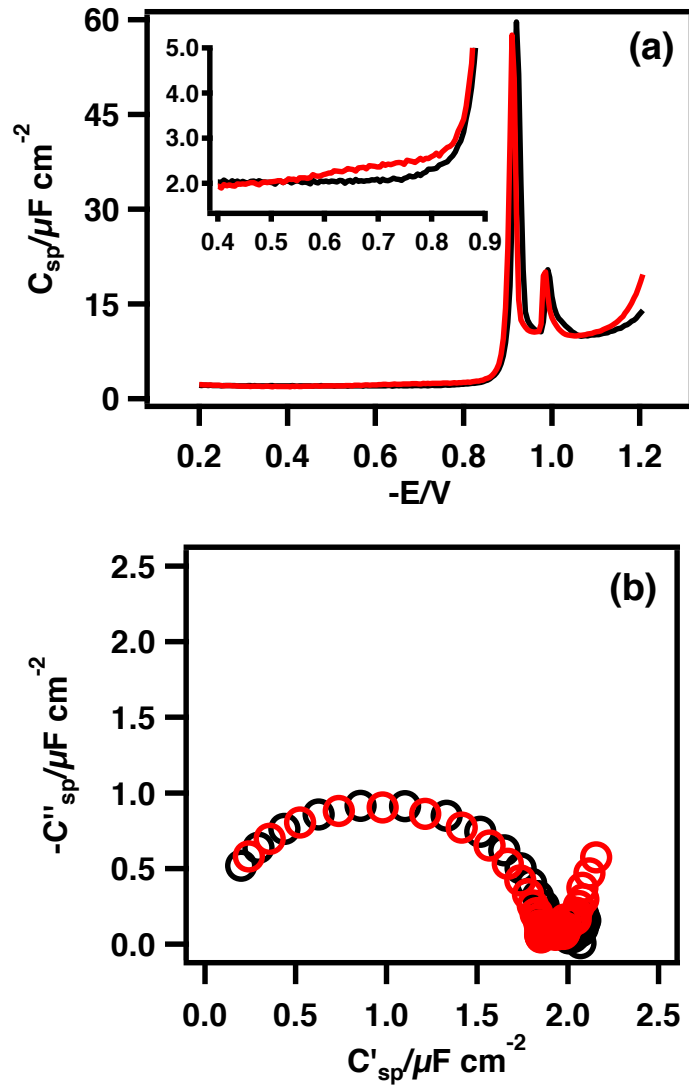


Figure 4.3: (a) Capacitance versus potential plots and (b) Impedance data transformed to complex capacitance plane of DOPC coated wafer based Pt/Hg electrode in 0.1 mol dm^{-3} KCl with $0.001 \text{ mol dm}^{-3}$ phosphate buffer (black) containing 0.2 mmol dm^{-3} of the Ser-Ser (red) acquired using ACV at 5 mVs^{-1} , 75 Hertz, $\Delta V = 5 \text{ mV}$ and EIS at -0.4 V respectively.

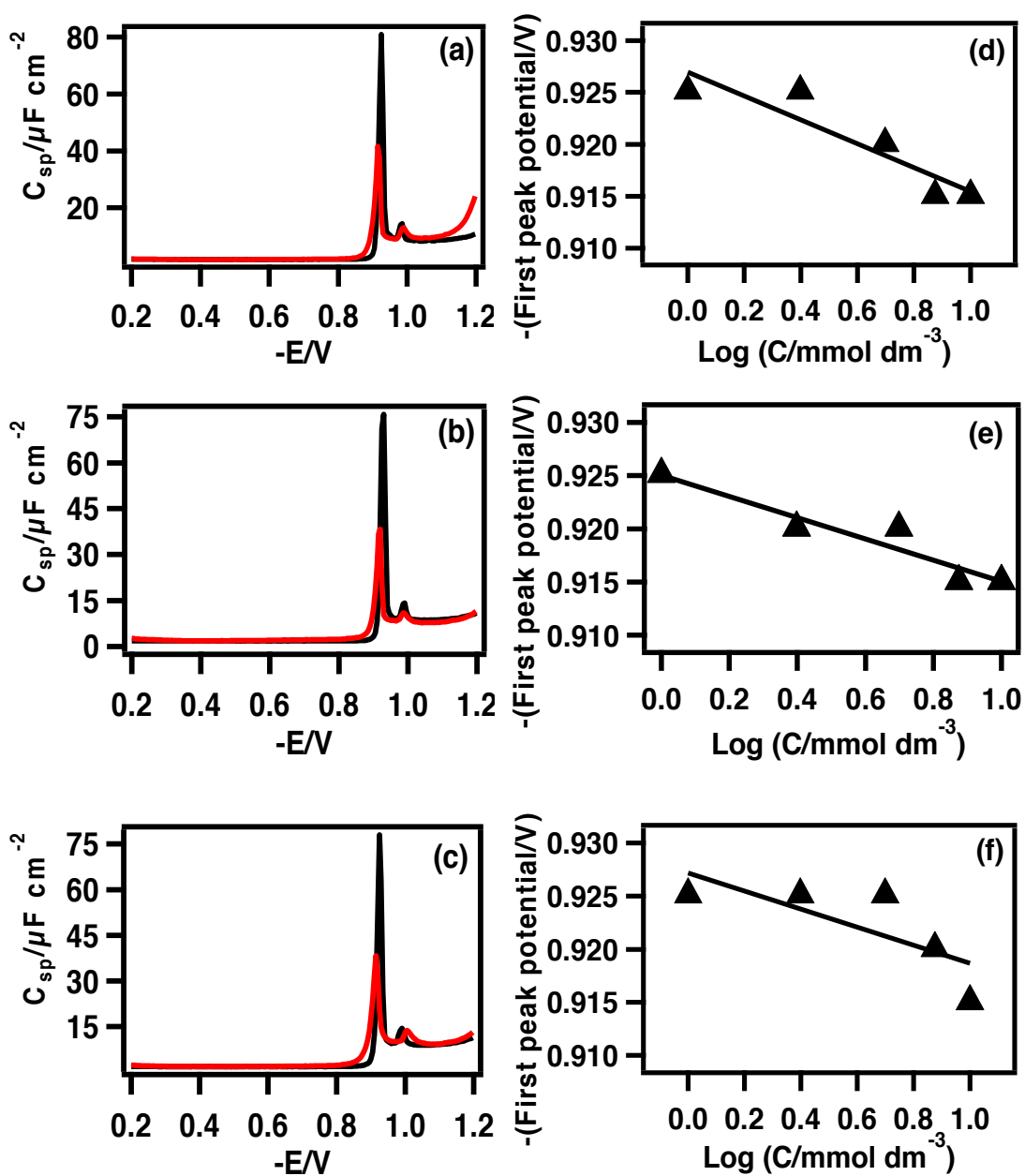


Figure 4.4: Capacitance versus potential plots of DOPC coated wafer based Pt/Hg electrode in 0.1 mol dm^{-3} KCl with $0.001 \text{ mol dm}^{-3}$ phosphate buffer containing 10 mmol dm^{-3} of the following dipeptides: (a) Gly-His, (b) Ala-His, (c) His-Ser (red) and DOPC without dipeptide (black). First peak potential versus concentration plots of (d) Gly-His, (e) Ala-His and (f) His-Ser (filled triangle) and lines representing the fits to the plots.

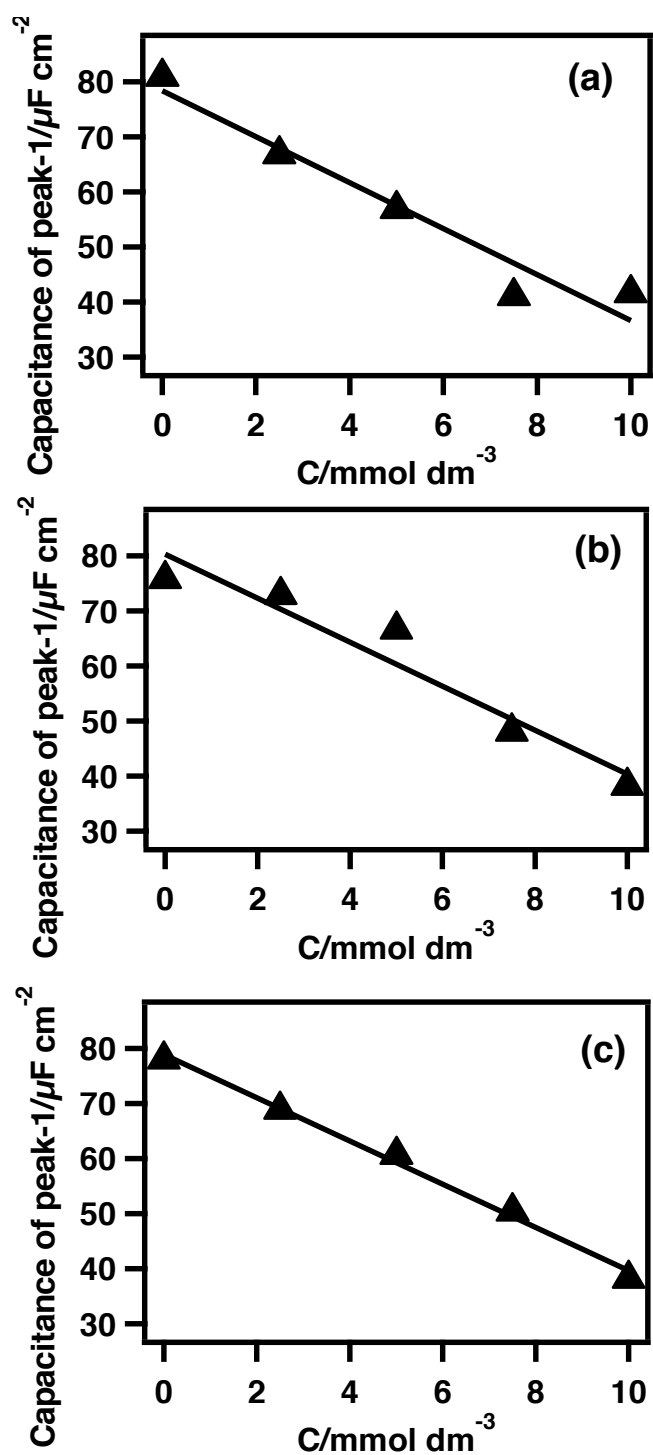


Figure 4.5: Capacitance of peak-1 versus concentration plots of DOPC coated wafer based Pt/Hg electrode in 0.1 mol dm^{-3} KCl with $0.001 \text{ mol dm}^{-3}$ phosphate buffer containing 10 mmol dm^{-3} of the following dipeptides: (a) Gly-His, (b) Ala-His, (c) His-Ser (red).

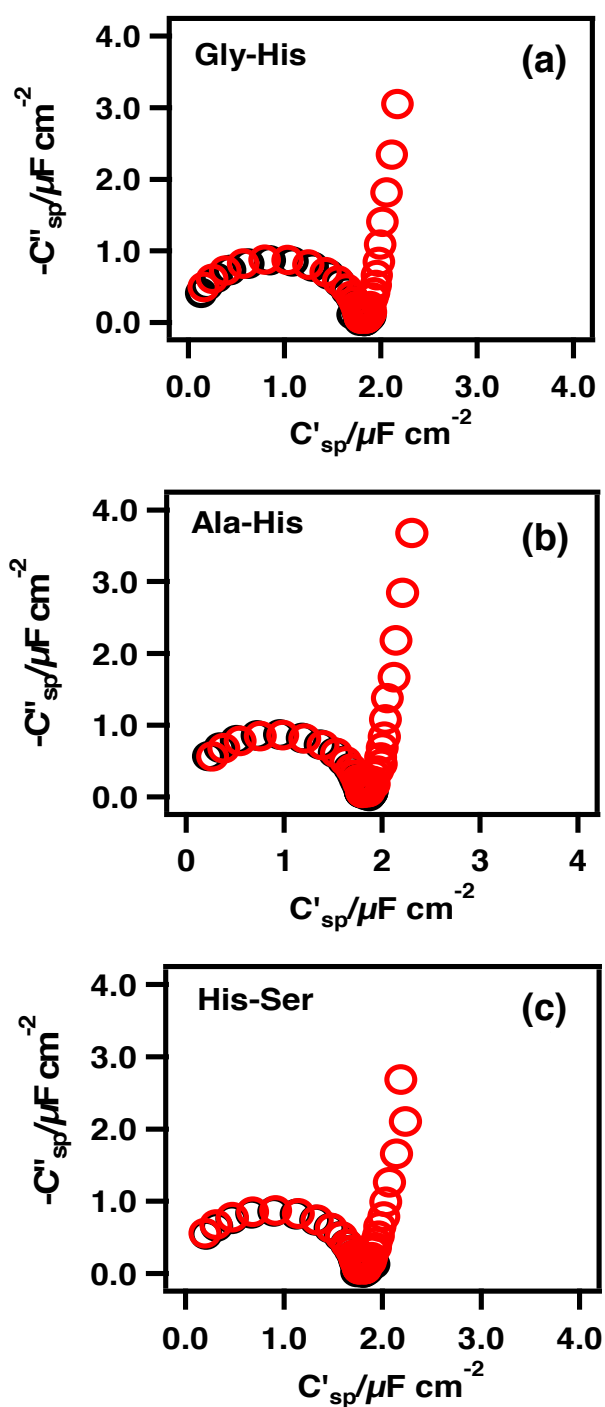


Figure 4.6: Impedance data transformed to complex capacitance plane of DOPC coated wafer based Pt/Hg electrode in 0.1 mol dm^{-3} KCl with $0.001 \text{ mol dm}^{-3}$ phosphate buffer containing 10 mmol dm^{-3} of the following dipeptides: (a) Gly-His, (b) Ala-His, (c) His-Ser (red) and DOPC without dipeptide (black), acquired using EIS at -0.4 V .

Figure 4.6 displays the effect of the histidine containing dipeptides on the DOPC monolayer using the impedance data expressed in the complex capacitance plane. It is clear from Figure 4.6 (a), (b) and (c) that interaction of DOPC with the three dipeptides resulted in the addition of a low frequency capacitive 'tail' in addition to the RC element. This capacitive 'tail' is more significant compared to that resulting from the adsorption of the other dipeptides on the DOPC monolayer. This indicates that these positively charged dipeptides adsorb on the surface of DOPC monolayer from the electrolyte solution compared to the other neutral dipeptides (Figure 4.1 and 4.3).

Figure 4.7 (a), (b) and (c) present the ZFC derived from the complex capacitance plots versus concentration plots of Gly-His, Ala-His and His-Ser respectively. It is found that ZFC of the DOPC monolayer decreases with an increase in concentration of these dipeptides up to a certain critical concentration and started to increase subsequently. Decrease in ZFC at low concentration represents the increase in thickness of DOPC monolayer and is attributed to the adsorption followed by incorporation of the dipeptides into and in between the polar lipid head making it more stable and thick. This results in the formation of defect/pore free monolayer. At higher concentration, saturation leads to the penetration of dipeptides deeper into the monolayer and the consequential thinning of monolayer and/or increase in ϵ_r of DOPC due to penetration of peptides as shown by an increase in ZFC. This also correlates to the shift of capacitance peak-1 to less negative potential at higher peptide concentration.

Among these histidine containing dipeptides, peptides containing apolar alanine start to penetrate deep into the hydrocarbon region of the monolayer at low solution concentration compared to the dipeptide containing glycine because of enhanced apolar-apolar interactions between the acyl chain of DOPC molecules and dipeptide (Figure 4.7 (b)). The terminal carboxyl group is more acidic in His-Ser because of Serine side chain. The penetration of His-Ser into the monolayer is less significant at 10 mmol dm^{-3} compared to both Ala-His and Gly-His due to the association of the negatively charged $-\text{COO}^-$ of serine with lipid head group (Figure 4.7 (c)).

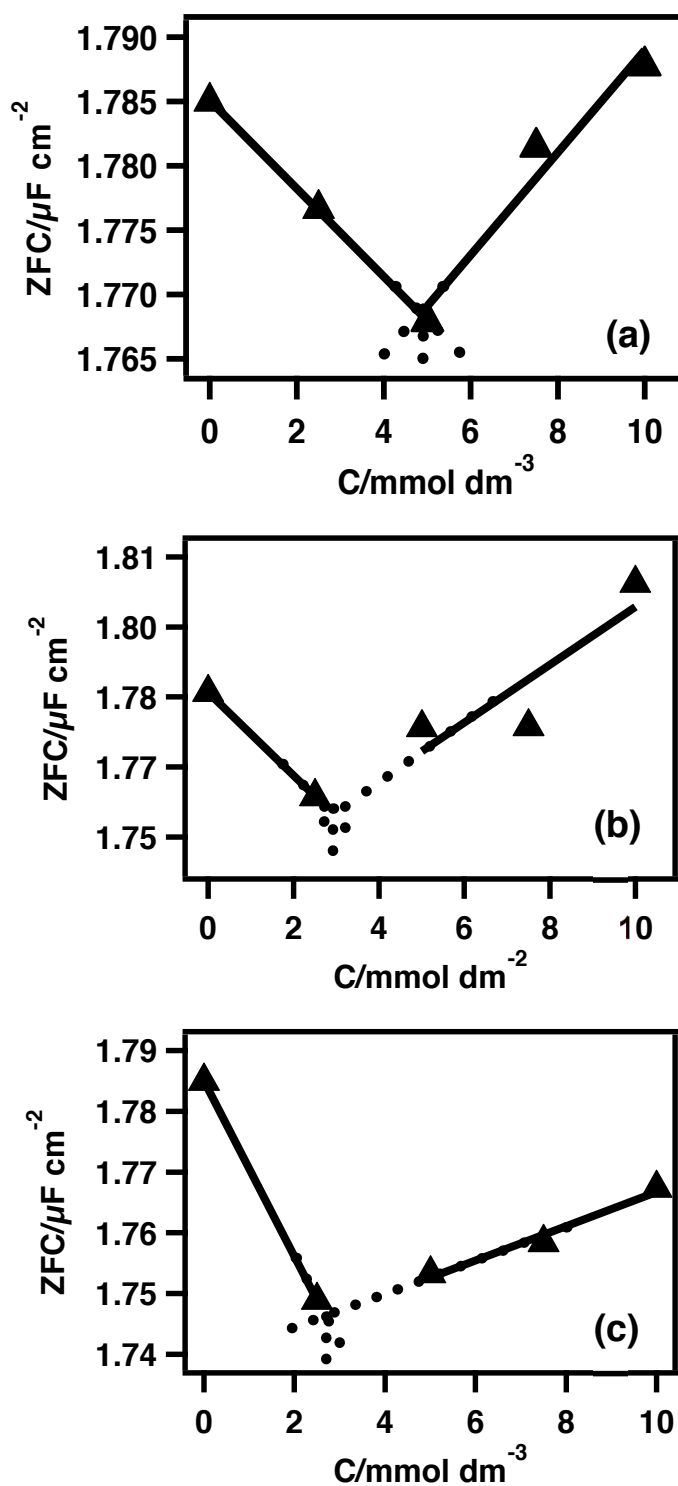


Figure 4.7: ZFC versus concentration plot of DOPC coated wafer based Pt/Hg electrode in 0.1 mol dm^{-3} KCl with $0.001 \text{ mol dm}^{-3}$ phosphate buffer containing 10 mmol dm^{-3} of the following dipeptides: (a) Gly-His, (b) Ala-His, (c) His-Ser, lines representing the linear fits to the plots, acquired using EIS at -0.4 V .

4.2.5 Aromatic, apolar and charged dipeptide

Figure 4.8 (a) shows the effect of highly apolar and aromatic dipeptide of phenylalanine (Phe-Phe OMe HCl with an approximate pKa 3.5 [18]) on monolayer capacitance and capacitance peaks exhibited by capacitance-potential plots of the DOPC monolayer. It can be seen that Phe-Phe OMe HCl has a profound effect on both the capacitance peaks due to the association of Phe-Phe OMe HCl with the DOPC monolayer. Phe-Phe OMe HCl suppressed both the capacitance peaks.

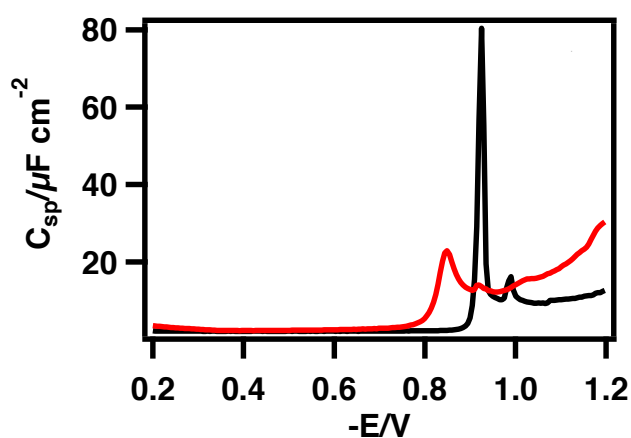


Figure 4.8: Capacitance versus potential plots of DOPC coated wafer based Pt/Hg electrode in 0.1 mol dm^{-3} KCl with $0.001 \text{ mol dm}^{-3}$ phosphate buffer containing 0.5 mmol dm^{-3} of the Phe-Phe OMe HCl dipeptide (red) and DOPC without dipeptide (black).

The impedance data expressed in the complex capacitance plane of Hg supported DOPC monolayer in the presence of 0.5 mmol dm^{-3} Phe-Phe OMe HCl is shown in Figure 4.9 (a). A significant 'tail' at low frequencies showed the association of Phe-Phe OMe HCl on the DOPC monolayer from the electrolyte solution. The effect of increasing concentrations of Phe-Phe OMe HCl on the ZFC is presented in Figure 4.9 (b). It is clear that the ZFC increases linearly with an increase in solution concentration of Phe-Phe OMe HCl. This suggests that Phe-Phe OMe HCl either decreases the thickness of the monolayer or most likely increases the relative permittivity of the apolar region of DOPC membrane having an overall destabilization effect on the layer.

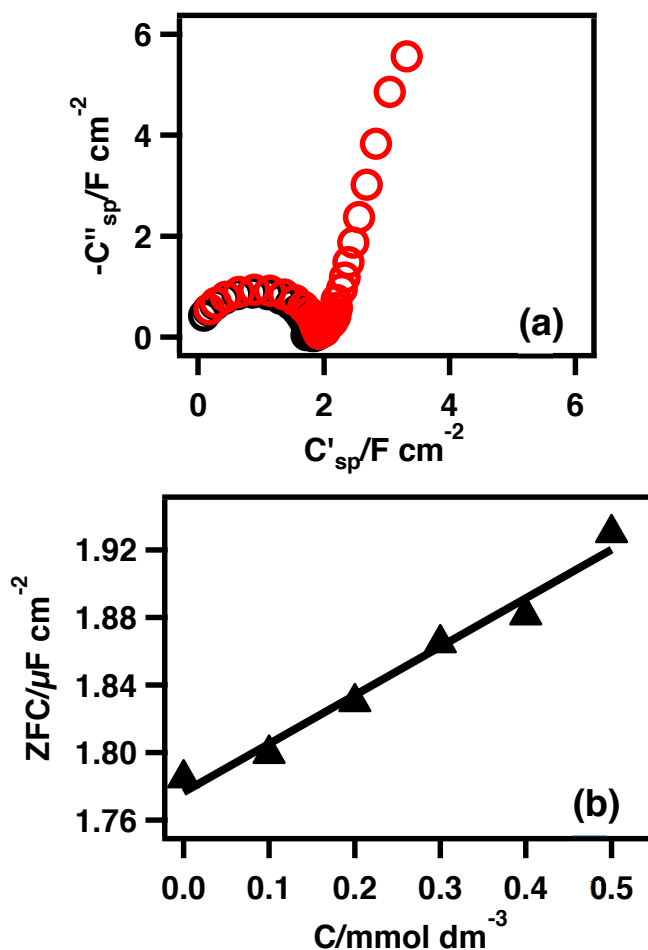


Figure 4.9: Impedance data transformed to complex capacitance plane of DOPC coated wafer based Pt/Hg electrode in 0.1 mol dm^{-3} KCl with 0.001 mol dm^{-3} phosphate buffer containing 0.5 mmol dm^{-3} of Phe-Phe OMe HCl (red) and DOPC without it (black) (a), and ZFC versus concentration plot of Phe-Phe OMe HCl (b), acquired using EIS at -0.4 V .

4.2.6 Effect of chain length

The impedance data expressed in the complex capacitance plane of Hg supported DOPC monolayer in the presence of 10 mmol dm^{-3} of homologous di- and tri-peptides of glycine and alanine in the electrolyte solution is shown in Figure 4.10. Both the di- and tri-glycine exhibited similar interactions with DOPC monolayer effected by the length of the side chain. In case of the alanine peptides in contrast to the glycine peptides, there is a significant increase in the low frequency 'tail' from di- to tri-alanine indicating an increase in the adsorption of these peptide on DOPC

monolayer. Since alanine is less polar than glycine, this apolarity is enhanced in the tri-peptide and increases its adsorption on to the DOPC monolayer.

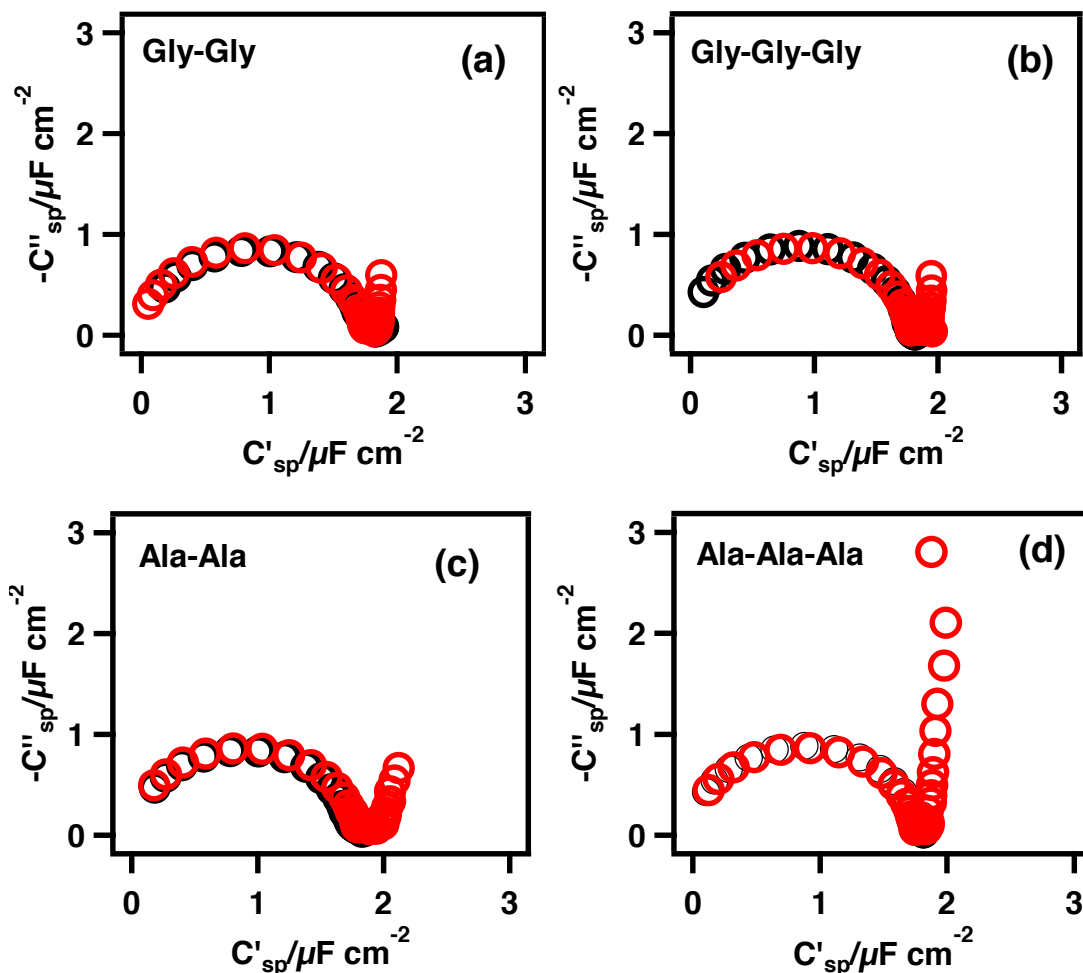


Figure 4.10: Impedance data transformed to complex capacitance plane of DOPC coated wafer based Pt/Hg electrode in 0.1 mol dm^{-3} KCl with $0.001 \text{ mol dm}^{-3}$ phosphate buffer containing 10 mmol dm^{-3} of Gly-Gly (a), Gly-Gly-Gly (b), Ala-Ala (c) and Ala-Ala-Ala (d) acquired using EIS at -0.4 V .

Figure 4.11 represents the effect of change in concentration of the homologous di- and tri-peptides of glycine and alanine on the ZFC of the monolayer. It can be seen that the monolayer capacitance decreases with an increase in concentration of both di- and tri-glycine up to a certain concentration and then increases afterwards.

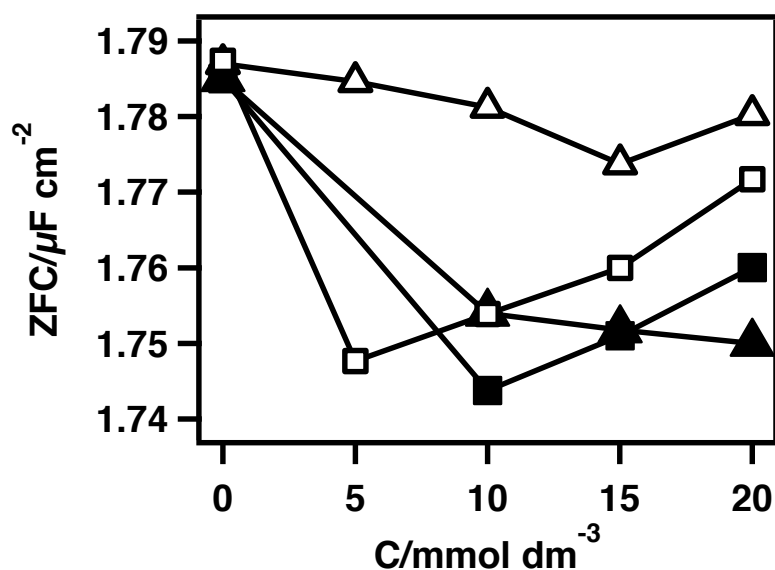


Figure 4.11: ZFC versus concentration plot of DOPC coated wafer based Pt/Hg electrode in 0.1 mol dm^{-3} KCl with $0.001 \text{ mol dm}^{-3}$ phosphate buffer containing Gly-Gly (closed triangle), Gly-Gly-Gly (open triangle) (b), Ala-Ala (closed square) (c) and Ala-Ala-Ala (d) acquired using EIS at -0.4 V (open square).

Decrease in monolayer capacitance at low solution concentrations suggested that glycine di- and tri-peptide incorporated into the spaces/gaps present in the lipid head groups resulting in the formation of a comparatively thick monolayer. This indeed have a stabilizing effect on the monolayer. But after reaching a certain concentration, these peptides started to penetrate into the hydrocarbon region of the phospholipid resulting in an increase in the monolayer capacitance from a contribution of the higher relative permittivity of the peptide (~ 20) [19-20] to the average dielectric permittivity.

Figure 4.12 illustrates the effect of a Leu-Gly-Gly on the DOPC coated Hg electrode under the influence of a potential scan from -0.2 to -1.2 V . It can be observed that both the constant capacitance region (-0.2 to -0.92 V) and capacitance peaks exhibited by DOPC monolayer remained unaffected by the presence of Leu-Gly-Gly. This shows that in spite of the peptide having a Leu amino acid with a relatively highly apolar side chain i.e. $-\text{CH}_2-\text{CH}(\text{CH}_3)_2$, no significant apolar-apolar interactions are observed between Leu-Gly-Gly and DOPC monolayer in the form of

any noticeable change/suppressions in C_{sp} -E profile as shown in the inset of Figure 4.12.

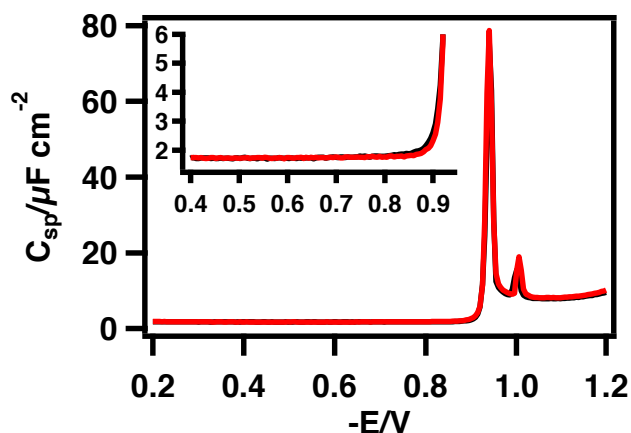


Figure 4.12: Capacitance versus potential plots of DOPC coated wafer based Pt/Hg electrode in 0.1 mol dm^{-3} KCl with $0.001 \text{ mol dm}^{-3}$ phosphate buffer containing 10 mmol dm^{-3} of Leu-Gly-Gly, acquired using ACV.

The impedance data expressed in the complex capacitance plane of Hg supported DOPC monolayer in the presence of 10 mmol dm^{-3} of Leu-Gly-Gly in the electrolyte solution is shown in Figure 4.13 (a). A capacitive element extra to the RC element at low frequencies is symbolic of strong adsorption of Leu-Gly-Gly at the monolayer surface from the electrolyte solution. The ZFC versus concentration plot of the DOPC coated Hg electrode in the presence of 10 mmol dm^{-3} of Leu-Gly-Gly is presented in Figure 4.13 (b). This shows that Leu-Gly-Gly continues to decrease the ZFC with an increase in its concentration due to enhanced monolayer thickness contributing towards the improved monolayer stability. This result indicates that it is only the apolar moiety of Leucine which penetrates the layer and facilitates an ordering of the layer and thickness increase.

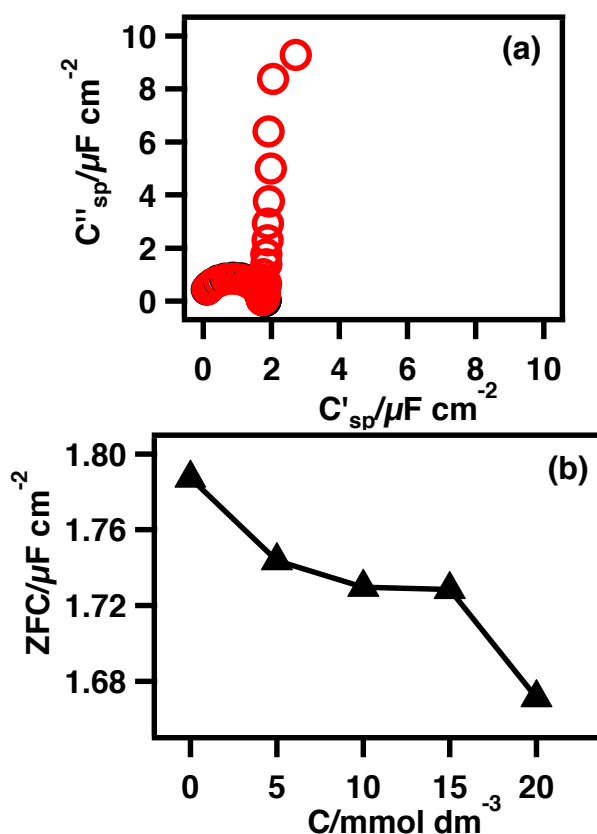


Figure 4.13: (a) Impedance data transformed to complex capacitance plane of DOPC coated wafer based Pt/Hg electrode in $0.1 mol dm^{-3}$ KCl with $0.001 mol dm^{-3}$ phosphate buffer containing $10 mmol dm^{-3}$ of Leu-Gly-Gly and (b) ZFC versus concentration plot of Leu-Gly-Gly, acquired using EIS at $-0.4 V$.

4.3 Conclusion

1. Small and short chain peptides are found to interact with the Hg supported DOPC monolayers depending on the interactive forces between the DOPC monolayer and the peptides:

(a) dispersion forces between the apolar side chain of peptide monomers and apolar DOPC acyl chains are responsible for the interactions between DOPC monolayer and for both the neutral and charged apolar dipeptides increasing the overall dielectric due to penetration of these peptides into the monolayer resulting in an increase in monolayer capacitance and/or decrease in the monolayer thickness.

(b) Electrostatic forces between the polar head groups of lipid molecules and charged groups in the side chain of peptide monomers are the key stimulus for

the interaction between DOPC monolayer and polar charged dipeptides such as dipeptide of negatively charged glutamic acid and dipeptides of positively charged histidine. The electrostatic interactions results in increased binding of the charged peptides with the lipid head groups increasing or decreasing the field strength required to instigate the phase transition underlying the capacitance peak-1 for negatively and positively charged peptides respectively. The extent of interaction is further determined by the apolarity of the peptides.

2. All the di- and tri-peptides mainly based on glycine such as Gly-Gly, Gly-Gly-Gly and Leu-Gly-Gly have a stabilizing effect on the monolayer.

3. An increase in chain length of the peptide containing apolar side chain results in an increase in the interactions between peptides and DOPC monolayer.

4. The glycine containing peptides are found to have a stabilization effect of the DOPC monolayer resulting from its incorporation into lipid head groups causing an increase in the monolayer thickness.

4.4 References

- [1] G.C. Barrett, D.T. Elmore, Amino acids and peptides, Cambridge University Press, 1998.
- [2] G.C. Barrett, J.S. Davies, Amino acids, peptides and proteins, Royal Society of Chemistry, 2002.
- [3] P. Van Der Gulik, S. Massar, D. Gilis, H. Buhrman, M. Rooman, Journal of theoretical biology, 261 (2009) 531-539.
- [4] M. Shimizu, Journal of biochemistry, 117 (1995) 23-26.
- [5] M. Shimizu, Journal of the Physical Society of Japan, 73 (2004) 323-326.
- [6] J.R. Cronin, Origins of life, 7 (1976) 337-342.
- [7] K. Kvenvolden, J. Lawless, K. Pering, E. Peterson, J. Flores, C. Ponnampereuma, I. Kaplan, C. Moore, (1970).
- [8] S.L. Miller, Science, 117 (1953) 528-529.
- [9] A.D. Keefe, S.L. Miller, G. McDonald, J. Bada, Proceedings of the National Academy of Sciences, 92 (1995) 11904-11906.

- [10] S.L. Miller, The atmosphere of the primitive earth and the prebiotic synthesis of amino acids, in: *Cosmochemical Evolution and the Origins of Life*, Springer, 1974, pp. 139-151.
- [11] S. Miller, *Proc. Cold Spring Harbor Symposia on Quantitative Biology*, 1987.
- [12] H.J. Cleaves, J.H. Chalmers, A. Lazcano, S.L. Miller, J.L. Bada, *Origins of Life and Evolution of Biospheres*, 38 (2008) 105-115.
- [13] K. Plankensteiner, H. Reiner, B.M. Rode, *Molecular diversity*, 10 (2006) 3-7.
- [14] E.C. Griffith, V. Vaida, *Proceedings of the National Academy of Sciences*, 109 (2012) 15697-15701.
- [15] I. Rubio-Aliaga, H. Daniel, *Trends in pharmacological sciences*, 23 (2002) 434-440.
- [16] G.L. Amidon, H. Lee, *Annual review of pharmacology and toxicology*, 34 (1994) 321-341.
- [17] A. Rashid, A. Vakurov, A. Nelson, *Electrochimica Acta*, (2014).
- [18] C. Tang, A.M. Smith, R.F. Collins, R.V. Ulijn, A. Saiani, *Langmuir*, 25 (2009) 9447-9453.
- [19] J. Wyman Jr, T. McMeekin, *Journal of the American Chemical Society*, 55 (1933) 908-914.
- [20] H. Nakamura, T. Sakamoto, A. Wada, *Protein engineering*, 2 (1988) 177-183.

Chapter-5

Interaction of biphenyl and derivatives with biomimetic lipid membranes

5.1 Introduction

Biphenyl and its derivatives are well known for their thermal stability, electrical insulation and resistance to redox processes and have been widely used in the past in transformers and capacitors as dielectric fluids [1-2]. Moreover, these substance have also been employed in the preparation of pesticides, optical brighteners [3], and as fungicides in waxing many fruits. However biphenyl and its derivatives are established environmental toxins [4]. Chlorobiphenyls (Cl-BPs) have posed a big issue for their toxicity, bioaccumulation and environmental persistence because of their stability [5]. Biphenyl and Cl-BPs metabolise to hydroxy biphenyls (OH-BPs) via formation of the arene oxide intermediate [6] with *para* (*p*)-hydroxybiphenyl (*p*-OH-BP) as a major product [5,7-8]. In addition to the monohydroxy metabolites, dihydroxy products can also be produced as a result of hydroxylation of biphenyl. The hydroxy metabolites of Cl-BPs have been shown to be retained in the blood of many animals and humans [9-12]. The structures of these metabolites resemble thyroid hormones in possessing two aromatic rings and are reported as endocrine disrupters because they compete with thyroxin for its active site [13-14]. In *ortho* (*o*) substituted biphenyls, the two phenyl rings have been reported to exhibit a twisted conformation with an increase in the torsional angle between the phenyl rings from

42.5° to 63.2° depending on the size of the substituent (Br>Cl>F). This can be explained by the destabilization effect based on the hydrogen substituent repulsion in the *o*- position. Another substitution at the other *o*- position on the same ring further increases the torsional angle close to 90° orienting the two rings perpendicular to each other [15]. Disubstituted biphenyls with both the substitutions at the *meta* (*m*) position have torsional angle close to biphenyl [15] because of less steric crowding [16]. Changes in the molecular structure caused by substitution at the *p*- position does not affect the structure of biphenyl derivatives compared to the biphenyl in both ground and excited states [17]. The average torsional angle for non *o*- substituted biphenyl derivatives is 44° and is influenced very little by *m*- or *p*- substitution. The *m*- substitution gives a slightly higher barrier height between 0°-90° than *p*- substitution responsible for slightly higher torsional angles for *m*-substitutions [18]. Hence coplanarity of the two phenyl rings decreases in the following order depending on the position of substitution: Biphenyl \approx *p*-substituted biphenyl > *m*-substituted biphenyl > *o*-substituted biphenyl.

There are many studies on the potential toxicity of these hazardous substances *in vivo* [2,19-20] but very little work had been carried out on the evaluation of the molecular characteristics responsible for their toxicity and the mechanism of their interaction at a cellular and plasma membrane level. According to some studies, non-planar *o*-substituted biphenyls increased the cell membrane leakiness and decreased the membrane integrity compared to the planar biphenyls [19-21]. While other studies have shown the non-planar *o*-substituted molecules to be less active compared to the planar *p*-substituted molecules because of the steric hindrance of the *o*-substituted species which influences their penetration into the phospholipid membrane [22-24].

In the present studies, free standing bilayers (vesicles) and Hg supported phospholipid monolayers have been used to investigate:- (1) structure-activity relationships and (2) mechanism of interaction of biphenyl and biphenyl derivatives with phospholipid membranes using fluorescence spectroscopy and electrochemical techniques respectively. Monolayers of phospholipids on Hg surface act as a sensing-element for compounds containing two or more aromatic rings and other related compounds [24-25]. The rationale for using these two techniques was to

obtain a generic understanding of the interaction mechanism as well as looking at consistencies between the use of the bilayer and monolayer model. Phospholipid vesicles have been used extensively as a biological membrane mimic [26] to study the interactions of membrane active compounds [27-28] with membranes. The biphenyls have fluorescent properties which allow the use of fluorescence spectroscopy to estimate their fractions that have not penetrated into the phospholipid vesicles and are available for quenching by a quencher (I) [29-31]. Monolayers of phospholipids on the Hg surface act as a sensing-element for compounds containing two or more aromatic rings and other related compounds [24-25]. Table 5.1 summarises the biphenyl derivatives used in this study and their physical properties. A table of all the biphenyl derivatives studied is given below:

Table 5.1: Biphenyl and derivatives and their abbreviation.

	Compound	Abbreviation
1	Biphenyl	BP
2	<i>o</i> -Hydroxybiphenyl	<i>o</i> -OH-BP
3	<i>m</i> -Hydroxybiphenyl	<i>m</i> -OH-BP
4	<i>p</i> -Hydroxybiphenyl	<i>p</i> -OH-BP
5	<i>o</i> -Chlorobiphenyl	<i>o</i> -Cl-BP
6	<i>m</i> -Chlorobiphenyl	<i>m</i> -Cl-BP
7	<i>p</i> -Chlorobiphenyl	<i>p</i> -Cl-BP
8	<i>p</i> -Cyanobiphenyl	<i>p</i> -CN-BP
9	<i>p</i> -Sulfonicacidbiphenyl	<i>p</i> -HSO ₃ -BP
10	<i>p</i> -Methoxybiphenyl	<i>p</i> -OCH ₃ -BP
11	<i>p</i> -Methylbiphenyl	<i>p</i> -CH ₃ -BP

5.2 Results and discussion

Figure 5.1 displays the Stern Volmer plots for the quenching of biphenyl by I in the presence DOPC GUVs containing different concentration of DOPC. It can be seen that the amount of accessible fraction of biphenyl which is available for quenching to I is highest using 0.127 mmol dm⁻³ DOPC GUVs and decreases in the following order: 0.127 mmol dm⁻³ (88.61 %) > 0.254 mmol dm⁻³ (66.73 %) > 0.381 mmol dm⁻³ (66.94 %) > 0.508 mmol dm⁻³ (57.5 %) > 0.636 mmol dm⁻³ (53 %) on subsequent

increase in the DOPC concentration. Increase in concentration of DOPC increases the number of vesicles and hence the gaps/binding sites in the vesicles for the fluorophore to incorporate/penetrate in becoming less available for quenching to Γ^- . DOPC vesicles tend to disperse the incident light beam but the effect is negligible in solutions containing small number of vesicles. In solutions containing large number of DOPC vesicles, the contribution of vesicles to the intensity of re-emitted light becomes significant resulting in a decrease in precision and increase in standard deviation. Hence GUVs containing $0.254 \text{ mmol dm}^{-3}$ DOPC were used in the further study of interaction of biphenyl derivatives with DOPC bilayers.

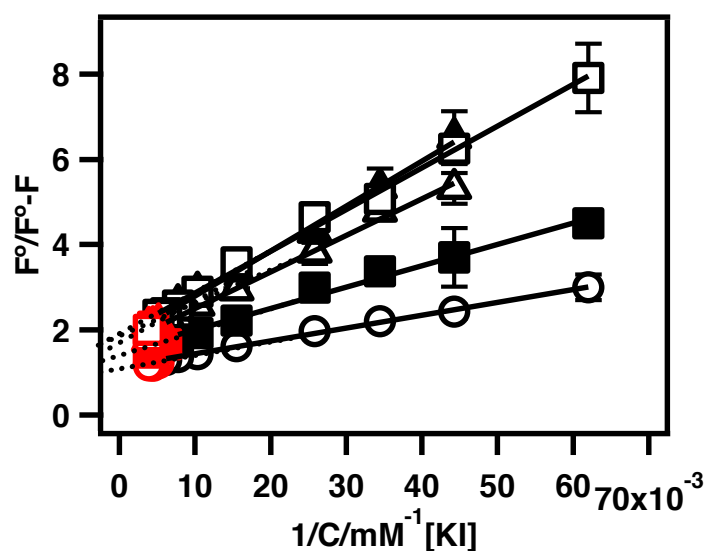


Figure 5.1: Modified Stern Volmer plots for iodide quenching of $1.0 \text{ } \mu\text{mol dm}^{-3}$ of biphenyl in the presence of 0.127 (open circle), 0.254 (close square), 0.381 (open triangle), 0.508 (close triangle) and $0.636 \text{ mmol dm}^{-3}$ (open square) DOPC GUV in 0.1 mol dm^{-3} of KCl containing $0.001 \text{ mol dm}^{-3}$ of phosphate buffer.

The slope of these plots gives a quenching constant (K) representing the quenching efficiency of the biphenyl derivatives by Γ^- and is not a significant parameter in terms of determining the structure activity relationship of biphenyls. At higher concentration of Γ^- , interactions between DOPC and Γ^- appeared as a discrete increase in the slope of the modified Stern-Volmer plots. This increase in slope is due to the Γ^- penetrating the apolar region of the monolayer and quenching

penetrated biphenyl. This data is therefore presented in red colour in above figure and not used to estimate the intercept values.

Figure 5.2 (black) shows the characteristic capacitance potential profile of a pure DOPC monolayer on mercury. At potentials around -0.4 V (\sim PZC of Hg), the Hg supported DOPC monolayer is completely intact and impermeable. At more negative potentials, capacitance peaks appear due to underlying field induced phase transitions occurring in the monolayer [32-34]. Alterations in the nature of these capacitance peaks are very sensitive to any changes in the monolayer structure. The effect of the biphenyl on the capacitance region corresponding to the stable monolayer on Hg and capacitance peaks-1 and 2 is shown in Figure 5.2 (red). Figure 5.3 shows the capacitance of peak-1 versus concentration plot of lipid coated Hg electrode in the presence of biphenyl. It can be seen from Figure 5.3 that there is a sharp decrease in the capacitance of peak-1 with an increase in concentration of biphenyl upto $1.0 \mu\text{mol dm}^{-3}$ and further increase in concentration does not have a significant effect on the capacitance of peak-1. Decrease in capacitance of DOPC monolayer in the presence of biphenyl represent the extent of interaction of biphenyl with the DOPC monolayer.

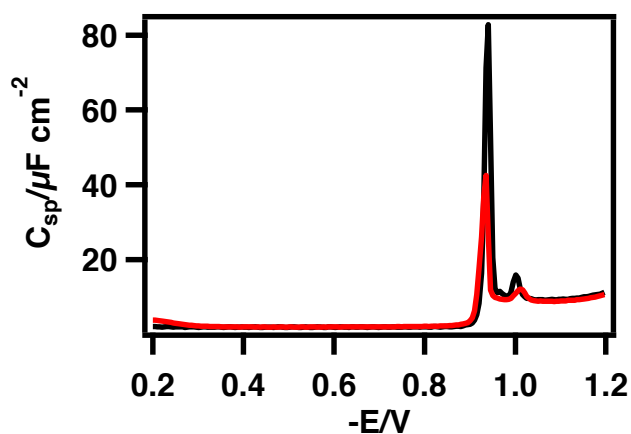


Figure 5.2: Capacitance versus potential plot of DOPC coated Hg electrode in 0.1 mol dm^{-3} KCl containing $0.001 \text{ mol dm}^{-3}$ phosphate buffer (black) in the presence of $1.0 \mu\text{mol dm}^{-3}$ biphenyl (red) acquired using ACV at 5 mVs^{-1} .

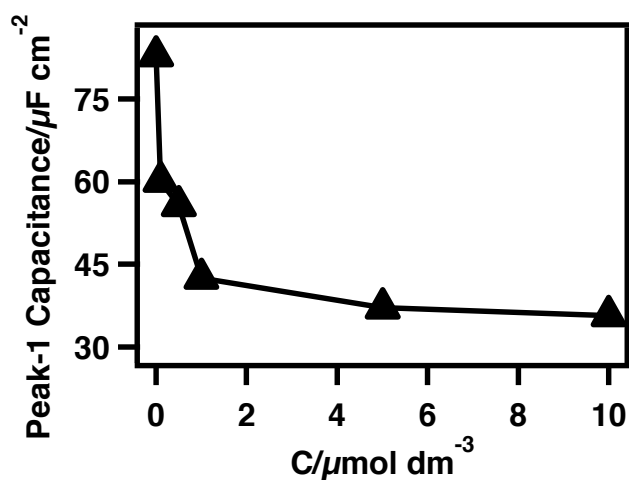


Figure 5.3: Capacitance of peak-1 versus concentration plot of DOPC coated Hg electrode in 0.1 mol dm^{-3} KCl containing $0.001 \text{ mol dm}^{-3}$ phosphate buffer in the presence of biphenyl.

The impedance data expressed in the complex capacitance plane of Hg supported DOPC monolayer in the presence of biphenyl in the electrolyte solution is shown in Figure 5.4 (a). A perfect DOPC monolayer deposited on Hg electrode shows a characteristic RC semicircle in complex capacitance plots (Figure 5.4 (a) (black)) with no frequency dispersion at potentials close to PZC of Hg ($\sim -0.4 \text{ V vs. Ag/AgCl}$ in 0.1 mol dm^{-3} KCl). where the adsorption of a membrane active species on to the electrode surface from the solution is represented by the presence of an extra low frequency tail. There is some surface adsorption observed in the case of biphenyl on the DOPC monolayer represented by a small 'tail' in addition to the RC element.

Figure 5.4 (b) shows the ZFC versus concentration plot of DOPC coated Hg electrode in the presence of different concentrations of biphenyl. A decrease in ZFC indicated the increase in thickness of the DOPC monolayer due to the incorporation of biphenyl into the spaces in between the lipid molecules.

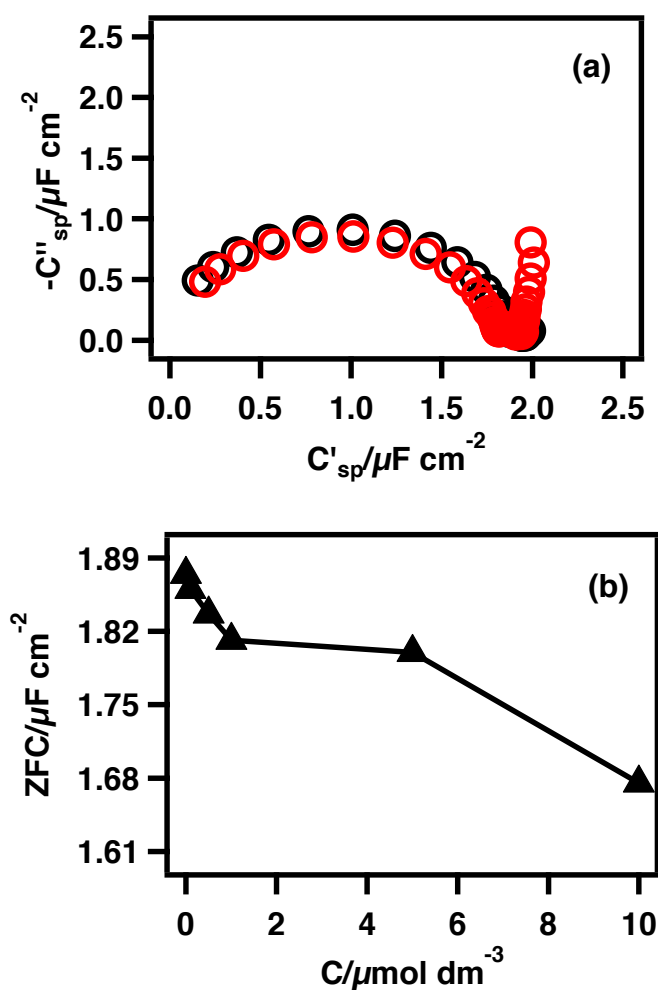


Figure 5.4: (a) Impedance data transformed to complex capacitance plane and (b) ZFC versus concentration plot of DOPC coated Hg electrode in 0.1 mol dm^{-3} KCl containing $0.001 \text{ mol dm}^{-3}$ phosphate buffer (black) in the presence of biphenyl acquired using EIS at -0.4 V respectively.

5.2.1 Effect of position of substitution

Figure 5.5 displays the modified Stern Volmer plots of OH-BPs in the presence of $0.254 \text{ mmol dm}^{-3}$ DOPC GUVs. It showed that the amount of accessible fraction is least for *p*-OH-BP and increases in the following order: *p*-OH-BP (17.21 %) < *m*-OH-BP (29.03 %) < *o*-OH-BP (90.63 %). Hence, a -OH substitution at *p*- position in biphenyl increases its tendency to penetrate into the phospholipid membrane because of its linearly symmetrical and planar structure). The *m*-OH-BP lacks two-fold symmetry and is less able to incorporate into the phospholipid membrane. As a result, the accessible fraction for quenching is higher for *m*-OH-BP compared to its *p*-isomer. Substitution of -OH at the *o*- position further impedes its ready

incorporation into the phospholipid membrane due to the twisted geometry arising from the increased torsion angle between the two phenyl rings. Hence such a molecule is available for quenching up to 90 %.

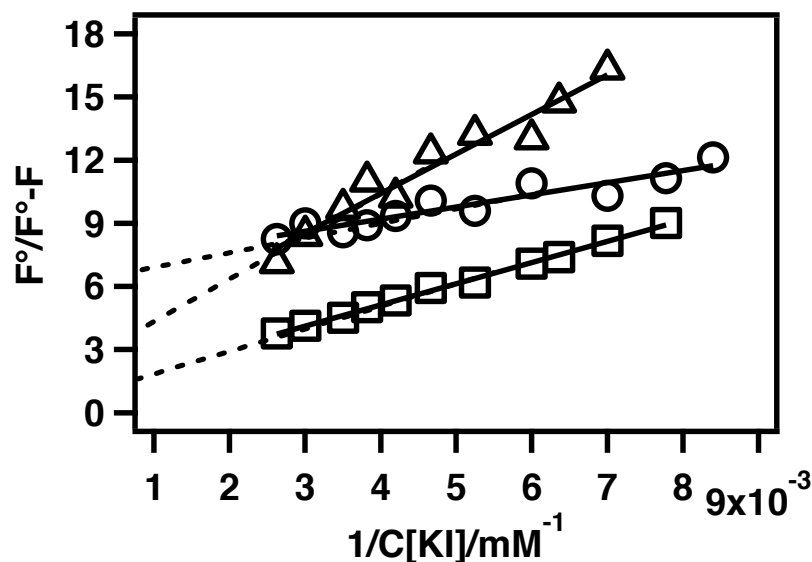


Figure 5.5: Modified Stern Volmer plots for iodide quenching of $1.0 \mu\text{mol dm}^{-3}$ of *p*- (circle), *m*- (triangle) and *o*- (square) OH-BPs in the presence of $0.254 \text{ mmol dm}^{-3}$ DOPC GUV in 0.1 mol dm^{-3} of KCl containing $0.001 \text{ mol dm}^{-3}$ of phosphate buffer.

The effect of the substituted mono OH-BPs on the capacitance region corresponding to the stable monolayer on Hg and capacitance peaks-1 and 2 is shown in Figure 5.6 (a). Figure 5.6 (b) shows that the suppression of the capacitance of peak-1 with an increase in concentration of *o*, *m* and *p*-OH-BPs is clear and the extent of suppression follows the order: $o < m < p$. This suppression in the capacitive current peak is directly related to the extent of interactions of these biphenyls with DOPC monolayer indicating that the *p*-OH-BP showed the strongest interactions with DOPC monolayer compared to the *m* and *o*-OH-BP. Notably the potentials characterising capacitance peaks-1 and -2 do not significantly change on penetration of the biphenyl into the monolayer as shown in Figure 5.6 (c).

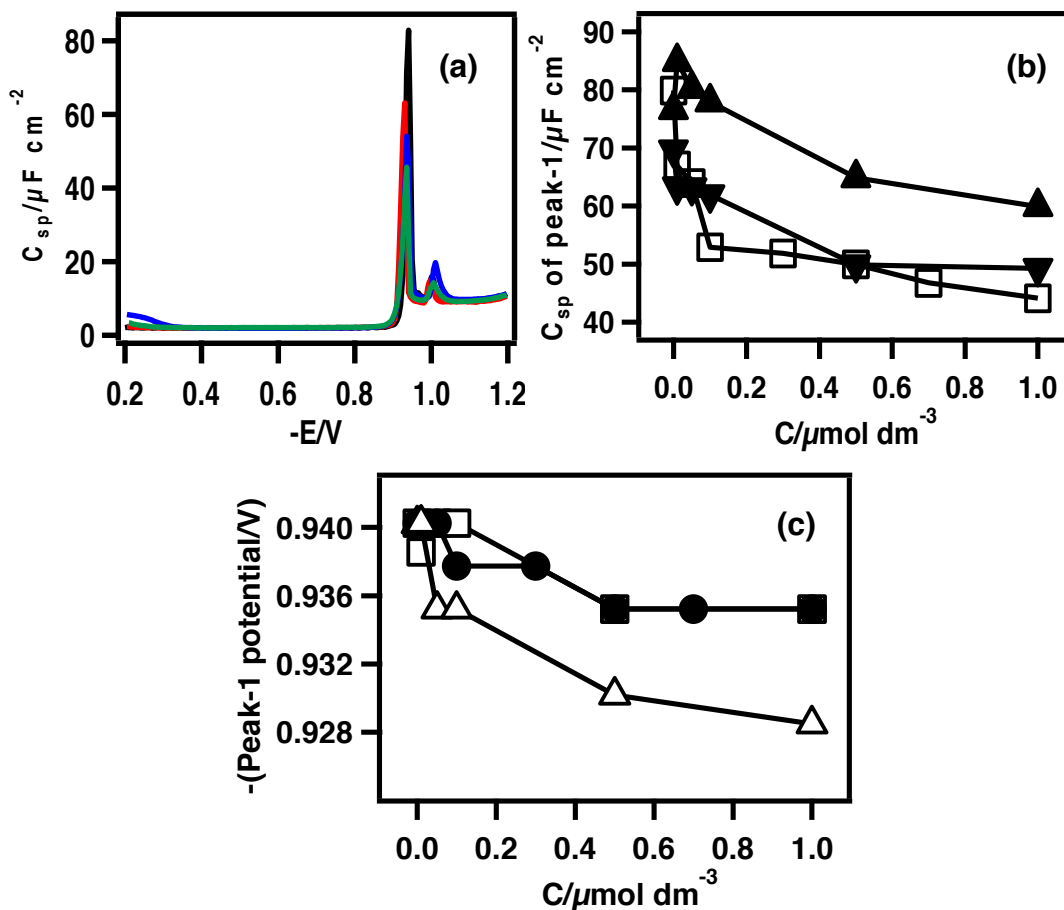


Figure 5.6: (a) Capacitance versus potential plot of DOPC coated Hg electrode in 0.1 mol dm^{-3} KCl containing $0.001 \text{ mol dm}^{-3}$ phosphate buffer (black) in the presence of $1.0 \mu\text{mol dm}^{-3}$ of *o*- (red), *m*- (blue) and *p*-OH-BP (green) (b) capacitance of peak-1 versus concentration plots of *o*- (close triangle), *m*- (close inverted triangle) and *p*- (open square) OH-BP and (c) potential of peak-1 versus concentration plots of *o*- (open triangle), *m*- (open square) and *p*- (closed circles) OH-BP, acquired using ACV at 5 mVs^{-1} .

The extent of suppression of peak-1 correlates with the accessible fraction of OH-BP for quenching (Figure 5.7), such that the less the penetration of OH-BP into the membrane, the less the observed peak suppression of capacitance peak-1 on the capacitance-potential plot of the DOPC monolayer on Hg.

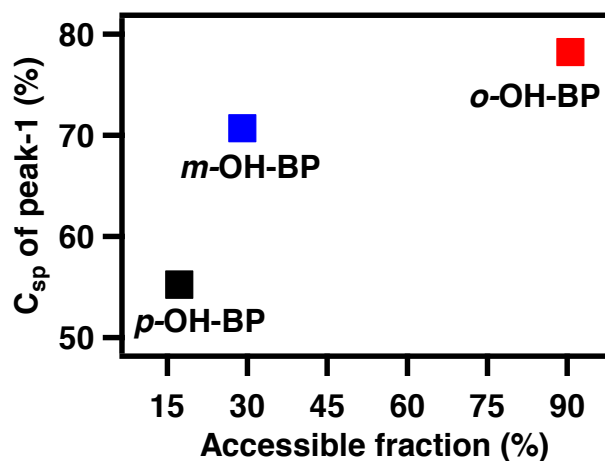


Figure 5.7: Plot capacitance of peak-1 against the accessible fraction for 1.0 $\mu\text{mol dm}^{-3}$ of OH-BPs on the vesicle surface.

Figure 5.8 (a) shows the impedance data expressed in the complex capacitance plane of Hg supported DOPC monolayer in the presence of *o*-, *m*- and *p*-OH-BPs in the electrolyte solution where the adsorption of these species on to the electrode surface from the solution is represented by the presence of an extra low frequency tail. It is interesting that the ZFC does not change significantly following the interaction with the different OH-BPs but the interaction with the *p*-OH-BP and its penetration introduces an additional extra small element to RC (Figure 5.8 (b)). This extra small element presumably relates to the presence of the *p*-OH-BP within the low dielectric region of the monolayer.

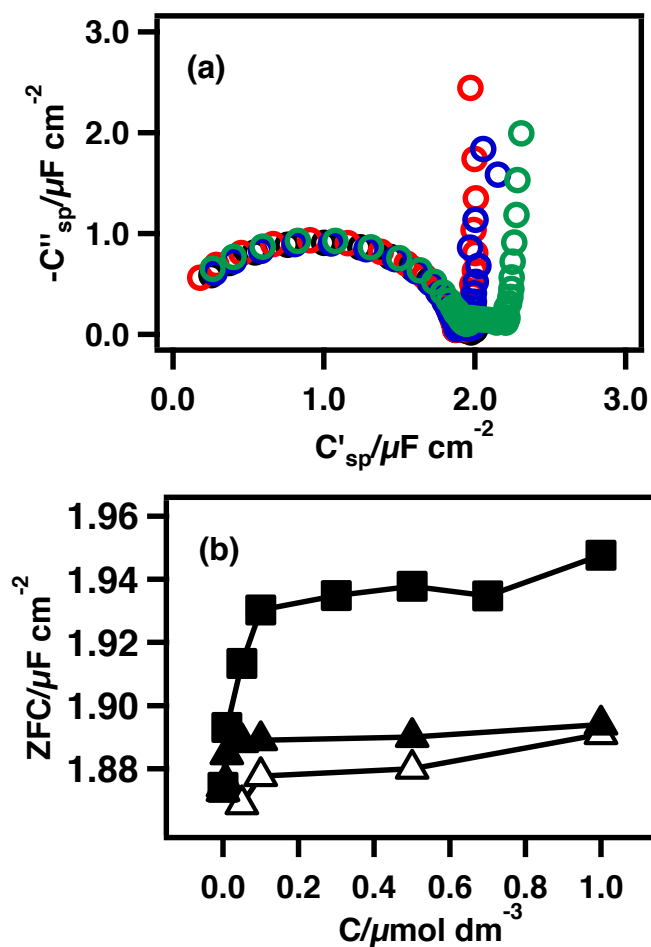


Figure 5.8: Impedance data transformed to complex capacitance plane of DOPC coated Hg electrode in $0.1\ mol\ dm^{-3}$ $1.0\ \mu mol\ dm^{-3}$ of *o*- (red), *m*- (blue) and *p*-OH-BP (green) and ZFC versus concentration of DOPC coated Hg electrode in $0.1\ mol\ dm^{-3}$ KCl containing $0.001\ mol\ dm^{-3}$ phosphate buffer in the presence of *o*- (open triangle), *m*- (close triangle) and *p*- (close square) OH-BP, acquired using EIS at $-0.4\ V$ respectively.

The fluorescence and electrochemical results are consistent with each other and support a hypothesis that the OH-BPs behave similarly at the vesicle electrolyte interface as they do at the monolayer electrolyte interface. A schematic diagram showing the location and mechanism of interaction of OH-BPs with DOPC monolayer supported on Hg electrode is shown in Figure 5.9.

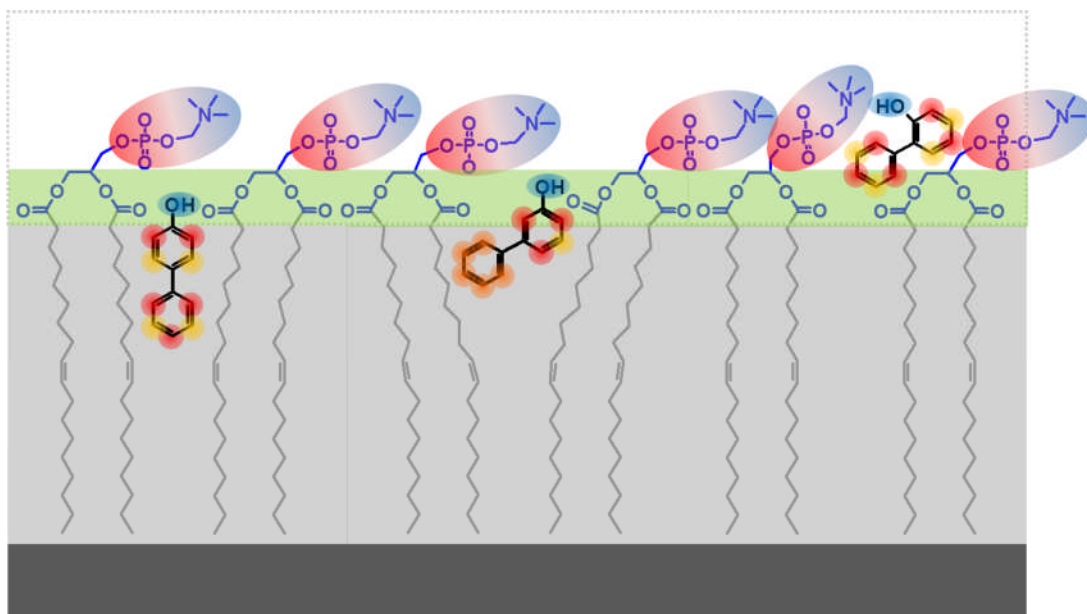


Figure 5.9: Schematic view of OH-BPs DOPC monolayer interaction.

Figure 5.10 displays the modified Stern Volmer plots of Cl-BPs in the presence of GUVs containing $0.254 \text{ mmol dm}^{-3}$ DOPC.

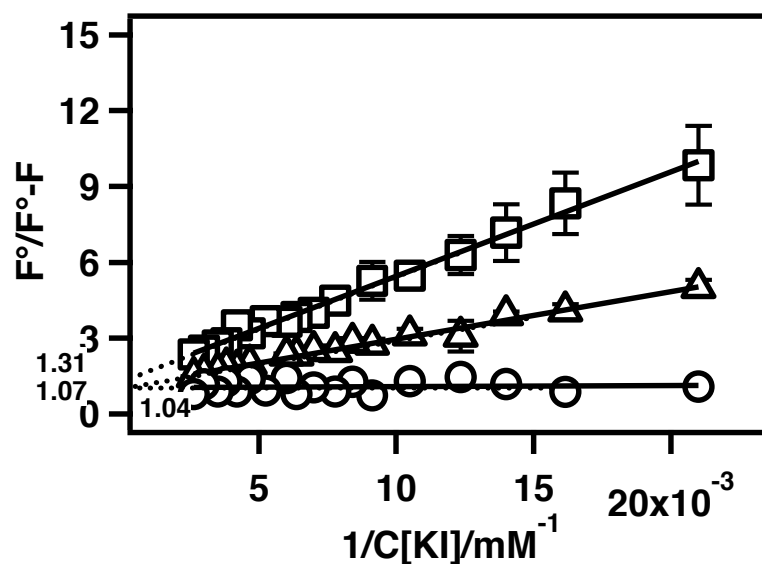


Figure 5.10: Modified Stern Volmer plots for iodide quenching of $1.0 \mu\text{mol dm}^{-3}$ of *p*- (square), *m*- (triangle) and *o*- (circle) Cl-BPs in the presence of $0.254 \text{ mmol dm}^{-3}$ DOPC GUV in 0.1 mol dm^{-3} of KCl containing $0.001 \text{ mol dm}^{-3}$ of phosphate buffer.

The results showed that the amount of accessible fraction increased in the following order: *p*-Cl-BP (76.47 %) < *m*-Cl-BP (93.14 %) < *o*-Cl-BP (96.08 %). All the isomers of mono Cl-BPs exhibited a similar order of incorporation/penetration into the bilayer to that of OH-BPs but the extent of the process is decreased to a great extent. Cl-BPs have similar 3D structure compared to their -OH analogues but there is an essential difference in distribution of electron density among atoms in these biphenyls. It is well known that the -OH group acts as an electron donor but the -Cl group acts as an electron acceptor when attached to aromatic rings. This is described by Hammett's substitution constant (σ_i) [35] of the functional group attached to aromatic ring. Therefore incorporation/penetration of biphenyls into hydrophobic core of DOPC monolayer corresponds to the electron donating/accepting properties of substitution group in aromatic ring.

Figure 5.11 displays the capacitance-potential plots of DOPC coated Hg in the presence of $1.0 \mu\text{mol dm}^{-3}$ of Cl-BPs in the electrolyte solution. Cl-BPs showed a more extensive influence on ACV. Following interaction between Cl-BPs and DOPC monolayer, ACV peaks suppression and shift were more extensive compared to that following OH-BPs -DOPC interactions (Figure 5.12 (a) and (b)).

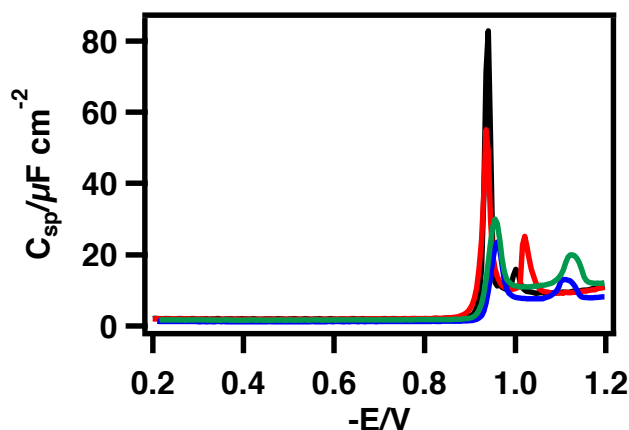


Figure 5.11: Capacitance versus potential plot of DOPC coated Hg electrode in 0.1 mol dm^{-3} KCl containing $0.001 \text{ mol dm}^{-3}$ phosphate buffer (black) in the presence of $1.0 \mu\text{mol dm}^{-3}$ of *o*- (red), *m*- (blue) and *p*-Cl-BP (green) acquired using ACV at 5 mVs^{-1} .

It is clear from Figure 5.12 that capacitance peaks-1 is not only suppressed but also shifted to more negative potential in the presence of Cl-BPs. Suppression of

capacitance peak-1 (Figure 5.12 (a)) specifies the strong interaction of Cl-BPs with DOPC monolayer that decreases in the following order: *p*-Cl-BP > *m*-Cl-BP and *o*-Cl-BP. The extent of peak shift in case of *m*- and *p*-Cl-BP-DOPC interaction is approximately the same whereas the peak shift for *o*-Cl-BP-DOPC interaction is insignificant.

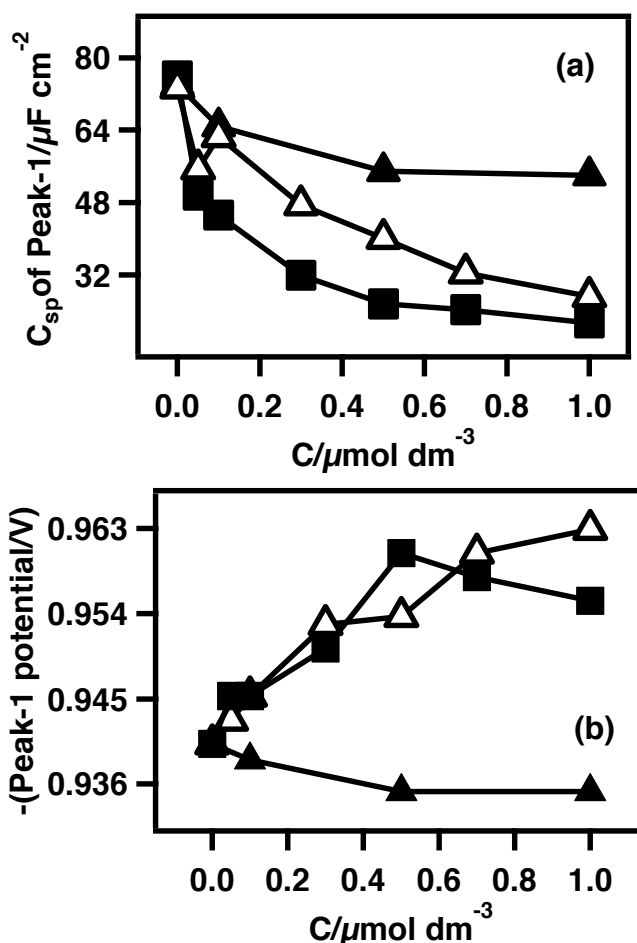


Figure 5.12: (a) Peak-1 capacitance: versus concentration and (b) Peak-1 potential versus concentration plots of DOPC coated Hg electrode in 0.1 mol dm^{-3} KCl containing $0.001 \text{ mol dm}^{-3}$ phosphate buffer in the presence of *o*- (close triangle), *m*- (open triangle) and *p*-Cl-BP (close square).

Figure 5.13 shows that the accessible fraction of Cl-BPs for quenching inversely correlates with suppression of peak-1. Comparing the results of OH-BPs and Cl-BPs, it is possible to conclude that the significant changes in the position of capacitance peaks in C_{sp} -E profile occur mainly as the result of interactions in the interfacial region of DOPC monolayer.

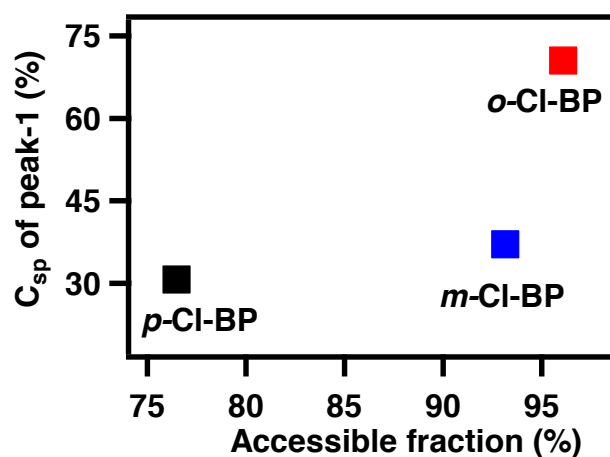


Figure 5.13: Plot capacitance of peak-1 against the accessible fraction for $1.0 \mu\text{mol dm}^{-3}$ of Cl-BPs on the vesicle surface.

Figure 5.14 (a) displays the impedance data expressed in the complex capacitance plane of Hg supported DOPC monolayer in the presence of Cl-BPs in the electrolyte solution. It is clear from the significant presence of the low frequency tail that the Cl-BPs adsorb on the surface of the DOPC monolayer. Figure 5.14 (b) displays the ZFC versus concentration plots of the Cl-BPs and shows that the monolayer capacitance decreases in the presence of Cl-BPs. The monolayer capacitance of the DOPC coated Hg electrode is lowered to the greatest extent in the presence of *p*-Cl-BP compared to the other positional isomers. Decrease in monolayer capacitance suggested the incorporation/penetration of these species in the spaces between the head groups or near hydrophobic regions filling up the gaps leads to the formation of more thick and stable monolayer. The Cl-BPs showed the following order of decrease in the ZFC following interaction with DOPC with *p*-Cl-BP instigating the greatest decrease: *p*-Cl-BP > *m*-Cl-BP > *o*-Cl-BP. The increase in thickness of the DOPC layer following Cl-BP interaction can explain the concurrent observed negative shift of capacitance peak-1. A more extensive negative shift of capacitance peak-1 in the presence of *m*- and *p*-Cl-BPs (Figure 5.12 (b)) can be explained by considering the incorporation of these biphenyls into the interfacial region of DOPC monolayer which leads to the formation of a thicker low dielectric region. This increases the field strength required for the penetration of electrolyte ions into the monolayer (Figure 5.12 (b)).

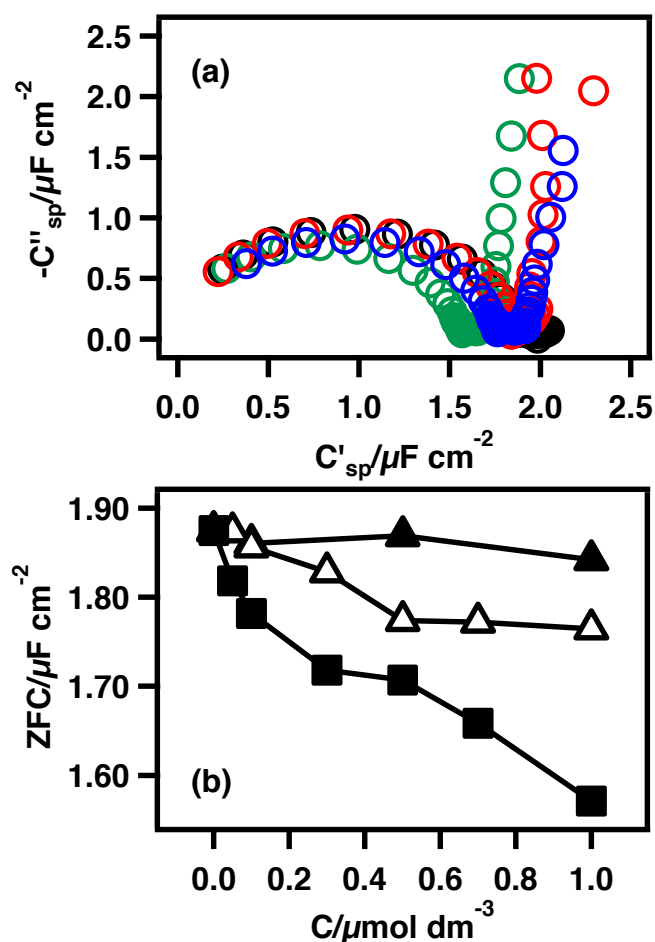


Figure 5.14: (a) Impedance data transformed to complex capacitance plane of DOPC coated Hg electrode in 0.1 mol dm^{-3} KCl with $0.001 \text{ mol dm}^{-3}$ phosphate buffer (black) containing $1.0 \mu\text{mol dm}^{-3}$ of *o*-Cl-BP (red), *m*- (blue) and *p*-Cl-BP (green) (b) ZFC versus concentration plot of *o*-Cl-BP (closed triangle), *m*-Cl-BP (open triangle) and *p*-Cl-BP (closed square), acquired using EIS at -0.4 V applied potential.

A further explanation for the peak shift is that of *m*-Cl-BP and *p*-Cl-BP are oriented in a more ordered form in the interfacial layer and the polarisability of the aromatic rings lessens the steepness of the potential drop across the layer. This leads to the need for applying a higher potential to instigate the phase transitions.

Similar to the example of the OH-BPs, the fluorescence and electrochemical results are consistent with each other and support the hypothesis that the Cl-BPs behave similarly at the vesicle electrolyte interface as at the monolayer electrolyte interface.

Figure 5.15 represents a schematic diagram showing the location and mechanism of interaction of Cl-BPs with DOPC monolayer supported on Hg electrode.

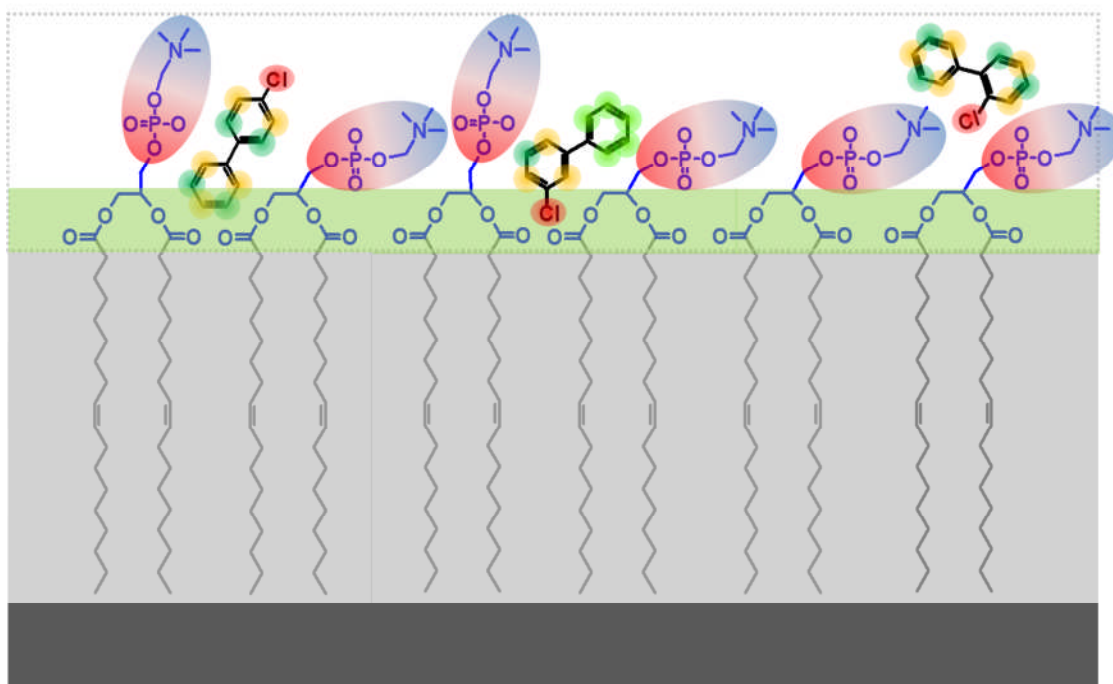


Figure 5.15: Schematic view of Cl-BPs DOPC monolayer interaction.

5.2.2 Effect of nature of substitution

Figure 5.16 shows the modified Stern Volmer plots of *p*-substituted biphenyls in the presence of GUVs prepared from $0.254 \text{ mmol dm}^{-3}$ DOPC solution. The results showed that the amount of accessible fraction is least for *p*-OH-BP and increases in the following order: *p*-OH-BP (17.21 %) < *p*-OCH₃-BP (39.07 %) < *p*-Cl-BP (76.47 %) < *p*-CN-BP (96.20 %) < *p*-CH₃-BP (96.24 %) < *p*-HSO₃-BP (100 %).

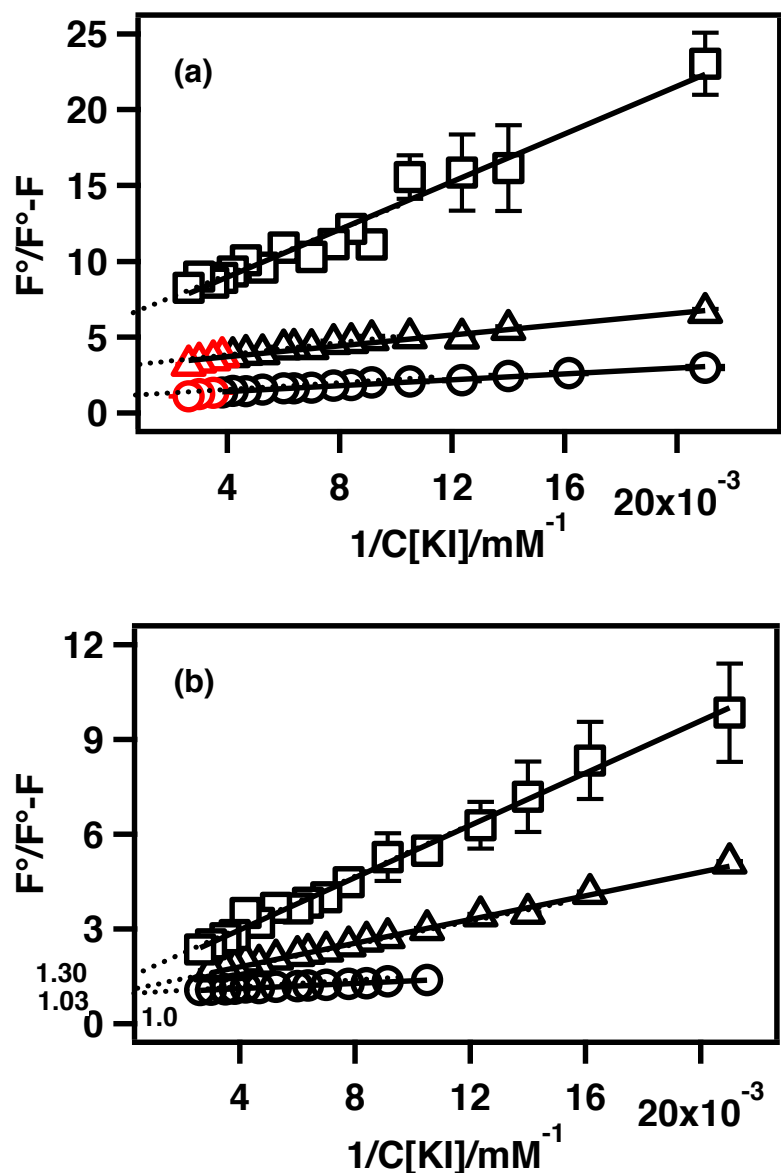


Figure 5.16: Modified Stern Volmer plots for iodide quenching of $1.0 \mu\text{mol dm}^{-3}$ of p -substituted biphenyls (a) $-\text{OH}$ (square), $-\text{OCH}_3$ (triangle) and $-\text{CH}_3$ (circle) and (b) $-\text{Cl}$ (square), $-\text{CN}$ (triangle) and $-\text{SO}_3$ (circle) in the presence of $0.254 \text{ mmol dm}^{-3}$ DOPC GUV in 0.1 mol dm^{-3} of KCl containing $0.001 \text{ mol dm}^{-3}$ of phosphate buffer.

Figure 5.17 shows the plot of the biphenyl's substituent Hammett constant (σ_t) values against the accessible fraction of the substituted biphenyl in the membrane for all substituted biphenyl–DOPC membrane interactions. It is significant that the penetration of p - CH_3 -BP and p - HSO_3 -BP into DOPC membranes does not correlate with the substituent σ_t values.

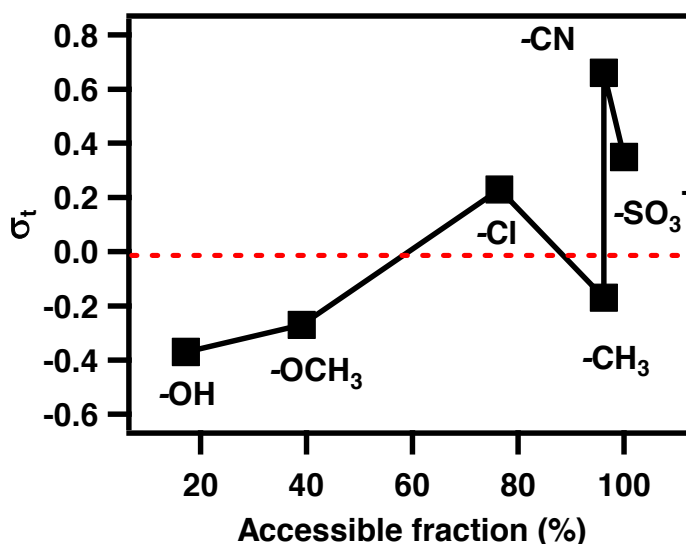


Figure 5.17: Plot of Hammett's constants of biphenyl substituents (σ_t) against the accessible fraction for $1.0 \mu\text{mol dm}^{-3}$ of *p*-substituted biphenyls on the vesicle surface.

The σ_t values used have been calculated for substituted benzenes and include both long range mesomeric and short range inductive effects of substitution [36]. The benzene molecule is small and the inductive effect is significant in changing its properties but in the case of biphenyl and other long molecules, the inductive effect does not have a strong influence on the second ring compared to the mesomeric effect. In order to estimate the precise and realistic electron density on biphenyl rings, mesomeric Hammett's constants (σ_m) were calculated by subtracting inductive Hammett's constant (σ_i) from σ_t [35]. Table-2 summarises the physical properties of biphenyl derivatives.

Table 5.2: Log *P* [37], Hammett's constant (σ_t [38] and σ_m) and torsional angle values of biphenyls used in this study.

Position	<i>o</i> -		<i>m</i> -		<i>p</i> -					
	-Cl	-OH	-Cl	-OH	-SO ₃	-CN	-Cl	-OH	-OCH ₃	-CH ₃
Log <i>P</i>	4.54	3.1	4.6	3.2	--	3.7	4.61	3.2	4.0	4.6
σ_t					0.35	0.66	0.23	-0.37	-0.27	-0.17
σ_m					0.05	0.1	-0.14	-0.49	-0.39	-0.1
ϕ	$45^\circ \leq \phi \leq 60^\circ$		$\square 45^\circ$		$\square 45^\circ$					

Figure 5.18 shows the correlation between the σ_m of the substituent and the accessible fraction of substituted biphenyls on the vesicle surface. An electron donating mesomeric effect results in an increased electron density in the rings of *p*-Cl-BP compared to the rings of *p*-CH₃-BP (Figure 5.18). This adjusted correlation with the σ_m showed a predominantly good correlation with the accessibility of biphenyls excepting *p*-HSO₃-BP. However *p*-HSO₃-BP is a negatively charged molecule with a large polar SO₃ group which will not favour its penetration into the apolar region.

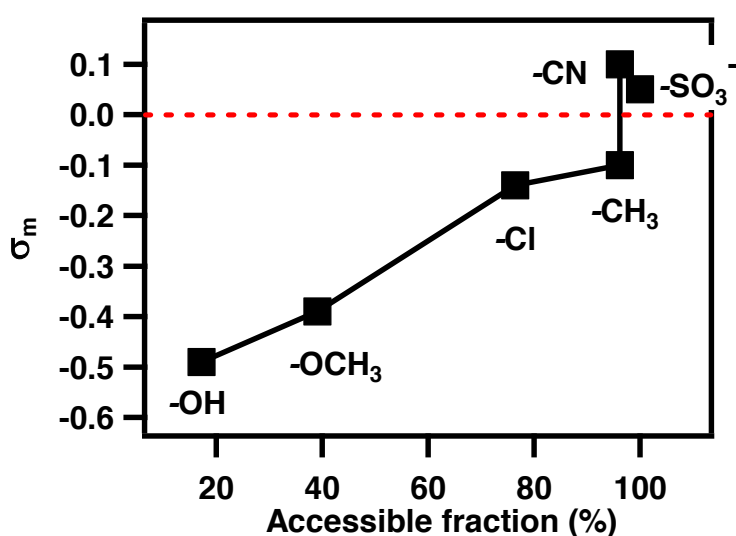


Figure 5.18: Plot of Hammett's constants of biphenyl substituents (σ_m) against the accessible fraction for 1.0 $\mu\text{mol dm}^{-3}$ of *p*-substituted biphenyls on the vesicle surface.

Also the difference in the accessible fractions of the CH₃-BP, SO₃-BP and CN-BP is not essential. A schematic diagram summarizing the effect of biphenyl substituent position and electron donating/withdrawing character on the biphenyl's interactions with the phospholipid membrane is shown in Figure 5.19.

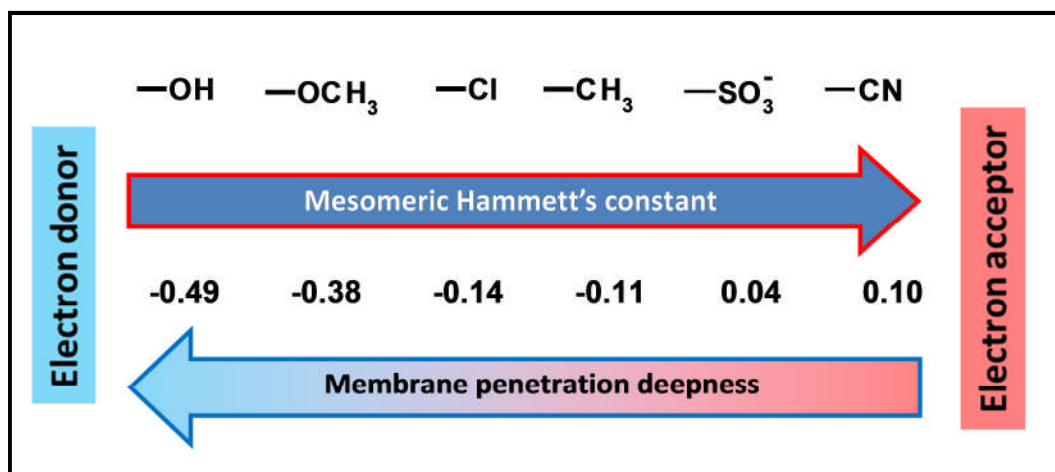


Figure 5.19: A schematic representation of effect of *p*-substituted biphenyls and their electron density (σ_m) on their interactions with lipid membranes.

Figure 5.20 shows the correlation between shift in capacitance peak 1 and the substituent σ_M and for *p*-substituted biphenyls. It can be seen that increase in both the electron accepting and donating powers of the functional groups relative to the -Cl group results in a shift of potential of capacitance peak-1 to less negative potentials. *p*-Cl-BP showed a marked shift of capacitance peak-1 to more negative and *p*-CN-BP and *p*-OH-BP showed a shift of capacitance peak-1 to less negative potential.

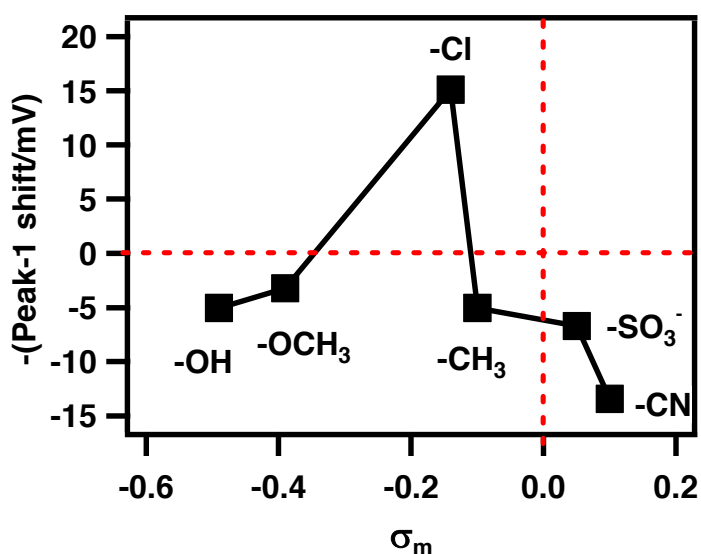


Figure 5.20: Plot of shift in capacitance peak-1 against substituent Hammett's constants of biphenyl substituents (σ_M) for $1.0 \mu\text{mol dm}^{-3}$ of *p*-substituted biphenyls.

Figure 5.21 (a) and (b) display the impedance data expressed in the complex capacitance plane of Hg supported DOPC monolayer in the presence of *p*-OH-BP, *p*-OCH₃-BP, *p*-CH₃-BP and *p*-Cl BP, *p*-CN BP and *p*-HSO₃-BP. The appearance of an extra element at low frequencies in complex capacitance plots of the substituted biphenyls (except *p*-CH₃-BP and *p*-OCH₃-BP) is evident and is indicative of their adsorption on lipid surface.

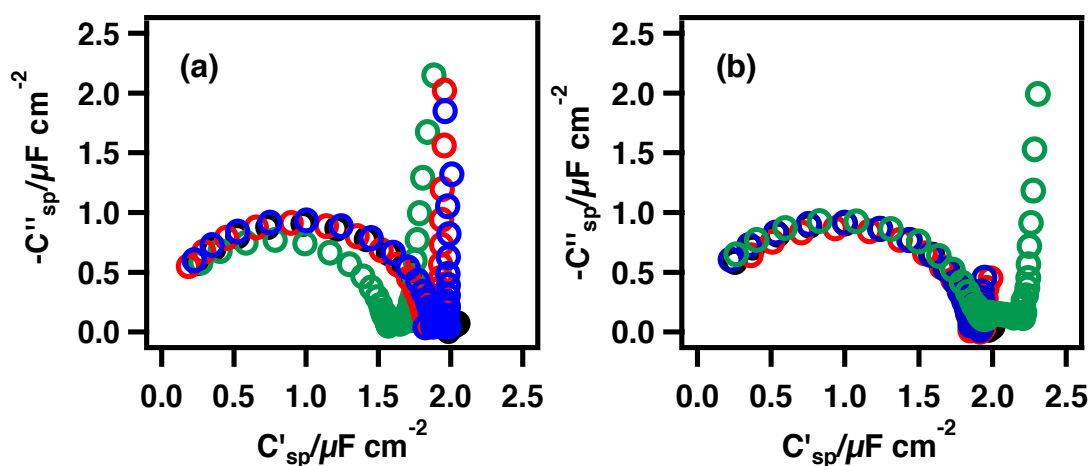


Figure 5.21: Impedance data transformed to complex capacitance plane of DOPC coated Hg electrode in 0.1 mol dm^{-3} KCl with $0.001 \text{ mol dm}^{-3}$ phosphate buffer containing $1.0 \mu\text{mol dm}^{-3}$ of (a) *p*-OCH₃ (red), *p*-CH₃ (blue) *p*-OH (green) and (b) *p*-CN (red), *p*-O₃SH (blue) *p*-Cl (green) substituted biphenyls, acquired using EIS at -0.4 V applied potential.

Figure 5.22 (a) and (b) shows the ZFC versus concentration plots of the *p*-substituted biphenyls. It can be seen that there is only a significant change in ZFC for the *p*-Cl-BP and *p*-OH-BP at their higher solution concentration. *p*-Cl-BP decreases the ZFC and hence increases the membrane thickness and *p*-OH-BP increases the ZFC and hence decreases the membrane thickness as described above. The increase in thickness is responsible for a decrease in steepness of the potential drop across the interface which leads to a shift in peak 1.

On the other hand, increases in concentration of *p*-CN-BP and *p*-HSO₃-BP have very little effect on ZFC and hence the membrane thickness. *p*-CH₃-BP and *p*-OCH₃-BP are different to others in having a dual effect on ZFC. Both these biphenyls increase the ZFC at very low concentrations and decrease the ZFC at high solution concentrations.

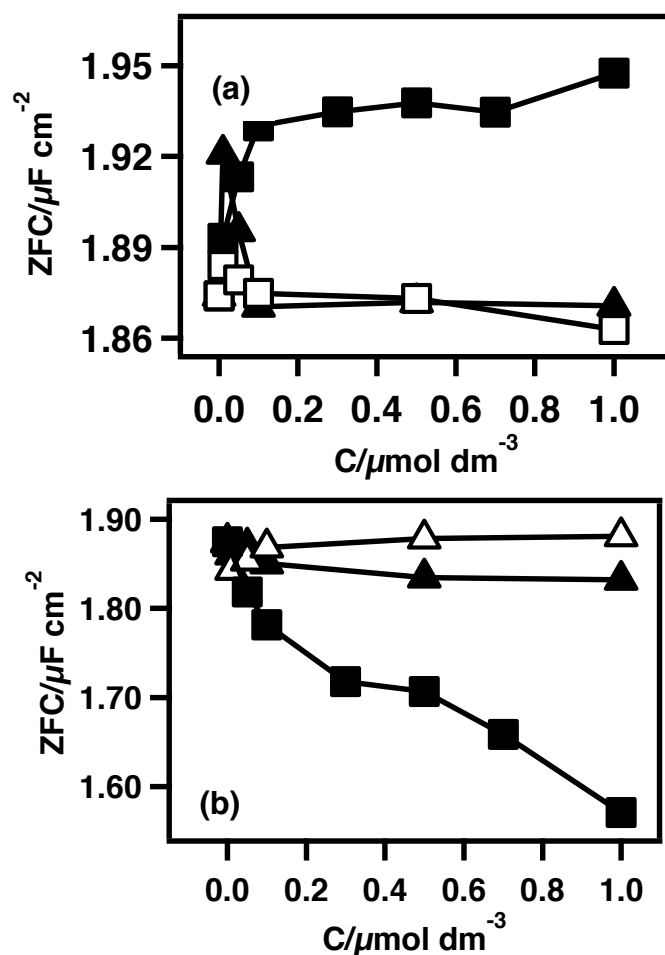


Figure 5.22: ZFC versus concentration plots of DOPC coated Hg electrode in 0.1 mol dm^{-3} KCl with $0.001 \text{ mol dm}^{-3}$ phosphate buffer containing (a) *p*-OCH₃ (close triangle), *p*-CH₃ (open square) *p*-OH (close square) and (b) *p*-CN (close triangle), *p*-O₃SH (open triangle) *p*-Cl (close square) substituted biphenyls acquired using EIS at -0.4 V applied potential.

This might be explained as related to the effects of *p*-CH₃-BP and *p*-OCH₃-BP on relative permittivity and thickness of apolar region of DOPC monolayer at their low solution concentration reaching a saturation value followed by subsequent

incorporation of these species in the interfacial region resulting in a decrease in membrane thickness at higher solution concentration.

Increase or decrease in ZFC and hence the membrane thickness is related to the accessible fraction and is shown in Figure 5.26. In the Figure 5.23, the V shaped plot shows a minimum ZFC representing a maximum thickness of the DOPC corresponding to the intermediate value of the accessible fraction. An outlier to the trend is the point representing the *o*-HO-BP/DOPC interaction which could be due to a variety of factors and requires further investigation. The accessible fraction represents the penetration depth of the substituted biphenyl in the bilayer membrane and, assuming that the penetration of biphenyls in the bilayer and monolayer are the same or similar, the mid-location of the Cl-BP in the monolayer is related to a maximum thickness of the monolayer. By the same token, when the biphenyl is located outside this region either nearer to the surface of the monolayer or deeper in the apolar core, the increase in thickness is not so pronounced.

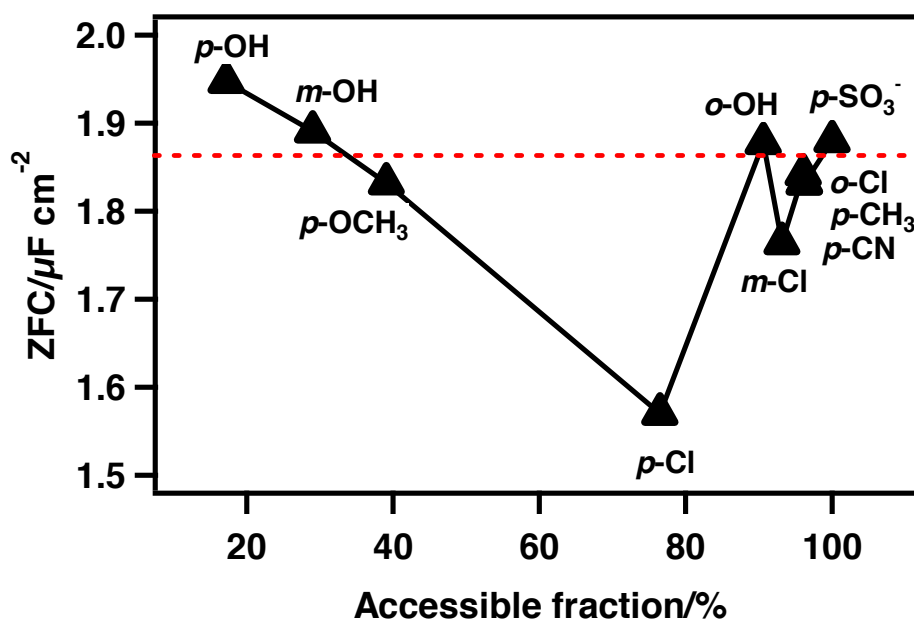


Figure 5.23: Plot of ZFC against the accessible fraction for $1.0 \mu\text{mol dm}^{-3}$ of *p*-substituted biphenyls on the vesicle surface and error bars are within the symbol size.

The interaction of substituted biphenyls with DOPC monolayers and bilayers can be related to two factors:

(1) Substituents with higher σ_m lead to biphenyl rings having a lower electron density which enhances the H-bonding tendency of the rings and their preference to locate in the DOPC interfacial layer. Biphenyl rings containing '=CH-' groups are electron rich however the presence of electron acceptor substituents with high σ_m on the ring decreases electron density in the ring and hence on the protons. Such electron deficient protons remain apolar but will exhibit a greater tendency to form hydrogen bonds with the strongly polar groups in the interfacial region of the DOPC monolayer and bilayer. This reasoning is supported by studies which have shown that apolar moieties '-CH=', '-CH₂-' and '-CH₃-' can participate in hydrogen bonding [39-49].

(2) Substituents with lower σ_m lead to biphenyl rings having a higher electron density which leads to a greater ring polarisability. A higher ring polarisability enables stronger dispersion interaction forces between the biphenyls and the DOPC alkyl chains [49-50] and a deeper penetration of the biphenyl into the DOPC monolayer and bilayer.

5.3 Conclusions

The interaction of monosubstituted biphenyls with DOPC bilayers and monolayers is strongly dependent on the structural configuration and planarity of the molecules.

- (1) p-substituted biphenyls compared to o- and m-substituted biphenyls exhibit stronger interactions with DOPC bilayers and monolayers because of retained coplanarity of the two aromatic rings irrespective of the nature of substituent.
- (2) Biphenyls with electron donor substituents penetrate the apolar core of the bilayer whereas biphenyls with electron acceptor substituents are incorporated in the polar group region of the DOPC bilayer. Biphenyls located on the interface between the polar and apolar region increase the DOPC layer thickness.
- (3) Both electrochemical and fluorescence studies exhibit a consistent pattern of interactions between substituted biphenyls and DOPC bilayers and monolayers respectively suggesting that the Hg support has an insignificant

influence on the interactions of bio-membrane active compounds with DOPC.

- (4) Results indicate that the two structural features influencing the location of substituted biphenyls in DOPC bilayers and monolayers are: (i) the hydrogen bonding capability and (ii) the polarisability of the biphenyl rings.

5.4 References

- [1] J.I. Kroschwitz, M. Howe-Grant, Kirk-Othmer concise encyclopedia of chemical technology, Wiley New York, 1999.
- [2] S. Bonora, A. Torreggiani, G. Fini, *Thermochimica acta*, 408 (2003) 55-65.
- [3] H.S.D. Bank, National Library of Medicine, National Toxicology Information Program, Bethesda, MD (USA), (1994).
- [4] U. EPA, (1984).
- [5] J. Borja, D.M. Taleon, J. Auresenia, S. Gallardo, *Process Biochemistry*, 40 (2005) 1999-2013.
- [6] O. Hutzinger, J. Paasivirta, *New types of persistent halogenated compounds*, Springer, 2000.
- [7] R.E. Billings, R.E. McMahon, *Molecular pharmacology*, 14 (1978) 145-154.
- [8] K.L. Kaiser, P.T. Wong, *Bulletin of environmental contamination and toxicology*, 11 (1974) 291-296.
- [9] E. Klasson Wehler, L. Hovander, B.-O. Lund, *Chemical research in toxicology*, 9 (1996) 1340-1349.
- [10] E.K. Wehler, L. Lindberg, C.-J. Jönsson, Å. Bergman, *Chemosphere*, 27 (1993) 2397-2412.
- [11] A. Bergman, E. Klasson-Wehler, H. Kuroki, *Environmental health perspectives*, 102 (1994) 464.
- [12] T.M. Sandanger, P. Dumas, U. Berger, I.C. Burkow, *Journal of Environmental Monitoring*, 6 (2004) 758-765.
- [13] A. Brouwer, D.C. Morse, M.C. Lans, A.G. Schuur, A.J. Murk, E. Klasson-Wehler, Å. Bergman, T.J. Visser, *Toxicology and industrial health*, 14 (1998) 59-84.
- [14] M.C. Lans, E. Klasson-Wehler, M. Willemsen, E. Meussen, S. Safe, A. Brouwer, *Chemico-biological interactions*, 88 (1993) 7-21.
- [15] F. Grein, *The Journal of Physical Chemistry A*, 106 (2002) 3823-3827.

- [16] J. Cioslowski, S.T. Mixon, *Journal of the American Chemical Society*, 114 (1992) 4382-4387.
- [17] Y. Takei, T. Yamaguchi, Y. Osamura, K. Fuke, K. Kaya, *The Journal of Physical Chemistry*, 92 (1988) 577-581.
- [18] O. Bastiansen, S. Samdal, *Journal of molecular structure*, 128 (1985) 115-125.
- [19] Y. Tan, D. Li, R. Song, D. Lawrence, D.O. Carpenter, *Toxicological Sciences*, 76 (2003) 328-337.
- [20] Y. Tan, R. Song, D. Lawrence, D.O. Carpenter, *Toxicological Sciences*, 79 (2004) 147-156.
- [21] Y. Tan, C.-H. Chen, D. Lawrence, D.O. Carpenter, *Toxicological Sciences*, 80 (2004) 54-59.
- [22] J.M. Cullen, K.L. Kaiser, *An Examination of the Role of Rotational Barriers in the Toxicology of Pcb's*, in: *QSAR in Environmental Toxicology*, Springer, 1984, pp. 39-66.
- [23] A.M. Bobra, W.Y. Shiu, D. Mackay, *Structure-activity relationships for toxicity of hydrocarbons, chlorinated hydrocarbons and oils to Daphnia magna*, in: *QSAR in Environmental Toxicology*, Springer, 1984, pp. 3-16.
- [24] A. Nelson, N. Auffret, J. Borlakoglu, *Biochimica et Biophysica Acta (BBA)-Biomembranes*, 1021 (1990) 205-216.
- [25] A. Nelson, *Langmuir*, 12 (1996) 2058-2067.
- [26] J.H. Fendler, *Accounts of Chemical Research*, 13 (1980) 7-13.
- [27] M. Magzoub, K. Kilk, L.G. Eriksson, Ü. Langel, A. Gräslund, *Biochimica Et Biophysica Acta (BBA)-Biomembranes*, 1512 (2001) 77-89.
- [28] K. Lohner, A. Latal, R.I. Lehrer, T. Ganz, *Biochemistry*, 36 (1997) 1525-1531.
- [29] J. Dufourcq, J.-F. Faucon, *Biochimica et Biophysica Acta (BBA)-Biomembranes*, 467 (1977) 1-11.
- [30] C. Casals, E. Miguel, J. Perez-Gil, *Biochem. J*, 296 (1993) 585-593.
- [31] R. Fato, M. Battino, M. Degli Esposti, G. Parenti Castelli, G. Lenaz, *Biochemistry*, 25 (1986) 3378-3390.
- [32] A. Nelson, N. Auffret, *Journal of Electroanalytical Chemistry and Interfacial Electrochemistry*, 244 (1988) 99-113.
- [33] A. Nelson, F. Leermakers, *Journal of Electroanalytical Chemistry and Interfacial Electrochemistry*, 278 (1990) 73-83.

- [34] A.V. Brukhno, A. Akinshina, Z. Coldrick, A. Nelson, S. Auer, *Soft Matter*, 7 (2011) 1006-1017.
- [35] C. Hansch, A. Leo, R. Taft, *Chemical reviews*, 91 (1991) 165-195.
- [36] C.K. Ingold, *Chemical reviews*, 15 (1934) 225-274.
- [37] H.E. Pence, A. Williams, *Journal of Chemical Education*, 87 (2010) 1123-1124.
- [38] J. Durand-Niconoff, L. Cruz-Kuri, M. Matus, J. Correa-Basurto, J. Cruz-Sanchez, F. Ramos-Morales, *Journal of Chemical Sciences*, 123 (2011) 719-725.
- [39] A. Allerhand, P. Von Rague Schleyer, *Journal of the American Chemical Society*, 85 (1963) 1715-1723.
- [40] R.L. Brinkley, R.B. Gupta, *AIChE journal*, 47 (2001) 948-953.
- [41] M.S. El-Shall, Y.M. Ibrahim, E.H. Alsharaeh, M. Meot-Ner, S.P. Watson, *Journal of the American Chemical Society*, 131 (2009) 10066-10076.
- [42] J.R. Murdoch, A. Streitwieser Jr, *The Journal of Physical Chemistry*, 85 (1981) 3352-3354.
- [43] P. Mignon, S. Loverix, J. Steyaert, P. Geerlings, *Nucleic acids research*, 33 (2005) 1779-1789.
- [44] M. Levitt, M.F. Perutz, *Journal of molecular biology*, 201 (1988) 751-754.
- [45] M. Tamres, *Journal of the American Chemical Society*, 74 (1952) 3375-3378.
- [46] I. Rakipov, M. Varfolomeev, A.Y. Kirgizov, B. Solomonov, *Russian Journal of Physical Chemistry A*, 88 (2014) 2023-2028.
- [47] E. Arras, A.P. Seitsonen, F. Klappenberger, J.V. Barth, *Physical Chemistry Chemical Physics*, 14 (2012) 15995-16001.
- [48] V. Borisenko, S. Krekov, M.Y. Fomenko, A. Koll, P. Lipkovski, *Journal of molecular structure*, 882 (2008) 9-23.
- [49] E.A. Meyer, R.K. Castellano, F. Diederich, *Angewandte Chemie International Edition*, 42 (2003) 1210-1250.
- [50] P. Atkins, J. De Paula, R. Friedman, *Quanta, matter, and change: a molecular approach to physical chemistry*, Oxford University Press, 2009.

Chapter-6

Characterization and application of DOPC bilayer on Hg in the presence of electric field

6.1 Introduction

Biomimetic lipid bilayers have been investigated extensively over the past several years to develop an understanding about the properties and functions of biomembranes. These model lipid bilayers varied from free standing vesicles to bilayers supported on various solid substrates such as gold [1-2] and mica [3-4] directly or via linkers. Using Hg as a substrate, only tethered lipid bilayers have been developed and investigated using different tethering materials such as alkanethiols [5-11], polymer [12] and peptides [13] until recently. Potential dependant phospholipid bilayer formation directly on the surface of Hg from the lipid electrolyte interface has been reported recently at potentials negative to -1.0 V due to favourable energetics and consistency with physicochemical and thermodynamical aspects [14]. This DOPC bilayer supported directly on Hg was described using rapid cyclic voltammetry (RCV) and atomic force spectroscopy (AFM). In RCV, the DOPC bilayer on Hg has been shown to exhibit a constant low capacitance region from -1.0 V to -1.3 V followed by a sharp, well-defined and cathodic capacitance current peak due to an underlying phase transition at about -1.3 V with a reverse anodic process which is represented by a capacitance current peak shifted due to rapid voltage scanning [14]. These bilayers are described as stable in

potential range from -1.0 V to -1.4 V and are unstable at potentials positive to -0.9 due to conversion to monolayer. AFM studies have shown that the thickness of the bilayer is 6.5-7 nm with 95 % coverage in voltage domain from -1.0 V to -1.35 V and decreases to 2.5-3 nm (thickness of monolayer) at higher negative potentials with same coverage [14]. In this study, the properties of this bilayer such as permeability and ion diffusion processes are investigated. This is the first study to our knowledge to report on the characterization of DOPC bilayer structure directly supported on the surface of Hg electrode.

6.2 Experimental

6.2.1 Materials and methods

The electrolyte, KCl (0.1 mol dm^{-3}) was prepared from KCl (Fisher Chemicals Ltd.) calcined at $600 \text{ }^\circ\text{C}$ in a muffle furnace and dissolved in $18.2 \text{ M}\Omega$ MilliQ water containing $0.001 \text{ mol dm}^{-3}$ phosphate buffer with pH 7.4 (19 % of $0.002 \text{ mol dm}^{-3}$ $\text{NaH}_2\text{PO}_4 \cdot \text{H}_2\text{O}$ and 81 % of $0.002 \text{ mol dm}^{-3}$ Na_2HPO_4) and was used in all the experiments except for the permeability studies. In experiments involving use of ZnCl_2 , 0.1 mol dm^{-3} KCl without buffer is used to avoid precipitation of Zn in the electrolyte solution. ZnCl_2 (Sigma Aldrich) was employed to prepare a 0.2 mol dm^{-3} stock solution using $18.2 \text{ M}\Omega$ MilliQ water. The electrolyte solution was purged with argon gas for 15-20 minutes prior to experiment. After deaeration, a blanket of argon gas was maintained above the fully deaerated solution to avoid penetration of any oxygen into the solution during all experiments. A DOPC solution (Avanti Lipid) of $2.54 \text{ mmol dm}^{-3}$ was prepared in pentane (HPLC grade, Fisher Scientific Chemicals Ltd.) in a clean glass vial and was stored in the freezer. A glass syringe was used to transfer the lipid solution to the electrolyte surface in the electrochemical cell. DOPC bilayers were prepared by spreading $\sim 15 \text{ }\mu\text{L}$ of the DOPC solution at the argon-electrolyte interface in the electrochemical cell [15-16]. A period of about 5-10 minutes was required for the pentane to evaporate.

A Kemula-type hanging Hg drop electrode (HMDE) was used for the experiments. The HMDE assembly (Polish Academy of Sciences, Warsaw-Poland) with a Hg drop at the lower end of capillary was lowered through the lipid-electrolyte surface

slowly to allow the lipid deposition. The HMDE was coated with a fresh DOPC layer prior to each series of experiments. The electrochemical cell and all other glass apparatus were washed with piranha solution to remove organic contamination. Piranha solution was kept in the cell for at least an hour for efficient cleaning before performing experiments. Also, the counter electrode and reference electrode were immersed in the same solution for a few seconds to remove any organic contamination before each experiment. Cleaning the ceramic frit of the reference electrode is necessary because a blocked or dirty frit will cause erroneous results in the electrochemical measurements. The apparatus and the electrodes were then rinsed with Milli-Q water to remove any piranha residue since the presence of trace piranha in the electrolyte can damage the lipid.

6.2.2 Electrochemical set-up

The experiments were performed in a standard three electrode cell using an Ag/AgCl electrode as reference electrode with a porous sintered glass frit separating the inner 3.5 mol dm^{-3} solution of reference electrode from the outer electrolyte solution and a Pt rod as a counter electrode. The electrochemical apparatus was contained in a Faraday cage. RCV measurements were carried out with a PGSTAT 30 Autolab potentiostat (Ecochemie, Utrecht, Netherlands) interfaced to PowerLab 4/25 signal generator (AD Instruments Ltd.) controlled by Scope software. The potential step measurements were carried out using the Autolab system, GPES (General purpose electrochemical system) with PGSTAT 30 and controlled with Autolab software. The integrity of the DOPC bilayer was checked at the beginning and end of each experiment. The Autolab system FRA (frequency response analyser) with PGSTAT 30 and controlled with Autolab software was used for the impedance measurements. The impedance data were transformed to complex capacitance plane and fitted for the model as described below.

6.2.3 Electrochemical techniques

6.2.3.1 RCV

RCV was used as the main technique to deposit the DOPC bilayers on Hg and to probe the properties of bilayer by recording a fast scan "fingerprint" at a scan rate

(v) of 40 Vs^{-1} . The underlying principle of the bilayer formation involves the conversion of a lipid monolayer supported on HMDE electrode to a bilayer by decreasing the area of electrode. Different bilayers varying in lipid density can be formed by changing the electrode area.

The following procedure was used to deposit a DOPC bilayer on the surface of HMDE. Subsequent to the formation of DOPC monolayer in the potential regime of -0.2 to -1.6 V, the potential programme was switched to -1.0 V to -1.6 V. In this potential excursion, the monolayer exhibited the phase transitions characterized by the stable capacitive current peaks in the current-potential voltammogram that has been well described [17-18]. The area of HMDE is gradually decreased in a controlled fashion until the first two monolayer capacity current peaks disappear completely and a new capacity current peak indicating an underlying phase transition appear in the place of the third and fourth monolayer capacity current peaks (see Figure 6.3) on the cathodic scan. The reorientation in the bilayer is reversible as shown by a similar but potentially shifted current peak on the anodic scan. It is difficult to obtain a full 'fingerprint' representing the capacity current peaks in both forward and reverse scan respectively using RCV because of the instability of the DOPC bilayer at or below -1.0 V. Therefore, a triangular waveform was generated using the scope software where the applied potential excursion commenced at -1.25 V, decreased to -1.6 V followed by a subsequent increase to -0.9 V and return to -1.25 V. Three different configurations of bilayer (low density, intermediate density and high density) were found to exist on successively decreasing the electrode areas.

6.2.3.2 Potential step experiments

Potential step experiments were performed to investigate the permeability properties of DOPC bilayers supported on HMDE to Zn^{2+} at different applied negative potentials involving the faradaic reduction of Zn^{2+} to $\text{Zn}(\text{Hg})$. The basic principle of the Zn^{2+} experiments involves the suppression of the electrochemical reduction of Zn^{2+} in the presence of the DOPC bilayer because of the restricted access of metal ions to the mercury surface. The following procedure was used to investigate the permeability of the DOPC bilayer to Zn^{2+} ions. Following deaeration of the electrolyte, the DOPC bilayer was deposited on the electrode surface and a cyclic

voltammogram was recorded. After the formation of DOPC bilayer on the HMDE, 25 μL of the stock solution was added to the electrolyte to 0.2 mmol dm^{-3} Zn^{2+} concentration. Following addition of Zn^{2+} to the electrolyte and stirring for 30 s, voltage pulses from -0.85 V to potentials from -1.0 to -1.6 V were executed and the corresponding current transients were recorded. The standard redox potential of Zn is -0.95 V. After the pulsing programme had been performed, an RCV scan was recorded to ensure that the phospholipid bilayer had not degraded during the experiment. The current is sampled after a time interval of 10 ms from the beginning of the pulse. This specific time is used to allow complete decay of capacitive current. The data are plotted as current versus potential plots called sampled current voltammograms. All the potential step experiments were carried out on a freshly deposited DOPC bilayer on the Hg surface. The data from potential step experiments of uncoated Hg, DOPC monolayer and intermediate density DOPC bilayer on Hg were fitted to the Cottrell equation [19];

$$I = nFAD^{1/2}C/\pi^{1/2}t^{1/2} \quad \text{Equation-6.1}$$

n is the number of electron transferred in the redox reaction, F is the Faraday's constant (96500 C mol^{-1}), A is the area of electrode, C is the concentration of Zn^{2+} in electrolyte solution and D is the diffusion constant. The slope of the Cottrell plots were used to calculate the diffusion constants for Hg electrode and Hg supported DOPC monolayer and intermediate density DOPC bilayer.

Because of the restricted access of Zn^{2+} to the Hg surface in case of DOPC bilayer, the DOPC monolayer and bilayer do not obey the Cottrellian behaviour of linear diffusion and the diffusion constants for diffusion of Zn^{2+} to the DOPC monolayer and bilayer were small (section 6.3.2) compared to that on uncoated Hg electrode. Therefore, the kinetics of the electron exchange process at the surface becomes the slowest and hence the rate determining step. Therefore, kinetic analysis of the irreversible reduction of Zn^{2+} to Zn were performed using the equation of irreversible reduction of an electroactive species at a planar [19] electrode and the potential dependent rate constant (k) was determined;

$$I = nFAkC * \exp \left[\frac{k^2 t}{D} \right] \operatorname{erfc} \left[\frac{kt^{1/2}}{D^{1/2}} \right] \quad \text{Equation-6.2}$$

6.3.2.3 Electrochemical impedance

Impedance (Z) versus frequency measurements were carried out on the HMDE electrode coated with DOPC bilayer using frequencies logarithmically distributed from 65,000 to 0.1 Hz, with $\Delta V = 0.005V$ ac amplitude at potentials ranging from -1.0 to -1.6 V. The experimental conditions for the measurement of impedance were used exactly as described previously [20]. The impedance data were transformed to the complex capacitance plane and were expressed as real and imaginary frequency normalized admittances ($\operatorname{Re} Y\omega^{-1}$ and $\operatorname{Im} Y\omega^{-1}$), respectively. The values of $\operatorname{Re} Y\omega^{-1}$ plotted against $\operatorname{Im} Y\omega^{-1}$ in the complex capacitance plane for all values of frequency [20] always yield a single semi-circle corresponding to the RC element with no frequency dispersion for a series RC circuit containing an ideal capacitor. Curve fitting of the data was carried out using IGOR (Wavemetrics) in the same way as described previously [20-21]. The results of the impedance measurements are considered in terms of the properties of the phospholipid bilayer. Low density bilayer on HMDE is not stable to impedance measurements and degrades on application of a sinusoidal voltage.

Impedance model

The impedance data of DOPC coated electrodes were fitted to equation-6.3 below [20]:

$$Y = \frac{1}{R + 1/[(i\omega)^\beta ((A_s - A)/1 + (i\omega\tau)^\alpha) + A]} \quad \text{Equation - 6.3}$$

Y is admittance, R is the uncompensated solution resistance and τ is relaxation time constant. α is the coefficient which represents distribution of time constant around the most probable value (either 1 or less than 1) and β is a coefficient which is less than or equal to unity and has been shown to be inversely related to the homogeneity of the lipid layers [20]. A_s and A are the constant phase element constants and are used to calculate the capacitance values according to Sluyter's equation [22]. All the experimental data derived from the monolayer on the electrode were fitted to Eq.

(2). The six variable parameters: A , A_s-A , α , β , R and τ were obtained from the subsequent curve fitting of the $\text{Re } Y\omega^{-1}$ versus $\log \omega$ and $\text{Im } Y\omega^{-1}$ versus $\log \omega$ plots respectively. The mean of the coefficients or fit parameters (α , β , A_s-A_{inf} , A_{inf} and τ) is then graphed as fitting to the real versus imaginary admittance plots. The overall goodness of the fit was examined visually comparing the experimental and model, $\text{Re } Y\omega^{-1}$ and $\text{Im } Y\omega^{-1}$ versus $\log \omega$ plots.

Where A_s and A are related to capacitance as follows:

$$C_s - C = ((A_s - A) - A)\tau^{(1-\beta)}$$

$$C = [A * R^{(1-\beta)}]^{1/\beta}$$

C is identified as zero frequency capacitance of the monolayers and C_s-C is the additional low frequency capacitance element. The errors stated for these coefficients are treated according to error propagation rule for a mean function.

6.2.3.4 Interaction of DOPC bilayer with SiO₂ nanoparticles

Interactions of SiO₂ nanoparticles with the DOPC bilayer were studied by RCV using the same system as described above for the characterization of bilayer. The following procedure was used to study the interaction of SiO₂ nanoparticles with DOPC bilayer. SiO₂ nanoparticles (SM-30) from Sigma Aldrich were used to prepare a 3 % w/v stock solution of each of them using 18.2 MΩ MilliQ water. Following the deposition of DOPC bilayer on the electrode surface, the calculated amount of SiO₂ nanoparticles (to keep the same solution concentration for all nanoparticle) were injected into the electrolyte with added buffer (pH 7.4) from their stock solution. After the addition of SiO₂ nanoparticles, multiple numbers of RCV scans of DOPC bilayer deposited on HMDE were recorded with an interval of 1 s between each scan at a scan rate of 40 Vs⁻¹ along with simultaneous stirring of the electrolyte solution.

6.3 Results and discussion

6.3.1 Bilayer formation

A perfect DOPC monolayer assembled on Hg electrode displays two sharp and descriptive capacitance current peaks 1 and 2 at -0.94 and -1.0 V respectively on application of a negatively increasing applied potential (Figure 6.1-black) due to the phase transitions occurring in the monolayer. The capacitance current peak-2 has been explained as the transformation of a porous monolayer to the bilayer patches in several past studies [16,24-25]. Further broad capacitance current peaks-3 and 4 occurring at higher negative potentials (-1.25 to -1.3 V) are shown to exhibit the structures with a thickness three times to that of a monolayer which might explain the formation of liposomal structures [26]. Hence in the potential region negative to the capacitance current peak-2 representative of bilayer formation, there is a significant likelihood to stabilize this bilayer on the Hg surface after its formation under appropriate conditions such as applied electric potential. The appearance of the capacitance current peaks characteristic of the DOPC monolayer during a negative potential excursion between -0.9 and -1.65 V indicates the presence of monolayer (Figure 6.1-red).

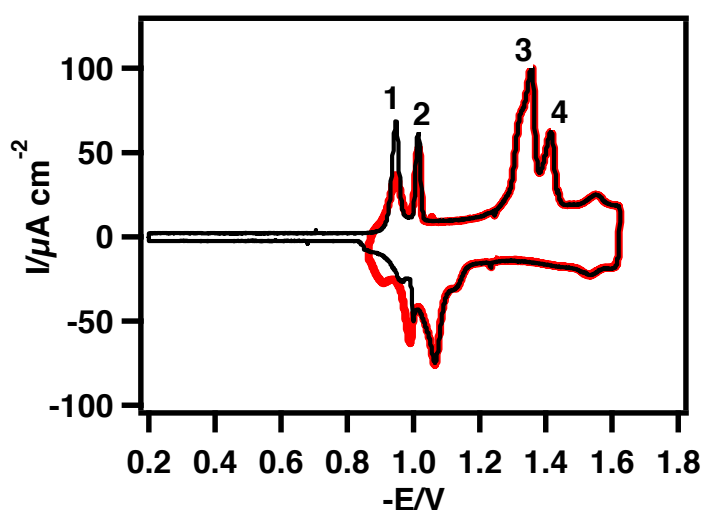


Figure 6.1: Capacitance current versus potential plots of DOPC coated HMDE in 0.1 mol dm^{-3} KCl with added phosphate buffer ($0.001 \text{ mol dm}^{-3}$) measured by RCV at 40 Vs^{-1} in potential range -0.2 to -1.65 V (black) and -0.9 to -1.65 V (red).

The property of HMDE having an adjustable area is manipulated to transform a monolayer into the bilayer. The area of HMDE coated with DOPC monolayer is decreased in small amounts of $\sim 0.0005 \text{ cm}^2$. Preliminary reduction in the electrode area leads to the formation of a relatively compact monolayer as seen by a relative increase in height of capacitance current peak-1 (Figure 6.2-red) due to the movement of lipid molecules close to each other followed by the movement of excessive lipid molecules to build up the opposing leaflet of bilayer on successive reduction of electrode area. The beginning of the bilayer formation is marked by the start in suppression of capacitance current peak-1 and 2 and a complete transformation of a monolayer to a bilayer is manifested by thorough suppression of capacitance current peaks and formation of a flat low capacitance region at these potentials parallel to a decrease in resolution and increase in sharpness of the capacitance current peaks-3 and 4 at higher negative potential.

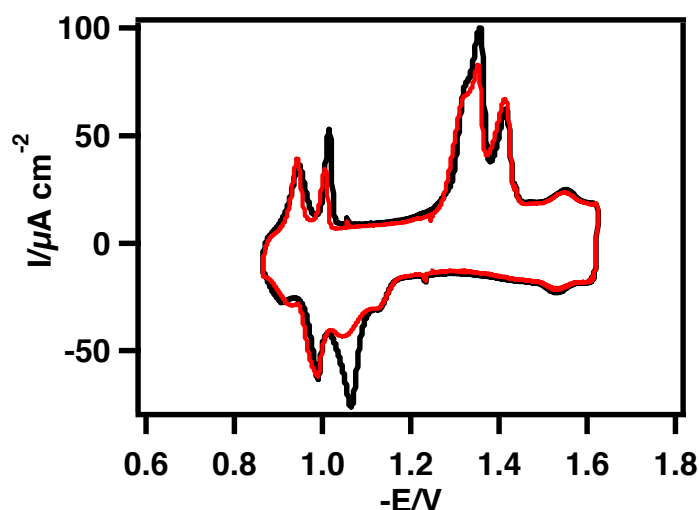


Figure 6.2: Capacitance current versus potential plots of DOPC coated HMDE in 0.1 mol dm^{-3} KCl with added phosphate buffer ($0.001 \text{ mol dm}^{-3}$) measured by RCV at 40 Vs^{-1} in potential range -0.9 to -1.65 V with electrode area ratio of 1 (black):0.88 (red).

Figure 6.3 displays the capacitance current-potential plots for some of the significant stages during the transformation of the DOPC monolayer (a) to bilayer (b-d) on the surface of HMDE. Three major different types of bilayers were encountered depending on the density of DOPC molecules varying in the resolution and

sharpness of the capacitance current peaks representing the phase transition in the cathodic and anodic scan. The DOPC bilayer for which the area of the electrode is reduced to 0.59 times to the initial electrode area (Figure 6.3 (b)) and is termed as a low density bilayer. On decreasing the electrode area further, the two capacitance current peaks 3 and 4 merge together at an electrode area 0.5 times smaller to initial electrode area as shown in Figure 6.3 (c). This bilayer is termed as intermediate density in this study. A further increase in lipid density of the bilayer by successive decrease in the area of the electrode leads to the formation of high density bilayer (Figure 6.3 (d)) with an area of electrode reduced to 0.4 times to the initial electrode area.

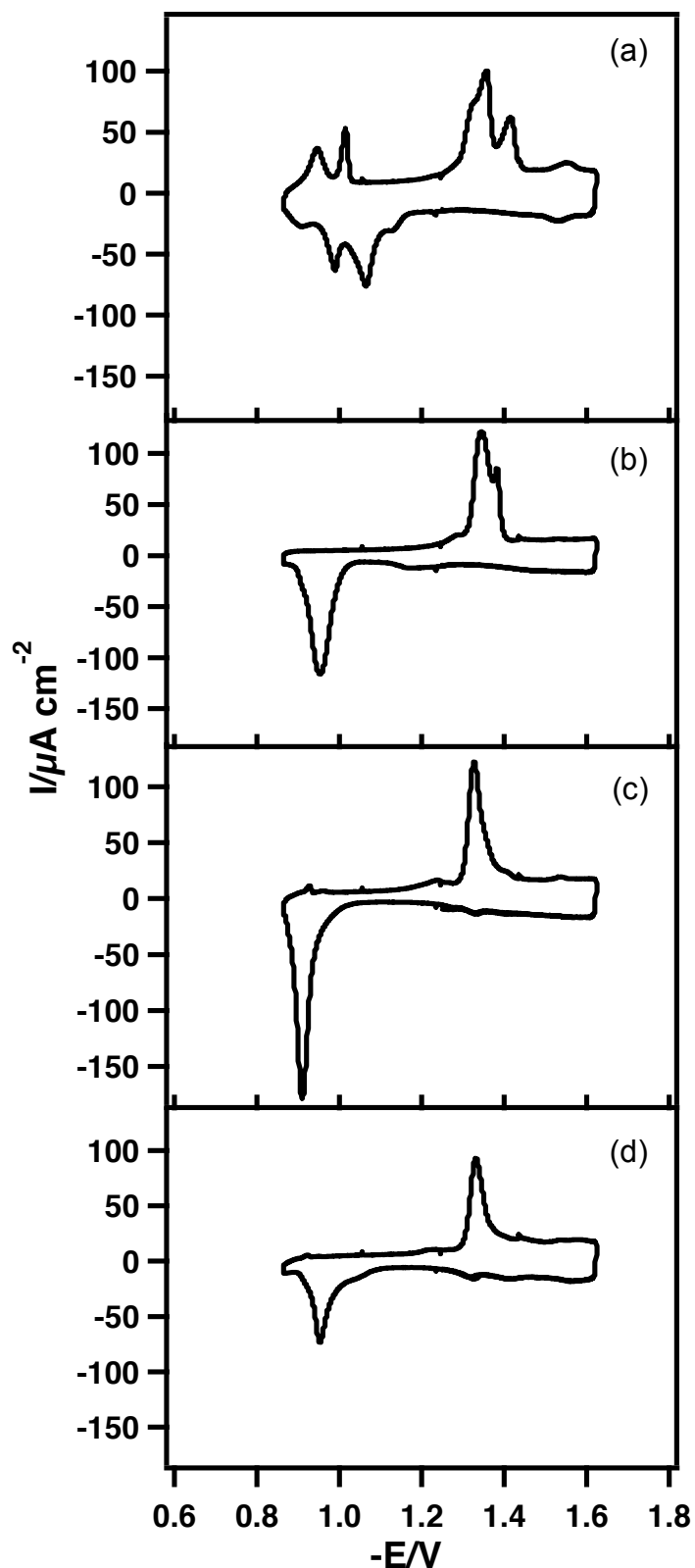


Figure 6.3: Capacitance current versus potential plots of DOPC bilayers deposited on HMDE in 0.1 mol dm^{-3} KCl with added phosphate buffer ($0.001 \text{ mol dm}^{-3}$) measured by RCV at 40 Vs^{-1} (a) monolayer (b) low density (c) intermediate density (d) high density.

Subsequent compression of a low density bilayer to a high density bilayer also causes the capacitance current in the constant capacitance region to decrease as seen in the inset of Figure 6.4.

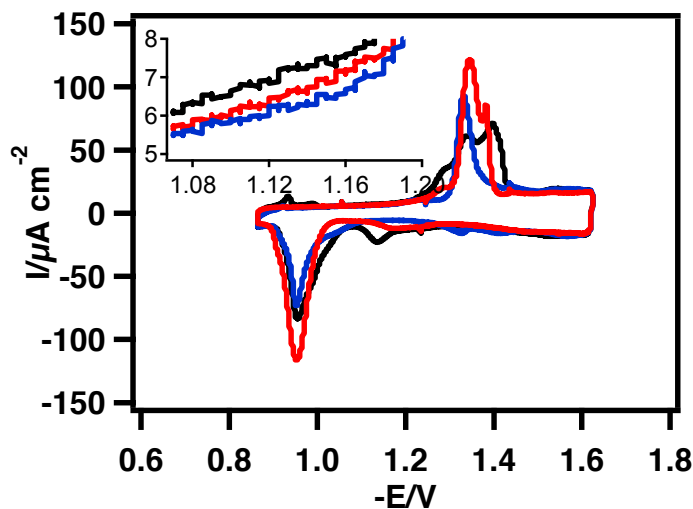


Figure 6.4: Capacitance current versus potential plots of DOPC coated HMDE in 0.1 mol dm^{-3} KCl with added phosphate buffer ($0.001 \text{ mol dm}^{-3}$) measured by RCV at 40 Vs^{-1} in potential range -0.9 to -1.65 V with electrode area ratio of 0.67 (black): 0.59 (red): 0.39 (blue).

After these experiments, the electrode was expanded back to original position to observe any changes in the monolayer due to loss of lipid to the capillary walls or electrolyte solution due to contraction of the lipid coated electrode. Figure 6.5 shows the capacitance current-potential plots of DOPC coated HMDE before and after the area altering experiments. It can be seen that the capacitance current-potential plots before and after the drop shrinking experiments looks similar and no significant change is observed in these plots suggesting that lipid stays on the electrode surface during the course of experiments with no loss to surrounds.

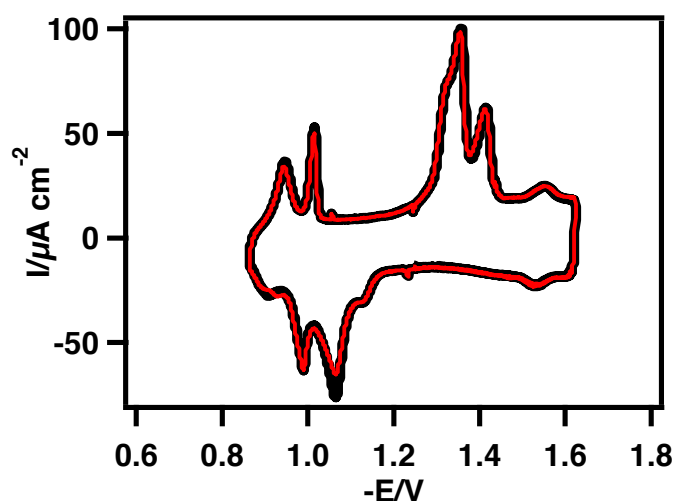


Figure 6.5: Capacitance current versus potential plots of DOPC coated HMDE in 0.1 mol dm^{-3} KCl with added phosphate buffer ($0.001 \text{ mol dm}^{-3}$) measured by RCV at 40 Vs^{-1} before decreasing the electrode area to form bilayer and after increasing the electrode area to restore monolayer shown as black and red respectively.

6.3.2 Permeability studies

These studies investigated the transport of Zn^{2+} through the DOPC bilayers in a potential range from -1.0 to -1.6 V . A complete layer will prevent Zn^{2+} from reaching the electrode surface and any ion transport is a result of the defects/pores in the bilayer. DOPC monolayer assembled on Hg electrode is found to be permeable to ions in the potential range of -1.0 to -1.6 V [27]. Figure 6.6 shows the current (I)-time (t) transients of HMDE and HMDE coated with DOPC monolayer and intermediate density bilayer in the presence of Zn^{2+} in the electrolyte solution at -1.1 V . The current decay for Zn^{2+} reduction is essentially greater for the DOPC bilayer on the Hg electrode compared to the uncoated Hg electrode. In case of a DOPC bilayer, smaller currents for Zn^{2+} reduction indicate the restricted access of Zn^{2+} to the Hg surface due to the phospholipid layer. In spite of the permeability of DOPC monolayer at this potential, it is found to show lower currents for Zn^{2+} permeation to Hg electrode compared to the uncoated Hg electrode but these currents are still higher than that of DOPC bilayer. The sampled current at 10 ms from these I-t transients at different potentials is plotted against the potential to obtain the sampled current voltammograms for each type of bilayer, monolayer and uncoated Hg electrode.

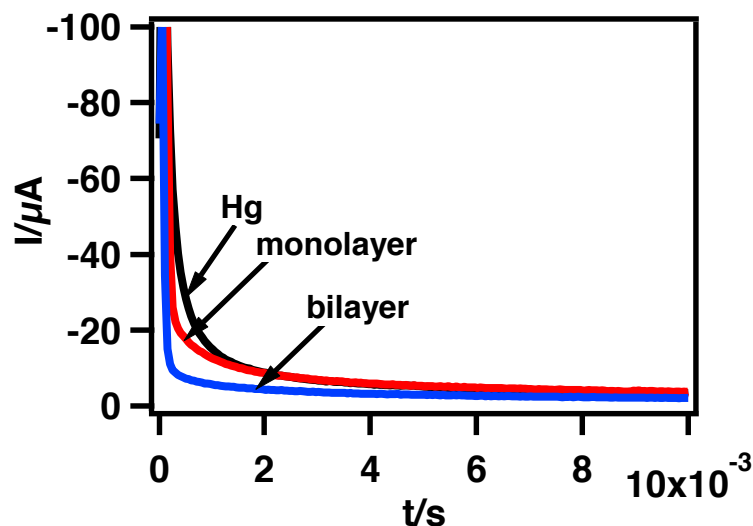


Figure 6.6: Current (I) - time (t) transients of uncoated HMDE, DOPC monolayer and an intermediate density DOPC bilayer in the 0.1 mol dm^{-3} KCl containing $0.2 \text{ mmol dm}^{-3} \text{ Zn}^{2+}$ at -1.1 V , acquired using chronoamperometry.

Figure 6.7 shows the sampled current voltammograms of Zn^{2+} at the three bilayer types deposited on Hg in the electrolyte solution. It is clear that the permeability of all three bilayer configurations is either lower or approaches that of the monolayer and uncoated Hg electrode. For uncoated Hg and DOPC monolayer coated Hg electrode, the current remains almost constant at all potentials varying between -4.7 to $5.4 \mu\text{A}$ and $3\text{-}4 \mu\text{A}$ respectively. Both the low density and high density bilayers showed a current between $2.3\text{-}3.8 \mu\text{A}$ which either increases gradually or remains constant on increasing the applied negative potential as shown in Figure 6.7 (a) and (c). The intermediate density bilayer is less permeable compared to low and high density bilayers at potentials below -1.3 V (Figure 6.7 (b)). The current for Zn^{2+} reduction are significantly lower (below $1.8 \mu\text{A}$) at potentials -1.1 to -1.2 V before the onset of the capacitance current peak representing a phase transition. An increase in sampled currents at -1.3 to -1.4 V indicates the increase in permeability of the membrane to Zn^{2+} . The reduction currents decrease at potentials negative to those characterising the capacitance current peak indicating a decrease in the permeability of the bilayer to the Zn^{2+} .

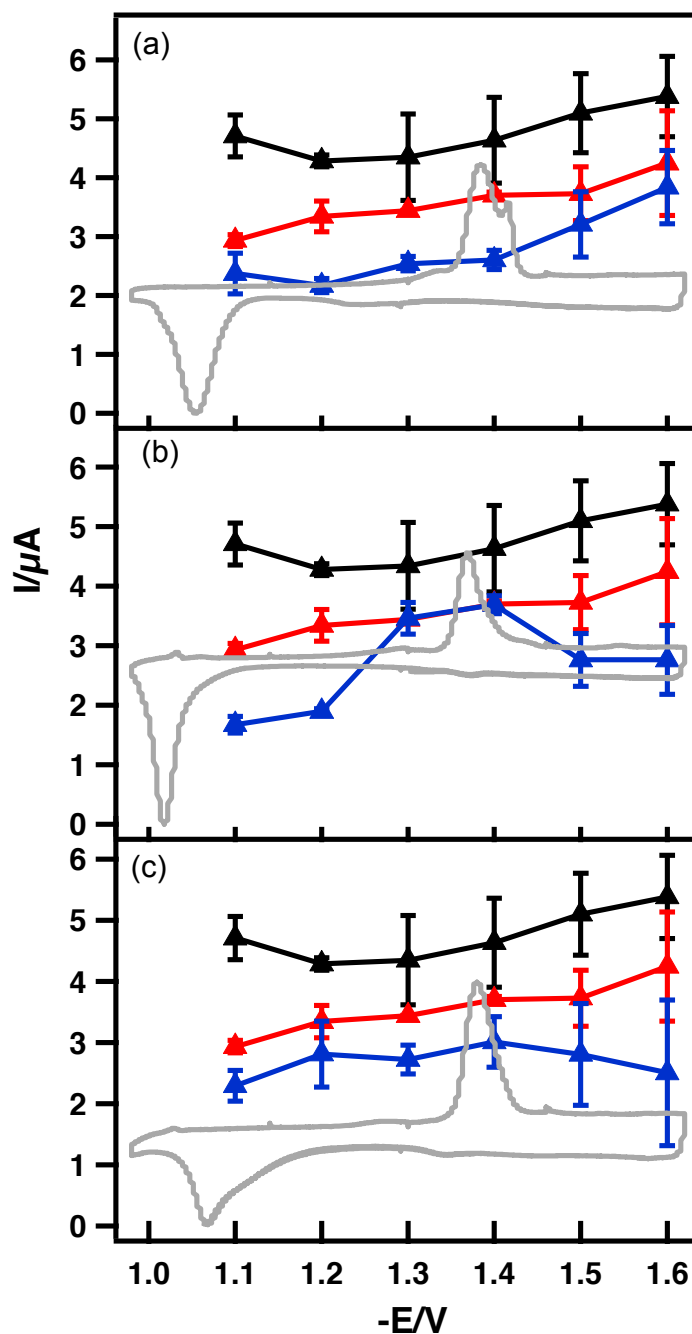


Figure 6.7: Sampled current voltammograms of uncoated HMDE (black), DOPC monolayer (red) and DOPC (a) low (b) intermediate and (c) high density bilayer (blue) in the 0.1 mol dm^{-3} KCl containing 0.2 mmol dm^{-3} Zn^{2+} , acquired using chronoamperometry and all the currents sampled at 10 ms.

Figure 6.8 displays the Cottrell plots of uncoated Hg electrode at different applied potentials. A linear fit to these plots indicate that the reduction of Zn^{2+} at the uncoated Hg electrode surface is Cottrellian. At -1.6 V , the fit is not so good because

of contribution of currents from both Zn^{2+} reduction and hydrogen evolution processes to the overall current. The diffusion constants for the diffusion of Zn^{2+} ions from bulk of electrolyte solution to the uncoated Hg is calculated from the slopes of the plots as $6.8 \times 10^{-6} \pm 0.0000012 \text{ cm}^2 \text{ s}^{-1}$ and is almost constant in the potential range -1.1 to -1.5 V.

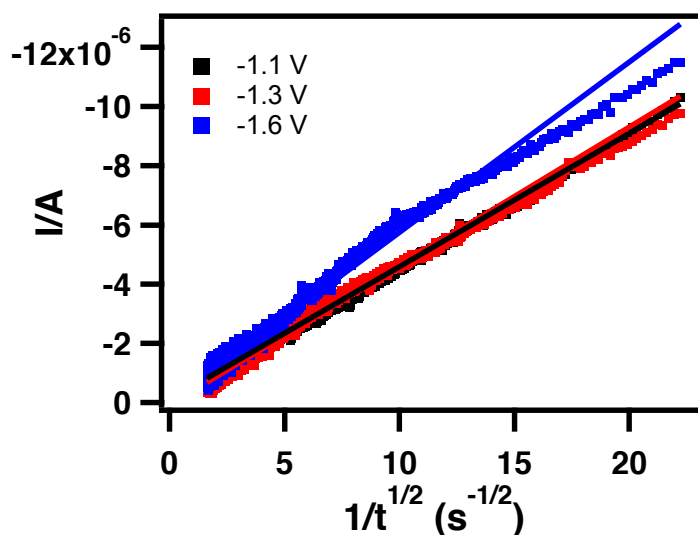


Figure 6.8: Plots of the I vs $1/t^{1/2}$ of uncoated HMDE in the $0.1 \text{ mol dm}^{-3} \text{ KCl}$ containing $0.2 \text{ mmol dm}^{-3} \text{ Zn}^{2+}$ at different potentials, acquired using chronoamperometry. Solid lines represent the linear fit to the data.

The I - t data for DOPC monolayer and intermediate density bilayer supported on Hg were also plotted as Cottrell plots and is shown in Figure 6.9 (a) and (b) respectively. The linear fits to Cottrell plots for DOPC monolayer and intermediate density bilayer supported on Hg apparently looks good but the diffusion constants calculated from the fits are significantly smaller than that for the uncoated Hg electrode. The calculated Zn^{2+} diffusion constant on DOPC monolayer coated Hg is $3.32 \times 10^{-6} \pm 0.00000037 \text{ cm}^2 \text{ s}^{-1}$ and is almost constant in potential range from -1.1 to -1.5 V as shown by small value of standard deviation. For the intermediate density DOPC bilayer, the diffusion constants varied considerably depending on the applied potential. The diffusion constant is found to be significantly low at potentials between -1.1 to -1.2 V with a value of $1.03 \times 10^{-6} \pm 0.000000030 \text{ cm}^2 \text{ s}^{-1}$. The diffusion constant increases to $3.23 \times 10^{-6} \pm 0.00000065 \text{ cm}^2 \text{ s}^{-1}$ at potentials

between -1.3 to -1.4 V followed by a decrease to $1.83 \times 10^{-6} \pm 0.00000008 \text{ cm}^2 \text{ s}^{-1}$ at potentials between -1.5 to -1.6 V.

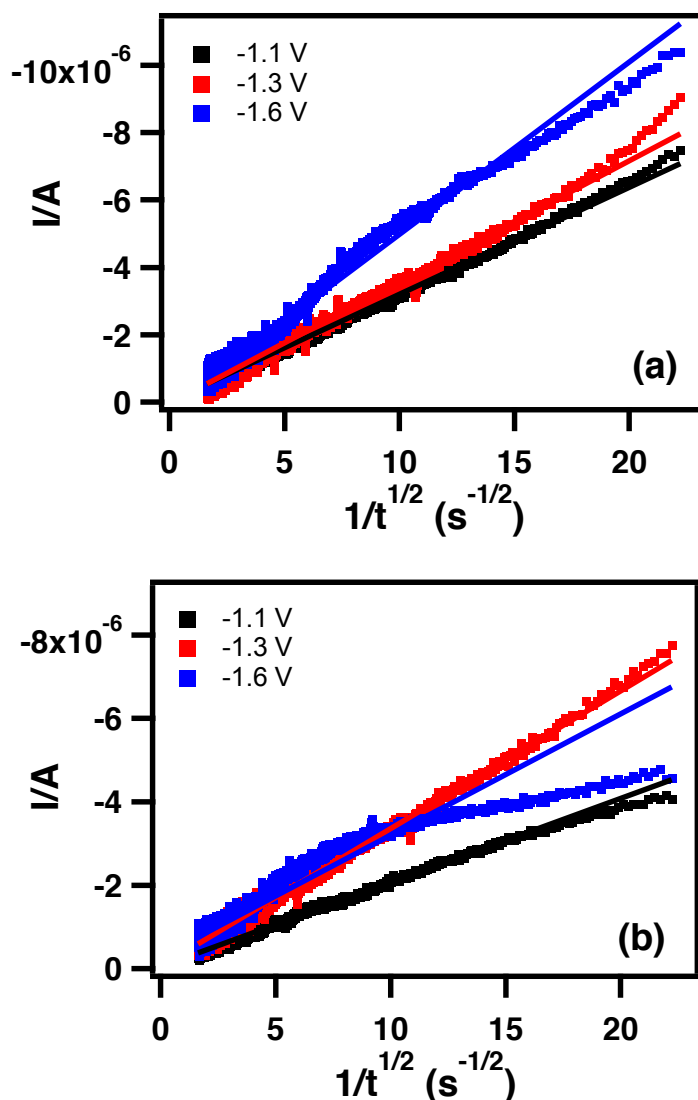


Figure 6.9: Plots of the I vs $1/t^{1/2}$ of (a) DOPC monolayer and (b) an intermediate density DOPC bilayer in the 0.1 mol dm^{-3} KCl containing 0.2 mmol dm^{-3} Zn^{2+} at different potentials, acquired using chronoamperometry. Solid lines represent the linear fit to the data.

The small values of diffusion constant of Zn^{2+} ions for reduction at intermediate density DOPC bilayer coated Hg compared to the uncoated Hg surface and variation in diffusion constant with applied potential suggests the presence of a kinetically controlled process occurring at the surface of Hg-DOPC bilayer. Therefore, the I - t data for intermediate density bilayer is fitted to the equation of irreversible reduction

of an electroactive species at a planar electrode described in equation 6.2 that takes into account both the diffusion and kinetically controlled processes simultaneously occurring at larger and smaller times respectively.

Figure 6.10 shows the I-t transients of the intermediate density bilayer (red) at different applied potentials and the corresponding fits to equation-6.2 (black). Figure 6.10 (a) shows that the model described in equation-6.3 does not fit precisely to the current-time dependence at less negative potentials (-1.1 V) due to the changes in the bilayer conformation following application of potential pulse which is also noticeable at the beginning of pulse at -1.2 and -1.5 V. Whereas in the potential regime, -1.2 to -1.6 V, the model fits well to the experimental data suggesting that the reduction of Zn^{2+} at bilayer surface at these potentials is kinetically controlled at smaller times and diffusion controlled at larger times (Figure 6.10 (c) and (d)).

The rate constants for reduction of Zn^{2+} at DOPC bilayer at different potential obtained from equation-6.2 as a fit parameter are plotted against potential in Figure 6.11. The values of rate constant for Zn^{2+} reduction are directly related to the permeability of the bilayer and establish that the permeability of DOPC bilayer to Zn^{2+} ions is low at less negative applied potential between -1.1 to -1.2 V due to restricted access of the Zn^{2+} ions to the Hg surface. The permeability of the DOPC bilayer increases on increasing the potential upto -1.4 V followed by a decrease at -1.5 V and a rise thereafter. The rate constants obtained for Zn^{2+} reduction at DOPC bilayer at different potentials are summarized in Table 6.1 below.

Table 6.1: Potential dependant rate constant for Zn^{2+} reduction at intermediate density bilayer supported on Hg electrode.

Potential/V	$k/cm\ s^{-1}$
-1.1	0.0016765 ± 0.0000268
-1.2	0.0041659 ± 0.0000369
-1.3	0.021715 ± 0.000204
-1.4	0.040139 ± 0.000387
-1.5	0.0065871 ± 0.0000503
-1.6	0.089806 ± 0.0307

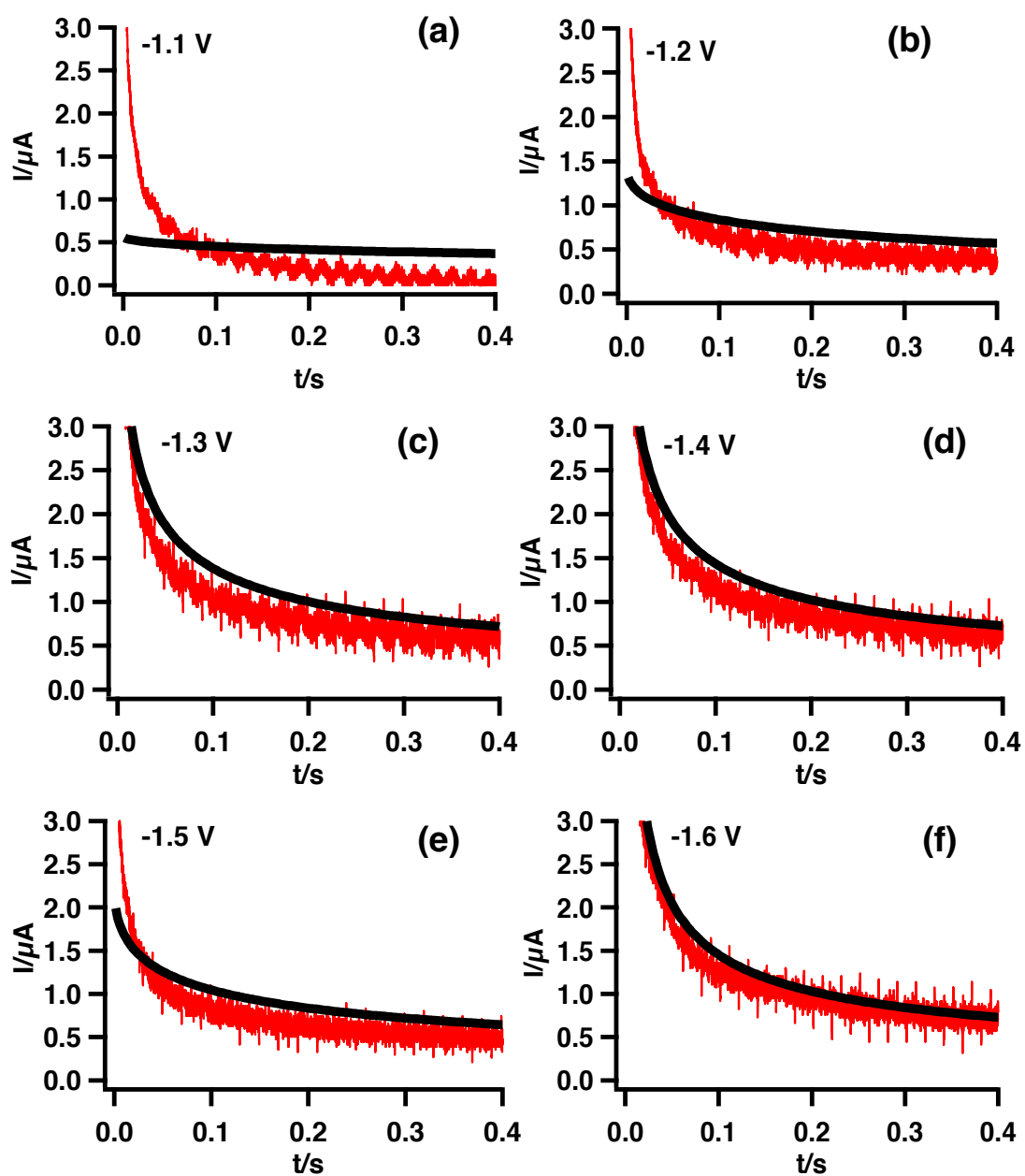


Figure 6.10: I-t transients of intermediate density bilayer (red) at potentials shown in the figure in the 0.1 mol dm^{-3} KCl containing 0.2 mmol dm^{-3} Zn^{2+} , acquired using chronoamperometry with corresponding fits (black) to equation-6.2.

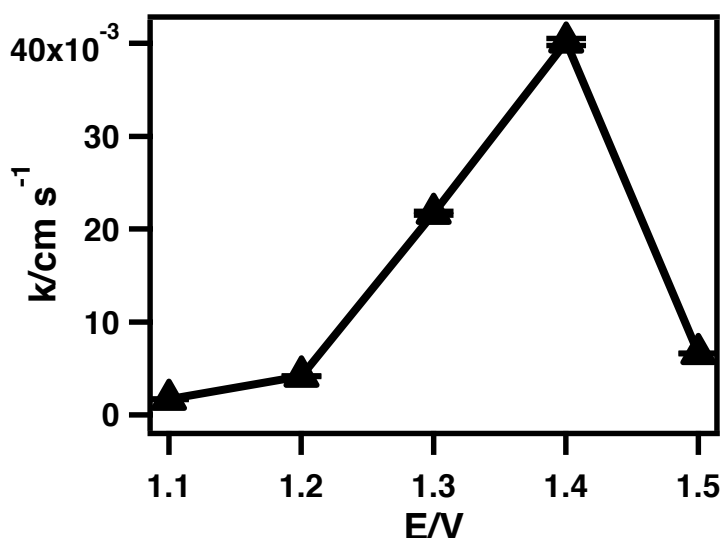


Figure 6.11: Rate constant vs potential plot of intermediate density bilayer on Hg in the 0.1 mol dm⁻³ KCl containing 0.2 mmol dm⁻³ Zn²⁺.

6.3.3 Impedance studies

The bilayer configurations were investigated for their impedance properties. The low density bilayer was found to degrade during the impedance measurements but was able to fully recover after potential cycling.

Intermediate density bilayer

The model described in equation-6.3 is fitted to the impedance data derived from an intermediate density DOPC bilayer at different potentials consistent with the existence of bilayer. This model is fitted to the real and imaginary normalised admittance versus $\log(\omega^{-1})$ plots separately as shown in the Figure 6.12. The mean of the coefficients or fit parameters (α , β , A_s - A_{inf} , A_{inf} and τ) obtained from the real and imaginary normalised admittance versus logarithmically distributed angular frequencies is graphed as fitting to the real versus imaginary normalised admittance plots. Figure 6.13 displays a series of plots of impedance data transformed to complex capacitance plane derived from an intermediate density DOPC bilayer acquired at potentials between -1.0 and -1.2 V subsequent to 50 mV potential increments and their fits to equation-6.3.

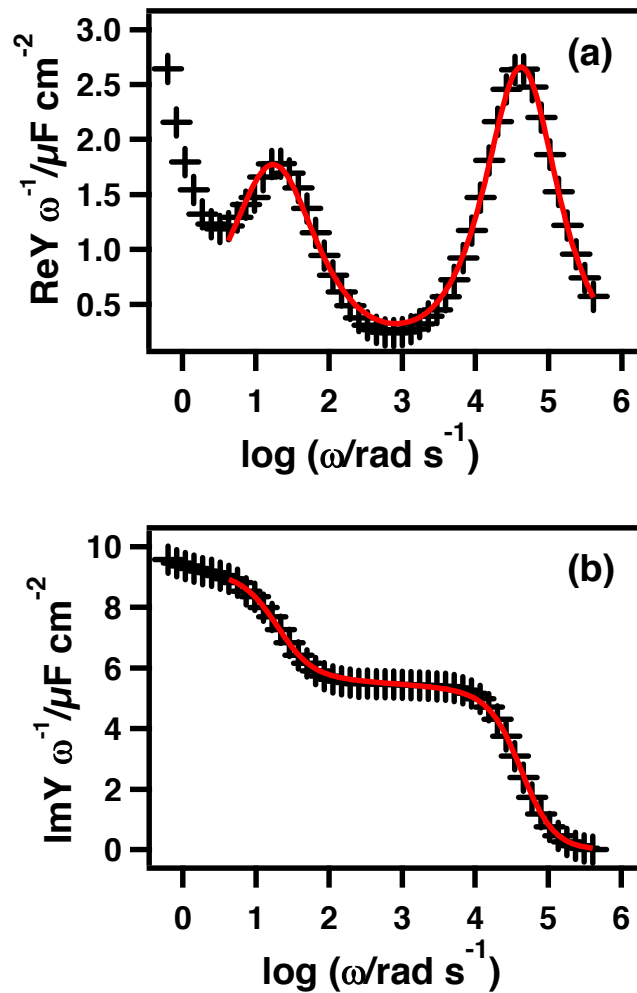


Figure 6.12: Plots (crosses) of (a) $\text{Re} Y \omega^{-1}$ and (b) $\text{Im} Y \omega^{-1}$ versus $\log \omega$ derived from impedance data of the DOPC-coated electrode in 0.1 mol dm^{-3} KCl buffered with $0.001 \text{ mol dm}^{-3}$ phosphate buffer at -1.1 V together with fits (solid red line) using equation-6.3.

The first semicircle in the capacitance plots corresponds to the RC charging process and shows that the DOPC bilayer on Hg behaves as a capacitor. Also displayed in Figure 6.13 is a significant dielectric relaxation at lower frequencies in the form of an additional capacitive second semicircle on the plots in the complex capacitance plane. β is obtained as one of the fitting parameters of equation-6.3 and is fractional between 1 and $\frac{1}{2}$ for an ideally smooth surface and porous surface respectively giving information on the heterogeneity of the capacitor. A β value less than 1 indicates the roughness at the interface [20]. In the potential range between -1.0 and -1.2 V, β remains high and almost constant but less than 1 as in all plots in Figure 6.13. Figure 6.14 displays the complex capacitance plots of intermediate density bilayer and their fit to equation-6.3 at potential from the onset of the phase transition at -1.25 V and at all the potentials characterizing the phase transition up to -1.4 V.

It can be clearly seen that the second semicircle becomes increasingly resolved and significant (Figure 6.14) in this potential range. At potentials more negative to those characterizing the phase transition, β decreases significantly and the second semicircle tends to become less distinct transforming into a tail. The value of β has been found to have consistently low error of estimation shown as SD in the complex capacitance plots.

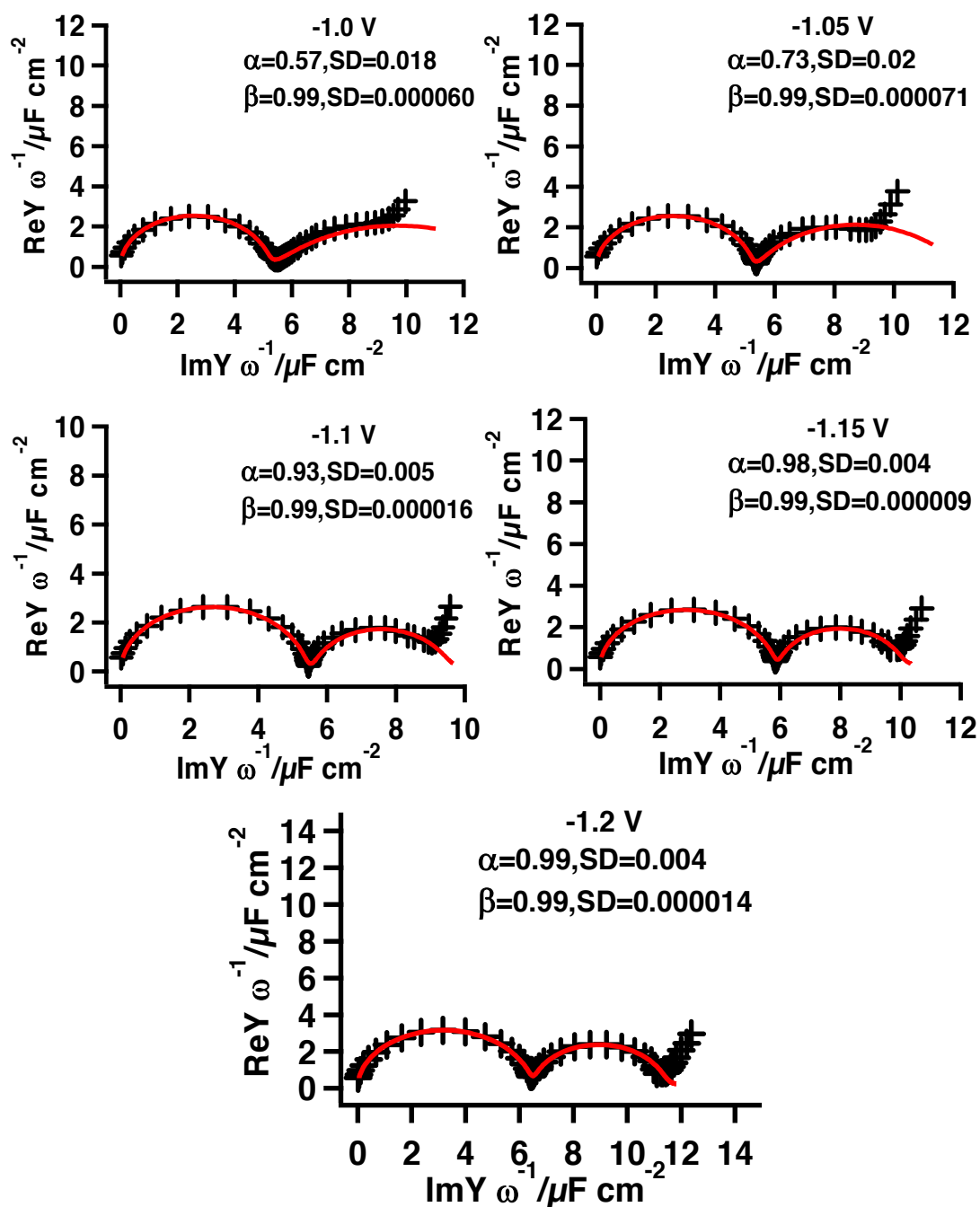


Figure 6.13: Impedance data transformed to complex capacitance plane derived from the intermediate density DOPC bilayer supported on Hg in 0.1 mol dm⁻³ KCl containing 0.001 mol dm⁻³ phosphate buffer at the potentials indicated on the diagram. Data are represented by cross and equation-6.3 fits are the solid red lines. α and β values with errors (SD) from the fits are indicated on the diagram.

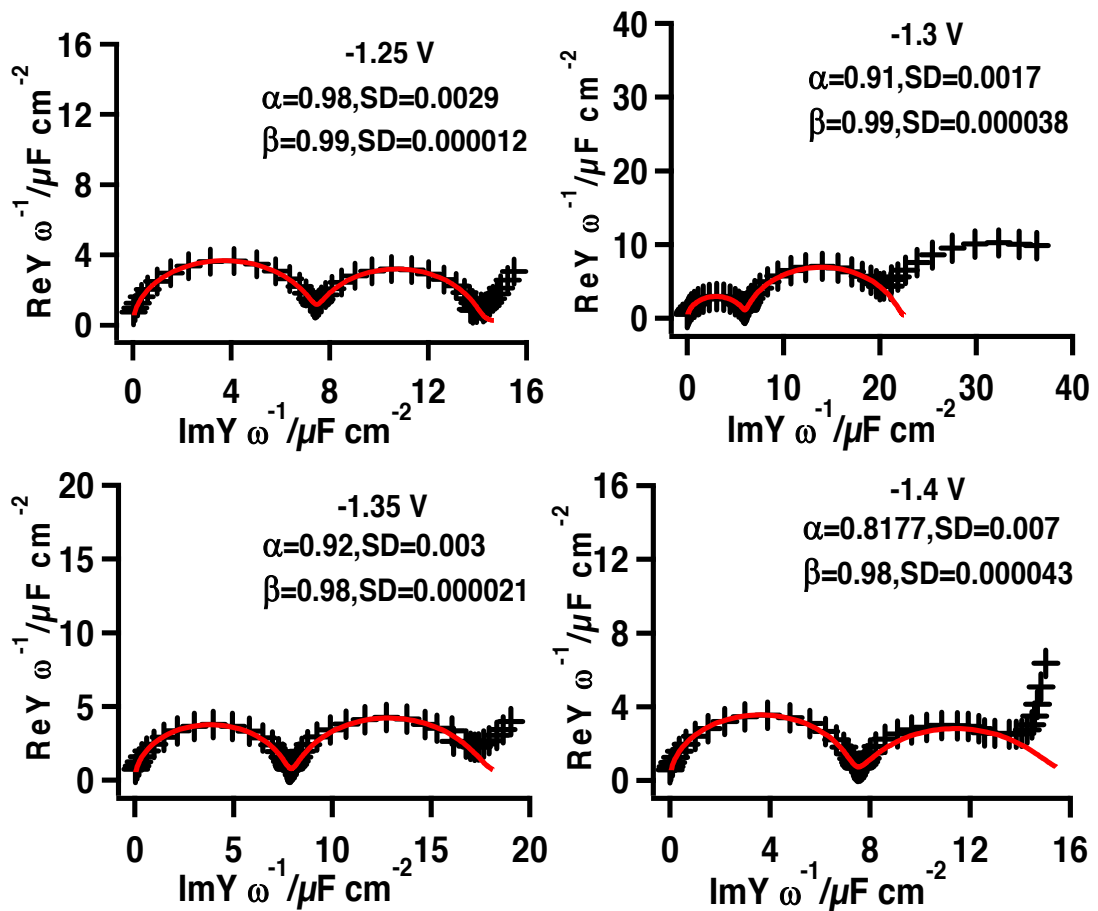


Figure 6.14: Impedance data transformed to complex capacitance plane derived from the intermediate density DOPC bilayer supported on Hg in 0.1 mol dm^{-3} KCl containing $0.001 \text{ mol dm}^{-3}$ phosphate buffer at the potentials indicated on the diagram. Data are represented by cross and equation-6.3 fits are the solid red lines. α and β values with errors (SD) from the fits are indicated on the diagram.

α is another fitting parameter having a value of 1 or less and is related to the distribution of relaxation time of the dielectric [20]. For intermediate density DOPC bilayer on Hg, the value of α is found low (< 0.6) at -1.0 V and increases progressively at higher negative potentials becoming close to 1 as the potential of the phase transition is approached as shown in Figure 6.13 and 6.14. At potentials negative to those characterizing the phase transition, α is decreased.

Figure 6.15 (a) and (b) summarizes the variation in the α and β respectively derived from the fitting of experimental impedance data to equation-6.3 for the intermediate density bilayer with changes in applied potential. An increase in the α value close to

1 on increasing the applied negative potential corresponding to the phase transition indicates an increase in significance of dielectric relaxation involving ionic movement (non-Debye type relaxations). For any movements or changes involving lipid molecules, α would be more dispersed and less than 1. A gradual decrease in α value on subsequent increase in negative potential indicate a lower significance of involvement of ion penetration in the Debye relaxation. In contrast, β remains almost constant or increases only slightly on increasing the negative potential corresponding to that of the phase transition. It means that surface roughness either remains unchanged or becomes smooth at these potentials. At more negative potentials, an essential decrease in β is related to increased porosity of the bilayer solution interface.

The extrapolation of the first semicircle to the $\text{Im } Y\omega^{-1}$ axis at a low frequency is termed the zero frequency capacitance (ZFC). Among the fit parameters, C is identified with ZFC [20]. The zero frequency capacitance ($\sim 5 \mu\text{F cm}^{-2}$) is nearly constant between the potential -1.0 and -1.1 V and increases to $\sim 7.5 \mu\text{F cm}^{-2}$ with an increase in applied negative potential (Figure 6.15 (c)) suggesting a decrease in the thickness of the bilayer and/or ingress of electrolyte. A small insignificant decrease in ZFC at -1.3 V, the potential consistent with phase transition indicates an increased thickness of the DOPC bilayer. The additional capacitive element C_s - C in the DOPC bilayer also relates to the low frequency relaxations [20]. Figure 6.15 (d) shows the variation in C_s - C derived from fits to admittance data on varying the negative applied potential for the intermediate density DOPC bilayer. It can be seen clearly that the extra capacitive element and hence the dielectric dispersion at low frequencies becomes increasingly significant at higher negative potential corresponding to the phase transition and the ionic penetration associated therewith.

The relaxation time of the dielectric known as time constant (τ) is also related to the low frequency relaxations [20] and ionic penetration. Figure 6.15 (e) displays the τ derived from the fit to experimental data versus potential plot of an intermediate density DOPC bilayer on Hg. The plot shows a minimum in the τ at the potential corresponding to the phase transition and an increase at higher negative potentials. The minimum in τ shows the decrease in the dielectric relaxation time due to

increased ionic movements during the phase transition which correlates very well with increase permeability of the bilayer to Zn^{2+} in potential step experiments.

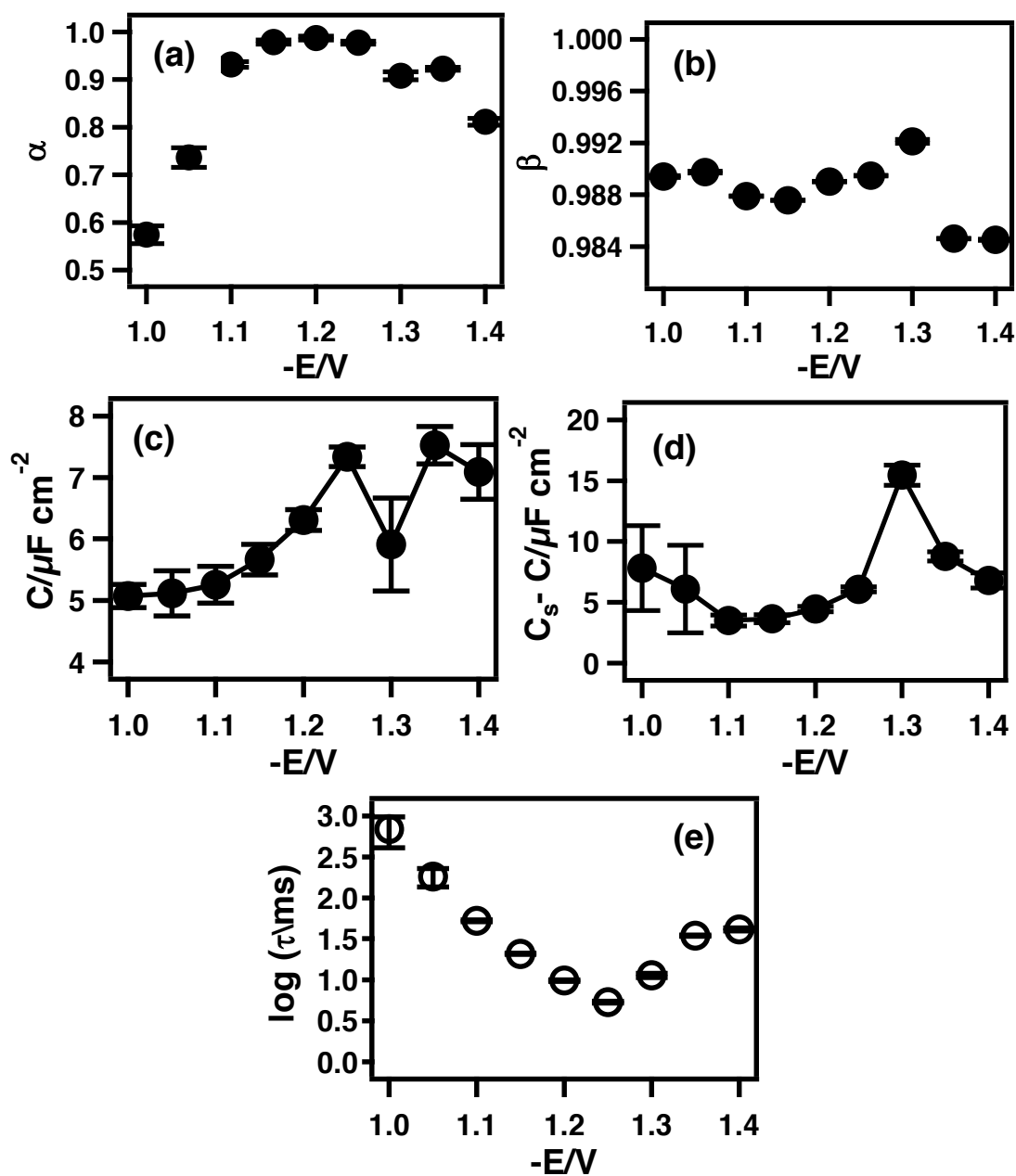


Figure 6.15: (a) α , (b) β , (c) C , (d) $C_s - C$ and (e) τ values derived from fits to admittance data using equation-6.3 for the intermediate density DOPC bilayer on Hg as a function of the potential.

6.3.4 Interaction of DOPC bilayer with SiO₂ nanoparticles

Figure 6.16 displays the capacitance current-potential plots of three DOPC bilayer configurations on Hg in the presence and absence of 12.5 % of SM-30 silica nanoparticles in the electrolyte solutions at different exposure times. It can be seen that location of capacitance current peak representing the underlying phase transition in the I-E plot is altered significantly both in anodic and cathodic scans at different exposure times. Interaction of nanoparticles with low density bilayer results in the depression of the bilayer capacitance current peaks and appearance of monolayer capacitance current peaks at more positive potentials (Figure 6.16 (a)). It is noticeable that the bilayer capacitance current peak in anodic scan is shifted to more negative potential considerably on increasing the sample exposure time.

Intermediate and high density DOPC bilayer/SiO₂ interactions results in the suppression of capacitance current peak in the cathodic scan in addition to a negative shift of capacitance current peak in anodic scan (Figure 6.16 (b) and (c)). The suppression in the capacitance peak with no essential change in capacitance at potentials -1.0 to -1.2 V shows that these silica nanoparticles adsorb and interact with DOPC bilayer making it more rigid decreasing its fluidity. This is also supported by the work of Zhang et al, according to which, small sized silica nanoparticles tend to adsorb and pack at the Hg supported monolayer surface having an overall freezing effect [28]. The shift in capacitance current peak in anodic scan to higher negative potentials indicates the shortening of the onset of reverse process. More work is needed to be done to understand the mechanism of interaction of these nanoparticles with DOPC membranes.

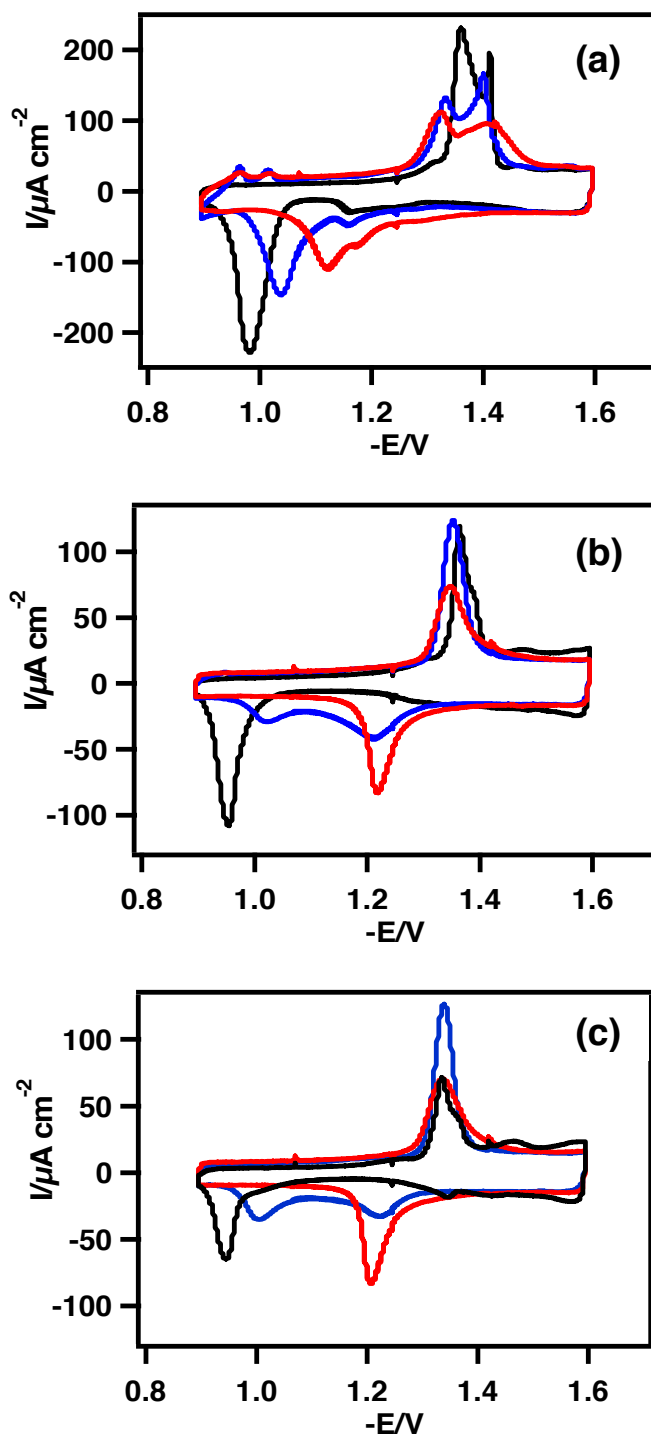


Figure 6.16: Capacitance current versus potential plots of (a) low density (b) intermediate density (c) high density DOPC bilayers deposited on HMDE in 0.1 mol dm⁻³ KCl with added phosphate buffer (0.001 mol dm⁻³) (black) containing 0.0012 % of SM-30 silica nanoparticles at 40 Vs⁻¹ after 45 s (blue) and 200 s (red) exposure time.

6.4 Conclusion

- (1) The DOPC bilayers on Hg show a reversible, sharp and characteristic capacitive current peak at ~ -1.3 V due to an underlying phase transition process occurring in the response to applied electric fields.
- (2) These bilayers are significantly less permeable to Zn^{2+} at less negative potentials between -1.1 to -1.2 V compared to monolayer and uncoated Hg electrode and their permeability increases at higher negative potential between -1.3 to -1.4 V.
- (3) Dielectric relaxations of the DOPC bilayer on voltage application in impedance measurements represent the ion movements across the bilayer that become increasingly significant at higher negative potentials between -1.2 to -1.4 V due to increased permeability of the bilayer to ions at these potentials.
- (4) DOPC bilayer supported on Hg interacts with the silica nanoparticle resulting in a negative potential shift of the anodic capacitance current peak in the capacitance potential profile. This property of the bilayer resulting in a change in the position of the capacitance current peak in the capacitance potential profile in the presence of biological compounds can be exploited to investigate the molecular scale interactions of membrane active compounds of biological relevance in detail leading to the application of Hg supported bilayer in biosensor industry.

Future work

DOPC bilayer supported on Hg needs considerable work to investigate the origin of potential induced phase transition, mechanism underlying the transition process, structural changes occurring in the bilayer during the phase transition and various factors affecting the phase transition such as electrolyte and pH of electrolyte solution etc.

6.5 References

- [1] R. Naumann, S.M. Schiller, F. Giess, B. Grohe, K.B. Hartman, I. Kärcher, I. Köper, J. Lübben, K. Vasilev, W. Knoll, *Langmuir*, 19 (2003) 5435-5443.
- [2] A.L. Plant, *Langmuir*, 9 (1993) 2764-2767.
- [3] R.P. Richter, A.R. Brisson, *Biophysical journal*, 88 (2005) 3422-3433.
- [4] M. Heim, G. Cevc, R. Guckenberger, H.F. Knapp, W. Wiegräbe, *Biophysical journal*, 69 (1995) 489-497.
- [5] L. Becucci, M.R. Moncelli, R. Naumann, R. Guidelli, *Journal of the American Chemical Society*, 127 (2005) 13316-13323.
- [6] L. Becucci, M.R. Moncelli, R. Guidelli, *Langmuir*, 22 (2006) 1341-1346.
- [7] L. Becucci, R. Guidelli, C. Peggion, C. Toniolo, M.R. Moncelli, *Journal of Electroanalytical Chemistry*, 576 (2005) 121-128.
- [8] L. Becucci, R. Guidelli, C.B. Karim, D.D. Thomas, G. Veglia, *Biophysical journal*, 93 (2007) 2678-2687.
- [9] L. Becucci, R.R. León, M.R. Moncelli, P. Rovero, R. Guidelli, *Langmuir*, 22 (2006) 6644-6650.
- [10] F.T. Buoninsegni, R. Herrero, M.R. Moncelli, *Journal of Electroanalytical Chemistry*, 452 (1998) 33-42.
- [11] M. Moncelli, L. Becucci, S.M. Schiller, *Bioelectrochemistry*, 63 (2004) 161-167.
- [12] J.C. Munro, C.W. Frank, *Langmuir*, 20 (2004) 10567-10575.
- [13] C. Peggion, F. Formaggio, C. Toniolo, L. Becucci, M.R. Moncelli, R. Guidelli, *Langmuir*, 17 (2001) 6585-6592.
- [14] A. Vakurov, M. Galluzzi, A. Podestà, N. Gamper, A.L. Nelson, S.D. Connell, *ACS nano*, 8 (2014) 3242-3250.
- [15] S. Zhang, A. Nelson, Z. Coldrick, R. Chen, *Langmuir*, 27 (2011) 8530-8539.
- [16] A. Nelson, *Journal of Electroanalytical Chemistry*, 601 (2007) 83-93.
- [17] A. Nelson, A. Benton, *Journal of Electroanalytical Chemistry and Interfacial Electrochemistry*, 202 (1986) 253-270.
- [18] A. Nelson, *Current Opinion in Colloid & Interface Science*, 15 (2010) 455-466.
- [19] D. Macdonald, *Transient techniques in electrochemistry*, Springer Science & Business Media, 2012.

- [20] C. Whitehouse, R. O'Flanagan, B. Lindholm-Sethson, B. Movaghar, A. Nelson, *Langmuir*, 20 (2004) 136-144.
- [21] E. Protopapa, A. Aggeli, N. Boden, P. Knowles, L. Salay, A. Nelson, *Medical engineering & physics*, 28 (2006) 944-955.
- [22] G. Brug, A. Van Den Eeden, M. Sluyters-Rehbach, J. Sluyters, *Journal of electroanalytical chemistry and interfacial electrochemistry*, 176 (1984) 275-295.
- [23] A. Nelson, N. Auffret, *Journal of Electroanalytical Chemistry and Interfacial Electrochemistry*, 244 (1988) 99-113.
- [24] A.V. Brukhno, A. Akinshina, Z. Coldrick, A. Nelson, S. Auer, *Soft Matter*, 7 (2011) 1006-1017.
- [25] F. Leermakers, A. Nelson, *Journal of Electroanalytical Chemistry and Interfacial Electrochemistry*, 278 (1990) 53-72.
- [26] Z. Coldrick, Phospholipid monolayers adsorbed on mercury electrodes with applications in sensing, in, University of Leeds, 2009.
- [27] E. Protopapa, S. Maude, A. Aggeli, A. Nelson, *Langmuir*, 25 (2009) 3289-3296.
- [28] S. Zhang, A. Nelson and P. Beales, *Langmuir*, 28 (2012) 12831-12837.

Chapter-7 Conclusion and Future work

DOPC monolayers supported on Hg are used primarily as a model phospholipid in all the experiments because of high compatibility achieved between the Hg and lipid due to the fluidity of DOPC. Electrochemical measurements yielding characteristic ACV scans and impedance plots of the DOPC coated Hg helped to explore the fundamentals of phase transitions exhibited by DOPC monolayer on Hg and the underlying structural changes in the monolayer. ACV scans and impedance plots of DOPC coated Hg are characteristic and very reproducible corresponding to a stable monolayer. Any change in the environment inside the electrochemical cell such as variation in the electrode type (HMDE or Hg/Pt), electrolyte composition and concentration or the presence of biomembrane active compounds such as substituted biphenyls and short peptides dispersed in an electrolyte affect the lipid coated Hg electrode in a characteristic mode. These effects can be identified as noticeable alterations observed in capacitance-potential plots and complex capacitance plots and represent modifications to the phospholipid layer conformation. The effect of electrolyte on the phase transitions are summarized as:

1. The phase transition underlying capacitance peak-1 is initiated at a critical value of field so an increase or decrease of this field through ion adsorption on DOPC will affect the applied potential required to initiate the transition. Cations in higher ionic strength electrolyte compress the double layer at the DOPC/electrolyte interface increasing the electric field across the lipid and decreasing the applied negative potential necessary to initiate the phase transition. For the same reason, in identical ionic strength solutions, cations with the strongest binding affinity to the DOPC head groups cause an

increase in field strength across the layer also decreasing the applied negative potential necessary to initiate the phase transition. Electrolyte anions e.g. I⁻ which adsorb on the DOPC polar groups decrease the field strength across the layer at applied negative potentials increasing the applied negative potential necessary to initiate the transition.

2. The influence of inorganic electrolyte ions on the occurrence of capacitance peak-2 underlying the N & G process which leads to re-adsorption of bilayer patches is related to the influence of the ions on the structure of the electrical double layer at the Hg interface following ingress of electrolyte into the DOPC layer. The kinetics of this phase transition is influenced by the strength of the electric field at the Hg interface. Higher concentration of cations compress the double layer increasing the electric field at the Hg interface requiring lower applied negative potentials to initiate the N & G mechanism increasing its rate. Smaller hydrated ions increase the rate of the N & G mechanism due to their more effective screening of the Hg interface so increasing the electric field strength.
3. Organic cations in inorganic electrolyte of constant concentration influence the characteristics of capacitance peak-1 in the same way as effected by the inorganic ions. These effects are directly related to their departure from polarity and their extent of adsorption on the DOPC monolayer. In addition organic cations in inorganic electrolyte of constant concentration slow down the kinetics of the N & G phase transition presumably by decreasing the effectiveness of K⁺ to screen the applied potential on the Hg surface.
4. The interactions between the pyrophosphate and other phosphate containing electrolytes and DOPC monolayer on Hg does not appeared to be significant in both the capacitance-potential and complex capacitance plots and only becomes noticeable on replacing the DOPC with DOPG (phospholipid lacking choline group).

Interactions of biological compounds with membrane models vary from adsorption to the penetration into the apolar lipidic core of the membrane. The driving forces

for these interactions also vary from simple electrostatic to dispersion forces, hydrophobic forces, hydrogen bonding, polarizability, dielectric properties etc. Using SAMs of DOPC on Hg as a model membrane system has allowed to investigate and propose the possible causes following the observed interactions.

Peptides interact with the DOPC monolayers depending on the interactive forces between the monolayer and peptides.

1. Dispersion forces are responsible for the interactions between DOPC monolayer and neutral apolar dipeptides.
2. Electrostatic forces are the key stimulus for the interaction between DOPC monolayer and polar charged dipeptides such as dipeptide of negatively charged glutamic acid and dipeptides of positively charged histidine. The extent of interaction further is determined by the apolarity of the peptides.

All the di- and tri-peptides mainly based on glycine such as Gly-Gly, Gly-Gly-Gly and Leu-Gly-Gly have a stabilizing effect on the monolayer.

The interaction of monosubstituted biphenyls with DOPC bilayers and monolayers is strongly dependent on the structural configuration and planarity of the molecules.

1. *p*-substituted biphenyls compared to *o*- and *m*-substituted biphenyls exhibit stronger interactions with DOPC bilayers and monolayers because of retained coplanarity of the two aromatic rings irrespective of the nature of substituent.
2. Biphenyls with electron donor substituents penetrate the apolar core of the bilayer whereas biphenyls with electron acceptor substituents are incorporated in the polar group region of the DOPC bilayer. Biphenyls located on the interface between the polar and apolar region increase the DOPC layer thickness.

3. Both electrochemical and fluorescence studies exhibit a consistent pattern of interactions between substituted biphenyls and DOPC bilayers and monolayers respectively suggesting that the Hg support has an insignificant influence on the interactions of biomembrane active compounds with DOPC.
4. Results indicate that the two structural features influencing the location of substituted biphenyls in DOPC bilayers and monolayers are: (i) the hydrogen bonding capability and (ii) the polarisability of the biphenyl rings.

The requirement of close resemblance to complex real biological system has uttered the need of establishing a bilayer system on Hg. The study on supported DOPC bilayers on Hg has helped to gain the following information about the properties of these bilayers.

1. The DOPC bilayers on Hg show a reversible, sharp and characteristic capacitive current peak at ~ -1.3 V due to an underlying phase transition process occurring in the response to applied electric fields.
2. These bilayers are significantly less permeable to Zn^{2+} at less negative potentials between -1.1 to -1.2 V compared to monolayer and uncoated Hg electrode and their permeability increases at higher negative potential between -1.3 to -1.4 V.
3. Dielectric relaxations in DOPC bilayer on voltage application in impedance measurements represent the ion movements within the bilayer that becomes increasingly significant at higher negative potentials between -1.2 to -1.4 V due to increased permeability of the bilayer at these potentials.
4. DOPC bilayer supported on Hg interacts with the silica nanoparticle resulting in a negative potential shift of the anodic capacitance current peak in the capacitance potential profile. This property of the bilayer resulting in a change in the position of the capacitance current peak in the capacitance potential profile in the presence of biological compounds can be exploited to investigate the molecular scale interactions of membrane active compounds

of biological relevance in detail leading to the application of Hg supported bilayer in biosensor industry.

COLLABORATIVE WORK

Peptide study (in relevance to prebiotic chemistry) was conducted in collaboration with Dr Terrence Kee from the School of Chemistry, University of Leeds, (Chapter 4). Electrochemical techniques were used to study the interaction of small and simple peptides with DOPC monolayer on Hg in terms of their effect on membrane stability suggesting their contribution towards making complex cell structures such as cell membranes as a preliminary step.

DIRECTIONS FOR FUTURE RESEARCH

Work will be carried out on following lines depending on the available opportunities:

Hg supported lipid bilayers

The DOPC bilayers deposited on Hg surface under applied electric fields need a further very extensive and detailed study (1) to gain a greater understanding of the nature and underlying mechanism of the exhibited phase transformation, (2) to transfer the system to the Pt chip electrode to develop into a credible and robust biosensor, (3) to explore the ion channel properties of DOPC bilayers in the presence of gramicidin, (4) to investigate the interaction of various membrane active compound such as peptides, toxins, antioxidants and pharmaceutical drugs with DOPC bilayers to get an insight into several parameters such their mechanism of action and structure activity relations (SAR), (5) to study the effects due to alteration in the model membrane lipid composition and (6) to characterize the bilayers in detail in the presence of other membrane components such as cholesterol and membrane bound proteins.

- (a) cholesterol: The effect of presence of cholesterol in the DOPC bilayer supported on Hg surface can be investigated in terms of changes in

permeability of the bilayer. In addition, effect of cholesterol on the ion channel properties of the gramicidin incorporated DOPC bilayers can also be very interesting to study.

- (b) membrane bound proteins: Study of inclusion and interaction of membrane bound proteins with DOPC bilayer on Hg to make it a more realistic biological membrane mimic can lead to its applications in the field of biotechnology.

Hg supported lipid monolayers

As a considerable amount of today's on-going research is in direction to investigate the role of many biological compounds as antioxidant and anti-cancer agents and their possible use in pharmaceutical drugs. I have a great interest in studying the interaction of these compounds of biological relevance such as terpenoids, alkaloids and steroids specially the ones with antioxidant activity in detail with the phospholipid monolayers supported on Hg conducting a parallel study on the free standing bilayer system to develop an understanding about their mechanism of action.